Evaporative behaviour of colloidal suspension droplets on surfaces: influence of suspension characteristics on the formation of dried microstructures and films

Miss Mahoulo Ahouansou

Submitted in accordance with the requirements for the degree of
Doctor of Philosophy

The University of Leeds

School of Chemical and Process Engineering

January 2020

Declaration

The candidate Mahoulo Ahouansou confirms that the work submitted is her own, except where work which has formed part of jointly-authored publications has been included. The contribution of the candidate and the other authors to this work has been explicitly indicated below. The candidate confirms that appropriate credit has been given within the thesis where reference has been made to the work of others.

The work in Chapter 4 and 5 of the thesis has appeared in publication as follows:

Ahouansou, M., Biggs, S. & Cayre, O. J. Attenuation of cracks pattern in dried silica colloidal droplets by anionic surfactant addition. NIP Digit. Fabr. Conf. ***2015,*** *443–447 (2015).*

I was responsible for the experimental design, work, interpretation and writing of the article. The contribution of the other authors was the proofreading and discussion of the experimental results.

The PMMA latex particles used in Chapter 4 and 5 of this thesis were synthesized by Mr Mohmed Mulla who also provided the training on the purification process of these said particles.

Acknowledgements

I would like to express my sincere gratitude to my supervisors, Prof Simon Biggs for offering me the opportunity to undertake a PhD and Dr Olivier Cayre for the guidance and advice during my doctoral research at the University of Leeds. I greatly appreciate their contributions to my growth as a researcher in the area of colloidal chemistry. I also appreciate the financial support of EPSRC under the grant EP/H018913/1. I would also like to thank all the persons involved in the I4T (Innovation in Industrial Inkjet Technology) project who made me a better researcher. I would also like to thank my academic colleagues (Maëlle, Luciana, Yuanyuan) and friends (George, Francis, Alain-Pascal, Alain-César) who made this PhD journey fun and memorable. I can consider myself lucky to have had their support during this journey.

I am also grateful for all the opportunities, which were offered to me at the University of Leeds and how it helped shape me into a great individual and set me on the path to become a better researcher.

I would also like to extent my gratitude to my work colleagues, Angela, Colin and Murray who graciously helped with this thesis proofreading.

Last but not least, I want to acknowledge my family for their support over a lifetime. I would like to extent my appreciation particularly to my mother and sister Sonate which were the rock that I stand on and that kept me going through their unwavering support and tough love during my darkest hours.

As I move on with my life, I will try my best to remember the life lessons and not to lose sight of what is important.

Abstract

The evaporation and wetting of a droplet on a surface is a trivial phenomenon encountered in daily life (water droplets on windows or flowers) and in many industrial processes (spraying of pesticides, micro/nano material fabrication, films coatings, DNA/RNA micro-arrays deposition, optical and electronic materials fabrication or ink jet printing). Since the addition of nanoparticles into base fluids leads to fluids with heightened physico-chemical properties (these fluids are commonly referred to as “nanofluids”); hence, it is mandatory to understand all the mechanisms at play in order to control/anticipate the stain geometry upon solvent evaporation. In fact, the specific physical phenomenon leading to well-ordered ring-like stains or films are yet to be fully uncovered. The main purpose of this experimental work is thus to enhance our current knowledge on deposit-stain formation while varying nanofluids composition.

A systematic study of the evaporative behaviour and final deposit structure produced upon solvent evaporation of nanoparticle laden fluids was undertaken. An attempt to explain the mechanisms leading to the formation of different patterns is proposed to help interpret the final distribution of particles throughout the evaporating surface area. The particle shape influence was studied and two main shapes were selected: spherical and disk-like particles.

For spherical nanoparticles, their addition to binary solvent mixtures and to additive laden base fluids (electrolyte and surfactant) were studied. Despite similar initial systems, various final patterns were observed from ring-like stain to films due to aggregated particles.

Disk-like nanoparticle were investigated in different compositions (binary mixtures and with additives such as electrolyte and surfactant). The sol-gel transition was observed at low nanoparticles concentration in the different systems leading to final films deposits and complex structures.

Conferences presentations and paper

Paper

1. Ahouansou, M., Biggs, S. & Cayre, O. J. Attenuation of cracks pattern in dried silica colloidal droplets by anionic surfactant addition. *NIP Digit. Fabr. Conf.* **2015,** 443–447 (2015).

Conference

1. Ahouansou, M., Biggs, S., "*Understanding the deposit behaviour of colloidal droplets"*, 14th European Student Colloid Conference (ESC), Potsdam, Germany, 2013

2. Ahouansou, M., Biggs, S., WCPT7, Beijing, China, *Influence of particle shape and concentration on the pattern of dried colloidal droplets",* 7th World Congress on Particle Technology (WCPT7), Beijing, China, 2014

3. Ahouansou, M., Biggs, S. and Cayre, O. J., "*Particle shape and concentration influence on the pattern of dried colloidal droplets"*, UK Colloids, London, UK, 2014

4. Ahouansou, M., Biggs, S. and Cayre, O.J., "IACIS, Mainz, Germany, *Attenuation of cracks pattern in dried silica colloidal droplets by anionic surfactant addition",* 15th Conference of the International Association of Colloid and Interface Scientist (IACIS), Mainz, Germany, 2015

Table of Contents

Declaration ... **ii**
Acknowledgements ... **iii**
Abstract ... **iv**
Conferences presentations and paper ... **v**
Table of Contents ... **vi**
List of Figures ... **x**
List of Tables ... **xxv**
Chapter 1 Introduction ... **1**
1.1 Background, motivation and objectives ... 2
1.1.1 Background ... 2
1.1.2 Motivation and objectives ... 5
1.2 Organisation of chapters ... 6
Chapter 2 Basic concepts and literature review ... **8**
2.1 Basic concepts ... 9
2.1.1 Stability of colloidal suspensions: Derjaguin, Landau, Verwey and Overbeek (DLVO) theory ... 9
2.1.2 Wetting properties, droplet profile characteristics and evaporation process ... 17
2.1.2.1 Wetting properties and droplet profile characteristics ... 17
2.1.2.2 Evaporation process of pure fluid ... 22
2.1.2.3 Evaporation of binary mixtures ... 26
2.2 Literature review ... 27
2.2.1 Particle transport during evaporation and influence of dried deposit patterns ... 27
2.2.2 Pattern formation and suitable variables to control final dried deposit structure ... 39
2.3 Summary and conclusions ... 44
Chapter 3 Experimental setup and procedures ... **46**
3.1 Particle characteristics ... 47
3.2 Fluids, surfactant and electrolyte ... 48
3.3 Characterisation of samples ... 48
3.3.1 Dynamic Light Scattering ... 48
3.3.2 Zeta potential ... 49
3.3.3 Turbiscan ... 50

3.4 Cleaning procedure and substrate preparation 51
3.4.1 Cleaning procedure 51
3.4.2 Preparation of uncoated glass slides 52
3.4.3 Preparation of coated glass slides 52
3.5 Wetting properties recording 53
3.5.1 Temperature and humidity monitoring 53
3.5.2 Image calibration 54
3.5.3 Wetting properties recording 56
3.5.4 Pendant drop measurements 61
3.6 Dried morphology analysis 64
3.6.1 Optical microscope analysis 64
3.6.2 Atomic Force Microscopy 64
3.6.3 Interferometer analysis 66

Chapter 4 Effect of nanoparticle concentration on the final deposit patterns of spherical Ludox AS-40® silica on uncoated solid surface 69

4.1 Introduction 70
4.2 Experimental methods 73
4.2.1 Materials 73
4.2.2 Characterisation and thickness measurements 73
4.3 Theoretical approach 75
4.3.1 Description of droplet evaporation 75
4.3.2 Cracks patterns 78
4.4 Results and discussion 79
4.4.1 Evaporative behaviour of Ludox AS-40® silica in aqueous suspensions 79
4.4.2 Residual dried deposits patterns 84
4.5 Summary 92

Chapter 5 Evaporative behaviour and subsequent deposit patterns for spherical silica and PMMA polymeric latex in binary solvent mixtures and with additives (electrolyte and surfactant): analysis of cracks patterns and aggregation of particles 95

5.1 Introduction 96
5.2 Experimental methods 98
5.2.1 Materials 98
5.2.1.1 Binary solvent ethanol/water system 99

5.2.1.2 Systems with additives (electrolyte and anionic surfactant) 99
5.2.2 Characterisation 100
5.3 Theoretical approach 102
5.3.1 Description of droplet evaporation 102
5.3.2 Crack patterns 105
5.4 Results and discussion 105
5.4.1 Evaporative behaviour and subsequent cracks pattern in ethanol/water binary mixtures 105
5.4.1.1 Ludox AS-40®: effect of the ethanol concentration in silica nanoparticles laden binary nanofluids droplets 105
5.4.1.2 PMMA latex in EtOH/H2O binary mixtures 114
5.4.2 Evaporative behaviour of Ludox AS-40 ® silica and PMMA latex with added electrolyte 119
5.4.2.1 Ludox AS-40 ® silica 119
5.4.2.2 PMMA latex with added electrolyte 125
5.4.3 Evaporative behaviour of Ludox AS-40 ® silica with added anionic surfactant 130
5.5 Summary 140
Chapter 6 Study of disk-like clay Laponite sessile droplets on solid surfaces: formation of film deposit by sol-gel transition and complex structure with electrolyte addition 143
6.1 Introduction 144
6.2 Materials and experimental methods 147
6.2.1 Suspensions preparation and characterization 147
6.2.2 Drying process monitoring 148
6.2.3 Deposition morphology measurements and characterization 148
6.2.4 Theoretical model 149
6.2.4.1 Main assumptions 149
6.2.4.2 Sol-gel transition 149
6.3 Results and discussion 151
6.3.1 Drying of sessile droplet of Laponite-base aqueous suspensions and deposit patterns 151
6.3.2 Drying of sessile droplets of Laponite-base effect of co-solvent addition 162
6.3.3 Effect of surfactant addition at low Laponite particles concentration 170

6.3.4 Formation of complex dried deposit patterns 175
6.4 Summary 182
Chapter 7 Conclusions and Future work 184
7.1 Key findings 185
7.1.1 Enhancing the “Coffee Ring Effect” for spherical particles, ... 185
7.1.2 Attenuation of crack patterns with anionic surfactant addition and formation of complex patterns 186
7.1.3 Suppression of “Coffee Ring Effect” by sol-gel transition with disk-like particles 186
7.2 Future work 187
7.3 Limitations of this work 188
7.4 Concluding statement 188
References 189
Nomenclature 206
Abbreviations 210
Appendix A 211

List of Figures

Figure 1-1: Pictures illustrating wetting in different situations: a) droplets on a glass window (Gate, 2014), b) raindrops on leaves (Lobb, 2016) and c) dew droplets on a cobweb (Parada, 2011). 2

Figure 1-2: Schematic representation of drying process of a colloidal sessile droplet: 1) generated droplet, 2) droplet impacting and spreading on the solid substrate, 3) droplet evaporating with evaporation flux showed by black arrows, 4) possible dried deposit patterns obtained upon solvent evaporation (ring-like, uniform or complex deposit). 4

Figure 1-3: Schematic representation of (a) CIJ printer (b) thermal inkjet printer(c) a piezo DoD inkjet printer (Derby, 2010). 4

Figure 2-1: Schematic representation of the electrical double layer for a negatively charge spherical silica colloidal particle of 20 nm diameter in an aqueous suspension. 12

Figure 2-2: Schematic of DLVO interactions for two negative same size spherical particles in aqueous suspension approaching each other. Left side represents stable suspension with electrostatic repulsive force overwhelming the attractive Van der Waals interaction. Right side represents the attractive Van der Waals interaction overwhelming electrostatic repulsive force which leads to particle aggregation hence unstable suspension. 14

Figure 2-3: Summary of interaction for a negatively charge spherical Ludox AS-40 colloidal particle of 40 mV in an aqueous suspension. 15

Figure 2-4: Schematic illustration of (a) how intermolecular interaction provoke surface tension due to the imbalance of forces between the molecules located at the liquid/vapour interface and the molecules in the bulk. When, the surface tension is high, the Bond number is low and the droplet contact radius is below the Capillary length, the gravitational forces are negligible, thus the droplet maintains a spherical cap shape. (b) when, the surface tension is low, the Bond number is high and the droplet contact radius is superior to twice the value of the Capillary length thus the gravitational forces are not negligible hence the droplet shape is deformed and flattens. 18

Figure 2-5: Schematic representation of a sessile droplet (a) on an ideal substrate forming a Young-Laplace/equilibrium contact angle, θ, with an apex height of H, a drop radius, r_d and the radius of sphere reshaping the spherical cap of the drop, R_S ,(b) Representation of the three interfacial tensions dictating the contact angle the droplet makes on the surface through the Young-Laplace equation at the three-phase contact line, (c) the apparent contact angle on an irregular substrate (angle measured experimentally), θ_{ACA} and (d) the real contact angle on an irregular substrate, θ_{RE}..... 20

Figure 2-6: Schematic representation of a droplet (a) Wenzel state, where the droplet penetrates the roughness of the substrate and (b) Cassie-Baxter state where the droplet rests on top of the substrate roughness features. 22

Figure 2-7: Schematic illustration of the diffusive evaporation of a spherical droplet resting on a smooth substrate. 24

Figure 2-8: Schematic of the evaporation of a droplet following a convective flow. A surface gradient is generated along the liquid/vapour interface due to an internal flow, thus surface tension will go from the highest temperature T_+ towards the lowest temperature T_-. 25

Figure 2-9: Schematic representation of the two main evaporation modes: (a) CCAM where the droplet dries with a decreasing contact radius r_d and a constant contact angle; (b) CCRM where the droplet dries with a decreasing contact angle and a constant contact radius (Picknett and Bexon, 1977). 26

Figure 2-10: (a) Schematic of the outward capillary flow carrying the solid particles from the centre towards the droplet periphery of a pinned sessile droplet resting on a flat substrate leading to the "coffee ring effect", (b) Schematic of the quantities responsible for the capillary flow. The volume loss contracts the height $h(r)$ vertically (Deegan et al., 1997). The non-uniform evaporative flux is represented by the thick black arrows while the internal capillary flow is in thin black arrows, (c) Coffee drops leave a ring stain upon evaporation. The majority of the particles are concentrated in the outer ring while a small quantity of coffee is localised in the centre of the drop. Precipitation of the dissolved coffee near the contact line is caused by super-saturation..... 28

Figure 2-11: Pictures of the resulting deposit for three identical drops dried under different conditions. The initial droplet radius was approximatively 4 mm. A schematic of the evaporation rate, J, is plotted next to the photographs. The dashed line of the curve represents the interface height variation (Deegan et al., 2000)..... 29

Figure 2-12: Pictures of dried deposits patterns left upon drying of 0.1 µm microspheres droplets at several concentrations on mica from (a) to ((d):(a) 1.0 %, (b) 0.25t%, (c) 0.13%, (d) 0.063% volume fractions while (e) represents the droplet width, W, normalised by its radius, R, as a function of the microspheres volume fractions (Deegan, 2000). **30**

Figure 2-13: Comparison between (a) experimental pictures of whole deposits structure of 113 nm polystyrenes on hydrophilic platinum substrate and (b) corresponding modellisation of experimental results using a Finite Element Model (FEM) (Breinlinger and Kraft, 2014). Dc represents the critical droplet diameter to exceed to form a coffee ring (Shen et al., 2010). **31**

Figure 2-14: Results showing in the left column the top-view of the final coffee-ring structures for different volumetric particle concentration and sticking parameter values (data series a represents low sticking while data series b represents high particle sticking). The right column represents the corresponding cross-sectional height profiles of the two series (Crivoi and Duan, 2014). **32**

Figure 2-15: Pictures of self-assembled particulates by "coffee ring effect"/capillary flow upon solvent evaporation (a) nanoparticles self-assembly patterning (Zavelani-Rossi et al., 2012) and (b)size discrimination (Monteux and Lequeux, 2011). **33**

Figure 2-16: Schematic representation of Marangoni flow in an evaporating sessile droplet on (a) outward motion along substrate (b) inward flow alongside the substrate with a central stagnation point. **35**

Figure 2-17: (a) On the left, a schematic of the thermal Marangoni flow inside the pinned evaporating droplets showcasing the stagnation point. On the right side, the dimensionless surface temperature T of the drying droplet as a function of the dimensionless radial distance to the centre r droplet radius at contact angles from 10 to 90°. The solid lines show the Finite Element Method results while the dashed lines represents the analytical equation (Xu et al., 2012), (b) In the left column, time evolution of water droplet volume with and without thermal Marangoni flow contribution compared to the experimental data at 50°C. The right column shows the infrared image of an evaporating sessile drop on an aluminium substrate heated at 40°C. The colour coding indicates the values of the actual temperatures in °C. It is worth noting that the apex of the drop is the coolest (Girard et al., 2008). **37**

Figure 2-18: (a) (i) Schematic description of the solutal Marangoni flow; Pictures of a sample containing 0.5 wt.% polystyrene particles (1330 nm) and 0.5 wt.% sodium dodecyl sulfate showcasing solutal Marangoni flow at different stages in the evaporation (ii) $t \approx 0.28t_E$, (ii) $t \approx 0.42t_E$, (iv) $t \approx 0.7t_E$, (v) $t \approx 0.86t_E$ and (vi) dried deposit (Still et al., 2012) and (b) Particle image velocimetry results showing flow field in terms of velocity vectors and vorticity for the three evaporation stages (Christy et al., 2011) 38

Figure 2-19: Different features obtain solvent evaporation. From left to right: (a) ring stain from a dried colloidal microspheres droplet with cracks in the structure (Deegan et al., 2000), (b) dried droplet of sodium poly styrene sulfonate containing 0.1 mol/L sodium chloride (Kaya et al., 2010), (c) multiple concentric rings of colloidal sulfate-modified polystyrene beads at 0.5 vol% (Yang et al., 2014), (d) uniform film deposit of ellipsoidal polystyrene particles (Yunker et al., 2011), (e) non-circular deposit of polystyrene particles (Biswas et al., 2010), (f) spider-web deposit of 200 nm polystyrene particles at 0.1 vol% (Yang et al., 2014). 40

Figure 3-1: Picture of a single Milli-Q-water droplet deposited on (a) silanized coated glass slides, the apparent contact is measured at $\Theta_{ACA} = 89 \pm 6°$ and (b) untreated glass slide the measured apparent contact is $\Theta_{ACA} = 34 \pm 2°$. 52

Figure 3-2: Picture of the ceramic chamber, constituted of two borosilicate glass viewing windows embedded in the side-walls, used to protect the experiment from the atmospheric contaminants and to measure the surface tensions and apparent contact angle Θ_{ACA} of the different systems..... 53

Figure 3-3: Picture of a calibrated image with the Krüss DSA-100 contact angle goniometer. The needle used to assess the sharpness of the image has a 1.25 mm outer diameter. 55

Figure 3-4: Snapshot of a calibration experiment done with the KSV CAM 200 contact angle goniometer. The needle used to assess the sharpness of the image has a 1.25 mm outer diameter. 56

Figure 3-5: Image of the Krüss DSA-100 contact angle goniometer composed of a CCD camera to record the side-view droplet profiles, a moving stage to adjust the sample position, a motor to automatically dispense the droplet volume, a syringe holder to fix the glass syringe, a LED light source to illuminate the sample from the side, a moving base to adjust the CCD camera focus and a built-in temperature and humidity chamber to record the atmospheric variation during the course of an experiment. 57

Figure 3-6: Image of the KSV CAM 200 contact angle goniometer composed of a digital CCD-camera, an adjustable stage, a syringe holder, an adjustable base to improve the focus of the camera, a LED light source to illuminate the droplet and allow a good contrast image, a temperature and humidity recorder with its associated probes to monitor the experiments conditions and a computer to process the recorded images. 57

Figure 3-7: Schematic representation of Young's force at equilibrium at the three-phase contact line of Milli-Q water resting on a substrate..... 58

Figure 3-8: Picture of a droplet of Ludox AS-40® suspended in Milli-Q water deposited on a glass slide and the manual circle fitting used to calculate its volume and contact angle. 59

Figure 3-9: Snapshot of a contact angle measurement of a Ludox AS-40® droplet at 2 wt% in 60 vol% EtOH deposited on a silanized glass slide. The Young-Laplace fitting was used to calculate the droplet apparent contact angle and volume of the droplet..... 60

Figure 3-10: Schematic representation of a pendant drop experiment with a droplet hanging at the tip of a needle, and the parameters used to calculate the shape factor (Attension Theta, 2015). 61

Figure 3-11: Snapshot of a Milli-Q water droplet hanging from the tip of a needle performing a pendant drop experiment to calculate the surface tension using the shape factor equation. Here, the surface tension of Milli-Q water is 72.2 mN/m. The fitting methods selected to calculate the surface tension was the Young-Laplace equation..... 63

Figure 3-12: Illustration of a dried deposit studied. The larger square represents the area observed by interferometer. The smaller square represents the area examined by optical microscopy. The illustration is not to scale. 64

Figure 3-13: Schematic representation of an AFM equipment, the laser beam is aimed at the cantilever tip which bent at it resonance frequency. The tip is then in contact with the sample and the reflection of the beam on the sample is send to the photodetector which transform the signal into a topographical image (Butt et al., 2005). 66

Figure 3-14: Image of the Bruker NPFLEX Interferometer system..... 67

Figure 3-15: (a) Schematic representation of the Interferometer (b) schematic representation of the vertical scanning of the sample..... 67

Figure 4-1: AFM 2-D images of the left side of the dried residual deposit of Ludox AS-40 ® at C_{Lud}= 10 ppm and the corresponding five profiles generated for the second droplet depositions. 74

Figure 4-2: Schematics illustration on a solid substrate for (a) droplet parameters: droplet contact radius, r_d, droplet height at its apex, H and apparent contact angle Θ_{ACA} (b) drying mode behaviour for a pinned contact line/ constant contact radius mode (CCRM) and (c) schematic illustration of nanoparticle transport during the evaporation process. The dashed line represents the initial contact line of the droplet. 77

Figure 4-3: Schematics of crack formation during the droplet evaporation process. With Pcap dimensionless number representing the flow through consolidated particles and X is the length scale at which the capillary pressure is relaxed. 78

Figure 4-4: Surface tension measurements of Ludox AS-40® as a function of nanoparticle concentration. 80

Figure 4-5: Drying sequence of aqueous base spherical Ludox AS-40® silica droplets on uncoated glass slides as a function of nanoparticle concentration (C_{Lud}=1 to 20000 ppm) at different time of droplet lifetime (1) 0%, (2) 25%, (3) 50%, (4) 75% and (5) 100%. The images are taken from side-view video recordings of the deposition with a contact angle goniometer. The scale bars on all images represents 1 mm. The red dotted lines represent the initial droplet contact diameter. 81

Figure 4-6: Evolution of normalized (a) droplet contact diameter $2r_d$ and (b) apparent contact angle θ_{ACA} with time of sessile droplet (initial volume V_0= 12.1 ± 0.7 µL) of aqueous base spherical Ludox AS-40 silica as a function of nanoparticle concentration on uncoated glass slides. The evolution was extracted from contact angle goniometer recordings. 82

Figure 4-7: (a) Time evolution of sessile droplets normalized volume of Ludox AS-40® silica as a function of nanoparticle concentration on uncoated glass slides. (b), (c) and (d) Comparison between the theoretical and experimental time evolution of sessile droplets volume of Ludox AS-40® silica at three concentrations 1, 1000 and 20000 ppm respectively. 83

Figure 4-8: Drying patterns photographs of dried sessile micro-droplets of aqueous Ludox AS-40® silica at different concentration (C_{Lud}= 1,10,100,1000,10000 and 20000 ppm) and the optical micrographs corresponding to the magnification of the area inside the black box on uncoated glass slides. The edges features are highlighted by black lines. The white scale bars represent 1 mm on all images. 86

Figure 4-9: Three-dimensional topographical images of the residual dried deposit patterns of Ludox AS-40® on uncoated glass slides (a) to (d) AFM images and corresponding cross-sectional profiles of the left side edge at Ludox particle concentration C_{Lud}= 1,10,100 and 1000 ppm; (d) and (e) WLI images corresponding to cross-sectional profiles of the left side edge at C_{Lud}= 10000 ppm and 20000 ppm respectively. 88

Figure 4-10: (a) Dimensionless analysis of (a) film thickness and (b) width of the residual dried deposit normalised with the initial droplet contact radius against the initial Ludox AS-40® particle concentration extracted from AFM (C_{Lud}=1 to 1000 ppm) and WLI (C_{Lud}=d10000 and 20000 ppm). 90

Figure 4-11: (a) Residual dried deposit thickness against cracks spacing for aqueous Ludox AS-40® silica droplets, (C_{Lud}= 1 to 20000 ppm); (b) Collapse of the crack spacing data with the nanoparticle hydrodynamic diameter. The value above the points correspond to the particle concentration in ppm..... 90

Figure 4-12: (a) Crack spacing as a function of the film thickness (b) Noncollapse of the crack spacing data when scaled with the film thickness. For different dispersions and different particles size (Lee and Routh, 2004). 91

Figure 5-1: Schematics illustration on a solid substrate for (a) droplet parameters: droplet contact radius, r_d, droplet height at its apex, H and apparent contact angle Θ_{ACA} (b) drying mode behaviour for a pinned contact line/ constant contact radius mode (CCRM) and (c) Mixed drying mode (MDM) decreasing contact radius and apparent contact angle. The dashed line represents the initial contact line of the droplet, (d) Schematic illustration of nanoparticle transport during the evaporation process. 104

Figure 5-2: Surface tension measurements of MilliQ-water and Ludox AS-40® silica aqueous suspensions particle at 20000 ppm in different ethanol/water concentration (C_{EtOH}= 50 to 90 vol%). 106

Figure 5-3: Drying sequence of Ludox AS-40® silica droplets (at 20000 ppm) in different water/ethanol mixtures (ethanol concentration, C_{EtOH}= 50 to 90 vol%) at different time of droplet lifetime (1) 0%, (2) 25%, (3) 50%, (4) 75% and (5) 100%. The images are side-view recordings of the deposition using a contact angle goniometer. The scale bars on all images represents 1 mm. The red dotted lines represent the initial droplet contact diameter. Droplets were deposited on silane coated glass slides. 108

Figure 5-4: Evolution of (a) droplet contact diameter $2r_d$ (b) apparent contact angle θ_{ACA} and (c) volume V of Ludox AS-40® at 2wt% in different water/ethanol mixtures (ethanol concentration, C_{EtOH}= 50 to 90 vol%) with time on the entire droplet lifetime and a zoom in between 0 to 1000 s. The droplets were deposited on silane coated glass slides. The evolution was extracted from contact angle goniometer recordings. 109

Figure 5-5: The averaged evaporation rate of C_{Lud}= 2 wt% nanofluid droplets as a function of ethanol concentration and the comparison with the literature data where substrates were not heated and cooled (Sefiane et al., 2003; Cheng et al., 2006; Liu et al., 2008; Zhong and Duan, 2014). 111

Figure 5-6: Two-dimensional WLI images of dried deposit of Ludox AS-40® silica in different ethanol/water mixtures (C_{EtOH}= 50 to 90 vol%) and optical micrographs corresponding to the magnification of the area inside the black box on uncoated glass slides. The white scale bars represent 1 mm on all images. 112

Figure 5-7: Evolution of (a) droplet contact diameter $2r_d$, (b) apparent contact angle θ_{ACA} (c) volume V of PMMA polymeric particles at 0.4 wt% in different ethanol/water mixtures (C_{EtOH}= 50 to 90 vol%) with time on the entire droplet lifetime and a zoom of the evolution between 0 to 300 s is presented. The droplets were deposited on silane coated glass slides. The evolution was extracted from contact angle goniometer recordings. 116

Figure 5-8: Three-dimensional topographical WLI images of PMMA latex dried droplets on silane coated glass slides and corresponding cross-sectional profiles along the black dotted line in different ethanol/water mixtures..... 117

Figure 5-9: Particle size and Zeta-potential (ZP) measurements of Ludox AS-40® at 20 000 ppm as a function of NaCl concentration (C_{NaCl}= 0 to 300 mM). 120

Figure 5-10: Evolution of (a) droplet contact diameter $2r_d$, (b) apparent contact angle θ_{ACA} and (c) droplet volume V with time of Ludox AS-40® (at 20000 ppm) sessile droplets with added electrolyte (C_{NaCl}= 0 to 300 Mm). The droplets were deposited on uncoated glass slides. The evolution was extracted from contact angle goniometer recordings. 121

Figure 5-11: Drying patterns photographs of dried micro-droplets of Ludox AS-40® (at 2wt%) and the optical micrographs corresponding to the magnification area inside the black box with different added electrolyte concentration (C_{NaCl}= 0 to 300 mM) on uncoated glass slides. The white scale bars represent 1 mm on all images. 123

Figure 5-12:Three-dimensional topographical WLI images of Ludox AS-40® dried droplets on uncoated glass slides at 20 000 ppm as a function of NaCl concentration: (a) 10 mM, (b) 50 mM, (c) 150 mM (d) 250 mM, (e) 300 mM and (d) chart represents the influence of NaCl concentration on the dried deposits edges features (height and width). 125

Figure 5-13: Evolution of (a) droplet contact diameter $2r_d$, (b) apparent contact angle θ_{ACA} and (c) volume V with time of PMMA latex at 0.4 wt% sessile droplets with added electrolyte (C_{NaCl}= 0.03 to 1.0 M). the droplets were deposited on silane coated glass slides. The different evolutions were extracted from contact angle goniometer recordings. 126

Figure 5-14: Three-dimensional topographical WLI images of dried droplets of PMMA latex (at 0.4 wt%) on silane coated glass slides and corresponding cross-sectional profiles along the black dotted line with added electrolyte (C_{NaCl}= 0.03 to 1.0 M).... 128

Figure 5-15: Particle size and zeta-potential (ZP) of aqueous based Ludox AS-40® suspensions with different added SDS concentration (C_{SDS}= 0 to 30 mM). 131

Figure 5-16: Surface tensions measurements of aqueous based Ludox-AS® suspensions (C_{Lud}= 2 wt% in final suspensions) with and without addition of SDS (C_{SDS}= 0 to 30 mM). 131

Figure 5-17: Evolution of droplet contact diameter $2r_d$ of Ludox AS-40® at 2 wt% droplets with different added SDS concentration (C_{SDS}= 0 to 30 mM) with time on the entire droplet lifetime and a zoom in between 0 to 600 s. The droplets were deposited on uncoated glass slides. The evolution was extracted from contact angle goniometer recordings. 132

Figure 5-18: Evolution of apparent contact angle θ_{ACA} of Ludox AS-40® at 2wt% as with different added SDS concentration (C_{SDS}= 0 to 30 mM) with time on the entire droplet lifetime and a zoom in between 0 to 600 s. The droplets were deposited on uncoated glass slides. The evolution was extracted from contact angle goniometer recordings. 134

Figure 5-19: (a) Evolution of volume V of Ludox AS-40® at 2wt% with different added SDS concentration (CSDS= 0 to 30 mM) with time on the entire droplet lifetime and a zoom in between 0 to 600 s. The droplets were deposited on uncoated glass slides. The evolution was extracted from contact angle goniometer recordings. (b) Evolution of SDS local concentration in the micro-droplets with time in the different initial concentration C_{SDS}= 4 to 30 mM. 135

Figure 5-20: Two-dimensional WLI images of dried deposit of Ludox AS-40® silica with different added SDS concentration (C_{SDS}= 0 to 30 mM) and optical micrographs corresponding to the magnification of the area inside the black box on uncoated glass slides. The white scale bars represent 1 mm on all images. 138

Figure 5-21: Data for aqueous based Ludox AS-40® suspensions with different added SDS concentration (C_{SDS}= 0 to 30 mM) (a) collapse of crack spacing data with hydrodynamic scaling and (b) cracks spacing as a function of film thickness. 139

Figure 6-1: Side-view evolution profile of an evaporation-driven sol-gel Laponite sessile droplet of contact radius r_d. The light blue represents the sol part while the dark blue represents the gel part of the deposit. 150

Figure 6-2: Surface tension measurements of MilliQ-water and aqueous based Laponite suspensions as a function of Laponite concentration (C_{Lap}= 1 to 20000 ppm). 152

Figure 6-3: Drying sequence of Laponite sessile droplets (at C_{Lap}= 1000 ppm) at different time of droplet lifetime (1) 0%, (2) 12.5%, (3) 25%, (4) 50% and (5) 75% and (6) 100%. The images are side-view recordings of the deposition using a contact angle goniometer. The scale bars on all images represents 1 mm. The red dotted lines represent the initial droplet contact diameter while the yellow dotted lines represent the receding of the droplet contact diameter. Droplets were deposited on uncoated glass slides 153

Figure 6-4: Evolution of normalized (a) droplet contact diameter $2r_d$ (b) apparent contact angle θ_{ACA} and (c) volume V of aqueous based Laponite suspensions at different concentration C_{Lap}=1 to 20000 ppm with time on the entire droplet lifetime. The droplets were deposited on uncoated glass slides. The evolution was extracted from contact angle goniometer recordings. .(d), (e) and (f) comparison between the theoretical and experimental time evolution of sessile droplets volume of Laponite at three concentrations 1, 1000 and 20000 ppm. 154

Figure 6-5: (a) Evolution of volume V of aqueous based Laponite droplets at different Laponite concentration (C_{Lap}=1 to 20000 ppm) with time on the entire droplet lifetime. Evolution of local Laponite concentration of aqueous based Laponite droplets at (b) 1000 ppm, (c) 10000 ppm and (d) 20000 ppm. The droplets were deposited on uncoated glass slides. The evolution was extracted from contact angle goniometer recordings. 156

Figure 6-6: Three-dimensional topographical WLI images of dried droplets of aqueous based Laponite (at C_{Lap}=1,10 and 100 ppm) on uncoated glass slides and corresponding cross-sectional profiles along the black dotted line..... 159

Figure 6-7: Three-dimensional topographical WLI images of dried droplets of aqueous based Laponite (at C_{Lap}=1000 to 20000 ppm) on uncoated glass slides and corresponding cross-sectional profiles along the black dotted line..... 160

Figure 6-8: Influence of Laponite concentration (C_{Lap}= 1 to 20000 ppm) on the droplet dried deposits features (height and width). 161

Figure 6-9: Evolution of contact diameter $2r_d$ with time of aqueous based Laponite (C_{Lap}= 0.1 wt%) micro-droplets in different ethanol/water mixtures on silane-coated substrates (a) 50 vol%, (b) 60 vol%, (c) 70 vol%, (d) 80 vol%, (e) 90 vol%. The different evolutions were extracted from contact angle goniometer recordings 163

Figure 6-10: Evolution of apparent contact angle θ_{ACA} with time of aqueous based Laponite at C_{Lap}= 0.1 wt% sessile droplets in different ethanol/water mixtures (a) 50 vol%, (b) 60 vol%, (c) 70 vol%, (d) 80 vol% and (e) 90 vol%. The droplets were deposited on silane coated glass slides. The different evolutions were extracted from contact angle goniometer recordings. 165

Figure 6-11: (a) Evolution of volume V with time of aqueous based Laponite at C_{Lap}= 0.1 wt% sessile droplets in different ethanol/water mixtures (C_{EtOH}= 50 to 90 vol%). Evolution of Laponite local concentration in the micro-droplets with time in the different ethanol/water mixtures at (b) 50 vol%, (c) 60 vol%, (d) 70 vol%, (e) 80 vol% and (f) 90 vol%. The droplets were deposited on silane coated glass slides. The different evolutions were extracted from contact angle goniometer recordings. 166

Figure 6-12: Three-dimensional topographical WLI images of aqueous based Laponite at C_{Lap}= 0.1wt% dried droplets on silane coated glass slides in different ethanol/water mixtures (C_{EtOH}=50 to 90 vol%) and the corresponding cross-sectional profiles along the black dotted lines. 168

Figure 6-13: Evolution of dried deposit features (width W and height T_H) of aqueous based Laponite droplets C_{Lap}= 0.1wt% in different ethanol/water mixtures (C_{EtOH}=50 to 90 vol%). The droplets were deposited on silane coated glass slides..... 169

Figure 6-14: Evolution of (a) droplet contact diameter $2r_d$ and (b) apparent contact angle θ_{ACA} with time of aqueous based Laponite at C_{Lap}=1000 ppm droplets with different added surfactant concentration (C_{SDS}= 0 to 30 mM) over the entire droplets lifetime and a zoom in between 0 to 300s. The droplets were deposited on uncoated glass slides. The evolution was extracted from contact angle goniometer recordings. 171

Figure 6-15: (a) Evolution of volume V with time of aqueous based Laponite at C_{Lap}=0.1 wt% sessile droplets with different added surfactant concentration (C_{SDS}= 0 to 30 mM). Evolution of local concentration in aqueous based Laponite sessile droplets with different added surfactant concentration b) 4 mM (c) 7.5 mM (d) 15 mM and (e) 30 mM. The droplets were deposited on uncoated glass slides. The different evolutions were extracted from contact angle goniometer recordings. 172

Figure 6-16: Three-dimensional topographical WLI images of aqueous based Laponite (at C_{Lap}= 0.1 wt%) dried deposits on uncoated glass slides with different added surfactant concentration (C_{SDS}= 0 to 30 mM) and their corresponding cross-sectional profiles along the black dotted line. 174

Figure 6-17: Features (height, T_H and width W) evolution of dried deposits of aqueous based Laponite sessile droplets at C_{Lap}= 0.1 wt% with different added surfactant concentration (C_{SDS}= 0 to 30 mM). 175

Figure 6-18: Evolution of (a) droplet contact diameter $2r_d$ and (b) apparent contact angle θ_{ACA} of Laponite at C_{Lap}=0.1wt% with different added electrolyte concentrations (C_{NaCl}= 1 to 10 mM) with time on the entire droplet lifetime and a zoom in between 0 to 300 s. The droplets were deposited on uncoated glass slides. The evolution was extracted from contact angle goniometer recordings. 177

Figure 6-19: (a) Evolution of volume V with time of aqueous based Laponite at C_{Lap}=0.1 wt% sessile droplets with different added electrolyte concentration (C_{NaCl}= 1 to 10 mM). Evolution of local concentration in aqueous based Laponite sessile droplets with different added electrolyte concentration b) 1 mM (c) 2 mM (d) 4 mM (e) 6 mM and (e) 30 mM. The droplets were deposited on uncoated glass slides. The different evolutions were extracted from contact angle goniometer recordings. 178

Figure 6-20: Three-dimensional topographical WLI images of dried deposits of Laponite at C_{Lap}= 1000 ppm with different added electrolyte concentration (C_{NaCl}= 1 to 10 mM) and their corresponding cross-sectional profiles along the black dotted lines. The droplets were deposited on uncoated glass slides. 180

Figure 6-21: Features variation of dried deposit (height, T_H and width W) of aqueous based Laponite droplets at C_{Lap}= 0.1wt% with different added electrolyte concentration (CNaCl= 1 to 10 mM). **181**

Figure A-1: FE-SEM micrograph of PMMA latex particles at 0.03 wt% after purification with average diameter Dp= 32 ± 9 nm. **214**

Figure A-2: Drying sequence of aqueous based PMMA latex particles droplets on uncoated glass slides at C_{Lat}= 4000 ppm at different time of droplet lifetime: (1) 0%, (2) 25%, (3) 50%, (4) 75% and (5) 100%. The images were taken from side-view video recordings of the deposition with a contact angle goniometer. The white scale bars represent 1 mm. The red dotted lines represent the initial droplet contact diameter. **215**

Figure A-3: Evolution of (a) droplet contact diameter $2r_d$ (b) apparent contact angle θ_{ACA} and (c) volume V_{Lat} of PMMA latex at C_{Lat}= 0.4 wt% with time on the entire droplet lifetime. The droplets were deposited on uncoated glass slides. The evolution was extracted from contact angle goniometer recordings. **216**

Figure A-4: Dried deposit of PMMA latex droplets (C_{Lat}= 4000 ppm) (a) optical micrograph of right side of the deposit, (b) three-dimensional topographical cross-sectional profile WLI image of dried deposit. **216**

Figure A-5: Drying sequence of aqueous based Ludox AS-40® droplets on uncoated glass slides as a function of electrolyte concentration (C_{NaCl}= 0 to 300 mM) at different time of droplet lifetime: (1) 0%, (2) 25%, (3) 50%, (4) 75% and (5) 100%. The images were taken from side-view video recordings of the deposition with a contact angle goniometer. The white scale bars represent 1 mm. The red dotted lines represent the initial droplet contact diameter. **217**

Figure A-6: Drying sequence of aqueous based Ludox AS-40® droplets on uncoated glass slides as a function of surfactant concentration (C_{SDS}= 0 to 30 mM) at different time of droplet lifetime: (1) 0%, (2) 25%, (3) 50%, (4) 75% and (5) 100%. The images were taken from side-view video recordings of the deposition with a contact angle goniometer. The white scale bars represent 1 mm. The red dotted lines represent the initial droplet contact diameter. **218**

Figure A-7: Surface tension of PMMA latex at C_{Lat}= 4000 ppm in different ethanol concentration C_{EtOH}= 50 to 90 vol%. **219**

Figure A-8: Drying sequence of aqueous based PMMA latex particles droplets on silane coated glass slides as a function of ethanol/water concentration (C_{EtOH}= 50 to 90 vol%) at different time of droplet lifetime: (1) 0%, (2) 25%, (3) 50%, (4) 75% and (5) 100%. The images were taken from side-view video recordings of the deposition with a contact angle goniometer. The white scale bars represent 1 mm. The red dotted lines represent the initial droplet contact diameter. 220

Figure A-9: Two-dimensional topographical WLI images of dried deposit of PMMA latex particles droplets in different ethanol/water mixtures (C_{EtOH}= 50 to 90 vol%) and optical micrographs corresponding to the magnification of the area inside the black box on silane coated glass slides. The white scale bars represent 1 mm on all images. 221

Figure A-10:Transmitted intensity profiles given by Turbiscan as a function of the height of the sample and versus time for the PMMA latex in different EtOH/H2O mixtures (a) 50 vol%, (b) 60 vol%, (c) 70 vol%, (d) 80 vol% and (e) 90 vol%. 222

Figure A-11: Drying sequence of aqueous based PMMA latex particles droplets on silane coated glass slides as a function of electrolyte concentration (C_{NaCl}= 0.03 to 1.0 M) at different time of droplet lifetime: (1) 0%, (2) 25%, (3) 50%, (4) 75% and (5) 100%. The images were taken from side-view video recordings of the deposition with a contact angle goniometer. The white scale bars represent 1 mm. The red dotted lines represent the initial droplet contact diameter. 223

Figure A-12: Two-dimensional topographical WLI images of dried deposit of PMMA latex particles with different added electrolyte concentration (C_{NaCl}= 0.03 to 1.0 M) and optical micrographs corresponding to the magnification of the area inside the black box on uncoated glass slides. The white scale bars represent 1 mm on all images. 224

Figure A-13:Backscattered intensity profiles given by Turbiscan as a function of the sample height and versus time for the PMMA latex with different added NaCl concentration (a) 0.03 M, (b) 0.1 M, (c) 0.4 M and (d) 1.0 M. 225

Figure A-14: Surface tension measurements of MilliQ-water and aqueous based Laponite suspensions (at C_{Lap}= 0.1 wt%) as a function of ethanol concentration (C_{EtOH}= 50 to 90 vol%)..... 230

Figure A-15: Surface tension measurements of MilliQ-water and aqueous based Laponite suspensions (at C_{Lap}= 0.1 wt%) as a function of SDS concentration (C_{SDS}= 4 to 30 mM). 230

Figure A-16: Drying sequence of aqueous based Laponite droplets on uncoated glass slides as a function of Laponite concentration (C_{Lap}= 0 to 20000 ppm) at different time of droplet lifetime: (1) 0%, (2) 25%, (3) 50%, (4) 75% and (5) 100%. The images were taken from side-view video recordings of the deposition with a contact angle goniometer. The white scale bars represent 1 mm. The red dotted lines represent the initial droplet contact diameter. 231

Figure A-17: Drying sequence of aqueous based Laponite droplets on silane coated glass slides as a function of ethanol concentration (C_{EtOH}= 50 to 90 vol%) at different time of droplet lifetime: (1) 0%, (2) 25%, (3) 50%, (4) 75% and (5) 100%. The images were taken from side-view video recordings of the deposition with a contact angle goniometer. The white scale bars represent 1 mm. The red dotted lines represent the initial droplet contact diameter. 232

Figure A-18: Drying sequence of aqueous based Laponite droplets on uncoated glass slides with different added surfactant concentration (C_{SDS}= 0 to 30 mM) at different time of droplet lifetime: (1) 0%, (2) 25%, (3) 50%, (4) 75% and (5) 100%. The images were taken from side-view video recordings of the deposition with a contact angle goniometer. The white scale bars represent 1 mm. The red, green and yellow dotted lines represent the initial, advancing and receding droplet contact diameter respectively. 233

Figure A-19: Drying sequence of aqueous based Laponite droplets on uncoated glass slides with different added electrolyte concentration (C_{NaCl}= 0 to 10 mM) at different time of droplet lifetime: (1) 0%, (2) 25%, (3) 50%, (4) 75% and (5) 100%. The images were taken from side-view video recordings of the deposition with a contact angle goniometer. The white scale bars represent 1 mm. The red and yellow dotted lines represent the initial and receding droplet contact diameter respectivel..... 234

List of Tables

Table 3-1: Particle systems properties. 47

Table 4-1: Bond number and ratio of diffusion time to evaporation time for all systems studied. 75

Table 4-2: Droplet pinning time as a function of Ludox AS-40 (R) nanoparticle concentration. 87

Table 5-1: Bond number and ratio of diffusion time to evaporation time for all systems studied for spherical Ludox and PMMA latex. 103

Table 5-2: Summary of evaporation rate of ethanol/water droplets laden with PMMA particles at different ethanol/water concentration. 115

Table 5-3: Particle diameter of PMMA particles in the different ethanol/water mixtures with the Stokes sedimentation law and the Turbiscan data. 119

Table 5-4: Particle diameter of PMMA particles with electrolyte addition using the Stokes sedimentation law and the Turbiscan data. 126

Table 5-5: Evaporation rate of Ludox AS-40® at 2 wt% with different added SDS concentration CSDS= 4 to 30 mM. 136

Table 6-1: Measurements of Bond number for aqueous based Laponite, in binary mixtures and with additives (surfactant and electrolyte) 149

Table 6-2: Summary of different evaporation rate of aqueous based Laponite droplets as a function of initial Laponite concentration (C_{Lap}= 0.0001 to 2 wt%) 157

Table 6-3: Summary of the different evaporation rate of Laponite sessile droplets with and without added electrolyte (C_{NaCl}= 0 to 10 mM). 179

Chapter 1
Introduction

1.1 Background, motivation and objectives

1.1.1 Background

The drying of droplets is a commonly observed phenomenon in everyday life. From rain droplets on windows or leaves (macroscopic), to dew droplets on cobwebs (microscopic) or to the condensation of water to atmospheric aerosol particulates (nanoscale), the daily occurrence of evaporation at any scale is obvious. Typically, upon contact with a solid surface, a droplet shape evolves until it reaches a thermodynamic equilibrium (state of minimal energy), between the phases at the three-phase contact line (TPCL, solid-liquid, liquid-gas and solid-gas interfaces). In the 19th century, the work of Thomas Young (Young, 1805) initially described the interfacial forces at work through a relationship between the angle formed by the liquid and the solid where it rests on.

Figure 1-1: Pictures illustrating wetting in different situations: a) droplets on a glass window (Gate, 2014)**, b) raindrops on leaves** (Lobb, 2016) **and c) dew droplets on a cobweb** (Parada, 2011)**.**

This simple phenomenon, at first sight, is a straightforward and efficient way to organise, distribute and self-assemble particulates upon solvent (i.e the

liquid forming the droplet) evaporation when such droplets contain solid particles (for example colloidal particles). Indeed, at the nanometre scale materials properties are significantly different and unique in comparison with their bulk properties. These properties differences stem from the fact that at this scale nanoparticles have a high surface area to volume ratio, thus energy and molecular conformation when compared to the bulk (Everett, 1988). Hence, the drying of a sessile particle-laden droplet (droplet resting on a solid surface) is of interest in several industrial applications. Indeed, the evaporation of colloidal suspensions is found throughout many fields: painting, coating, functional materials and inkjet printing. The variety of droplet deposition applications conveys the relevance of improving colloidal systems formulation in order to reach a deeper understanding of the behaviour and processes occurring during drying.

Inkjet printing has been a widely applied technology used for professional purposes in the office, personal uses at home (e.g. pictures, flyers, etc.) and in the industrial market (e.g. printed packaging, labels, etc.) since the 1950s (Magdassi, 2010). Apart from these classical printing applications, recently due to its high reproducibility and accuracy of droplet deposition, its applications have increased (e.g printing of metallic nanoparticles (Fuller, 2002; Molesa et al., 2003; Lee and Oh, 2010), in the life sciences area with tissue engineering (Nakamura et al., 2005; Boland et al., 2006), tracking and security with dyes in bar codes (Baretta et al., 2006), for 2-D and 3-D printing for electronics and ceramics (Mott et al., 2004; Noguera et al., 2005; Soltman and Subramanian, 2008; Chen and Evans, 2009).

The industrial inkjet process involves several aspects: during an inkjet printing operation, the first key feature is the generation of a droplet through some form of nozzle. This droplet must then be accurately deposited on a substrate with good control of its location. Subsequently, the drop dries out depositing its contents (e.g. particles, pigments, molecules or dyes) onto the substrate where they should ideally persist (cf. Figure 1-2).

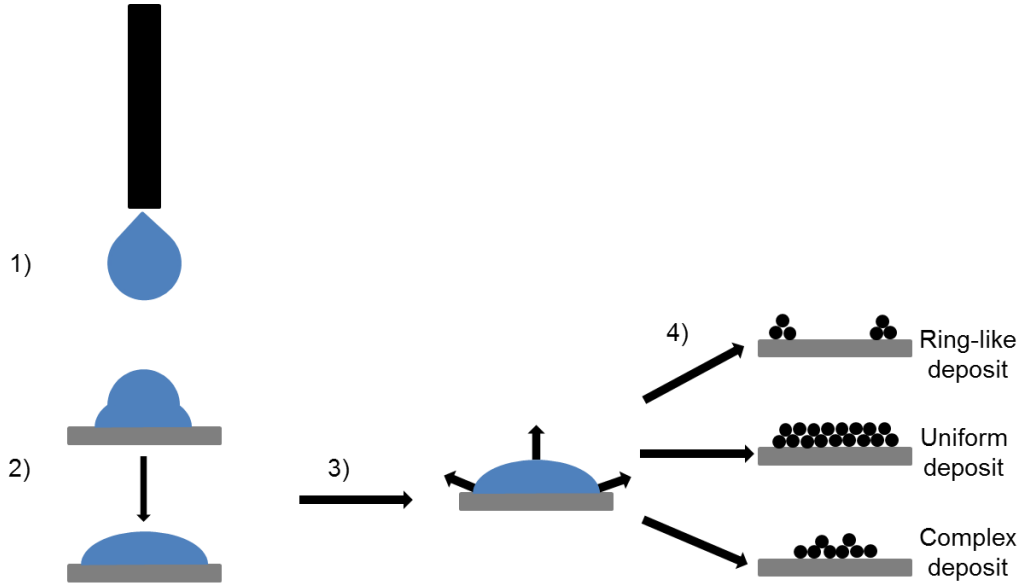

Figure 1-2: Schematic representation of drying process of a colloidal sessile droplet: 1) generated droplet, 2) droplet impacting and spreading on the solid substrate, 3) droplet evaporating with evaporation flux showed by black arrows, 4) possible dried deposit patterns obtained upon solvent evaporation (ring-like, uniform or complex deposit).

Currently, to obtain a droplet, two main approaches are used to control the ejection of a fluid from a nozzle. These techniques are known as continuous inkjet (CIJ) and Drop-on-Demand (DoD) (Magdassi, 2010).

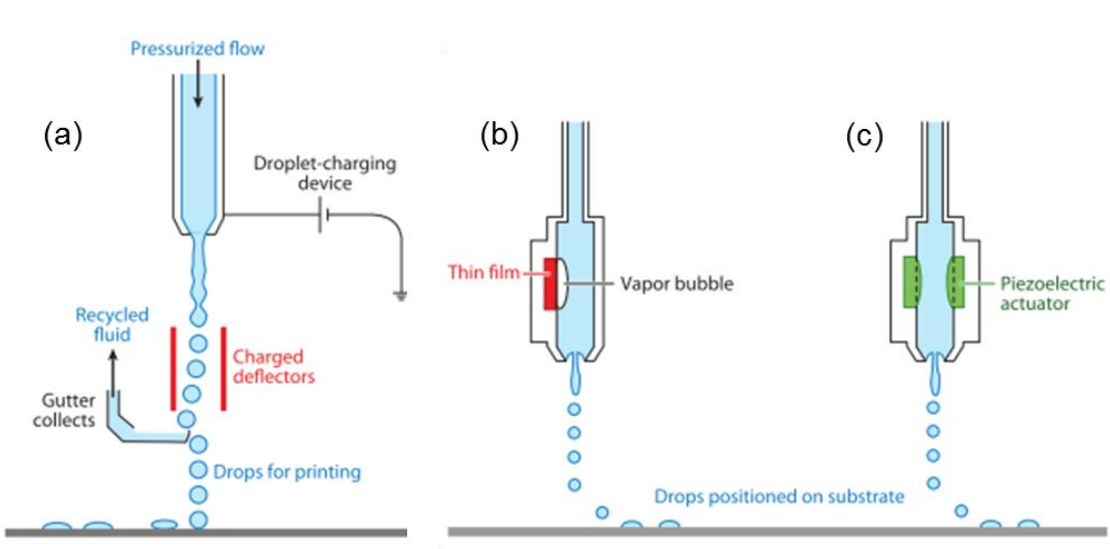

Figure 1-3: Schematic representation of (a) CIJ printer (b) thermal inkjet printer (c) a piezo DoD inkjet printer (Derby, 2010)**.**

The CIJ technique implies a continuous drop generation from a liquid stream (cf. Figure 1-3a). The DOD approach, by contrast, is a technique where the droplet is only generated when required. DOD can be further divided into three main drop generation mechanisms, viz. thermal (cf Figure 1-3b), piezo (cf. Figure 1-3c) and electrostatic.

1.1.2 Motivation and objectives

In this thesis, the focus is aimed at increasing the understanding of the complex phenomena involved in the deposition of solid particles during a droplet evaporation process. Extensive work has been done to further the knowledge and thus control the dried deposit patterns. However, total control of the dried deposit patterns upon solvent evaporation is still a challenge yet to overcome for microliter droplets. Any work, that developpes an in-depth comprehension of how the drying process works and its influence on the dried deposit structure is therefore of obvious interest. As such, the study of drop generation, drop deposition and the formation of complex deposits for industrial purpose are mandatory. To this end, this thesis has investigated the drying of colloidal nanoparticles.

Furthermore, extensive studies have focused their efforts to control the end results in industrial inkjet printing. For a clear understanding of the drying processes, internal flows for the duration of the droplet evaporation can be studied to correlate how the final deposit is formed. Modification of the formulation of the droplet's suspension can also be undertaken to control the final deposit structure. Despite, intensive work done on the subject, anticipating the final patterns is complicated. The knowledge gained from this work is significant in order to achieve a better control over the solids deposit morphology and, as such, a better end product in many application areas. Previous work has already shown that particles in the system assemble and structure themselves depending on several factors to form different dried patterns : the substrate properties and solvent (Pauliac-Vaujour et al., 2008), the size, concentration (Léopoldès et al., 2003), (Sefiane, 2010) , shape (Yunker et al., 2011) or type of nanoparticles in suspension (Sefiane, 2014); application of external force (Mampallil et al., 2012). The experimental research has been done to further the knowledge governing the evaporation of fluids containing different nanoparticles in suspension, aiming for the complete understanding of this phenomenon for inkjet printing applications.

The specific goals during this dissertation are to:

- analyse the dried deposit from microliter droplets,
- investigate the dried deposit of different shape particles to mimic industrial inks,
- analyse aggregation of particles during the drying process,
- analyse the influence of solvents on particle aggregation and deposit structure,
- find the conditions necessary to form a uniform film deposit,

and thereby increasing the applicability of inkjet printing in different areas linked to the practical industrial applications.

1.2 Organisation of chapters

The content of this thesis is organized in seven chapters as follows. The first three chapters discuss the background and basic knowledge about droplet drying and its inkjet printing applications as well as the experimental procedures and equipment used to conduct this experimental work. These three initial chapters are aimed at easing the reader into the ground working science used in the next three experimental chapters. Main conclusions are displayed in Chapter 7.

Chapter 1 contains an outline of the background of evaporation, wetting and processes, the importance of this field and potential applications with a focus on inkjet printing. A summary of what is found in each chapter of the thesis is also found. Chapter 2 displays in greater detail the background and understanding required for the knowledge of the physical, chemical and engineering aspects surrounding evaporation, wetting and control of the final deposit structure. This chapter is organised as follows: to start with, the stability of colloidal suspensions, the fundamentals of wetting of droplets and the physical aspects of an evaporation process are introduced. Finally, a review of the work on droplet drying and patterns formation upon solvent evaporation including the most important findings and applications conclude this chapter. Chapter 3 covers the experimental setup and procedures selected to undertake this experimental work.

In Chapter 4, the dynamics of the contact line and the forces acting at the three-phase contact line of evaporating sessile droplets containing silica nanoparticles in aqueous base fluid were investigated. In this chapter, a systematic study of the evaporative behaviour of silica nanoparticles with varying initial concentration has been conducted. A thorough analysis of the evaporation behaviour both experimentally and theoretically was investigated. The residual deposit patterns and the cracks patterns generated upon solvent evaporation have been thoroughly reviewed as well. Chapter 5 focuses on the evaporation behaviour of multicomponent droplets and their resulting dried deposits patterns. Similarly, to Chapter 4, a systematic study of the evaporative behaviour of spherical silica particles was done. Also, a comparison with a similar spherical system was done, while adding sedimentation parameters to the suspensions have been reviewed and discussed. A scaling relationship for the experimental spacing between cracks by comparison with theoretical model was also outlined.

The final experimental Chapter, Chapter 6 explores a different particle shape namely a disk-like synthetic clay nanoparticle with gelling properties. A systematic study of the evaporative behaviour was investigated, and the formation of a film deposits of various homogeneity was thoroughly reviewed as well as an attempt to an explanation is provided.

Finally, Chapter 7 discusses the contribution made towards the discovery of mechanisms during: wetting, evaporation of fluids loaded with nanoparticles, the limitations of this study are also discussed. Experimental results related to discussions and theory have been detailed in this dissertation to deepen the knowledge on these phenomena and to suggest future directions for further the investigation on drying droplets and subsequent dried deposits patterns for future academic, industrial or medical applications

Chapter 2
Basic concepts and literature review

2.1 Basic concepts

As seen in Chapter 1, the drying of colloidal suspensions can be encountered in daily life (rain droplets on windows or coffee droplets) different fields (paints, coatings and inks industries) and has a wide variety of applications (agrochemicals with crop spraying (Faers and Pontzen, 2008), medicals with organs printing (Nakamura et al., 2005), (Nishiyama et al., 2008) or energetics with organic solar cells fabrication (Jeong et al., 2010) for instance).

The drying of colloidal suspensions involves several main aspects. These aspects can be divided into three main parts: First the suspension preparation, followed by the droplet generation, impact and spreading and finally the evaporation process.

Therefore, ahead of creating new formulations, it is necessary to understand the basic concepts, and theories of colloidal suspensions, such as colloidal stability. Then, the main parameters and criterions to describe a droplet need to be highlighted. Finally, the physical aspects associated with evaporation (such as diffusion and convection) have to be considered to further the overall understanding of an evaporation process.

A large review of the current state of the art on experimental and theoretical work on the drying of colloidal suspensions will then be detailed. This literature review will focus on the drying behaviour of single solvent colloidal suspensions in the presence of electrolyte and surfactants, binary mixtures and where the suspensions potentially contain more than one type of particles.

The information displayed in this chapter will subsequently be used in the experimental chapters as a basis to analyse and compare the collected data from this work.

2.1.1 Stability of colloidal suspensions: Derjaguin, Landau, Verwey and Overbeek (DLVO) theory

Colloidal suspensions are homogeneous suspensions of solid particulates (typically of diameters < 10 μm) in a fluid. In colloidal suspensions, colloidal particles are much bigger than the molecule of the dispersion fluid. Hence, colloidal particles have a high surface area to volume ratio in comparison to

the bulk solution fluid. Thus, a considerable fraction of colloidal particles are localised at the interfacial area. Colloidal suspensions are thermodynamically unstable and their apparent stability can vary from a few seconds to several years. A stable colloidal suspension usually refers to a state where the particles do not form clusters together. For a system to remain dispersed and thus stable the particles need to stay far apart from each other, and as that the system has a high interfacial area, hence high energy is required to maintain this state. In practice colloidal particles aggregation occurs over time in order to reach a lower energy state (this energy state is characterised by a small interfacial area). To attain this energy state, the distance between the particles decreases dramatically (the distance falls down way below, h, the inter-particle distance separating two colloidal particles in a fluid). Thus, in stable colloidal suspensions, an energy barrier has to be overcome in order to form the dispersion of the bulk phase. Typically, colloidal suspensions can be observed under two states, they can either be stable or unstable. In that respect, an unstable state means that the particles form clusters together following aggregation. The action resulting from the generation of cluster of particles held together is known as aggregation. Aggregation occurs following these two processes (see Figure 2-1):

- coagulation: is the result of electrolyte-driven aggregation and is an irreversible process leading to densely packed particle aggregates (also known as coagulum)

- flocculation: is the result of aggregation driven by the addition of polymers into the colloidal suspension and is typically a reversible process leading to loosely packed particle aggregates (also known as floc).

Two independent research groups in the 1940's worked to propose an explanation for the stability of colloids in aqueous suspensions.

This theory commonly referred to as the Derjaguin, Landau, Verwey and Overbeek (DLVO) theory is named after these researchers. The DLVO theory describes the different interaction energies between particles dispersed in water and defines a total interaction energy between the particles as the summation of all the Van der Waals attractive and electrostatic repulsive forces.

- Van der Waals attractive forces

Van der Waals interactions between colloidal particles stem from the interactions of the individual atoms and molecules forming these particles and

are based on dipolar interactions. The summation of all the attractive interaction, W_{VdW}, between each particle leads to the attractive forces and for two spherical particles it can be expressed as equation 2.1 (Polte, 2015),(Lyklema, 2005),(Hoath, 2016):

$$W_{VdW} = -\frac{A_H}{6}\left(\frac{2R_1R_2}{d_p^2-(R_1+R_2)^2}+\frac{2R_1R_2}{d_p^2-(R_1-R_2)^2} + \ln\left[\frac{d_p^2-(R_1+R_2)^2}{d_p^2-(R_1-R_2)^2}\right]\right) \quad (2\text{-}1)$$

Where A_H is the Hamaker constant which depends on the properties of the colloidal system (both dispersed and continuous phases) and is usually in the range of 10^{-21} to 10^{-19} J, R_1 and R_2 represent the particle radii, d is the centre-to-centre interval between the two particles, equation 2-2, thus represents the sum of the particle radii and $h\,is$ the distance separating the two approaching particle surfaces (see Figure 2-1) (Polte, 2015),(Lyklema, 2005),(Hoath, 2016):

$$d_p = R_1 + R_2 + h \quad (2\text{-}2)$$

As the particles come closer together, $h \ll R_1$ or R_2 , thus equation 2-1 can be expressed as equation 2-3 (Polte, 2015),(Lyklema, 2005),(Hoath, 2016):

$$W_{VdW} = -\frac{A_H R_1 R_2}{6h(R_1+R_2)} \quad (2\text{-}3)$$

This equation can be simplified further for same size spherical particles of radius R as equation 2-4 (Polte, 2015),(Lyklema, 2005),(Hoath, 2016),(Cosgrove, 2005):

$$W_{VdW} = -\frac{A_H R}{12h} \quad (2\text{-}4)$$

Therefore, for a system of identical particles dispersed in water, the attractive Van der Walls interactions are dictated by the dimensions of the particles, the distance between the approaching particles and the Hamaker constant. By convention, the attractive Van der Waals forces are negative (see Figure 2-3).

- Electrostatic repulsive forces and electrical double layer

In an aqueous suspension, most particles will develop a charge on their surface. The Van der Waals interaction between colloidal particles stems from the interactions of the individual atoms and molecules forming these particles and are based on dipolar interactions. This surface charge can stem from several possible processes: i) dissociation of surface groups (generally

depends on the pH of the solution), ii) ion replacement, iii) dissolution of ionic solids or iv) ion adsorption from the bulk solution. The presence of a net charge at the particle surface impacts on the co-ions and counter-ions distribution in the surrounding interfacial area. An increase concentration of ions (counter-ions with charge opposite the particle charge) near the particle surface will thus be generated to retain an electric neutral balance (see Figure 2-1). The balance is commonly known as the electrical double layer. The electrical double layer can be represented by three distinct areas: the particle surface, the region close to the particle surface where the counter-ions are physically attached to the surface - commonly known as the Stern layer, and the diffuse layer which is the volume away from the Stern layer where both counter-ions and co-ions accumulate to bring the whole system to electroneutrality (Polte, 2015). In practice, the stability of colloidal suspensions is determined by measuring the zeta-potential which corresponds to the meeting point of the Stern and diffusive layers. Suspensions are commonly considered stable when their zeta-potential is above +30 mV and below -30 mV.

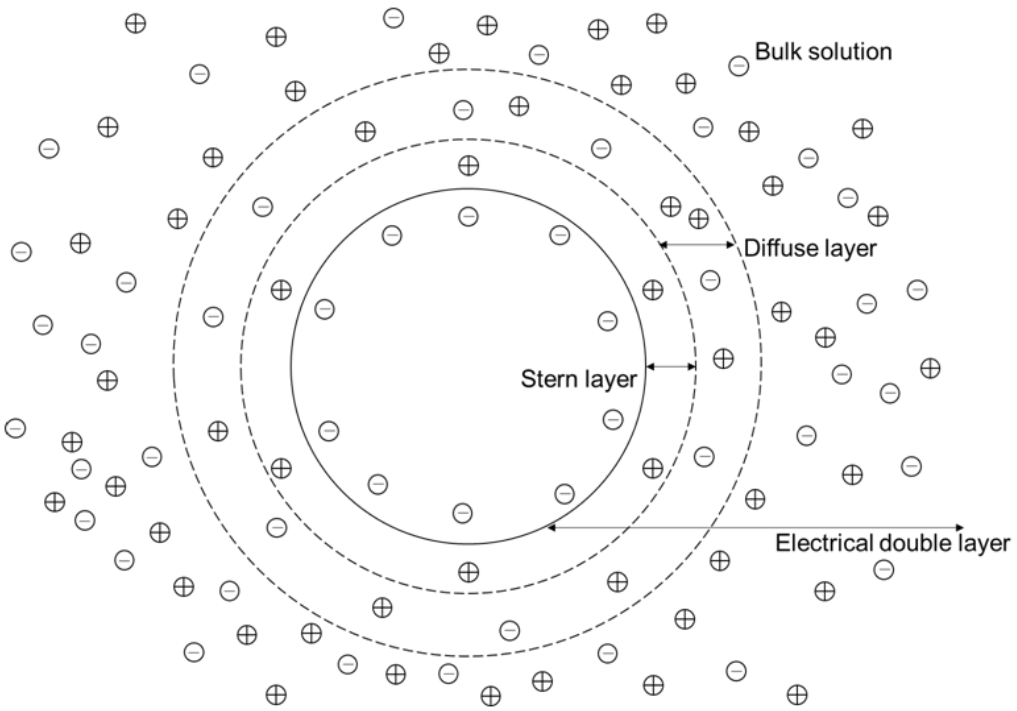

Figure 2-1: Schematic representation of the electrical double layer for a negatively charge spherical silica colloidal particle of 20 nm diameter in an aqueous suspension.

When two particles converge towards each other, their respective electrical double layer overlaps. This overlapping leads to a local increase of electrolyte concentration, which creates an osmotic pressure difference with the bulk concentration. The intensity of this repulsion depends on the electrical double layer width and the distance between the particles (see Figure 2-1 and Figure 2-2). The width of the electrical double layer commonly referred to as the Debye screening length, κ^{-1}, is determined by the following equation 2-5 (see Figure 2-2) (Hoath, 2016):

$$\kappa = \sqrt{\frac{e^2 \sum_i \rho_{Ni} z_i^2}{k_B T \varepsilon_0 \varepsilon_r}} \tag{2-5}$$

Where, e, is the fundamental charge, ρ_{Ni} is the number density of ions i, z_i is the ion valence, k_B is the Boltzmann constant, T is the temperature, ε_r is the dielectric constant of solution and ε_0 is the permittivity of vacuum.

This layer is strongly influenced by electrolyte addition. From equation 2-5, it can be noticed that when the electrolyte concentration is increased the Debye screening length will decrease. Indeed, the Debye screening length is inversely dependent on the electrolyte concentration.

For two same sized spherical particles, the electrostatic repulsive interaction, W_R, is thus described by equation 2-6 (Hoath, 2016):

$$W_R = \left(\frac{64\pi k_B T R \rho_{Ni} \gamma_0^2}{\kappa^2} \right) e^{-\kappa h} \tag{2-6}$$

Where, γ, the reduced surface potential is expressed as equation 2-7 (Hoath, 2016):

$$\gamma_0 = \tanh \frac{ze\psi}{4k_B T} \tag{2-7}$$

Where, ψ is the potential on the particle surface.

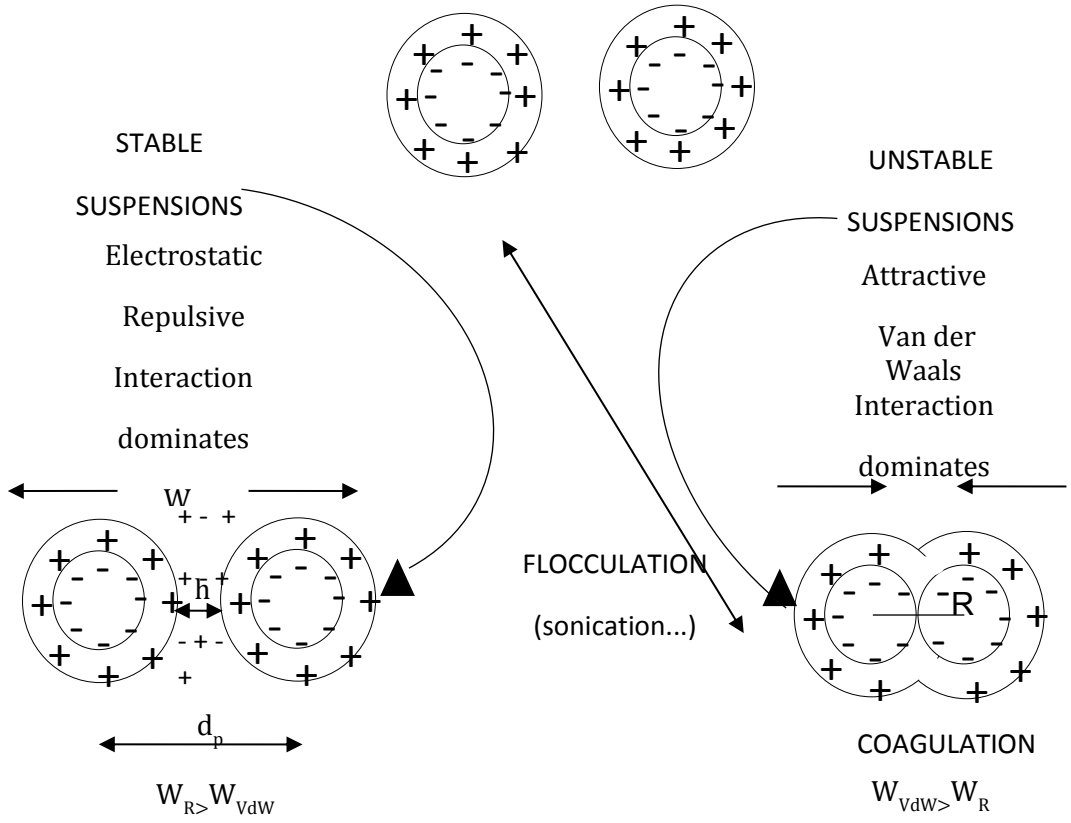

Figure 2-2: Schematic of DLVO interactions for two negative same size spherical particles in aqueous suspension approaching each other. Left side represents stable suspension with electrostatic repulsive force overwhelming the attractive Van der Waals interaction. Right side represents the attractive Van der Waals interaction overwhelming electrostatic repulsive force which leads to particle aggregation hence unstable suspension.

Consequently, for a system of identical particles dispersed in water, the strength of the repulsive interactions depends on the electrical double layer thickness, the ions valence and concentration. By convention, the electrostatic repulsive interactions are positive (see Figure 2-3).

- Stability of colloidal suspensions

As stated before, DLVO describes the total interaction energy between two approaching particles by adding the two opposite interactions together. Hence, the net force, W_T , for two same sized spherical particle, is given by equation 2-8 (Hoath, 2016):

$$W_T = -\frac{A_H R}{12h} + \left(\frac{64\pi k_B T R \rho_{Ni} \gamma_0^2}{\kappa^2}\right) e^{-\kappa h} \qquad (2\text{-}8)$$

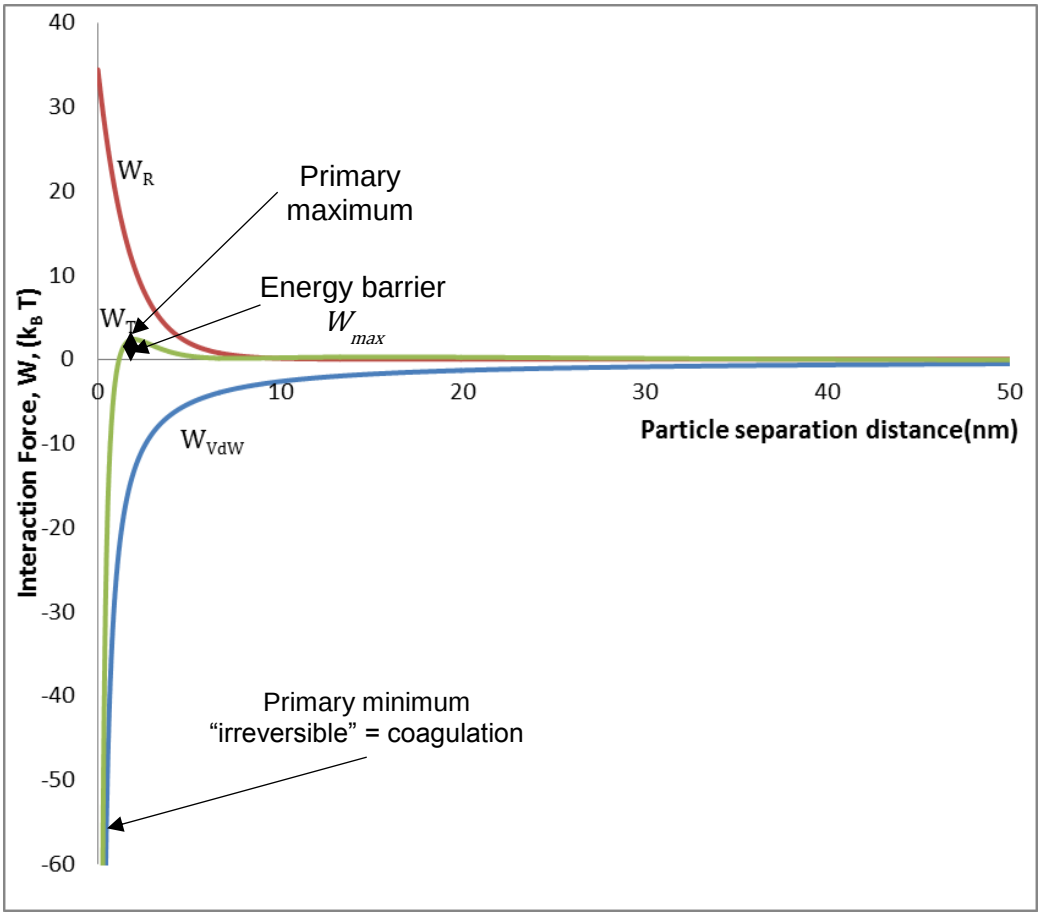

Figure 2-3: Summary of interaction for a negatively charge spherical Ludox AS-40 colloidal particle of 40 mV in an aqueous suspension.

The total interaction energy also known as the net force, W_T can be represented by an energy curve (see Figure 2-3). On Figure 2-3, it can be seen that when the particle separating distance is great the system remains stable. As the particles separating distance decreases, both the electrostatic repulsive, W_R, and attractive Van der Waals interactions, W_{VdW}, increase at a different rate. Hence, as the particles are approaching each other, the net interaction forces, W_T, go through a secondary minimum (which is a reversible process and is characterised by particles flocculation, the secondary minimum is not observed for our system), a primary maximum, W_{max}, (which corresponds to an energy barrier to overcome) and a sharp primary maximum (which is an irreversible process and is characterised by particles coagulation). Random collisions occur between particles and molecules from the aqueous medium due to Brownian motion. If the energy barrier, W_{max}, can be overcame using the energy generated from these collisions, the net interaction forces, W_T, will drop to reach the primary minimum leading to an "irreversible" coagulation. The height of the energy barrier, W_{max}, is thus a

determining factor which characterises the system stability. Commonly, a system remains stable over time, when the energy barrier is at least $W_{max} = 10k_BT$ which means that the particles separating distance is below twice the Debye screening length. Statistically, particles can either have lower or higher energy upon collisions, hence the energy barrier controls the time the suspensions will be stable (see Figure 2-2 and Figure 2-3).

- Critical coagulation concentration

The critical coagulation concentration commonly referred to as ccc represents the concentration of electrolyte required to induce a rapid aggregation of the particles in the suspension. This mechanism is irreversible thus the ccc is the concentration at which coagulation occurs. The Schultz-Hardy relation shows that the ccc is strongly dependent upon the electrolyte valency (2-9) (Cosgrove, 2005):

$$ccc \propto \frac{1}{z^6} \tag{2-9}$$

Thus, aggregation will be favoured for high valence of electrolytes.

The overall stability of colloidal suspensions thus can be influenced by electrolyte addition which will decrease the electrical double layer thickness and trigger particle aggregation.

In summary, the stability of the suspensions studied in this thesis can be controlled by the concentration and type of electrolyte used in the continuous phase. In particular, because the work in this thesis relates to systems where the concentrations of both particles and electrolytes increase over time as the droplets evaporate, understanding the dependence of suspension stability as a function of electrolyte concentration is paramount.

2.1.2 Wetting properties, droplet profile characteristics and evaporation process

2.1.2.1 Wetting properties and droplet profile characteristics

Once suspensions are prepared and their stability in the printing reservoir is ensured, a droplet can be generated through a needle and deposited onto the chosen substrates. The deposition processes is affected by several aspects, the suspension jetting, the jetting speed, the droplet impact velocity (upon impact the droplet goes through a range of shapes before reaching an equilibrium shape; this equilibrium shape depends on the velocity and it is usually formed in the order of several nanoseconds (Yarin, 2006)), followed by spreading and the subsequent drying. Upon the droplet impact, both gravity and surface tension influence a sessile droplet shape. Indeed, sessile droplets placed on a solid surface can exert several spreading behaviours, this spreading depends on the wetting properties of the liquid onto the substrate. Hence a droplet can exert a total or partial spreading over a solid surface. On one hand, a total wetting means that the droplets spread entirely over the solid surface; while on the other hand, for a partial wetting, the droplet will adopt a shape that can be characterised through several physical aspects as described below.

- Surface tension and contact angle on an ideal surface

A sessile droplet resting on an ideal substrate (a chemically homogeneous and smooth surface) will acquire a shape controlled by surface tension. In a liquid, molecules display cohesion which corresponds to an attractive intermolecular force. However, molecules present at the liquid/vapour interface will experience an asymmetric attractive force (this force pulls the molecules back towards the bulk- because of the largely reduced number of molecules present in the vapour phase above the interface; this phenomenon gives rise to a tension located at the surface and is known as the surface tension. Due to this created surface tension, the liquid will maintain a shape requiring the lowest surface free energy (see Figure 2-4).

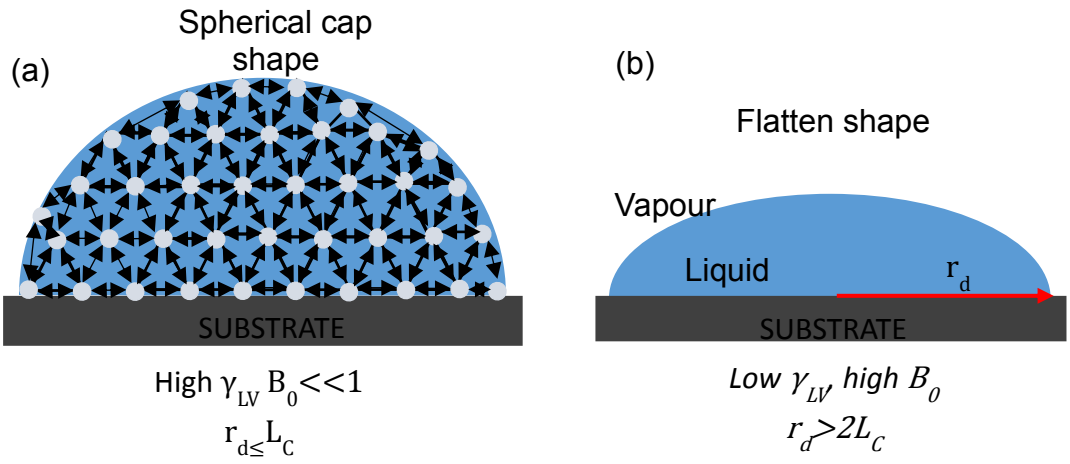

Figure 2-4: Schematic illustration of (a) how intermolecular interaction provoke surface tension due to the imbalance of forces between the molecules located at the liquid/vapour interface and the molecules in the bulk. When, the surface tension is high, the Bond number is low and the droplet contact radius is below the Capillary length, the gravitational forces are negligible, thus the droplet maintains a spherical cap shape. (b) when, the surface tension is low, the Bond number is high and the droplet contact radius is superior to twice the value of the Capillary length thus the gravitational forces are not negligible hence the droplet shape is deformed and flattens.

The angle formed by a sessile droplet resting on a solid surface is known as the contact angle. This important parameter describes the interplay between the different interfacial tensions at the three-phase contact line. The three-phase contact line is the point where the three phases: liquid, solid and vapour meet. The contact angle is described through the Young-Laplace equation 2-10 (see Figure 2-5a, b):

$$\gamma_{SV} = \gamma_{LV} \cos\Theta + \gamma_{LS} \qquad (2\text{-}10)$$

Where, γ_{SV}, γ_{LS}, γ_{LV} represents respectively the different interfacial tensions solid/vapour, liquid/solid and liquid/vapour and θ is the Young-Laplace/equilibrium contact angle (see Figure 2-5a, b) while neglecting the gravitational effect.

The spherical cap shape droplet can thus be characterised by four main parameters: contact angle, θ, the droplet height at its apex, H, the radius of a sphere, whose shape fits the spherical cap of the drop, R_S, and the radius of the drop, r_d(see Figure 2-5a). This is governed by the equation 2-11:

$$H = R_S(1 - \cos\theta) = r_d \tan\left(\frac{\Theta}{2}\right) \qquad (2\text{-}11)$$

The volume of the droplet maintaining a spherical shape, V, can be calculated using equation 2-12:

$$V = \frac{\pi H}{6}(3r_d^2 + H^2) = \pi r_d^3 \frac{\cos^3\theta - 3\cos\theta + 2}{3\sin^3\theta} \qquad (2\text{-}12)$$

In this thesis, the volume has been calculated using equation 2.12, in some cases the volume is calculated manually while in others it is calculated automatically by the software associated with the contact angle goniometer equipment.

Besides, the surface tension and contact angle, a sessile droplet can be characterised by two key parameters, the Bond number,B_0, and the Capillary length, L_c:

- Bond number

The Bond number represents the ratio of the gravitational effects and droplet diameter to the surface tension, it is obtained by the equation 2-13 (Yarin, 2006).

$$B_0 = \frac{\rho g r_d H}{\gamma_{LV}} \qquad (2\text{-}13)$$

- Capillary length

The Capillary length is the ratio of the surface tension parameter to the gravitational effect; hence the relationship is expressed by equation 2-14 (Yarin, 2006):

$$L_c = \sqrt{\frac{\gamma_{LV}}{\rho g}} \qquad (2\text{-}14)$$

Where, ρ, is the fluid density, r_d, is the droplet radius, H is the droplet height at its apex-and g is the acceleration due to gravity.

The surface tension parameter strives to maintain the droplet into a spherical cap shape while the gravitational force works to flatten the droplet. The higher the surface tension is, the smaller the Bond number will be thus the more spherical the droplet shape will be (see Figure 2-4). The Capillary length is a good indicator of the gravitational effect. If a droplet size is more than twice of the value of the capillary length, the gravitational forces cannot be ignored, the droplet shape will be deformed due to gravity and thus the shape will appear more as an ellipsoid (see Figure 2-4)(Carle and David, 2015).

In this thesis, these main parameters are used to help characterise the sessile droplets. The different systems studied are in aqueous suspensions, thus the capillary length of a sessile droplet of water (Milli-Q water used in all systems) can be determined. It is found to be at $L_C = 2.72\ mm$ (the surface tension was measured at 70 mN/m which is close to 72.8 mN/m surface tension of water at 20°C (Kim et al., 2006)). Considering the value of L_C, droplets size is calculated to be $r_d = 5.44\ mm$. In this instance, the contact angle can be determined. The contact angle is approximated from the application of the Young-Laplace. This equation is appropriate when a sessile droplet adopts a spherical cap shape.

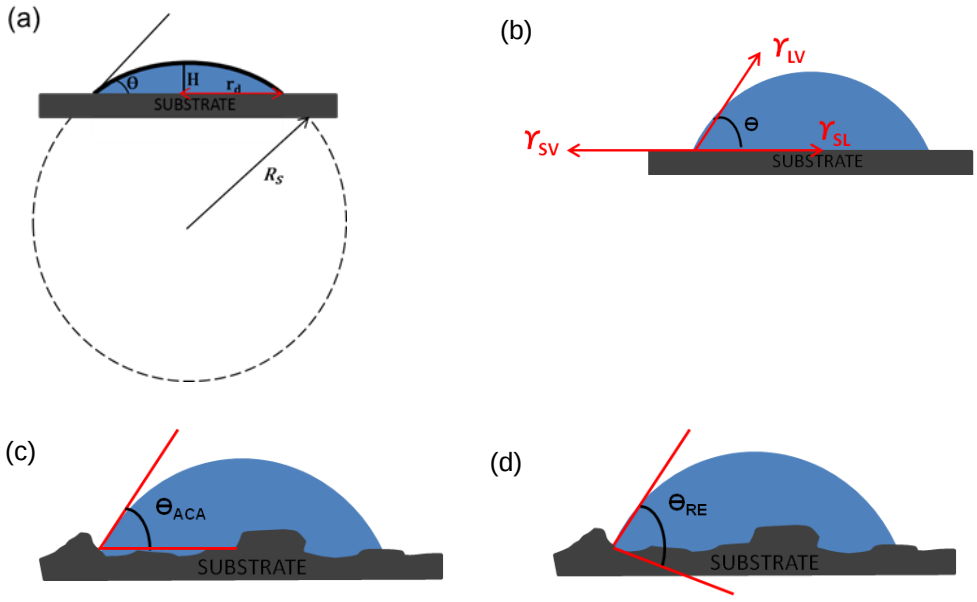

Figure 2-5: Schematic representation of a sessile droplet (a) on an ideal substrate forming a Young-Laplace/equilibrium contact angle, θ, with an apex height of H, a drop radius, r_d and the radius of sphere reshaping the spherical cap of the drop, R_S ,(b) Representation of the three interfacial tensions dictating the contact angle the droplet makes on the surface through the Young-Laplace equation at the three-phase contact line, (c) the apparent contact angle on an irregular substrate (angle measured experimentally), θ_{ACA} and (d) the real contact angle on an irregular substrate, θ_{RE}.

- Contact angle on non-ideal surface

In reality, a substrate has a non-ideal surface which is characterised by its roughness and chemical heterogeneity. Hence, the contact angle of a droplet

spreading on a typical surface will fluctuate between the advancing contact angle (highest, the contact area between the liquid droplet and the solid surface increases), θ_A and receding contact angle (lowest, the contact area between the liquid and the solid surface decreases), θ_R due to the surface characteristics. The difference between the advancing and receding contact angle is known as the contact angle hysteresis (Good, 1952),(Bartell and Shepard, 1953),(Carrier and Bonn, 2015).

Commonly, the contact angle hysteresis is explained to be due to the surface properties; more precisely its roughness (Shuttleworth and Bailey, 1948) and heterogeneity. As such, the texture of a surface is a determining factor leading to the spreading of a droplet (Xu et al., 2008). Hence, the Wenzel equation incorporates the roughness effect in the mathematical definition of contact angle as seen in equation 2-15 (Wenzel, 1936):

$$\cos\theta_W = r_W \cos\theta \qquad (2\text{-}15)$$

Where θ_W represents the apparent contact angle on a rough surface, θ represents the Young-Laplace/equilibrium contact angle on a smooth surface and r_W represents the qualitative relation between the surface domains depicting the roughness feature to the smooth surface. In this model, the liquid penetrates and thus spreads and wets all the protuberances of the solid surface (see Figure 2-6). The real contact angle θ_{RE} follows the actual surface geometry of the substrate (see Figure 2-5d).

When the liquid does not penetrate through the surface asperities, the Wenzel equation is no longer adequate to help describe the wetting behaviour , hence an alternative model was developed through Cassie's law as shown in equation 2-16 (known as the Cassie-Baxter equation) (Cassie and Baxter, 1944)(Chau et al., 2009). In this model, the droplet will not penetrate the surface roughness but rest on top of air pockets trapped in the protuberances of the surface. This generates a composite of solid-air surface which can be associated to a heterogeneous surface which is in contact with the liquid (see Figure 2-6b).

$$\cos\theta_{CB} = \Phi_S(\cos\theta + 1) - 1 \qquad (2\text{-}16)$$

Where θ_{CB} represents the apparent contact angle on a rough surface which is constituted of a solid and air pockets, θ represents the Young-Laplace/equilibrium contact angle and Φ_S represents the proportion of solid and air surface in contact with the liquid.

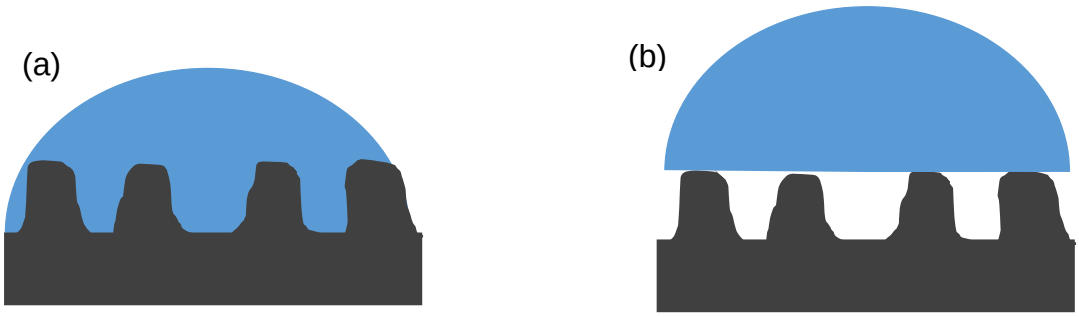

Figure 2-6: Schematic representation of a droplet (a) Wenzel state, where the droplet penetrates the roughness of the substrate and (b) Cassie-Baxter state where the droplet rests on top of the substrate roughness features.

However, these two models clearly do not consider the contact angle hysteresis, they rather depict the discrepancy with the Young-Laplace/equilibrium contact angle. Thus, the different states depend on the degree of droplet penetration in the surface features.

To summarize, a generated droplet (in an ink-jet device) impacts and spreads on the surface. When the equilibrium state is reached, upon spreading, the shape of the droplet on the substrate is determined by the surface properties (such as roughness, chemical heterogeneity, hydrophobicity and hydrophilicity) as well as the fluid properties (surface tension and viscosity). In practice, the contact angle measured is the apparent contact angle as the equipment used to monitor this parameter has not a high enough resolution to incorporate the roughness factor. Thus, the Young-Laplace equation describing the equilibrium is the one used to determine the contact angle throughout this thesis. Now that, the droplets main characteristics have been established, the next step in a printing process is the evaporation. In the following section, the principles leading to evaporation will thus be reviewed.

2.1.2.2 Evaporation process of pure fluid

The drying of a single solvent sessile droplet on a solid surface is a complex phenomenon. Commonly, during an evaporation process two main phenomena occur: diffusion and convection. To describe these phenomena

simplifying assumptions have to be made in order to model an evaporation process.

- Diffusion process

Droplets resting on a substrate dry through solvent evaporation unless a curing process is involved. Evaporation is a process during which a liquid changes state to become a gas. To change state, the liquid molecules are using energy to move between the two phases: the enthalpy of vaporisation, $\Delta_{vap}H$, can quantify this endothermic motion (see Figure 2-7). This change can be observed under two different perspectives within a typical evaporating system. At the molecular level, molecules are circulating between the two phases (liquid and gas) with the molecules in the liquid phase relocating into the vapour phase. Since droplet evaporation involves a non-saturation process, it is characterised by more molecules exchanged toward the vapour phase than the liquid phase.

Therefore, the evaporation process will go on at the liquid-vapour interface as long as saturation is not achieved. This is depicted by the vapour diffusion into the gas phase, hence evaporation takes place as long as the partial vapour pressure in the gas phase is lower than the saturation pressure. Because the vapour concentration surrounding the droplet is not uniform, saturation is reached at the interface. The vapour concentration at the droplet/air interface thus matches the saturated concentration, c_S while the vapour concentration away from the droplet reaches the value: $c_\infty \approx RHc_S$, where RH is the relative humidity of ambient air. An evaporation process is considered to be diffusion-limited when the diffusion time $\boldsymbol{t_D}$ ($\boldsymbol{t_D = \frac{r_d^2}{D} \approx \frac{c_S(1-RH)}{\rho}}$ (2-17)) of the vapour into the gas phase is negligible compared to the evaporation time t_E which means that expression (2-18) applies (Sobac and Brutin, 2015): $\boldsymbol{\frac{t_D}{t_E} \ll 1}$ (2-18). Where, D is the diffusion coefficient of the vapour in the gas phase. In this thesis, expression (2-18), $\boldsymbol{\frac{t_D}{t_E} \ll 1}$ is true for all the different systems studied, therefore, the droplet evaporation process can be defined as a quasi-steady and diffusion-limited process.

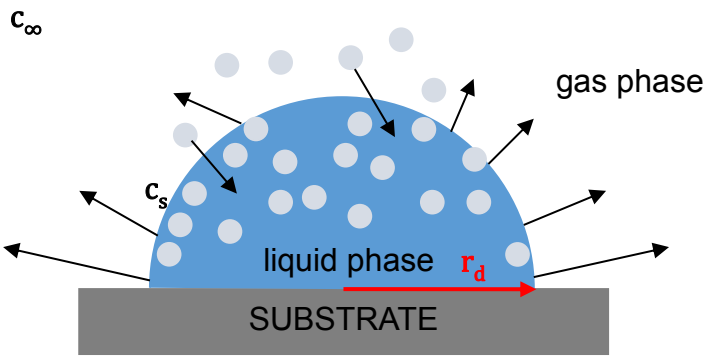

Figure 2-7: Schematic illustration of the diffusive evaporation of a spherical droplet resting on a smooth substrate.

At the macroscopic level, a mass transfer between the liquid and vapour interface occurs. Thus, for a sessile droplet evaporating into air, the rate of mass loss due to evaporation is proportional to the droplet radius and can be expressed by equation 2-19 (Sobac and Brutin, 2015), (Birdi et al., 1989), (Birdi and Vu, 1993):

$$-\frac{dM}{dt} = 4\pi r_d D c_S (1 - RH) \qquad (2\text{-}19)$$

The rate of volume loss can also describe the evaporation process as seen in equation 2-20 (Picknett and Bexon, 1977; Hu and Larson, 2002; Chhasatia et al., 2010; Sanyal et al., 2015):

$$-\frac{dV}{dt} = \frac{4\pi r_d D(c_S - c_\infty)}{\rho} f(\theta_{ACA}) \qquad (2\text{-}20)$$

Where, ρ is the fluid density and $f(\theta_{ACA})$ is a function of the apparent contact angle which incorporates the effect of a solid surface on the vapour field introduced by Picknett and Bexon (Picknett and Bexon, 1977). In this thesis, the evaporation rate is determined from the droplet volume variation over time.

Although, the diffusion-limited process can explain the evaporation, other parameters can be considered to describe evaporation such as the convection process due to heat transfer.

- Convection process

In general, the molecules which are more likely to cross the interface barrier are the molecules with the larger kinetic energy thus higher thermal energies.

Due to the loss of molecules with the highest thermal energy, the temperature of the droplet cools down following an evaporative cooling process. Thus temperature along the droplet interface is not homogeneous and the non-uniform evaporative flux is equivalent to temperature divergence. This divergence is expressed by a temperature gradient along the droplet interface which will generate differences in the surface tension. Consequently, an internal flow will be generated to balance this surface tension gradient. This internal flow is commonly known as the Marangoni flow (see Figure 2-8 and Section 2.2.1).

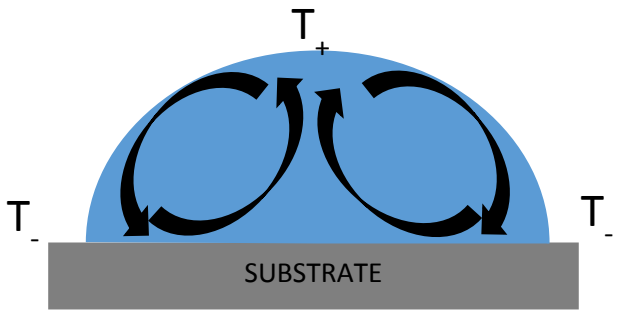

Figure 2-8: Schematic of the evaporation of a droplet following a convective flow. A surface gradient is generated along the liquid/vapour interface due to an internal flow, thus surface tension will go from the highest temperature T_+ towards the lowest temperature T_-.

- Modes of drying

Two main modes of drying are at work during the evaporation of a drying droplet of a pure fluid as determined by Picknett and Bexon (Picknett and Bexon, 1977).

(1) A constant contact angle mode (CCAM) where the contact angle is constant during evaporation, which is made possible by the droplet contact line receding throughout the evaporation: this phenomenon is expected for ideal system with equilibrium between the liquid, solid and gas phases.

(2) A constant contact radius mode (CCRM), where the contact radius is constant due to a pinned contact line and for which the contact angle is seen to constantly decrease throughout the evaporation process. During evaporation, the contact line motion is not always smooth, thus it is not uncommon to observe a combination of the two modes during an evaporation process. Usually, the CCRM dominates at the beginning of the evaporation process until the receding contact angle is reached when

the CCAM becomes more is favoured. When an alternative combination of the two modes is observed it is referred to as a stick and slip motion (Shanahan and Sefiane, 2009), (Orejon et al., 2011). The timescale of each phase is variable and depends on the nature of the substrate. Figure 2-9 schematically represents the two different drying modes.

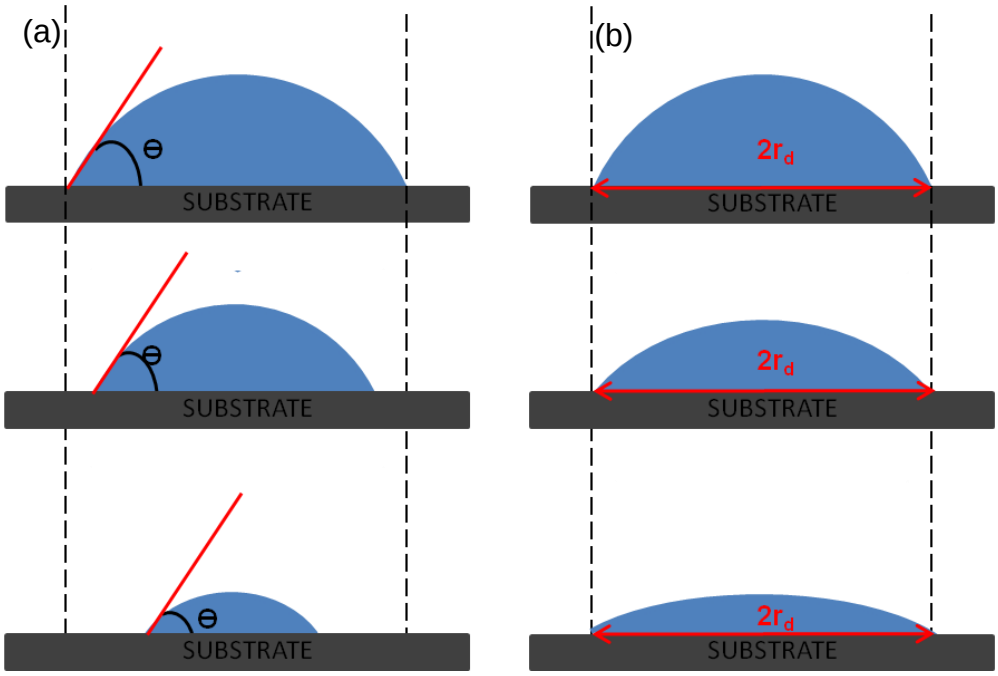

Figure 2-9: Schematic representation of the two main evaporation modes: (a) CCAM where the droplet dries with a decreasing contact radius r_d and a constant contact angle; (b) CCRM where the droplet dries with a decreasing contact angle and a constant contact radius (Picknett and Bexon, 1977).

2.1.2.3 Evaporation of binary mixtures

For binary mixtures, the droplet profile characteristics determined for a pure fluid still apply. However, the drying process of a binary mixture is different in the case of aqueous/alcohol mixtures and more precisely for water/ethanol mixtures. Sefiane *et al.* (Sefiane et al., 2003) investigated binary mixture droplets composed of water-ethanol. From their study, it was demonstrated that three stages were at work during evaporation of these droplets. Indeed, in the first stage, the evaporation follows only the drying behaviour of the most volatile solvent, in other words ethanol. This behaviour is characterized by a pinned contact line (CCRM) and a decreasing contact angle, thus indicating that the ethanol is reaching the liquid/vapour interface to dictate the drying

behaviour. In the later stage, the droplet drying behaves like a pure water droplet. The intermediate stage between these two stages follows a de-pinning of the contact line associated with a droplet volume which remains almost constant.

In summary, the evaporation process of solvent only droplets follow a quasi-steady diffusion-controlled process. Indeed, the diffusion time t_D of the vapour into the gas phase is negligible compared to the evaporation time t_E. The diffusion-limited mode is characterised by a mass transfer/volume loss and generated by a droplet shape change with a decrease in contact angle or constant contact radius during drying, or a combination of the two modes. For binary mixtures the evaporation is component dependent: in the early stage of drying the more volatile solvent dominates the evaporation rate while the least volatile will control the later drying process. This is the way evaporation works for solvent only droplets and binary mixture. The diffusion and convection will thus influence a particle-laden droplet too and a more detailed review will be illustrated in the subsequent section.

2.2 Literature review

2.2.1 Particle transport during evaporation and influence of dried deposit patterns

For particle-laden droplets the internal flows dictate the kinetics of the deposition process and the distribution of suspended particles. Indeed, the internal flows motion deposits the particles from the fluid onto the substrates hence forming a dried deposit upon solvent evaporation. Two main phenomena are causing these internal flows: Capillary and Marangoni flows as detailed below.

- Capillary flow: "Coffee ring effect"

Typically, solid particles suspended in solutes are carried towards the contact line during the drying process (see Figure 2-10a). This motion of particles

leaves a ring-like stain upon total solvent evaporation (see Figure 2-10c). This ring-like stain was first explained by Deegan *et al.* (Deegan et al., 1997), and is commonly referred to as the "coffee ring effect". In this pioneering study, the mechanism leading to this morphology was proposed. The given explanation was that the microspheres particles used in this study were carried towards the pinned contact line by capillary flow due to a geometrical constraint. Indeed, the presence of particles inside the droplets enhance the pinning of the contact line, hence in order to retain a spherical cap shape dictated by surface tension and to compensate for the volume loss at the contact line, a capillary flow is generated from the droplet centre toward the droplet edges (Deegan et al., 1997).

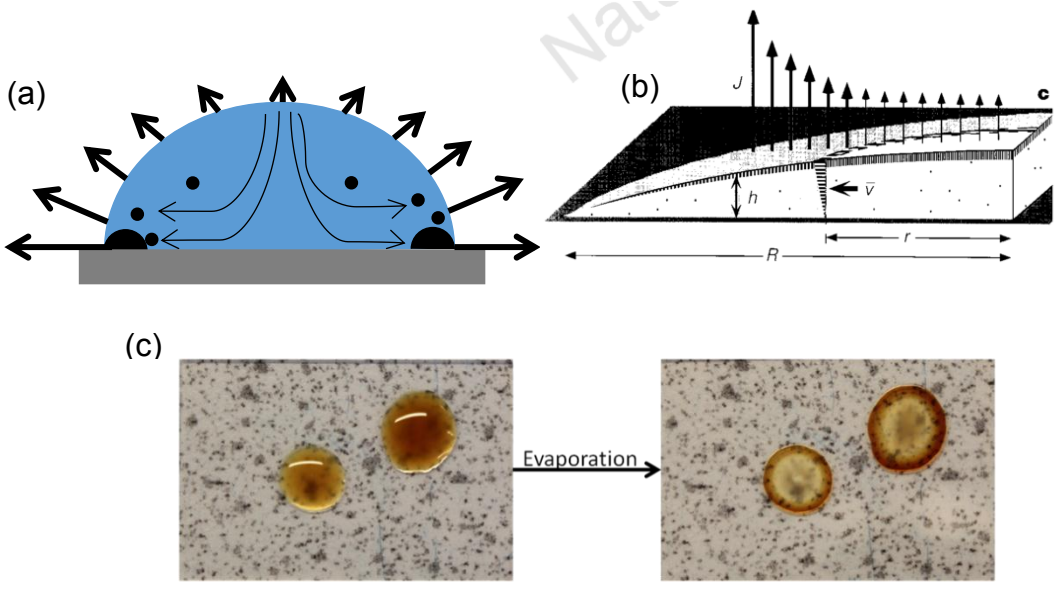

Figure 2-10: (a) Schematic of the outward capillary flow carrying the solid particles from the centre towards the droplet periphery of a pinned sessile droplet resting on a flat substrate leading to the "coffee ring effect", (b) Schematic of the quantities responsible for the capillary flow. The volume loss contracts the height $h(r)$ vertically (Deegan et al., 1997)**. The non-uniform evaporative flux is represented by the thick black arrows while the internal capillary flow is in thin black arrows, (c) Coffee drops leave a ring stain upon evaporation. The majority of the particles are concentrated in the outer ring while a small quantity of coffee is localised in the centre of the drop. Precipitation of the dissolved coffee near the contact line is caused by super-saturation.**

Further experimental work by Deegan *et al.* (Deegan et al., 2000), (Deegan, 2000) led to a more accurate description of the “coffee ring effect” phenomenon. Due to the enhanced pinned contact line, the deposit grows in

size and the contact line cannot de-pin thus leading to a single ring-like stain. The evaporative flux, J, along the droplet interface was found to be non-uniform and much higher at the droplet edge (see Figure 2-10b). This evaporative flux is expressed by 2-21:

$$J(r) \propto (r_d - r)^{-\lambda} \text{ where } \lambda = \frac{(\pi - 2\theta_{ACA})}{(2\pi - 2\theta_{ACA})} \qquad 2\text{-}21$$

Based on these assumptions, a series of identical droplets were prepared and led to different patterns by modifying the drying conditions. The first droplet was left to evaporate freely, the second droplet was mounted on a pedestal and surrounded by water, while the third droplet was deposited inside a box with a hole localised directly above the centre of the droplet. For the first two droplets the final deposit led to a ring-like stain (see Figure 2-11). These ring-like stains were observed due to the uniform evaporation flux along the droplet liquid/vapour interface. Whereas, the third droplet deposition led to a uniform deposition, indeed the presence of the hole above the droplet centre suppressed the outward capillary flow as this hole was the only possible escape path for the liquid (see Figure 2-11). Thus at the evaporative flux was strengthened at the droplet apex.

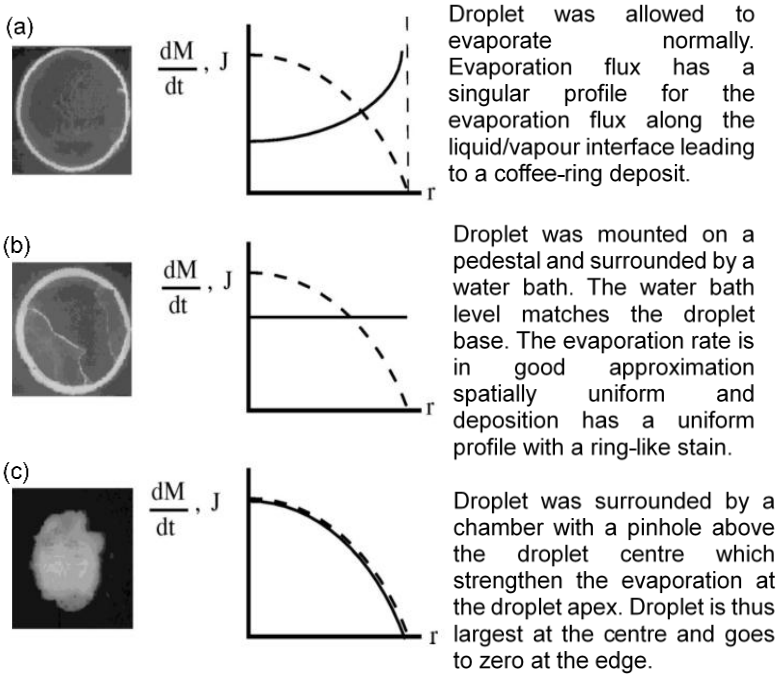

Figure 2-11: Pictures of the resulting deposit for three identical drops dried under different conditions. The initial droplet radius was approximatively 4 mm. A schematic of the evaporation rate, J, is plotted next to the photographs. The dashed line of the curve represents the interface height variation (Deegan et al., 2000)**.**

These results demonstrate that the evaporation flux is greater at the droplet periphery/edges and dependent on the droplet radius (Deegan et al., 2000). It was also observed that an increase in solutes concentration led to a linear increase of the droplet width (see Figure 2-12) (Deegan, 2000). The findings in this study were in good agreement with the evaporation of pure fluids (Birdi et al., 1989).

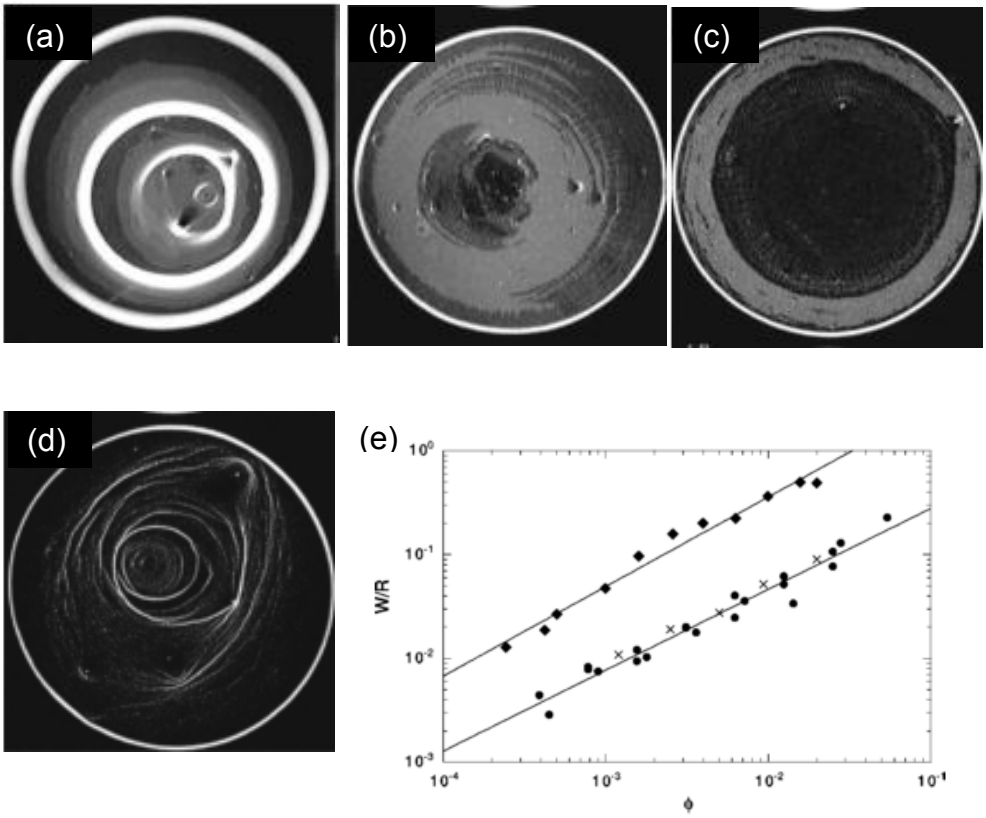

Figure 2-12: Pictures of dried deposits patterns left upon drying of 0.1 µm microspheres droplets at several concentrations on mica from (a) to ((d):(a) 1.0 %, (b) 0.25t%, (c) 0.13%, (d) 0.063% volume fractions while (e) represents the droplet width, W, normalised by its radius, R, as a function of the microspheres volume fractions (Deegan, 2000)**.**

Over the past few years, following, these initial studies, to further understand this phenomenon a large amount of investigations have been reported. Experimental work was undertaken on the pinning effect. Indeed it is usually observed on chemically heterogeneous (Larsen and Taboryski, 2009), (Brunet, 2012) or rough substrates (Sobac and Brutin, 2011; Jokinen et al., 2011) and a high particles concentration induces a self-pinning (Deegan, 2000; Maheshwari et al., 2008; Sangani et al., 2009). Other work investigated the minimal droplet size needed to form a "coffee ring effect" (Shen et al., 2010). A critical length scale, D_C, was found; and this length was linked to the

evaporation time (reduced for smaller particles) and the diffusion of particles during the evaporation process (see Figure 2-13).

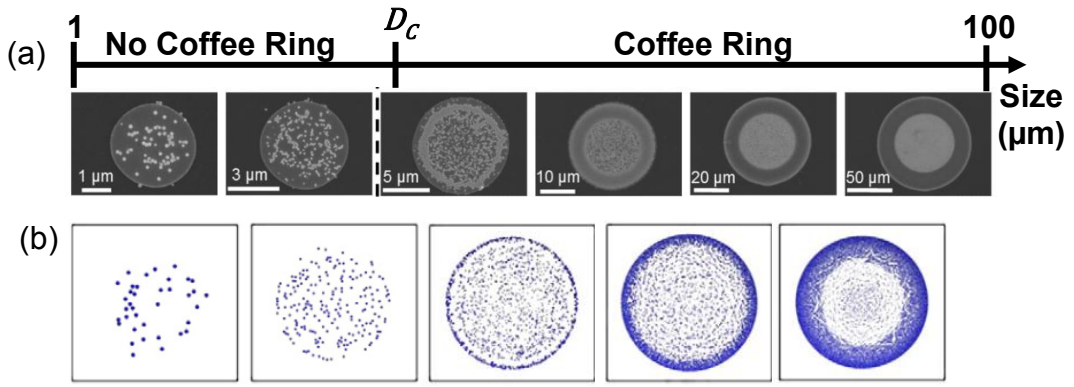

Figure 2-13: Comparison between (a) experimental pictures of whole deposits structure of 113 nm polystyrenes on hydrophilic platinum substrate and (b) corresponding modellisation of experimental results using a Finite Element Model (FEM) (Breinlinger and Kraft, 2014)**.** ***Dc*** **represents the critical droplet diameter to exceed to form a coffee ring** (Shen et al., 2010)**.**

Extensive theoretical work has also been done to describe the drying kinetics leading to the formation of the "coffee ring effect". Two methods are commonly used to simulate this effect: a numerical analysis and the Monte Carlo method. Popov successfully modelled numerically and analytically the formation of the "coffee ring effect" for low and random initial nanoparticle concentrations (Popov, 2005). Bhardwaj et al. simulated the deposit morphology through a Finite Element Model solving Navier-Stokes equation in the case of nanolitre droplets while considering a surface tension gradient (Bhardwaj et al., 2009). Hu and Larson (Hu and Larson, 2002) and Breinlinger and Kraft (Breinlinger and Kraft, 2014) also used a Finite Element Model (FEM) to explain the deposit (see Figure 2-13). Hu and Larson's (Hu and Larson, 2002) analytical model solved the vapour concentration distribution and the non-uniform evaporative flux along the liquid/vapour interface for spherical cap shape droplets. While Breinlinger and Kraft (Breinlinger and Kraft, 2014) using Hu and Larson(Hu and Larson, 2006) analytical model generated a three-dimensional structure of the deposit, in their model they consider low to highly concentrated suspensions (1 to 20 vol%), particles collisions and the presence of a Marangoni flow. Alternatively, Kim et al. (Kim et al., 2010), Crivoi and Duan (A. Crivoi and Duan, 2013), (Crivoi and Duan, 2014) used a Monte Carlo method to simulate the deposit. Kim et al. (Kim et al., 2010) obtained the final

deposit by modelling the droplet evaporation kinetics and the convection transport of particles to the contact line. Whereas, Crivoi and Duan modelling led to a two-dimensional (A. Crivoi and Duan, 2013) and three-dimensional structure of the deposit morphology (Crivoi and Duan, 2014) while considering the sticking probability of the particles (see Figure 2-14). All these simulations were in good agreement with experimental observations (see Figure 2-13 and Figure 2-14).

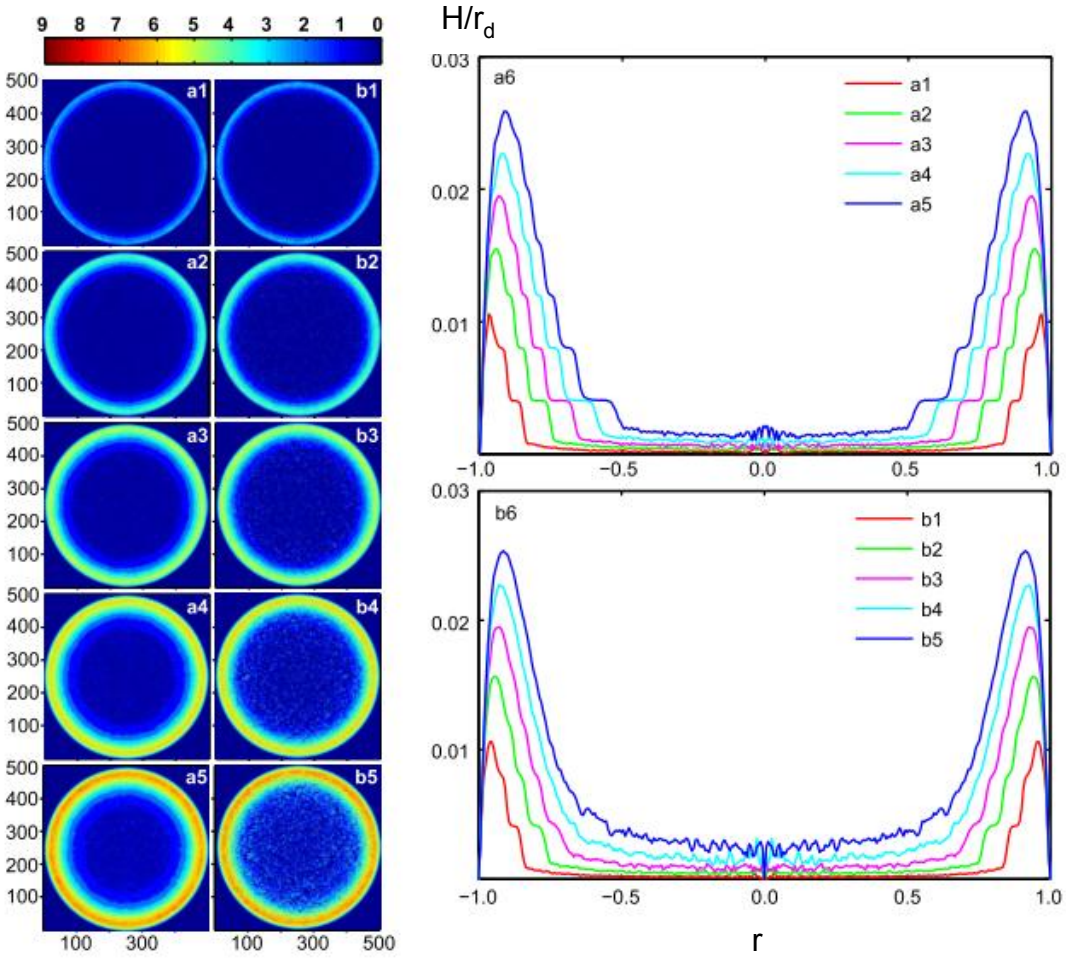

Figure 2-14: Results showing in the left column the top-view of the final coffee-ring structures for different volumetric particle concentration and sticking parameter values (data series a represents low sticking while data series b represents high particle sticking). The right column represents the corresponding cross-sectional height profiles of the two series (Crivoi and Duan, 2014)**.**

A ring-like stain is not always a hindrance. In the case of biomedical applications, the dried patterns of desiccated drops of blood revealed illnesses pathologies and health conditions (Brutin et al., 2011). For agrochemical

purposes, the "coffee ring effect" manages to blend ideally active ingredient particulate and oil adjuvant after crop spraying on leaves. The drops are pinned on the leaves, thus both active ingredients particulate and oil adjuvant are transported to the edge of the drying drop which will form a coffee ring stain rich in both components, hence forming an optimum blend. Furthermore as soon as the oil adjuvant is combined with the active ingredient, particulate in the ring, little spreading of the oil away from the particles are noticed (Faers and Pontzen, 2008) Also, for several nanotechnology applications this effect is highly desirable: nanoparticles and DNA self-assembly patterning (Zavelani-Rossi et al., 2012), (Wang et al., 2014), (Smalyukh et al., 2006) and size discrimination (Monteux and Lequeux, 2011). Indeed, as explained previously, due to the transport of solutes towards the droplet perimeter by capillary flow a ring stain will be formed. Thus, for nanoparticles and DNA a densely ordered structure will self-assemble at the periphery. In fact, it has been demonstrated that at the early stage of evaporation, the evaporation pace is slow, this enables the particle to form a well-ordered structure due to Brownian motion. Whereas, in the last moment of the droplet's life, the particle velocity increases radially due to a diverging evaporation near the three-phase contact line. This sudden change commonly referred to as "rush-hour", causes the particles to rush towards the contact thus forming a less ordered accumulation of particle (Marín et al., 2011a; Marín et al., 2011b; Mampallil, 2014). For nanoparticles, self-assembly can help in the fabrication of a micro-laser (Zavelani-Rossi et al., 2012), the self-assembly can enable hybridization study of DNA (Smalyukh et al., 2006) while it is proven to be an efficient technique to separate nanoparticles from microparticles (Monteux and Lequeux, 2011) (see Figure 2-15).

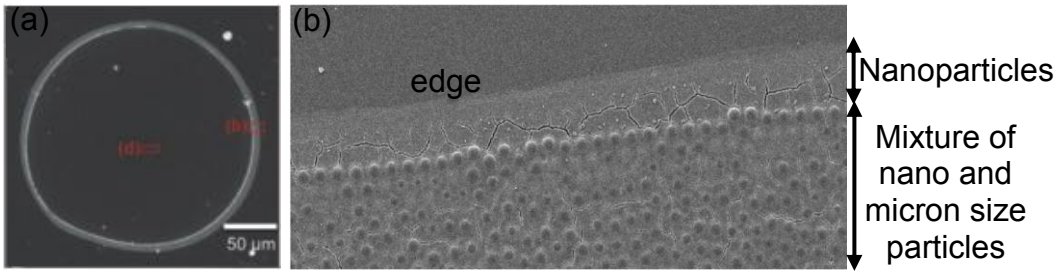

Figure 2-15: Pictures of self-assembled particulates by "coffee ring effect"/capillary flow upon solvent evaporation (a) nanoparticles self-assembly patterning (Zavelani-Rossi et al., 2012) **and (b)size discrimination** (Monteux and Lequeux, 2011)**.**

Nonetheless, in most cases the "coffee ring effect" (see Figure 2-13) is not a favourable outcome. An extensive amount of work has been aimed at suppressing this effect by modifying the particle transport mechanism. Particle transport mechanisms are detailed further in Chapter 4 while strategies to suppress the ring-like stain are discussed in more details in ensuing Chapters 5 and 6.

To summarize, the "coffee ring effect" is a ring-like stain due to the redistribution of uniformly distributed particles in solution. It is characterised by a high particle concentration at the contact line and low concentration in the centre of the deposit because evaporation is emphasized at the three-phase contact line compared to the apex of the droplet. Usually, this effect is undesirable in most applications (e.g. printing and coating) but can be a favourable result in nanoparticles self-assembly.

- Marangoni flow

In 1855, Thomson (Thomson, 1855) observed singular motions at the surface of alcoholic liquors which are constituted of a mixture of water and alcohol (Thomson, 1855). Because alcohol and water have different partial vapour pressure, the alcohol evaporates faster; hence a local modification of the surface tension occurs. Commonly, the surface tension, γ is temperature dependent and will change following equation 2.22 (Carle and David, 2015).

$$\gamma = \gamma_0 + \frac{\partial \gamma}{\partial T}(T - T_a) \qquad (2\text{-}22)$$

Where γ_0 is the surface tension at ambient temperature T_a and $\frac{\partial \gamma}{\partial T}$ is the temperature-dependence coefficient. To equalize the tangential stress generated, the fluid will flow from the warmest area T_+ (which are equivalent to the low surface tension Υ_- area) towards the coldest region T_- (which corresponds to the high surface tension Υ_+ area) with a stagnation point in the centre of the droplet (see in Figure 2-16 and Figure 2-17a). Ordinarily, this internal flow is called the “Marangoni flow” and can be of two natures: thermal which implies a temperature gradient or solutal which involves a component concentration gradient.

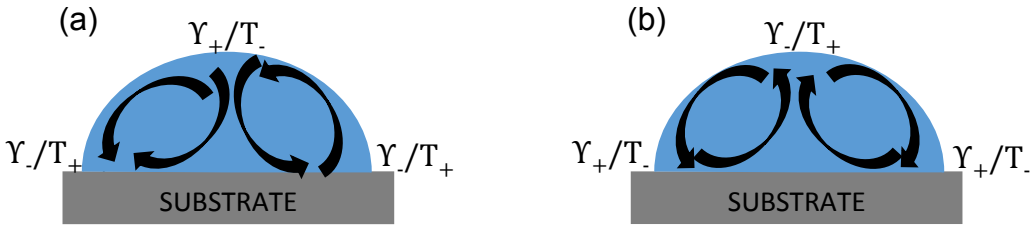

Figure 2-16: Schematic representation of Marangoni flow in an evaporating sessile droplet on (a) outward motion along substrate (b) inward flow alongside the substrate with a central stagnation point.

Several models have been developed to describe the thermal Marangoni flow. Hu and Larson modelled the internal thermal Marangoni flow of water droplets (Hu and Larson, 2005). A Finite Element Method (FEM) and a lubrication analysis were used in the Hu and Larson model. The finite element analysis was implemented to the heat equation in order to determine the temperature fields, which allowed to extract the droplet surface temperature profile. The analytical representation for the temperature fields alongside the liquid/vapour interface were used following a fitting of the FEM. Ristenpart *et al.* (Ristenpart et al., 2007) studied the evaporating behaviour of unmixed solvents. In their study, they determined the fundamental role of the thermal conductivity ratio (k_R) ($k_R = \frac{k_S}{k_L}$, where k_S is the thermal conductivity of substrate, and k_L is the thermal conductivity of liquid) and the contact angle (Θ) on the direction of the Marangoni flow. As such, for highly conductive substrates, energy is provided to the droplet, hence, temperature will be high at the three-phase contact line (since the convection pathway is shorter) and low at the apex (due to a longer convection pathway) as seen on Figure 2-16a. Hence, if particles are present inside the droplet, the thermal Marangoni flow will induce a circular motion along the liquid/vapour interface from the three-phase contact line towards the droplet apex. While for poorly conductive substrates, energy is not quickly accessible and has to be withdrawn from the droplet itself. Thus the three-phase contact line will become coolest and the apex of the droplet will be warmest (see Figure 2-16b). Hence, if particles are present in the droplet, the Marangoni flow will transport them from the warm droplet apex towards the cooler three-phase contact line. Both research groups Hu and Larson (Hu and Larson, 2005) and Ristenpart *et al.* (Ristenpart et al., 2007) were able to detect a critical contact angle, Θ_C (Θ_C<14°) at which the Marangoni flow direction is reversed. Xu *et al.* (Xu et al., 2012) also studied the liquid velocity field for a small pinned sessile droplet evaporating on an isothermal substrate. The

surface temperature of the droplet was determined with a finite element and lubrication analysis. From these analyses, it was discovered that for the isothermal substrates, the surface temperature increases steadily from the droplet centre towards the droplet edges. Also, above a critical Marangoni number value (Marangoni number represents the force of thermal Marangoni effect in drying droplets) a stagnation point will appear. Due to this stagnation point, particles away from this point will be carried towards the edge while the particles at the point will be transported toward the centre of the drop. These results are in good agreement with (Hu and Larson, 2005), (Ristenpart et al., 2007) and are valid for small contact angles($\Theta < 40°$).

Marangoni flow is also observed when the substrate temperature is modified (heated or cooled substrates). In the case of heated substrate, the three-phase contact line will be warm due to the heated substrate, thus the thermal Marangoni flow will move from the solid surface towards the liquid/vapour interface (see Figure 2-16a). On cooling substrates, the motion is reversed, the Marangoni flow will be directed alongside the liquid/vapour interface from the droplet apex (warmer area) towards the droplet edges (see Figure 2-16b) (Kim et al., 2011). To prove this assumption, Girard *et al.* (Girard et al., 2008) experimentally and numerically studied the evaporation of sessile water droplets on heated substrates (rough aluminium substrates). They worked with two substrates temperatures (30 and 50°C) and found that the three-phase contact line was warmer than the apex (see Figure 2-16a and Figure 2-17b). It was also determined that the simulated evaporation rate with and without Marangoni flow is similar thus this flow is negligible in water droplets. The comparison of the two simulated systems and the experimental results were in good agreement (see Figure 2-17b). Infrared thermography was the key technique to disclose the temperature gradients for droplets evaporating on heated substrates as seen on Figure 2-17b (Girard et al., 2008), (Fabien et al., 2011), (Sefiane et al., 2013). Hence, these different studies give a clearer idea of how the particles present will be redistributed within the droplet as a result of the thermal Marangoni flow.

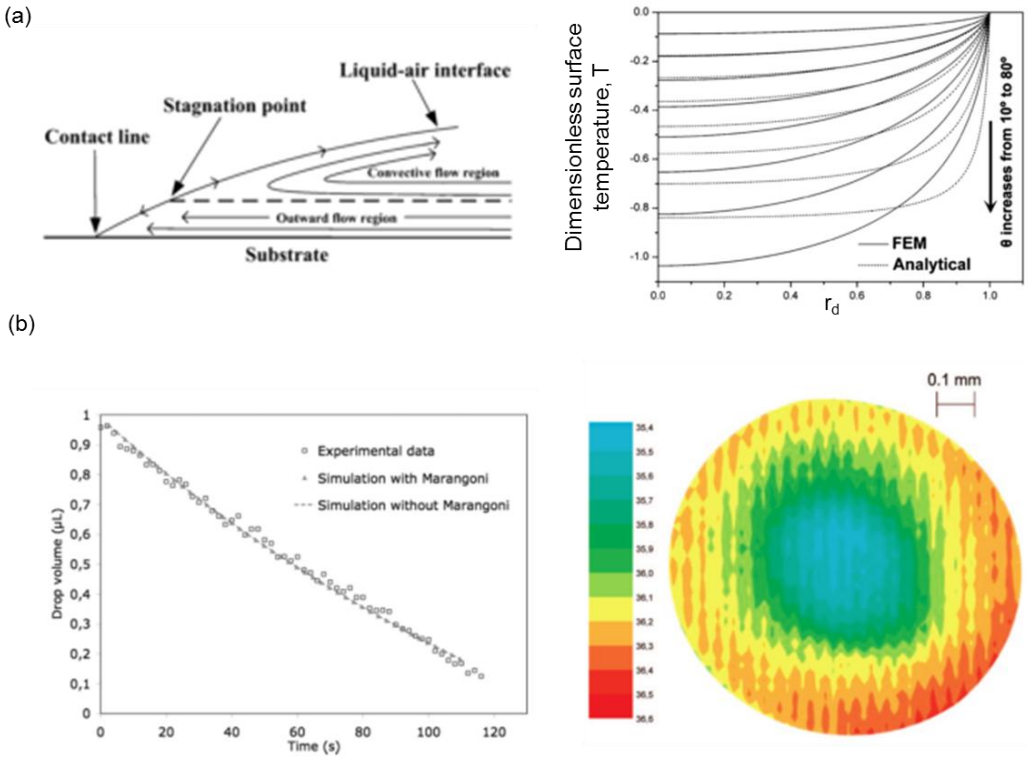

Figure 2-17: (a) On the left, a schematic of the thermal Marangoni flow inside the pinned evaporating droplets showcasing the stagnation point. On the right side, the dimensionless surface temperature T of the drying droplet as a function of the dimensionless radial distance to the centre r droplet radius at contact angles from 10 to 90°. The solid lines show the Finite Element Method results while the dashed lines represents the analytical equation (Xu et al., 2012)**, (b) In the left column, time evolution of water droplet volume with and without thermal Marangoni flow contribution compared to the experimental data at 50°C. The right column shows the infrared image of an evaporating sessile drop on an aluminium substrate heated at 40°C. The colour coding indicates the values of the actual temperatures in °C. It is worth noting that the apex of the drop is the coolest** (Girard et al., 2008)**.**

Together with the thermal Marangoni flow, a solutal Marangoni flow can be observed upon addition of surfactants (Nguyen and Stebe, 2002; Kajiya, Kobayashi, et al., 2009; Still et al., 2012), polymers (Poulard and Damman, 2007; Kajiya, Monteux, et al., 2009; Cui et al., 2012) as well as in binary mixtures (Park and Moon, 2006; Christy et al., 2010; Christy et al., 2011; Hamamoto et al., 2012; Talbot et al., 2013; Cecere et al., 2014). For the system with additives (surfactants and polymers), the surface tension will be reduced, thus the additives will be concentrated at the three-phase contact line due to capillary flow. This build-up of the additives will cause a compositional Marangoni flow along the liquid/vapour interface oriented from the three-phase contact line (which will exhibit a lower surface tension)

towards the apex (where the surface tension is high) of the droplet along the liquid/vapour interface (see Figure 2-16a and Figure 2-18a). Hence, the particles will be transported along by the compositional Marangoni flow.

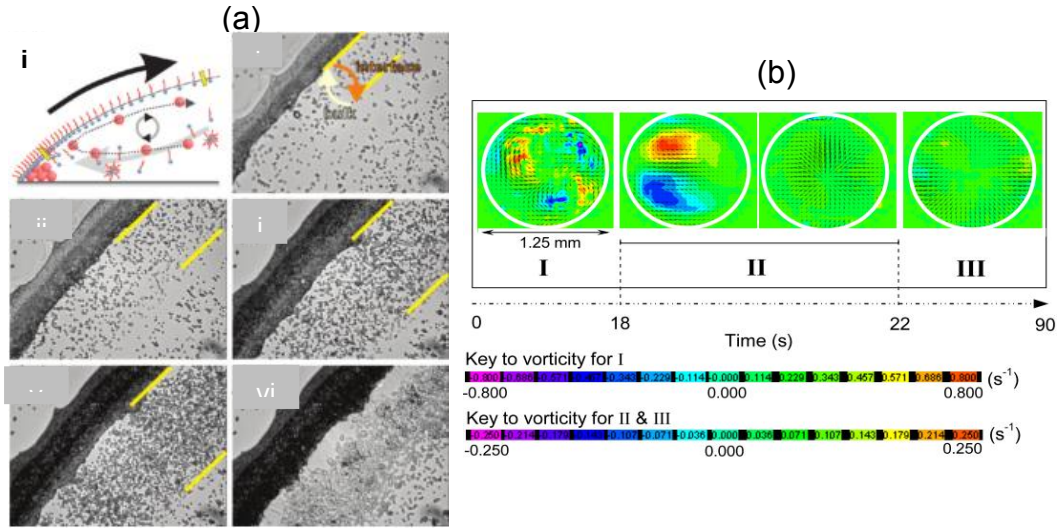

Figure 2-18: (a) (i) Schematic description of the solutal Marangoni flow; Pictures of a sample containing 0.5 wt.% polystyrene particles (1330 nm) and 0.5 wt.% sodium dodecyl sulfate showcasing solutal Marangoni flow at different stages in the evaporation (ii) t≈0.28t_E, (ii) t≈0.42t_E, (iv) t≈0.7t_E, (v) t≈0.86t_E and (vi) dried deposit (Still et al., 2012) **and (b) Particle image velocimetry results showing flow field in terms of velocity vectors and vorticity for the three evaporation stages** (Christy et al., 2011)

In the case of binary mixtures, the direction of the solutal Marangoni flow is determined by the surface tension of the more volatile component. The more volatile component will reach the liquid/vapour interface. Thus, for volatile solvent exhibiting a low surface tension, the flow will be directed as described by Figure 2-16b. The flow is illustrated by Figure 2-16a in the opposite situation. Christy *et al.* (Christy et al., 2010; Christy et al., 2011; Hamamoto et al., 2012) by using a particle image velocimetry observe flow in evaporation of ethanol/water droplets. This equipment enabled them to characterize the flow inside the droplets divided into three stages. In the early stage of evaporation, random vortices inside the droplets were observed which was induced by an ethanol concentration gradient. Then, a spike in radial velocity was also noticed while the vortices were experiencing exponential decaying with their migration towards the three-phase contact line- linked to a depletion of ethanol at the apex of the droplet. Finally, in the last stage, an outward flow towards the three-phase contact line was observed and consistent with the drying behaviour of the pure water droplet. Thus, at the end of the evaporation

process particles can be carried towards the three-phase contact (see Figure 2-18b).

In summary, Marangoni flow induces particle transport driven by surface tension gradients. These surface tension gradients are generated either by thermal or concentration gradient along the liquid/vapour interface. Thus a circular motion inward or outward along the substrate and the liquid/vapour interface will distribute the particles onto the substrate. This flow is a prime alternative to the "coffee ring effect" to promote a different particle transport inside evaporating droplets. In the subsequent chapters, the use of additives and binary water/ethanol mixtures were used to create a solutal Marangoni in order to redistribute the particles within the droplet and control the final deposit structure.

Thus, to obtain an optimum material deposition for the chosen application, the capillary flow or the Marangoni have to be implemented during the droplet evaporation process. In the subsequent section, the focus is placed on the pattern formation and particle transport mechanisms with an emphasis on the different conditions to create in order to suppress/avoid the ring stain.

2.2.2 Pattern formation and suitable variables to control final dried deposit structure

To target a better end product in many applications area, it is essential to anticipate and control the solids deposit morphology. The desired end results can fluctuate from the extreme cases of a ring stain or a uniform deposit to a plethora of complex structure (see Figure 2-19).

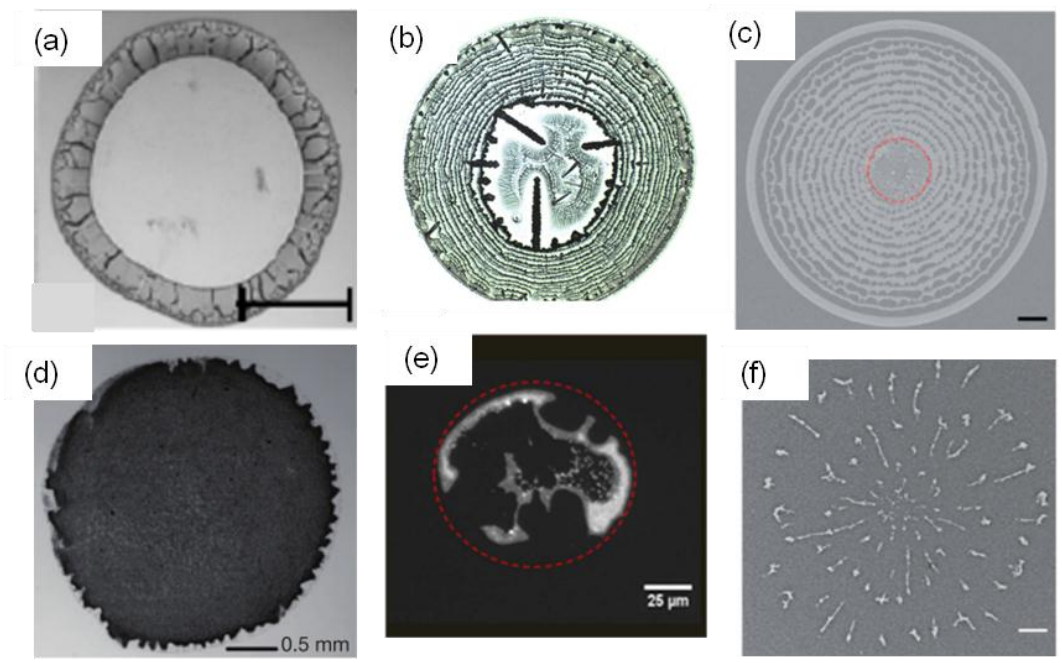

Figure 2-19: Different features obtain solvent evaporation. From left to right: (a) ring stain from a dried colloidal microspheres droplet with cracks in the structure (Deegan et al., 2000)**, (b) dried droplet of sodium poly styrene sulfonate containing 0.1 mol/L sodium chloride** (Kaya et al., 2010)**, (c) multiple concentric rings of colloidal sulfate-modified polystyrene beads at 0.5 vol%** (Yang et al., 2014)**, (d) uniform film deposit of ellipsoidal polystyrene particles** (Yunker et al., 2011)**, (e) non-circular deposit of polystyrene particles** (Biswas et al., 2010)**, (f) spider-web deposit of 200 nm polystyrene particles at 0.1 vol%** (Yang et al., 2014)**.**

Several techniques have been developed and explored for this purpose. These techniques can be divided in three major groups: substrate influence, internal flow motion and particle influence as detailed below.

- Substrate influence

As previously explained, the controlled deposition of colloidal particles on a surface involves the interplay of many parameters. The liquid properties are obviously critical to the spreading (such as viscosity for instance) as are the characteristics of the substrate.

When a de-pinning of the contact line occurs this can promote the generation of a wide varieties of patterns. When particles are carried towards the droplet centre due to a receding contact line this can form: saw-toothed (Deegan, 2000), central dot (Sun et al., 2009) or spider-web deposits patterns (Yang et al., 2014). Several concentric rings formed at the pinned location can be

observed due to a series of stick-slip motions of the pinned contact line (Shanahan and Sefiane, 2009), (Orejon et al., 2011), (Moffat et al., 2009), (Askounis et al., 2014). While as seen previously a pinned contact line leads to a ring-like stain (Deegan et al., 1997). Another interesting method to avoid a ring-stain like final deposit is by substrate patterning in changing the wetting on different area of the same substrate. Léopoldès *et al.* (Léopoldès et al., 2003) managed to produced geometrical shaped deposits by interspacing hydrophobic and hydrophilic bands at a smaller length range than the droplet diameter. The geometry of the surface is also a factor to consider in order to avoid a "coffee ring stain". The presence of protuberances of different size and shape can thus alter the droplet spreading (Alam et al., 2007). Similarly, polygonal posts are another way to promote a non ring-like stain (Vrancken et al., 2013).

- Internal flow influence

A change in the internal droplet flow can suppress the formation of the "coffee ring effect". In that respect, capillary forces created by particles along the liquid/vapour interface can suppress the ring stain by carrying the particles through an inward motion towards the centre of the drop (Weon and Je, 2010), (Jung et al., 2010). The capillary forces are observed in conditions similar to the "coffee ring effect": pinned contact line, free liquid interface and a gradually decreasing contact angle and depends on the apparent contact angle of the droplet as well as the size of the particles. As explained previously a Marangoni flow will transport particle away from the three-phase contact line by recirculation which can reverse the ring-like stain formation (Truskett and Stebe, 2003; Park and Moon, 2006; Hu and Larson, 2006; Majumder et al., 2012; Still et al., 2012; Talbot et al., 2013) and can help promote a highly ordered crystalline structure (Lim et al., 2008). Another way to suppress the "coffee ring effect" is by modifying the evaporative flux and its characteristic non-uniformity (Deegan et al., 2000). Evaporation lithography is also an efficient technique in order to avoid the "coffee ring effect" (Harris et al., 2007). A mask composed of several holes is displayed above a droplet and the evaporation is heightened in the open regions thus transporting the particles. Mampallil *et al.* (Mampallil et al., 2012), Eral *et al.* (Eral et al., 2011) used electrowetting to modify the internal flow of droplets. The presence of an electric field suppresses the capillary flow and concentrates the particles in

the centre of the deposit. Evans *et al.* (Chen and Evans, 2010) by use of superhydrophobic substrates and a vertical wall manage to hinder the evaporation on one side leading to an arched structure while the "coffee ring effect" was formed on the other side.

- Particle influence

Particle size, shape and the different interactions such as particle-particle and particle-substrate all can alter the feature of the final deposit. In mixtures of particles of different size, it has been noticed that the particle can be discriminated with the smaller particles collecting at the contact line. This size segregation is caused by a height constraint nearby the contact line (Monteux and Lequeux, 2011). Chhasatia and Sun (Matter et al., 2011) also observed this size segregation and investigated the effect of substrate wettability (from hydrophilic to hydrophobic) on the influence the final deposit morphology as well. These different wettabilities lead to a mixture of the two particles size in the centre of the drop to separate rings.

It was also proven that particle shape can affect the dried deposit structure in height and width with the key factor being the stacking ability of the particles. Hodges *et al.* (Hodges et al., 2010) investigated the dried features of spherical Ludox silica and disk-like shape Laponite of comparable size. A higher ring stain for the disk-like Laponite compare to the spherical Ludox was noticed, caused by a stronger affinity for stacking of the disk-like particles. Yunker *et al.* (Yunker et al., 2011) in that respect demonstrated that ellipsoid particles form a uniform film deposit upon drying. Indeed, during evaporation, particles are transported to the liquid/vapour interface by an outward capillary flow but the strong inter-particle interactions form loosely packed structures at the interface. These structures stop particles being carried towards the edge and thus lead to the formation of a uniform deposit. Silver nanoellipsoids were also seen to suppress the "coffee ring effect" due to strong inter-particle interaction which weakens the Marangoni flow and forms a uniform film deposit by comparison with the deposit left by silver nanospheres (Tang et al., 2014). Gold nanorods can self-assemble as well and not form a "coffee ring effect" if the repulsive interactions are adjusted (Guerrero-Martínez et al., 2009), (Xie et al., 2011), (Ming et al., 2008), (Martín et al., 2014). While, other work showed that gold nanotriangle leaves a perfectly ordered ring stain upon drying (Walker et al., 2010). The growth of a film at the liquid/vapour interface

can also be achieved thanks to inter-particle attractive forces of surface active particle (Bigioni et al., 2006). The change in pH linked to DLVO interactions can also modify the final deposit. For acidic and basic solutions, a "coffee ring" is generated while at intermediate pH a uniform film is obtained. A ring-like stain is formed due to prominent repulsive interaction (Bhardwaj et al., 2010), (Dugyala and Basavaraj, 2014).

Besides, particle-particle interaction, particle-substrate interaction also plays a major part in the final deposit structure (Jung et al., 2010), (Anyfantakis et al., 2015) . The charge difference between the substrate and the particle prevents particle movement which leads to a disordered arrangement at the contact line and weakens the "coffee ring effect" formation (Yan et al., 2008). Whereas, the same charge between the substrate and the particle prevents attraction thus an ordered lattice is formed at the contact line cause by an outward flow.

The concentration of particles is another factor used to modify the final deposit morphology. Deegan *et al.* (Deegan, 2000) observed a variety of deposit patterns while increasing polystyrene microspheres concentration (see Figure 2-12). Numerous rings of diverse thickness and saw-tooth or fine structure of radial lines arrangement were noticed. Park and Moon (Park and Moon, 2006) studied microspheres mixed-ink solutions, in their work they observed that at low loading content a ring-like deposit was formed whereas at high concentration mixed-solvent ink led to a monolayer build-up. Sefiane *et al.* (Sefiane, 2010) studied alumina and titania nanofluids. For the titania system, it was observed upon solvent evaporation that as the temperature increased concentric rings were formed whereas in the case of the alumina system, the thickness was seen to increase proportionally with the particle concentration regardless of the temperature. By addition of hydrosoluble polymers (Cui et al., 2012), the "coffee ring effect" was also suppressed. Concretely, solutal Marangoni flow will be generated due to the non-uniform evaporation flux along the droplet liquid/vapour interface. Thus, non-homogeneity in the polymer concentration will be generated alongside a rise in viscosity of the droplet. The higher viscosity hence blocks the outward capillary flow and suppresses the “coffee ring effect”. The crystalline ordering of the contact line of a dried droplet can also alter the deposit. This structure is due to a time dependency (Marín et al., 2011a). Addition of electrolyte such as sodium chloride also leads to interesting features due to the crystallisation of the salt in the dried deposit structure (Takhistov and Chang, 2002; Kaya et al., 2010;

Gorr et al., 2013; Dutta et al., 2013; Sperling et al., 2014; Dutta Choudhury et al., 2015; Shahidzadeh et al., 2015).

2.3 Summary and conclusions

- Summary

The evaporation of a droplet is a process commonly found in the daily life. Yet, despite its apparent triviality several physical parameters are at work. Indeed, an evaporation process can be engineered, especially upon addition of solutes in the fluid matrix. Upon, addition of solutes, several forces (Van der Waals attractive forces and electrostatic repulsive forces) have to be considered to work with a stable suspension or to destabilise the suspension on purpose as seen previously in Section 2.1.1.

Following, the suspension preparation, the droplet can be deposited on a surface, in our case a solid surface is exploited. The characteristics of the substrate, the velocity at which the droplet impacts the surface as well as physical aspects govern the shape that the droplet will form with the substrate as thoroughly explained in Section 2.1.2.1.

Then, the final step is the evaporation process itself through diffusion or convection. Thus, the droplet shape will evolve overtime. The droplet shape evolution implies the presence of internal flows. These internal flows are paramount to allow the generation of several patterns. Commonly, solutes dispersed in a suspension will be transported due to a capillary flow leading to the formation of a “coffee ring effect” as explained previously in Section 2.2.1. However, this pattern is usually avoided and significant work has been done to use the Marangoni to hinder its formation as seen in Section 2.2.2.

- Conclusions

A full understanding of the evaporation of a particle-laden particle is still challenging. The formation of the “coffee ring effect” is well understood and can be simulated in good agreement with experimental data. Yet, overcoming,

its formation is still a great challenge due to its plethora of applications (e.g. paint, coating, inkjet printing to cite a few).

In the next chapter, the techniques and materials used to collect the different data are reviewed. While in the subsequent, result chapters, the evaporation process of particle-laden colloidal droplets was studied for different systems. The overall aim was to further the knowledge on droplet drying, how the composition variation can have a direct impact on the final deposit morphology and propose novel strategies to suppress the “coffee ring effect”.

Chapter 3
Experimental setup and procedures

3.1 Particle characteristics

In this study, three types of particles have been employed. Two commercially available nanoparticle samples, namely Ludox AS-40® (40 wt% silica suspension in water (with sodium counter-ions and traces of chloride ions), Sigma-Aldrich, UK), Laponite RD (synthesized clay powder, Rockwood Additives Ltd, UK) and a Polymethylmethacrylate (PMMA) latex suspension synthesised in-house by Mr Mohmed Mulla. We selected these particles because they have a number of key differentiating physical characteristics (see Table 3-1).

Table 3-1: Particle systems properties.

System type	Inorganic		Organic
Particle name	Laponite RD	Ludox AS-40 ®	PMMA latex
Surface charge	Face: negative Edge: positive	Negative	Negative
Particle size, nm	Diameter: 25-30 Thickness: 1 (Li et al., 2009)	25	73
Chemical composition, wt%	59.5% Si_2O, 27.5% MgO, 2.8% Li_2O and 0.7% Na_2O (Hodges et al., 2010)	40% SiO_2 ,0.16% NH_3, 0.08% Na_2O, 0.02% Formaldehyde	$(C_5O_2H_8)_n$
Particle shape	Disk-like	Spherical	Spherical
Density, g/cm^3	2.53 (Labanda and Llorens, 2004)	2.2	1.1
Potential applications	Inkjet printing	Inkjet printing	Inkjet printing, biomedical

Each sample also presents different wettability behaviour which may have an influence on the structures of any dried deposits upon solvent evaporation.

3.2 Fluids, surfactant and electrolyte

Milli-Q-water was obtained from a Millipore ultrapure water system with a conductivity of 18.2 MΩ.cm. Ethanol (EtOH, absolute HPLC grade, Fisher Scientific, UK), was used to formulate a low surface tension binary mixture. Sodium dodecyl sulfate (SDS, VWR Prolabo, ≥98%) was the anionic surfactant selected and sodium chloride (NaCl) was used as the added electrolyte (Sigma-Aldrich).

All experiments were performed on freshly 1000 ppm samples diluted from a stock solution. These samples were placed for 5 minutes in a 25°C ultrasonic water bath to break down any aggregates before undertaking any type of characterising measures.

3.3 Characterisation of samples

The Zetasizer Nano ZS (Malvern Instruments, UK), with Zetasizer software (Version 6.32), was used to measure the size of the hydrodynamic diameter, the dispersed state and the zeta potential of the different samples studied.

3.3.1 Dynamic Light Scattering

Typically, Dynamic Light Scattering (DLS) measures the different intensities of scattered light due to the Brownian motion of particles in suspension as a function of time. The processing of these intensity variations produces the velocity of the Brownian motion and thus the particle size using the Stokes-Einstein equation (3-1):

$$\boldsymbol{D = \frac{k_B T}{6\pi\mu r_H}} \qquad \textbf{3-1}$$

Where D represents the particle diffusion rate, k_B is the Boltzmann's constant, T is the temperature, μ is the mobility of the particle and r_H the hydrodynamic radius of the particle.

Experimentally, the DLS measurements were collected following this procedure. With the help of a 2 mL syringe, 1.5 mL of our prepared samples was added slowly into a cuvette to avoid any bubbles formation. The sample was further filtered through a 0.45

µm syringe filter before each measurement and loaded into the allocated cell area inside the instrument. Inside, this device a laser beam is aimed at the sample and the scattered laser light is then collected by a detector positioned at 173° to the incident ight. The collected intensities are then processed by the pre-installed Malvern Zetasizer software version 6.32. Our measurements were performed for five minutes, with each measurement taken as an average of ten runs for the same sample. For each sample, the measurement was repeated five times. The standard deviation between these five measurements was used as an estimate of the measurement error.

3.3.2 Zeta potential

Typically, the incorporated laser Doppler micro-electrophoresis measures the zeta potential. This method consists in the application of an electrical field to the sample and the determination of the velocity at which a particle moves in the suspension. The zeta potential is then calculated using the Henri equation (3-2):

$$U_E = \frac{2\varepsilon\zeta f(Ka)}{3\eta} \qquad \textbf{3-2}$$

Where ζ represents the zeta potential, U_E is the electrophoretic mobility, ε is the dielectric constant, η is the viscosity of the liquid and *f(Ka)* is the Henry's function.

Experimentally, the zeta potential measurements were collected following this standard operating procedure. With the help of a 2 mL syringe, 1.5 mL of our prepared samples was added slowly through a 0.45 µm syringe filter into a capillary cell avoiding any bubbles formation and residual aggregates. The capillary cell was then positioned inside the instrument. Inside the device, a laser beam is aimed at the sample to which a potential is applied. This laser beam is split in two to provide an incident and reference beam. The incident beam is aimed at the sample and the scattering light is detected at a 17° angle on a combining optics. Due to the potential applied, any particles moving in the suspension will alter the intensity of light detected at a frequency proportional to the particle velocity. The reference beam is then combined to this scattered light on the optics. This combination relayed to a detector sends this information to the Malvern software version 6.32 which produces a frequency spectrum extracting the electrophoretic mobility and thus the zeta potential. Our measurements were performed for five minutes, with each measurement taken as an average of ten runs for the same sample. For each sample, the measurement was repeated five times. The standard deviation between these five measurements is used as an estimate of the measurement error.

3.3.3 Turbiscan

Classically, Turbiscan TLab apparatus (Formulaction, France) was the apparatus used to investigate the sedimentation profile of the particles upon electrolyte and ethanol addition at 25°C. This technique involves a vertical multiple light scattering, where the intensity of a pulse near-infrared light (850 nm) is measured from bottom to top along the sample as a function of time.

Initially, the dispersed suspension was illuminated with a narrow light beam. Interferences between waves scattered from particles were overlooked, hence, under these stipulations, the mean free path of light, *l*, which corresponds to the mean distance travelled by photons before being subjected to a scattering occurrence, can be evaluated through the particle surface density, this latter value is derived from the particle mean diameter *d* and particle volume fraction *φ,* and the scattering efficiency factor Q_s (3-3):

$$l(\varphi, d) = \frac{2d}{3\varphi Q_s} and\ \varphi = \rho_p \frac{\pi d^3}{3\varphi Q_s} \quad \textbf{3-3}$$

Where ρ_p is the particle density.

Experimentally, a reading head constituted of a pulsed near-infrared light (850 nm) and two synchronous detectors, move along the sample to scan its entire length. The transmission detector collects the transmitted light while the backscattering detector receives the backscattered light at a 135° angle. Thus, the reading head gains transmission and backscattering information and sends it to the pre-installed TLab software for post-processing and analysis. The distinguishing size of the backscattered spot light is characteristic of the photon transport mean free path *l**. The backscattered light flux *BS* calculated through a thin detection area of thickness *dh* is given by (3-4):

$$BS = \sqrt{\frac{dh}{l^*}} \quad \textbf{3-4}$$

The photon transport means free path l* is linked to the particle mean diameter and the particle volume fraction through (3-5):

$$l^*(d, \varphi) = \frac{2d}{3\varphi(1 - g_a)Q_S} \quad \textbf{3-5}$$

Where, g_a is the asymmetry factor.

The transmission T_r measured by an optical analyser is a function of the photon mean free path *l* defined as (3-6):

$$T_r(lr_i) = T_0 exp^{\frac{-2r_i}{l}} \quad \textbf{3-6}$$

Experimentally, the data were collected following this experimental standard procedure. With the help of a 40 mL syringe, 20 mL of the sample was filled in a clean 55 mm borosilicate glass tube and placed in the measuring chamber. The data displayed as curves on the TLab software show the percentage of transmitted and/or backscattered light as a function of the sample length in millimetre. For each studied system, the sample was running for several minutes (45 minutes in ethanol added system and 2 hours for electrolyte added system) to match the drying behaviour of the deposited droplets. The collected data were post-processed using the Turbiscan software 1.3. A picture of the sample was taken before and at the end of each measurement to correlate the sedimentation behaviour of our samples.

3.4 Cleaning procedure and substrate preparation

3.4.1 Cleaning procedure

Ethanol (EtOH, absolute HPLC grade, Fisher Scientific, UK), Methanol (MeOH, HPLC grade, Fischer Scientific, UK), Hydrochloric acid (HCl, 37% acid fuming, Merck KGaA, UK), and surfactants Decon-90 solution (Decon Laboratories LtD., UK), and sodium dodecyl benzene sulfonate (SDBS, Santa Cruz Biotechnology Inc., USA) were used to clean the glassware prior to use.

All glassware including the 1 mL glass syringe (1001 TLL, PTFE Luer Lock, Hamilton, UK) and needle (1.25 mm outer diameter, nickel plated brass needle, Hamilton, UK) were cleaned by soaking in SDBS diluted (10 wt%) with Milli-Q-water for 20 minutes in an ultrasonic water-bath, before being rinsed with copious amount of Milli-Q water, followed by a final rinse with EtOH. The clean glassware was then further dried using compressed gas from either a nitrogen gun or a dust remover. The glassware was then used immediately.

The different particle systems are deposited on treated and untreated glass slides (microscope slides, Menzer-Glaser, Thermo Scientific, UK) to explore the effects of both hydrophilic and hydrophobic substrates. The substrate preparation is detailed below.

3.4.2 Preparation of uncoated glass slides

Each glass slide was cut in half using a diamond pen. These glass slides were then soaked in a SDBS solution at 10 wt% for 20 minutes in an ultrasonic bath to remove any small particles and contaminants from the surface. After being thoroughly rinsed in Milli-Q-water, the slides were soaked in EtOH immediately prior to use. Before, a droplet deposition was made, each glass slide was carefully dried using compressed gas from either a nitrogen gun or a dust remover ensuring to remove any visible fibres and contaminants.

3.4.3 Preparation of coated glass slides

The cut glass slides were cleaned following the approach described for the uncoated glass slides. The glass slides were then soaked in a 1:1 mixture of MeOH/HCl for 30 minutes before being thoroughly rinsed with Milli-Q-water. Once again, the glass slides were dried using compressed gas from either a nitrogen gun or a dust remover. The glass slides were then placed in a dessicator along with approximately 1 mL of Chlorotrimethylsilane (TMSCl, 99% GC grade, Sigma Aldrich, UK), the glass slides were removed after the TMSCl had completely evaporated (it was observed to be after five days).

Following the silanization, 5 drops of water were deposited on a coated slide to verify the increase of the apparent contact angle (Θ_{ACA}) for a sessile drop. From the different batches prepared here, an average Θ_{ACA} of 89±6° is measured. The glass slides are now considered to be hydrophobic (see Figure 3-1).

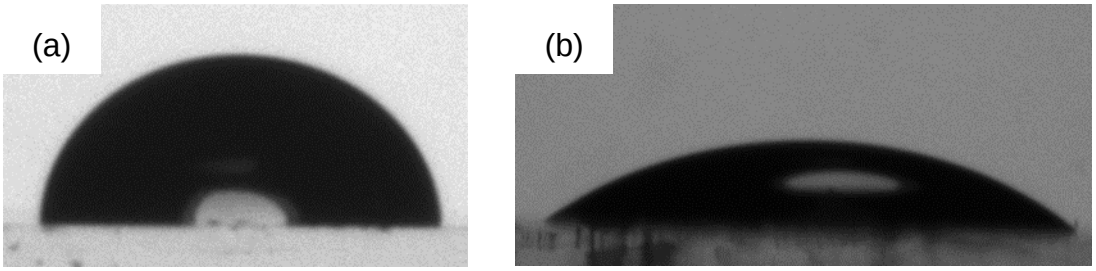

Figure 3-1: Picture of a single Milli-Q-water droplet deposited on (a) silanized coated glass slides, the apparent contact is measured at Θ_{ACA}= 89 ± 6° and (b) untreated glass slide the measured apparent contact is Θ_{ACA}= 34 ± 2°.

In comparison, the average Θ_{ACA} for Milli-Q-water droplets on the untreated slides was measured as 34±2º (Lim et al., 2015),(Arayanarakool et al., 2011),(Sumner et al., 2004),(Vicente et al., 2012). This high apparent contact angle, Θ_{ACA}, is consistent with the presence of organic contaminants from the atmosphere.

Following the substrate preparation, droplet deposition and evaporation test were undertaken for various particle samples according to the protocol detailed below.

3.5 Wetting properties recording

3.5.1 Temperature and humidity monitoring

In order to monitor the surrounding environment of the droplets during the drying process, a ceramic chamber was used with the KSV CAM 200 (see Figure 3-2). This chamber was used to ensure that the experiments were undertaken in a clean and controlled atmosphere. Besides, preventing contamination from atmospheric particulates, the chamber was also used to control the working conditions.

Figure 3-2: Picture of the ceramic chamber, constituted of two borosilicate glass viewing windows embedded in the side-walls, used to protect the experiment from the atmospheric contaminants and to measure the surface tensions and apparent contact angle Θ_{ACA} of the different systems.

The chamber included two borosilicate glass viewing windows in the side-walls. These windows allowed for the recording of the side view profile of the sessile droplet inside the chamber. Two digital probes were fitted inside the chamber in order to record the temperature and relative humidity variation over the drying period (Evaluation Kit STH71, Sensirion, Switzerland). Mean data were determined from the probes using a set of three experimental droplet depositions for each particle system.

3.5.2 Image calibration

Two contact angle goniometers were used in this study: a Krüss DSA-100 (Krüss GmbH, Germany) and a KSV CAM 200 from KSV Scientific.

For both contact angle and surface tension measurements, the images were calibrated to ensure the calculation accuracy from the images before each deposition. Two standard calibration balls were used. A standard 3 mm magnification sphere (ruby ball, First Ten Angstroms, USA) was associated with the Krüss DSA-100 goniometer. While a 4 mm spherical magnification sphere (Tungsten carbide, Ultra Prazision Messzeuge GmbH, Germany) was used in correlation with the KSV CAM 200.

The same procedure for the Krüss DSA-100 was followed to collect the data reported for Ludox AS-40 ® in Milli-Q water and Laponite in Milli-Q water. In the pre-installed Drop Shape Analysis (DSA, v1.9) software a contact angle experiment was selected. Then, the experiment parameters were added such as needle diameter, recording time for the drying sequence and density of the solvent. Then an experimental window was opened, and the calibration ball was positioned on the moving stage. The calibration ball was adjusted as to be visible on the experiment screen. The needle was then fixed to the needle holder and automatically lowers down. As the calibration ball is 0.4 x bigger than our needle (1.25 mm outer diameter), while calibrating, the image was focused as to have a clear visual of the needle as well as the calibration ball. A small gap was left to allow an easy calibration of the needle size. The illumination and contrast were then adjusted as to optimize a good reflection of the droplet, hence an easy determination of the baseline (contact line between the droplet and the substrate). A snapshot of this was then taken to help in the post-processing of the images using a Matlab code (see Figure 3-3).

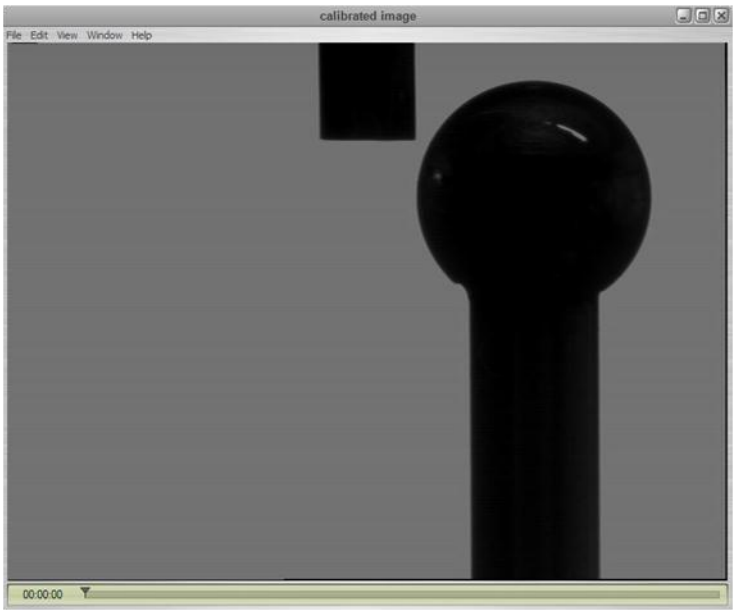

Figure 3-3: Picture of a calibrated image with the Krüss DSA-100 contact angle goniometer. The needle used to assess the sharpness of the image has a 1.25 mm outer diameter.

The calibration procedure for the KSV CAM 200 was as follow. In the Attension Theta v4.1.9.8, a calibration experiment was selected, while the needle was fixed to the needle holder, while the calibration ball was positioned on the moving stage. Similarly, since the calibration ball is 0.3 x bigger than the needle (1.25 mm outer diameter), the calibrated image was focused as to have a clear visual of the needle and the calibration ball. The camera focus and contrast were then optimised as to have a white to light grey background. This frame was then recorded. Using a calibration fitting window, two thirds of the ball was then placed inside the calibration box (standard procedure of the equipment company) and the calibration diameter was then entered. To assess, the good calibration a purple line was seen around the calibration ball. Once this calibration was done, the only actions allowed were for the removing of the needle to fill it with the sample and the stage. Upon calibration, an automatic calculation of the wetting was then possible with the software (see Figure 3-4).

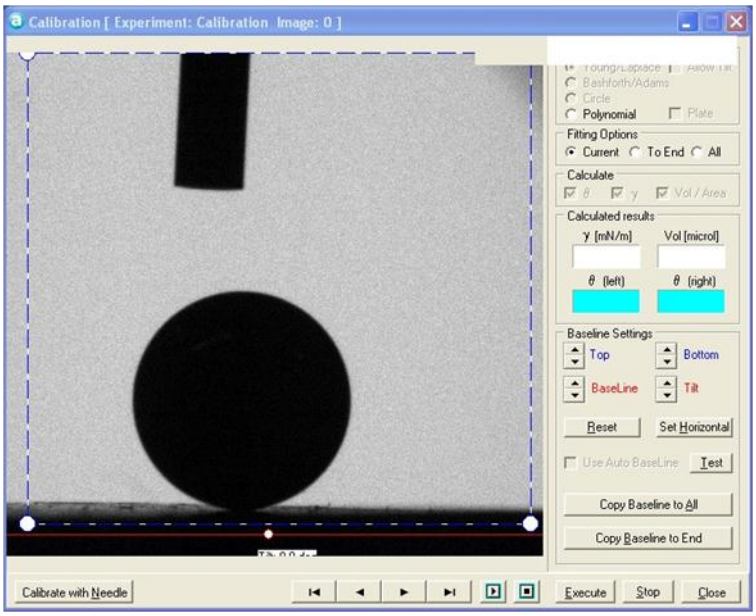

Figure 3-4: Snapshot of a calibration experiment done with the KSV CAM 200 contact angle goniometer. The needle used to assess the sharpness of the image has a 1.25 mm outer diameter.

Once the calibration was set the recording of an experiment was undertaken.

3.5.3 Wetting properties recording

Initially, a Krüss DSA-100 contact angle goniometer with a temperature-controlled stage (Figure 3-5) was used to record the evolution of colloidal droplets during drying. The DSA-100 is equipped with an adjustable moving stage, a light source, a CCD camera capable of transferring a droplet profile sequence to a computer up to 25 frames per second (fps) and a computer dosing built in system. The Drop Shape Analysis, version 3.0 software was used to control the dosing system, droplet deposition, and to capture the droplet profile sequences based on the droplet sessile technique.

The second contact angle goniometer used was a KSV CAM 200 (Figure 3-6). It is also equipped with a LED light, an adjustable moving stage, a CCD camera to digitally analyse the recorded droplet profile of the generated colloidal droplets up to 60 fps. Unlike the other equipment, the droplets are manually generated.

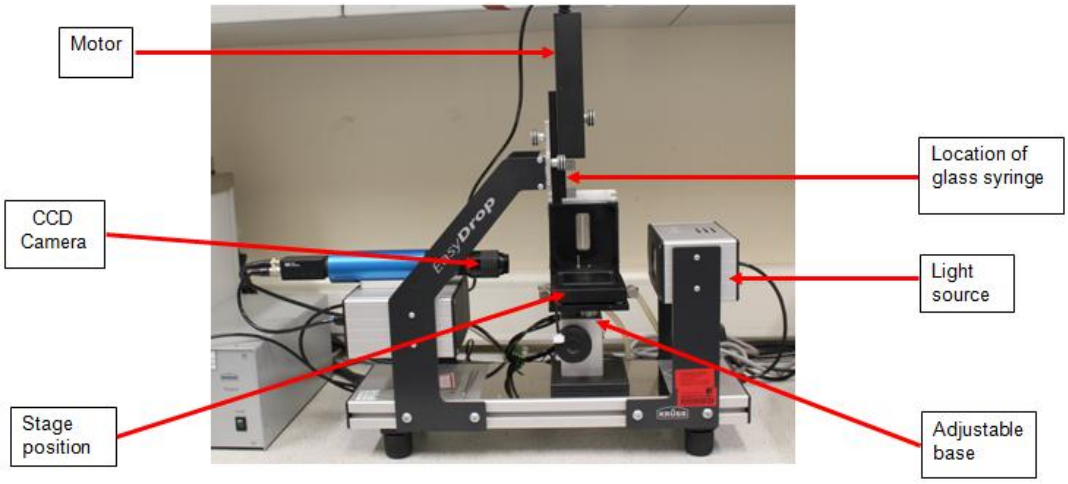

Figure 3-5: Image of the Krüss DSA-100 contact angle goniometer composed of a CCD camera to record the side-view droplet profiles, a moving stage to adjust the sample position, a motor to automatically dispense the droplet volume, a syringe holder to fix the glass syringe, a LED light source to illuminate the sample from the side, a moving base to adjust the CCD camera focus and a built-in temperature and humidity chamber to record the atmospheric variation during the course of an experiment.

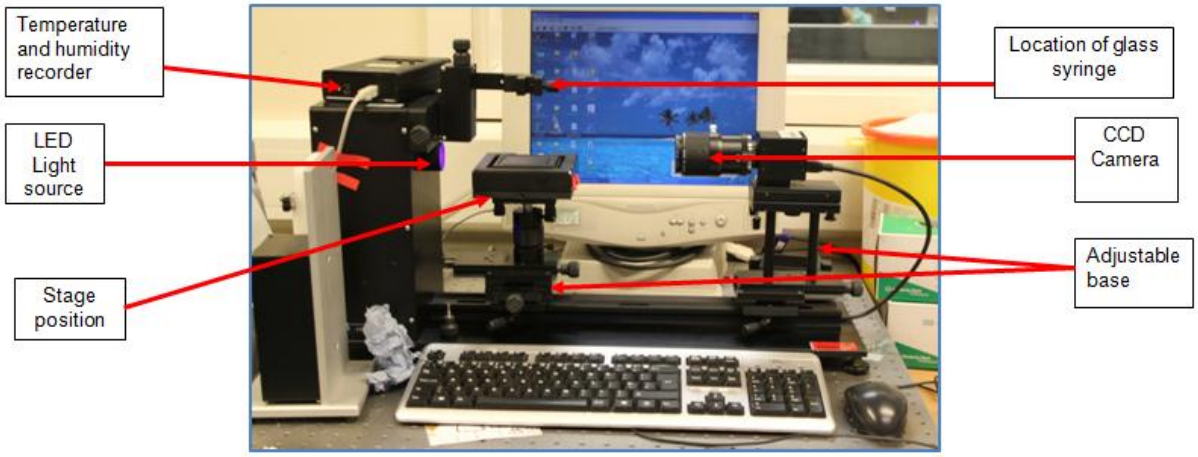

Figure 3-6: Image of the KSV CAM 200 contact angle goniometer composed of a digital CCD-camera, an adjustable stage, a syringe holder, an adjustable base to improve the focus of the camera, a LED light source to illuminate the droplet and allow a good contrast image, a temperature and humidity recorder with its associated probes to monitor the experiments conditions and a computer to process the recorded images.

Typically, a sessile droplet resting on an ideally flat substrate is an important parameter that describes the interplay between the various interfacial tension values through the Young-Laplace equation (3-7):

$$\gamma_{SV} = \gamma_{LV} \cos\Theta + \gamma_{LS} \quad \textbf{3-7}$$

Where, γ_{SV}, γ_{LS}, γ_{LV} represents respectively the different surface tensions solid/vapour, liquid/solid and liquid/vapour and Θ_{ACA} is the equilibrium contact angle (see Figure 3-7) in disregard of the gravitational effect.

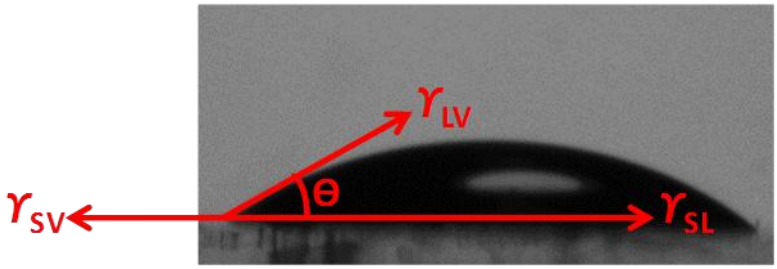

Figure 3-7: Schematic representation of Young's force at equilibrium at the three-phase contact line of Milli-Q water resting on a substrate.

Experimentally, following, the calibration, the 1 mL glass syringe was initially filled with 0.2 mL of the sample of interest. The 0.2 mL sample was then ejected as waste to clean the syringe and the needle. The syringe was then re-filled with another 0.5 mL of sample and 5 test drops were deposited on separate glass slides to assess the drop shape and to ensure drop consistency. The needle was place at a fixed distance from the substrate (4.7 ± 0.3 mm, averaged from the different system studied); this can be checked on the software screen. Subsequently, a previously prepared substrate (see description in 3.4.2 and 3.4.3) was placed on the moving stage, and a 16 ± 4 µL droplet (average from the droplet volume used in this thesis) was deposited gently on the desired substrate. The drying was recorded until complete evaporation of the solvent at a rate of one frame per second in the temperature and humidity chamber.

From the recorded sequence, the droplet apex height, H, and its contact diameter, thus its radius, r_d, can be calculated thanks to the initial calibration. The droplet was assumed to be spherical (see Figure 3-8) and as such can be characterised by four main parameters: contact angle Θ, droplet height at its apex, H, droplet radius, r_d, and the radius of a sphere shaping the spherical cap of the drop, R_S. Two mathematical relationships can be obtained:

$$\boldsymbol{H = R_S(1 - \cos\theta)} \text{ and } \boldsymbol{H = r_d \tan\frac{\Theta}{2}} \quad \textbf{3-8}$$

And the volume can be determined from the following equation:

$$V = \frac{\pi H}{6}\left(3r_d^2 + H^2\right) \qquad \textbf{3-9}$$

Where *V* is the droplet volume (see Figure 3-8).

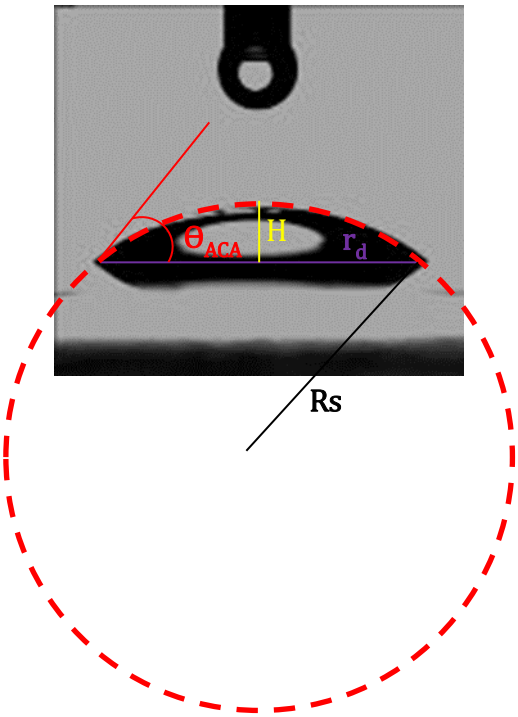

Figure 3-8: Picture of a droplet of Ludox AS-40® suspended in Milli-Q water deposited on a glass slide and the manual circle fitting used to calculate its volume and contact angle.

These four parameters were post-processed using a Matlab code provided by Dr Lisong Yang (University of Durham) for the DSA-100. The Matlab code used a Young-Laplace method for the fitting of the droplet shape. This technique was used to calculate all the data for Ludox AS-40® and Laponite in Milli-Q water. The Attension Theta was used for all the other data showed in this thesis. For the KSV system, the provided Attension Theta v.4.1.9.8. software allowed us to calculate directly these parameters. Each recording was started about 10 seconds before the droplet hit the substrate and up to 6000 frames per evaporated droplet were recorded and analysed (the recorded number of frames depends on the drying time of the droplet, hence the type of solvent use). The droplet can be visualised on the screen from the attached software and a movie can be generated from the combination of the frames. The set

standard procedure was at one frame per second. At the end of the recording the baseline was manually detected and the drop was fitted in a drop shape detecting window (blue score box see Figure 3-9). The fitting method was then selected, between Young-Laplace, circle (with this fitting, a circle curve is fitted on the droplet profile and the contact angle is calculated based on the circle equation) or polynomial fitting (with this method, part of the droplet profile is extracted and fitted by a quadratic polynomial function, the contact angle is then determined between the tangent and the baseline at the three-phase contact line). In all our experiments the Young-Laplace was selected.

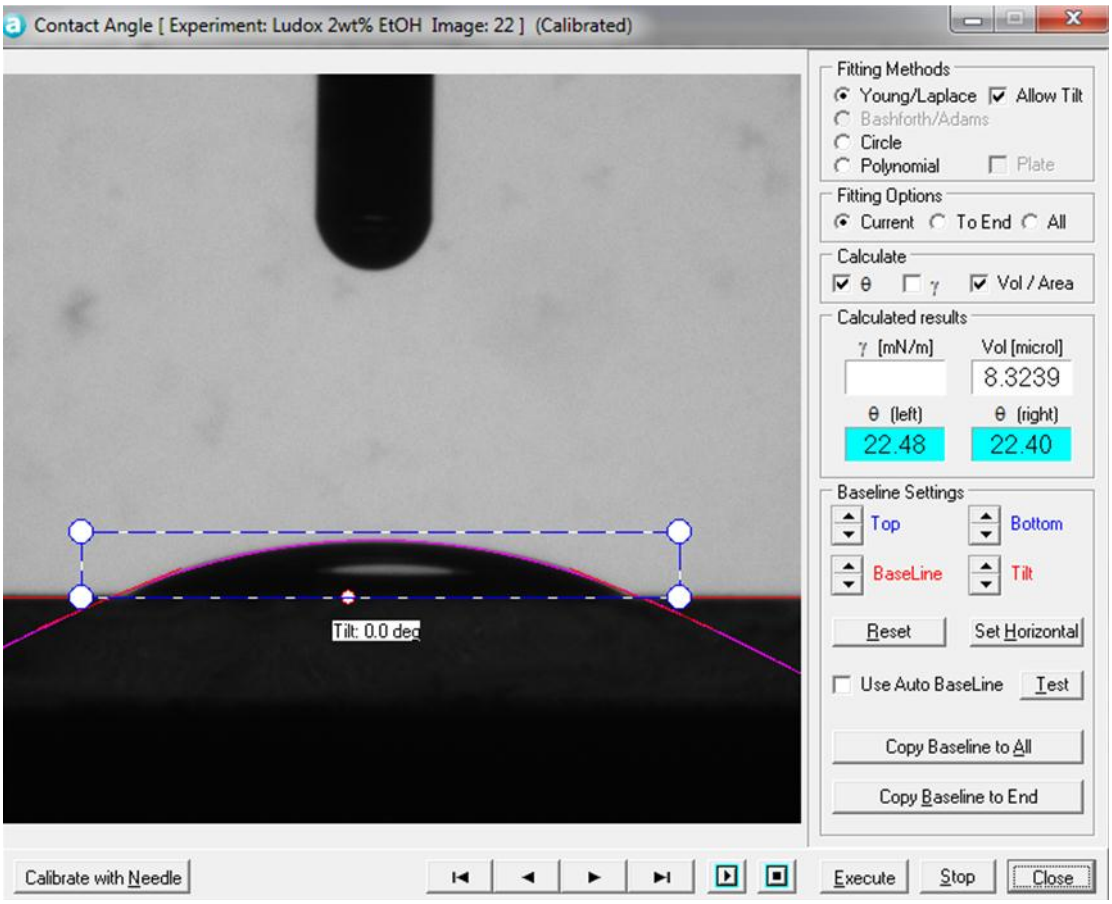

Figure 3-9: Snapshot of a contact angle measurement of a Ludox AS-40® droplet at 2 wt% in 60 vol% EtOH deposited on a silanized glass slide. The Young-Laplace fitting was used to calculate the droplet apparent contact angle and volume of the droplet.

Between each recorded drop, five test drops were again discarded to ensure consistency in drop handling and deposition. A total of three experimental drops were

recorded for each particle system, the standard deviation between these three measurements was used as the experimental error.

3.5.4 Pendant drop measurements

In order to quantify any changes in liquid-vapour surface tension, γ_{LV} due to the addition of nanoparticles, solvent (ethanol), surfactant and electrolyte, additional pendant drop measurements were carried out. The KSV CAM-200 was used to perform all the measurements. Up to five different measurements were carried out in the chamber for each system.

Physically, the surface tension measurements are determined by analysing the shape of the drop. In fact, the shape of a drop hanging at the tip of a needle are determined from a balance between the gravitational forces dragging the droplet down and the surface forces keeping it attached to the needle. Hence, the surface tension at the liquid interface can be related to the drop shape through this equation:

$$\gamma = \frac{\Delta \rho g R_0^2}{\beta} \qquad \textbf{3-10}$$

Where, γ is the surface tension, β is the shape factor, $\Delta\rho$ is density difference between fluids at the interface, g is the gravitational constant and R_0 is the radius of the drop.

Experimentally, to determine the surface tension, the shape factor is defined through the Young-Laplace as seen on Figure 3-10.

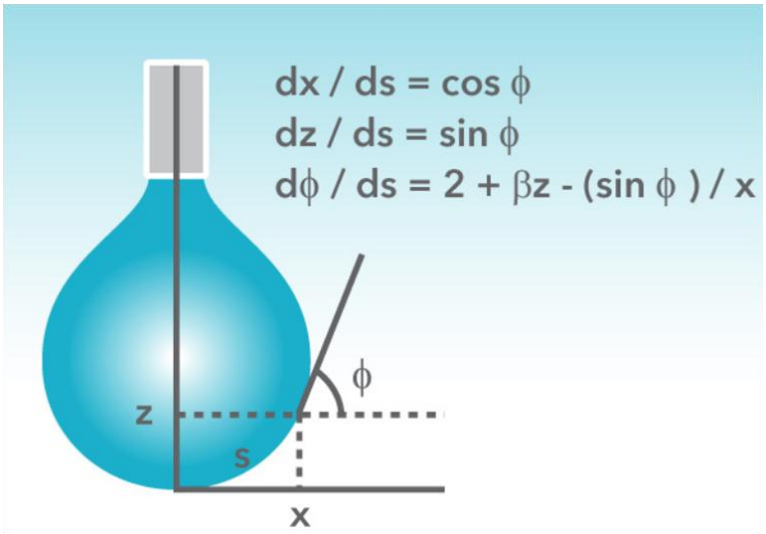

Figure 3-10: Schematic representation of a pendant drop experiment with a droplet hanging at the tip of a needle, and the parameters used to calculate the shape factor (Attension Theta, 2015)**.**

Experimentally, the first step was the calibration procedure. Upon completion of this step, the ceramic chamber was fitted to the deposition stage. An experimental set up was then defined by adding the following parameters:

- the experiment name,
- the substrate use,
- the experiment type
- and the phase involved, heavy phase was water and light phase was air.

Typically, when the pendant drop experiment is carried out, a glass slide was placed underneath to collect any detached droplets. The recording was started before the generation of the droplet, then the droplet was manually dispensed from the needle, the droplet can be visualised on the screen from the attached software and a movie can be generated from the combination of the frames, the set standard procedure was at one frame per second. At the end of the recording the baseline is detected using the tip of the needle. The drop shape is fitted in a drop shape detecting window (blue dotted box see Figure 3-11). The fitting method is then selected, between Young-Laplace and Bashforth/Adams (this fitting relates the droplet profile to a nonlinear differential equation). In all our experiments the Young-Laplace was selected.

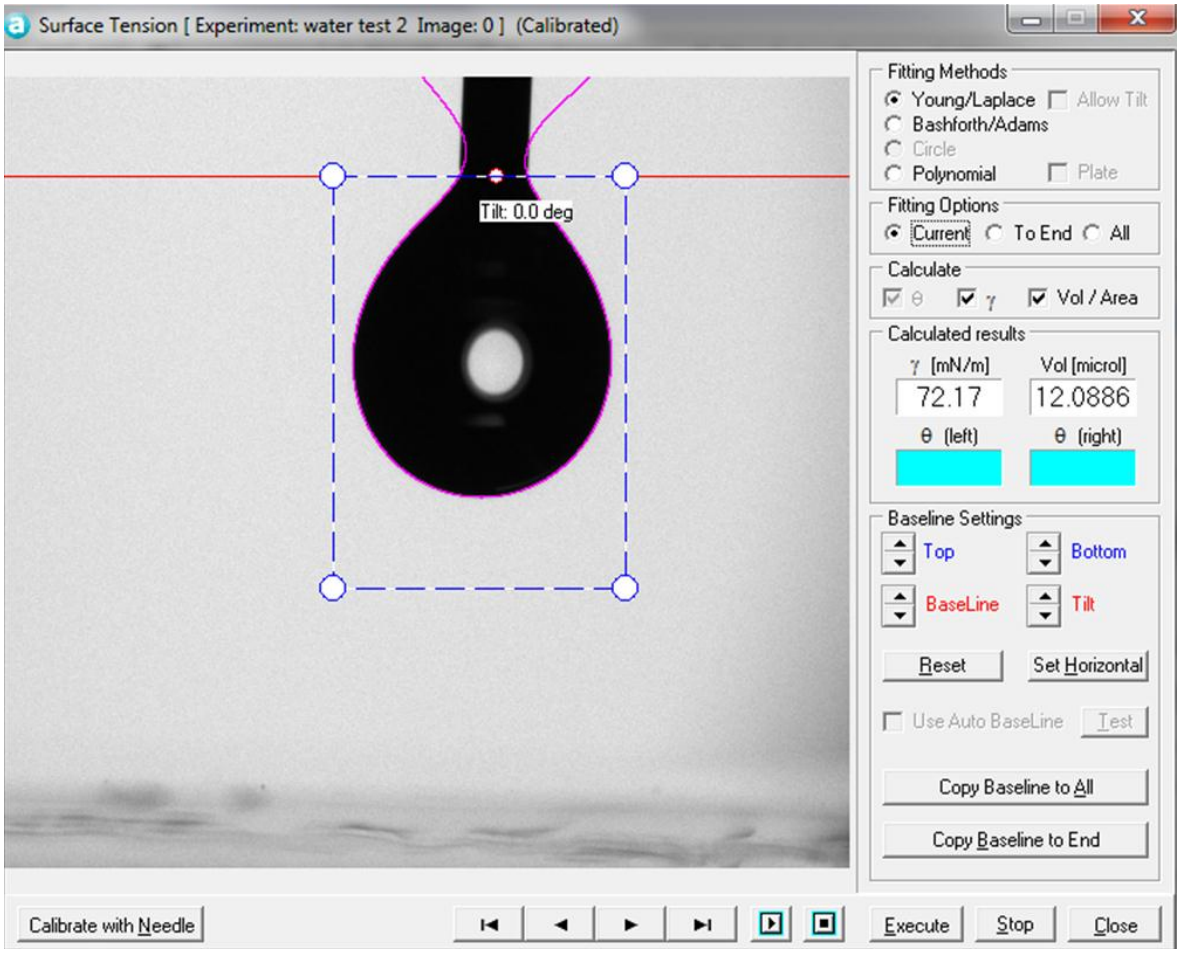

Figure 3-11: Snapshot of a Milli-Q water droplet hanging from the tip of a needle performing a pendant drop experiment to calculate the surface tension using the shape factor equation. Here, the surface tension of Milli-Q water is 72.2 mN/m. The fitting methods selected to calculate the surface tension was the Young-Laplace equation.

With this setting, the software was able to automatically detect the shape and a fitting curve can be seen as a border around the droplet (purple line, see Figure 3-11). The surface tension was thus automatically calculated. This experiment was repeated five times and the surface tension indicated was the average of these five measurements.

3.6 Dried morphology analysis

Following, the drying droplet process, the dried deposit structure was analysed. Since, the dried deposit is spherical; we can assume that the four quadrants of the deposit have the same features, as such for the coffee-ring stain only a 3 µm of the left side is studied (see Figure 3-12) and the whole deposit for the uniform deposit.

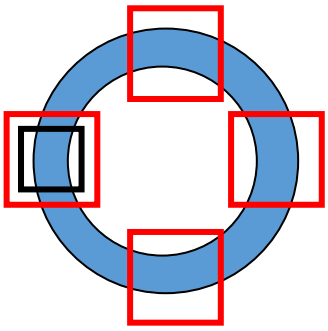

Figure 3-12: Illustration of a dried deposit studied. The larger square represents the area observed by interferometer. The smaller square represents the area examined by optical microscopy. The illustration is not to scale.

3.6.1 Optical microscope analysis

The dried features of the drops were studied using an Olympus U-MNUA2 (Olympus Corporation, Japan) optical microscope. The transmitted mode was used as the light source is emitted from below the glass slides, and two objective lenses were used to analyse the sample at 10x and 50x magnifications. The image was captured by a computer-controlled digital camera using the Cell^D software.

3.6.2 Atomic Force Microscopy

An Atomic Force Microscope (AFM) was used as an optical characterisation technique to collect 3-Dimensional topographical images on the edge features upon complete solvent evaporation. To realize this work, a Veeco Instruments Bioscope II (Nanoscope, version 7.30) was used.

An AFM is a scanning probe microscope which allows the collection of topographical images from conducting and isolating surfaces to an atomic resolution. This equipment is constituted of a tip mounted on a cantilever, a laser-light, a photo-detector, a scanner and a lens (see Figure 3-13). Usually, the data are collected by measuring and controlling the forces between the probe and the surface of the sample. A 3D-image is obtained by plotting, the deflection of the cantilever as a function of its position on the sample. This function is known as a force curve and can be described by the Hooke's Law relation:

$$F = -kx \qquad \textbf{3-11}$$

Where, *F* is the force, *k* is the spring constant and *x* is the cantilever deflection.
Typically, tapping mode (intermittent mode, where the probe lightly taps the sample surface while scanning) was used to record the images in air and at room temperature. In this mode, the distance between the probe and surface is $0.5 < d < 2$ nm; and the cantilever is oscillated at its resonant frequency. The probe lightly taps the sample surface while scanning, and a constant tip-sample interaction is maintained by moving the surface towards and away from the probe, allowing the detection of surface structure. The key parameters used to record a good image are the integral gain, proportional gain and amplitude setpoint. By adjusting the amplitude setpoint, the applied force is optimised to measure the sample topography. The tips used to analyse the sample were: a phosphorus (n) doped silicon cantilever (Veeco model RTESP, spring constant – capacity of the probe to bend – 40 N/m), and two micromasch probe NSC14 and NSC15 aluminium doped silicon cantilever (with spring constant at 5.7 N/m for NSC14 and 40 N/m for NSC15).

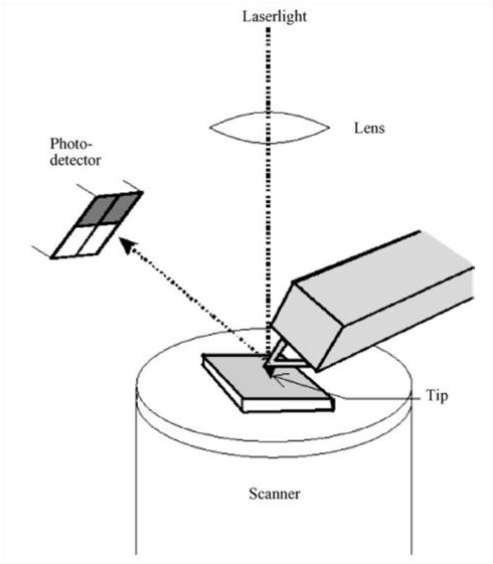

Figure 3-13: Schematic representation of an AFM equipment, the laser beam is aimed at the cantilever tip which bent at it resonance frequency. The tip is then in contact with the sample and the reflection of the beam on the sample is send to the photodetector which transform the signal into a topographical image (Butt et al., 2005)**.**

This technique was later discarded in favour of the Interferometer analysis due to the brittle nature of the majority of the samples. The WSxM 5.0 version 6.2 software (Nanotech Electronica, Spain) was used thereafter to process the collected data.

3.6.3 Interferometer analysis

Scanning white light Interferometer technique was adopted to characterize the patterns upon solvent evaporation. This technique is a non-contact system which offers great vertical resolution down to the nanometre scale in every pixel and can be used to determine surface texture. The NPLEX Bruker Interferometer equipment (NPFLEX, Bruker Corporation, USA) was used to this effect.

This equipment is comprised of: an optical metrology module (OMM) fitted on an automated tip/tilt attached to the gantry which performs the optical measurements, control the magnification, scanning and final focusing, a motorised stage moveable in the vertical and horizontal directions with a joystick to accurately focus on the sample, a super-long working distance magnifying objectives and field of view lenses, an Emergency Off Button (EPO) powering the system on and off, a computer operator

station preloaded with the Vision64 software, a mounted vibration table, a live video feature and a white light LED source (see Figure 3-14).

Figure 3-14: Image of the Bruker NPFLEX Interferometer system.

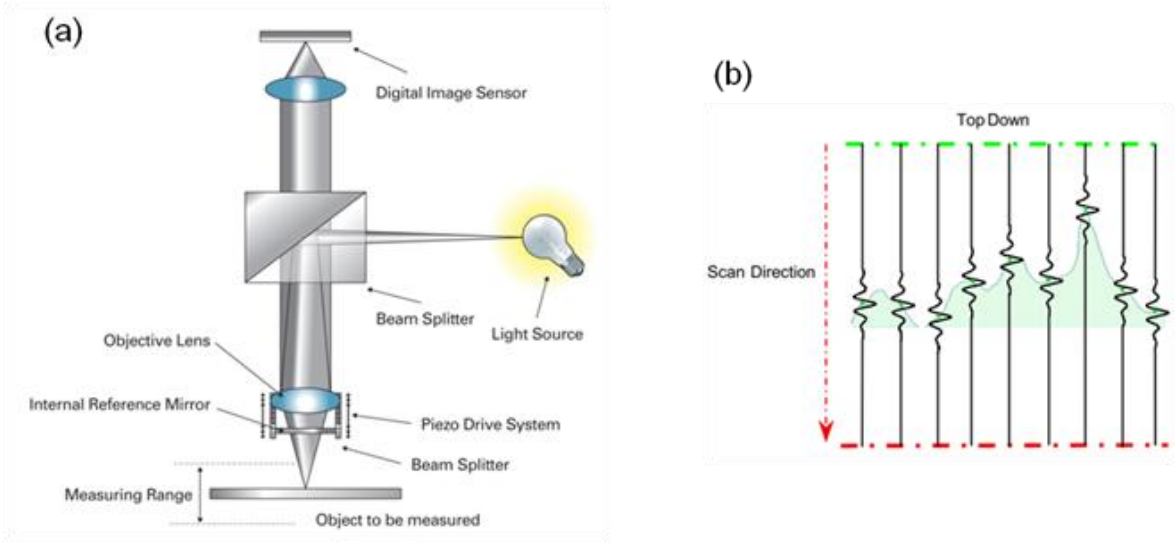

Figure 3-15: (a) Schematic representation of the Interferometer (b) schematic representation of the vertical scanning of the sample.

The instrument process is the following: a beam is aimed at a beam splitter which generates two waves. One wave will be directed towards the surface of the sample

and the other to an internal reference mirror (see Figure 3-15 (a)). While scanning the sample vertically, the detector measures the intensity of light at different position on the sample. Since, the scan is vertical; the highest peaks of the sample will be detected (see Figure 3-15 (b)). Two paths from the light source are observed: if the waves are in phase they will add to each other (constructive interference) if they are out of phase they will cancel each other (destructive interference). The combination of these two paths results in the set of dark and bright fringes. The construction of the surface topography is achieved by the combination of these fringes as a function of time. The live video images are collected and analysed using the software in order to digitalise the two-dimensional and three-dimensional topographical features of the deposit

Chapter 4
Effect of nanoparticle concentration on the final deposit patterns of spherical Ludox AS-40® silica on uncoated solid surface

4.1 Introduction

Drying of colloidal system is of high interest due to their wide array of applications as thoroughly reviewed in Chapter 2. Its applications include inkjet printing (Bermel and Bugner, 1999), virus detection (Wong et al., 2011), DNA stretching (Abramchuk et al., 2001; Smalyukh et al., 2006) and self-assembly of colloidal particles (Bigioni et al., 2006; Ulmeanu et al., 2009; Bi et al., 2012; Hamon et al., 2014). Typically, the drying of dispersions of small solid particles will generate a variety of residual patterns. A ring-like stain known as the "coffee-ring effect" (CRE) (Deegan et al., 1997) is one of the main patterns observed. Characteristically, most of the solid material is deposited at the periphery of the droplet leading to a non-uniform structure. This non-uniform deposition is observed when the contact line is pinned and a capillary flow (Deegan et al., 1997),(Deegan, 2000),(Deegan et al., 2000) is generated carrying the suspended solutes from the drop centre towards the edges.This flow is generated to compensate for the faster solvent evaporation at the edges. This effect is observed regardless of particle size (i.e, from micrometer-sized particles down to macromolecules) (Deegan, 2000),(Sefiane, 2014),(Erbil, 2012), droplet volume or the substrates used (i.e., glass slides, Teflon or silicon wafers) (Dugyala and Basavaraj, 2015),(Sefiane, 2010). In the case of inkjet printing, the pigment size range is wide (tens to hundreds of nanometers) (Bermel and Bugner, 1999) and this can impact on the quality of the printed images. Smaller particle size pigments have been proven to improve resolution of the images (Bermel and Bugner, 1999), however, smaller particles are prone to form ring-shape deposit patterns.

Since, this effect is prevalent in most systems, in-depth work has been carried out to understand the parameters and key factors that describe its mechanisms (Hu and Larson, 2002),(Crivoi and Duan, 2014). It has already been established that droplet evaporation rate is directly dependent on the apparent contact angle θ_{ACA} and the droplet contact radius, r_d (Picknett and Bexon, 1977). Previous work studied the influence of the nanoparticle size and initial concentration on the dried droplet residual patterns both experimentally and theoretically (Crivoi and Duan, 2014; Breinlinger and Kraft, 2014). As such during the evaporation, the droplet edges increase in height

and width, with a direct dependence with the local particle concentration increase (Yunker et al., 2013), (Breinlinger and Kraft, 2014). Chon *et al.* (Chon et al., 2007) investigated four types of nanofluids to see the effect of nanoparticle size on the final deposition patterns of microliter droplets (V= 5 µL). The four nanofluids studied were gold (2 nm), copper oxide (30 nm) and aluminium oxide nanoparticles at 11 and 47 nm. It was observed that smaller particles formed patterns with wider edge and more central deposit (gold and 11 nm aluminium oxide particles) whereas larger particles formed thinner edge features and less central residue patterns (copper oxide and 47 nm aluminium oxide nanoparticles). Wong *et al.*(Wong et al., 2011) while using carboxylate-modified polystyrene systems at micrometer and nanometer scale displayed significantly different behaviour than Chon *et al.* as they implied that other factors might play a part in the residual patterns such as size segregation near the three-phase contact line (TPCL). Deegan (Deegan, 2000) and Brutin (Brutin, 2013) studied the influence of polystyrene nanoparticles concentration on the residual deposit patterns as well. The former worked with 0.1 µm microspheres while the droplet initial volume was 0.5 µL. Brutin worked with 24 nm polystyrene sphere with the droplet initial volume determined at 7 µL and considered the influence on the relative humidity in his study. Their respective work demonstrated that the dried droplet residual patterns width scale with the initial particle concentration following a different power law. It was suggested that this power law was dependent on the nanoparticle size and properties of the materials. Lee *et al.* (Lee et al., 2017) worked with aluminium oxide and titanium dioxide particle systems. In their study, they observed both the influence of nanoparticle concentration and substrates on the dried deposit residue patterns. It was concluded that titanium dioxide system formed a ring-shape patterns regardless of the initial particle concentrations and deposition substrates, while, in the case of the aluminium oxide systems, at lower concentration (below 2 vol%) and smaller particle size (below 13 nm), ring-shape patterns were observed while at higher concentration (above 3 vol%) and for larger particles size (higher than 20 nm) a uniform dried deposit residue was generated. Other work, from Hodges *et al*. (Hodges et al., 2010) studied the effects of an increase in nanoparticle particle concentration and its influence on the dried deposit patterns. In their work, microliter droplets of Ludox AS-40® silica nanoparticles of varied initial concentration (C_{Lud}= 0.1 to 1000 ppm) were studied on untreated glass slides. It was observed that the edges feature of the dried deposit increased linearly with the particle concentrations in height and width. Upon complete solvent evaporation, cracks formed in the residual

dried deposit patterns. This occurrence can be a hindrance in inkjet printing as it can lower the resolution of the images. Several researchers have studied this phenomenon and determined several factors leading to their appearance in the final dried deposition patterns (Allain and Limat, 1995; Caddock and Hull, 2002; Lee and Routh, 2004; Lazarus and Pauchard, 2011)

In this chapter, our aim is to systematically investigate the evaporative behaviour of aqueous Ludox AS-40 ® silica nanoparticles microliter droplets (V_{Lud}= 12.1 ± 0.7 µL) at different initial particle concentration and observe its influence on the evaporation dynamics. The mechanisms leading to the formation of three-dimensional self-assembled structures at the TPCL is also studied. A series of aqueous suspension droplets containing C_{Lud}= 1, 10, 100, 1000, 10000 and 20000 ppm, monodisperse Ludox AS-40® spherical nanoparticles were carried out on clean flat, smooth and uncoated glass substrates following the preparation explained in Chapter 3. Upon complete solvent evaporation, the residual dried deposit patterns were captured by a camera, optical micrographs and non-contact imaging analysis (Atomic Force Microscopy, AFM and White Light Interferometry, WLI). Since, the evaporation dynamics affects the final patterns, the wetting properties were recorded by a contact angle goniometer over time. The different final residue patterns formed will be discussed and characterised. A comparison between the theoretical and experimental evaporation rate over time is presented using two theoretical models. Finally, the analysis of the residual dried deposit edge features (height and width) of the ring-shape patterns is also discussed as well as a correlation between the cracks spacing in this subsequent work.

4.2 Experimental methods

4.2.1 Materials

Solutions of varying concentrations (C_{Lud}= 1, 10, 100, 1000, 10000 and 20000 ppm by weight%) were prepared for analysis by diluting an original stock suspension of 40 wt% Ludox AS-40® silica with Milli-Q water (18.2 M.Ω.cm).

The particle diameter was measured at ~21 nm from DLS measurements, which is similar to the overall average particle diameter given by the manufacturer in the range d= 20-24 nm. The electrostatic charges of the particles were checked by measuring the zeta potential of the different suspensions concentration and gave a result of ζ= -37.3±1.8 mV.

The evaporation of single sessile droplets of spherical Ludox AS-40® silica solutionswere conducted in a chamber and under natural diffusion conditions for uncoated glass slides (Thermo Scientific, hydrophilic) following the cleaning method explained in Chapter 3, Section 3.4.1. Each droplet deposition was repeated three times and the variation between measurements was used as the standard deviation. The measurements were taken at environmental temperature and humidity at T= 24±1°C and RH= 43±3%.

4.2.2 Characterisation and thickness measurements

- Measurement of droplet evaporation using contact angle goniometer

A Krüss DSA1000 droplet shape analysis (DSA) system and DSA software was used to analyse the profile of drops of water containing Ludox from C_{Lud}= 1 to 20000 ppm. The DSA100 equipment was used to record the droplet base radius, r_d, apex height, H, apparent contact angle, Θ_{ACA}, and volume, V_{Lud} of the droplet with change with time. A Matlab code was then used to calculate the droplet contact angle value and volume from the droplet base radius and height information.

- Droplet deposit structure imaging

The topographical characteristics of the dried deposits for the aqueous system were determined by an Atomic Force Microscope for C_{Lud}= 1 to 1000 ppm (AFM, Veeco, Bioscope II) in tapping mode. All 3-D images of the surfaces were obtained from 100x100 µm areas. As explained in Chapter 3, Section 3.6.2. for the remaining systems, C_{Lud}= 10000 and 20000 ppm a white light interferometer (WLI, NP FLEX, Bruker, USA) was used to determine the features of the dried deposit patterns. Additionally, the crack patterns observed on the dried deposit were studied using an optical microscope, (Olympus, U-MNUA2).

- Thickness and width measurements

The dried residual deposits were examined using the Atomic Force Microscope. To obtain an average, an area of 100x100 µm of the dried residual deposits was scanned which generated a 3-D topographical images for each of the three droplets deposition done for each different concentration. For each dataset, the obtained area was divided in five sections at 20,40,60,80 and 100 µm respectively. These five profiles were used to generate an average profile.

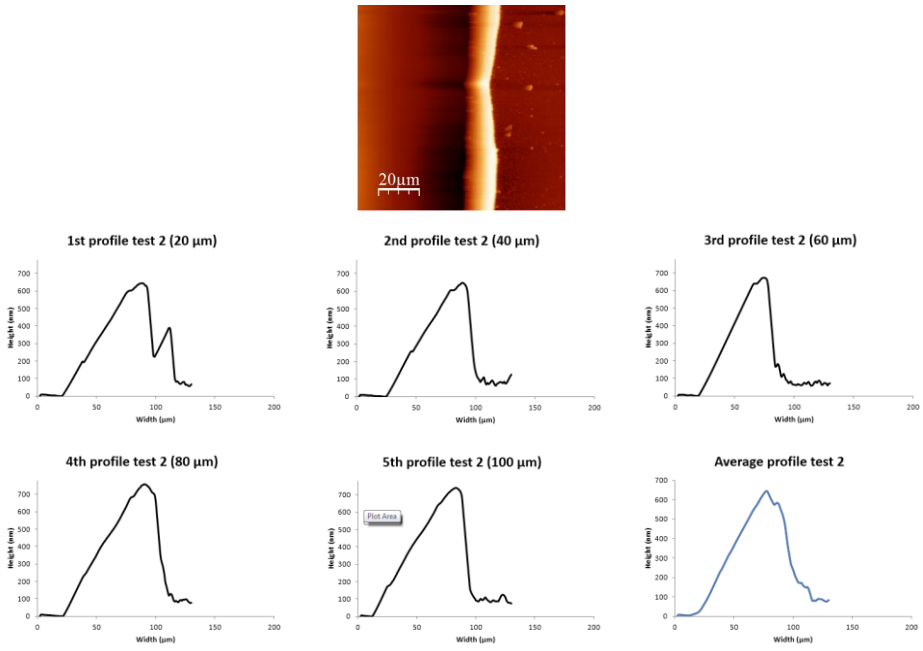

Figure 4-1: AFM 2-D images of the left side of the dried residual deposit of Ludox AS-40 ® at C_{Lud}= 10 ppm and the corresponding five profiles generated for the second droplet depositions.

The standard deviation reported on the dried residual average height or thickness T_H, and width W comes from the measurement variation of these profiles. Figure 4-1 shows the five profiles from one of the three depositions carried out for Ludox AS-40® at C_{Lud} = 10 ppm. This methodology was repeated for the three depositions at C_{Lud} = 1 to 1000 ppm.

The same methodology using WLI images was adopted to determine the dried residual topographical characteristic for Ludox at C_{Lud}= 10000 and 20000 ppm respectively.

4.3 Theoretical approach

4.3.1 Description of droplet evaporation

In our experiments, a sessile droplet having the shape of a spherical cap resting on a flat substrate is considered. The droplet shape is limited by the Bond number, $B_0 = \frac{\rho g r_d H}{\gamma_{LV}}$ which as explained in the previous Chapter 2 accounts for the effect of surface tension and gravitational forces on the droplet shape. Here, ρ is the fluid density, g is the acceleration of gravity, r_d is the droplet contact radius, H is the initial height of the droplet at its apex and γ_{LV} is the liquid/air surface tension measured by the pendant drop method. In all the systems, the Bond number is low, $B_0 < 1$, so that the droplet shape can be regarded as a spherical cap (see Table 4-1).

Table 4-1: Bond number and ratio of diffusion time to evaporation time for all systems studied.

System	Bond number, B_0	t_D/t_E
Aqueous	$\sim 3.3x10^{-1}$	$\sim 3.1x10^{-10}$

In Figure 4-2a, a schematic of a spherical cap droplet on a glass slide surface with the interfacial forces balance is presented. Under these assumptions, the evaporation process can be described by using three parameters, that of,

droplet contact radius r_d, droplet height H and apparent contact angle Θ_{ACA}. Thus, the following relationships are satisfied:

$$\theta_{ACA} = 2\tan^{-1}\left(\frac{H}{r_d}\right) = \cos^{-1}\left(\frac{\gamma_{SV} - \gamma_{SL}}{\gamma_{LV}}\right) \quad \textbf{(4-1)}$$

$$V_{Lud} = \frac{\pi H(3r_d^2 + H^2)}{6} = \pi {r_d}^3 \frac{\cos\theta_{ACA}^3 - 3\cos\theta_{ACA} + 2}{3\sin {\theta_{ACA}}^3} \quad \textbf{(4-2)}$$

Where V_{Lud} is the droplet volume, $\gamma_{SV}$is the solid/vapour surface tension, γ_{SL} is the solid/liquid surface tension, γ_{LV}liquid/vapour surface tension respectively, and θ_{ACA} is the equilibrium contact angle of a droplet resting on a surface obtained by the balance of force acting at the three-phase contact line (TPCL) and expressed by the Young-Laplace equation (4-1).

The solvent evaporates into the ambient air, with the vapour concentration distributed non-uniformly above the droplet. Thus, at the liquid/vapour interface, the vapour concentration c is assumed to be equal to the solvent vapour concentration saturation value c_s. Far away above the droplet, the vapour concentration approaches the ambient value RHc_s, where RH is the relative humidity of the ambient air. The diffusion time t_D required for the vapour-phase solvent concentration to adjust to modification in the droplet shape is $t_D = r_d^2/D$, where D is the diffusion coefficient of the solvent vapour in air (Haynes, 2017). The ratio of diffusion time to the droplet evaporation is $t_D/t_E = r_d^2/Dt_E \approx c_s(1\text{-}RH)/\rho_{water}$. In our experiments, $RH=0.43$, $c_s=1.75\text{x}10^{-3}$ kg/m^3 (Dash and Garimella, 2013), and $\rho_{water}=997.2988$ kg/m^3, so that we obtain $t_D/t_E \ll 1$ (see Table 4-1). Hence, since the solvent vapour concentration adjusts rapidly compared to the time required for the droplet to evaporate, the evaporation process is considered to be a diffusion controlled quasi-steady state.

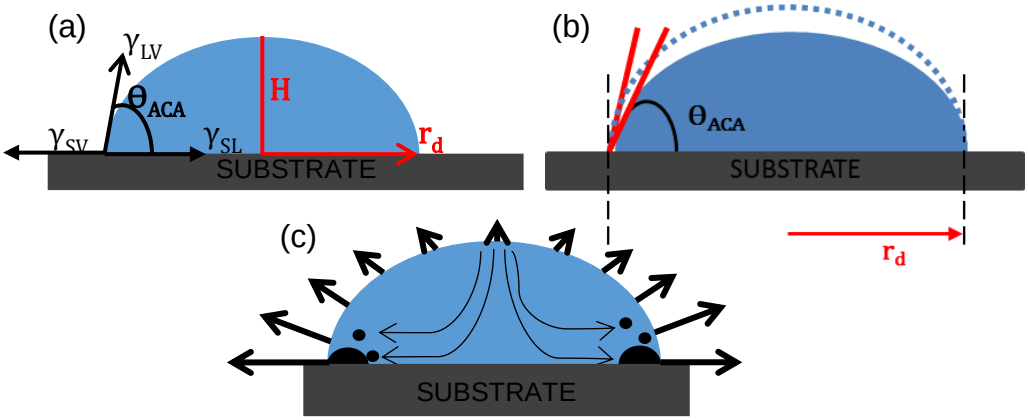

Figure 4-2: Schematics illustration on a solid substrate for (a) droplet parameters: droplet contact radius, r_d, droplet height at its apex, H and apparent contact angle Θ_{ACA} (b) drying mode behaviour for a pinned contact line/ constant contact radius mode (CCRM) and (c) schematic illustration of nanoparticle transport during the evaporation process. The dashed line represents the initial contact line of the droplet.

The investigation of a diffusion-controlled evaporation process has led to the expression of several models. To that effect, Birdi et al. (Birdi et al., 1989), (Birdi and Vu, 1993) expressed the evaporation rate for a water droplet evaporating on a solid surface as:

$$E = -\frac{dV}{dt} = \frac{4\pi r_d}{\rho} D(c_s - c_\infty) f(\theta) \qquad (4\text{-}3)$$

Where, *f(Θ)* is a function determined by Picknett and Bexon (Picknett and Bexon, 1977), this function enables to account for the effect of a solid surface on the vapour field. Through an analogy with an electrostatic problem evaluating the capacitance of a conductor of a spherical cap reminiscent of a sessile droplet, using a polynomial fit *f(Θ)* can be described with equations (**4-4**) and (4-5) depending on the angle values. Since, the boundary conditions are satisfied (the saturated concentration c_s is reached at the droplet surface and the solvent vapour concentration $c_\infty = RHc_s$ far away from the droplet surface), hence equation (**4-3**) can be rewritten as equation (4-6):

$$f(\theta) = \frac{1}{2} \times (0.6366\theta + 0.09591\theta^2 - 0.06144\theta^3) \text{ for } 0 \leq \theta < 10° \qquad (4\text{-}4)$$

$$\frac{1}{2} \times (0.00008957 + 0.6333\theta + 0.1160\theta^2 - 0.08878\theta^3 + 0.01033\theta^4) \text{ for } 10° \leq \theta \leq 180° \quad (4\text{-}5)$$

$$E = \frac{4\pi r_d}{\rho} D c_s (1 - RH) f(\theta) \quad (4\text{-}6)$$

A more recent model, developed by Hu and Larson (Hu and Larson, 2002) which corresponds to the results computed from a finite element method (FEM) has also been used to express a droplet evaporation following equation (4-7).

$$E = -\frac{dV}{dt} = \frac{\pi r_d}{\rho} D(1 - RH) c_s (0.27\theta^2 + 1.30) \quad (4\text{-}7)$$

Both expressions are used to determine the theoretical values of the evaporation rates for the particles different initial concentrations. To minimize disparities, the same values are used (*RH*, c_s and droplet contact radius r_d).

4.3.2 Cracks patterns

During drying, a meniscus is formed between the air/water interface and the particles. This meniscus gives rise to a capillary pressure, which is lower than the atmospheric pressure. This pressure difference will hence generate a compression manifested by the atmospheric pressure pulling on the film surface and inducing the formation of cracks. A schematic of the cracking mechanism is presented in Figure 4-3 (Lee and Routh, 2004).

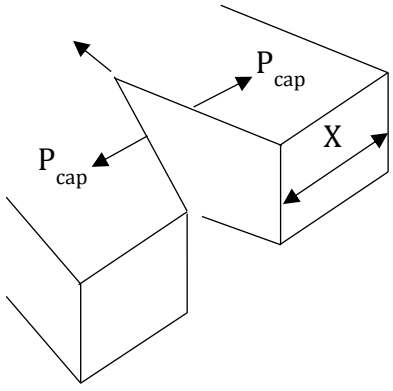

Figure 4-3: Schematics of crack formation during the droplet evaporation process. With Pcap dimensionless number representing the flow through consolidated particles and X is the length scale at which the capillary pressure is relaxed.

The horizontal length scale, X, at which the capillary pressure is relaxed was previously determined and its approximate expression was found to be expression (4-8) (Lee and Routh, 2004):

$$X \sim \frac{20R(1-\Phi)^2}{75\mu\Phi^2}\left(\frac{3\eta_0\gamma_{LV}^3}{E^3}\right)^{1/4} \quad (4\text{-}8)$$

Where R is the particle radius, Φ is the particle volume fraction, η_0 is the suspension viscosity, γ_{LV} is the solvent/vapour surface tension, μ is the solvent viscosity and E is the evaporation rate.

The cracks are mainly formed by capillary stresses release. A dimensionless number *Pcap* was introduced to characterise the flow going through the consolidated particles during the drying process, *Pcap* is given by equation (4-9):

$$P_{cap} = \frac{20}{75}\left(\frac{3\gamma_{LV}\eta_0}{E}\right)^{1/2}\frac{R(1-\Phi)^2}{\mu\Phi^2 T_H} \quad (4\text{-}9)$$

Where T_H is the dried film thickness.

4.4 Results and discussion

4.4.1 Evaporative behaviour of Ludox AS-40® silica in aqueous suspensions

Before the droplet deposition, the surface tension of the Milli-Q-water and the Ludox AS-40® as a function of the silica particle concentration were measured and compared to assess the surface activity of the particles as shown on Figure 4-4. The different Ludox AS-40® suspensions show no evidence of being surface active. Indeed, the surface tension measured by the pendant drop method did not vary significantly with the increase of Ludox AS-40® particle concentration. It was measured between $70.2 \leq \gamma_{LV} \leq 73.4$ mN/m which is in the same range as the surface tension of pure Milli-Q-water both theoretically $\gamma_{LV} = 72.1$ mN/m (Haynes, 2015) and experimentally $\gamma_{LV} = 71.6$ mN/m. As a result, γ_{SL} is also insensitive to Ludox AS-40® concentration according to Young-Laplace equation (4-1).

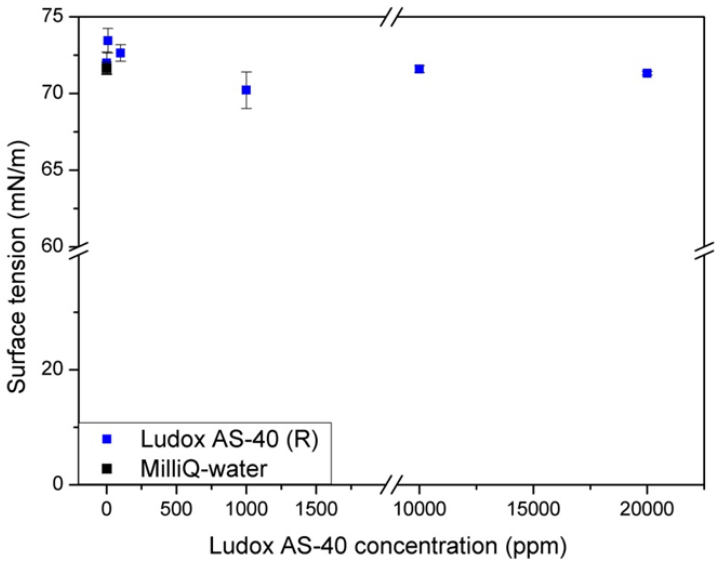

Figure 4-4: Surface tension measurements of Ludox AS-40® as a function of nanoparticle concentration.

One typical evaporation process was observed as shown on the drying sequence in Figure 4-5. Figure 4-6 shows the time variation of the normalized wetting contact diameter $2r_d$ and the normalized apparent contact angle Θ_{ACA} on the uncoated glass substrates. The wetting contact diameter $2r_d$ remains constant while the apparent contact angle θ_{ACA} decreases throughout the majority of the evaporation process regardless of the initial nanoparticle concentration, which is consistent with a CCRM (Picknett and Bexon, 1977) cf.Figure 4-2. These results where normalized with the initial contact diameter and apparent contact angle respectively. The Θ_{ACA} reaching zero is not plotted as towards lower Θ_{ACA}, the droplet shape does no longer adopt a spherical shape as seen on Figure 4-5 and Figure 4-6. In fact, when the initial nanoparticle concentration is increased, the pinning time increased accordingly, as observed in Table 4-2. This phenomenon can be attributed to the droplet self-pinning. This self-pinning results from the substrate chemical heterogeneity or the nanoscale roughness and has been reported previously (Deegan, 2000),(Deegan et al., 2000),(Sefiane, 2014). It can be noticed that the droplet radius starts to recede towards the end of the drying process regardless of the initial nanoparticle concentration. These findings confirm that as the droplet evaporates, the particles are carried toward the TPCL due to the capillary flow and the non-homogeneous evaporative flux along the droplet interface. At the TPCL, the particles consolidate into close-packed clusters since as the evaporation of the solvent progress the attractive Van der Waals force will govern the interparticle colloidal interaction.

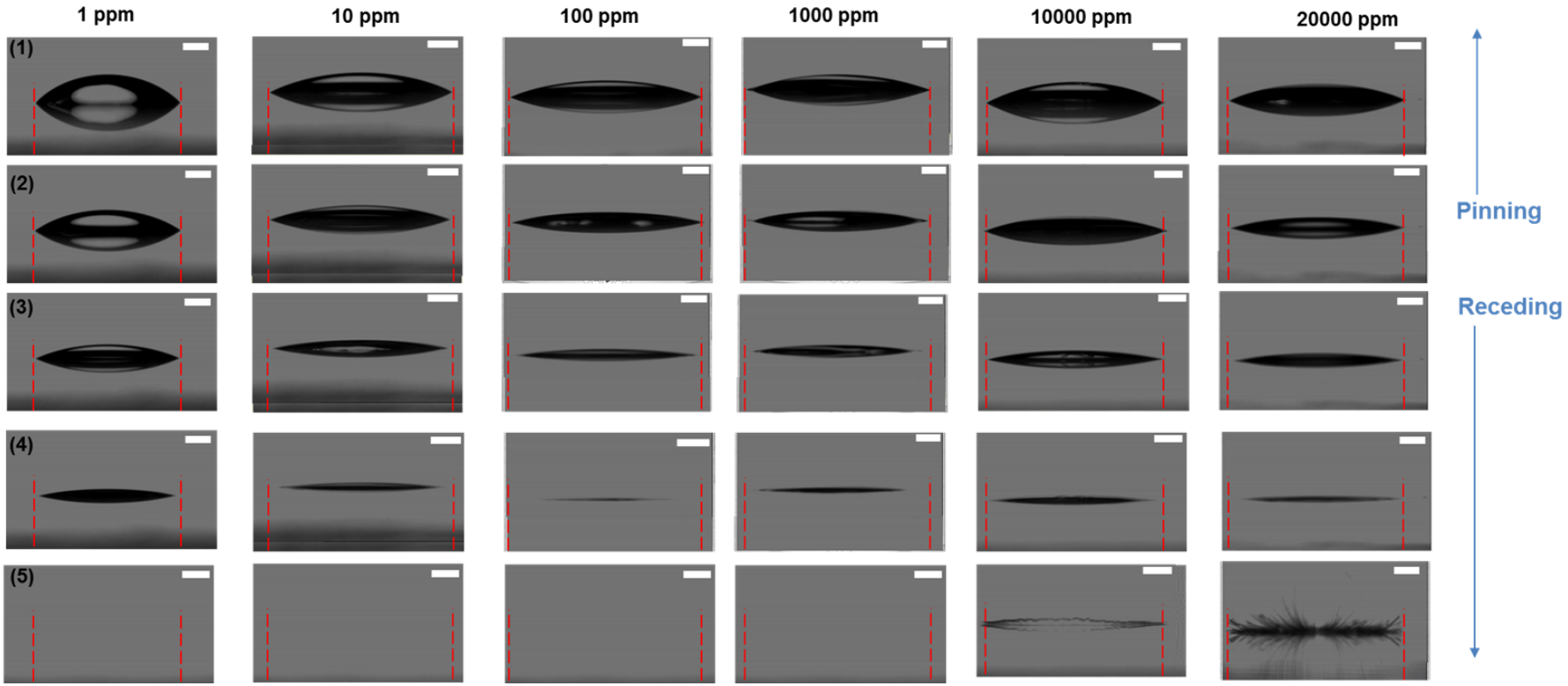

Figure 4-5: Drying sequence of aqueous base spherical Ludox AS-40® silica droplets on uncoated glass slides as a function of nanoparticle concentration (C_{Lud}=1 to 20000 ppm) at different time of droplet lifetime (1) 0%, (2) 25%, (3) 50%, (4) 75% and (5) 100%. The images are taken from side-view video recordings of the deposition with a contact angle goniometer. The scale bars on all images represents 1 mm. The red dotted lines represent the initial droplet contact diameter.

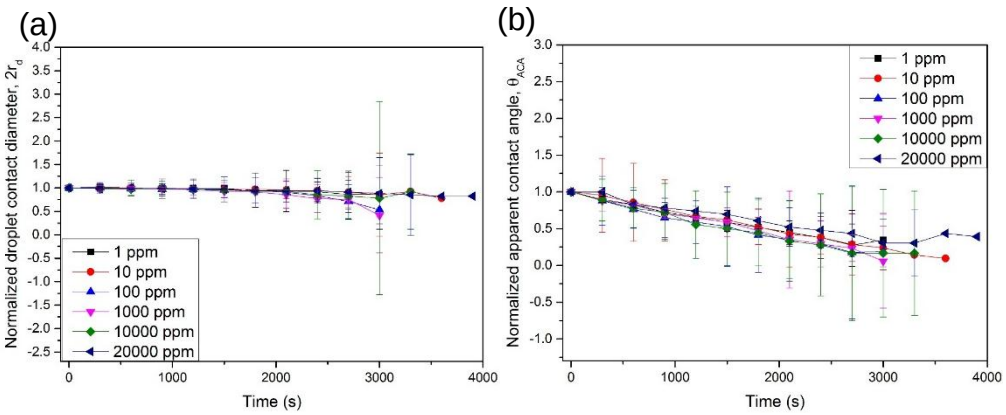

Figure 4-6: Evolution of normalized (a) droplet contact diameter $2r_d$ and (b) apparent contact angle Θ_{ACA} with time of sessile droplet (initial volume V_0= 12.1 ± 0.7 µL) of aqueous base spherical Ludox AS-40 silica as a function of nanoparticle concentration on uncoated glass slides. The evolution was extracted from contact angle goniometer recordings.

To have a clear idea of the initial nanoparticle concentration effect on the evaporation rate, we compared experimental results to theoretical values from Picknett and Bexon model using Equation (4-5) and Equation (4-7) . The nanoparticle concentration selected were at lowest range (C_{Lud}= 1 ppm), medium range (C_{Lud}= 1000 ppm) and highest range (C_{Lud}= 20000 ppm) (see Figure 4-7). As the evaporation rate corresponds to the variation of the volume over time, then from the experimental values of the Θ_{ACA} at different times the theoretical volume was determined. For a pinned TPCL, the theoretical values for aqueous Ludox AS-40 ® silica suspension are: $5.7x10^{-3}$, $6.1x10^{-3}$ and $5.8x10^{-3}$ µL.s $^{-1}$ for C_{Lud}= 1, 1000 and 20000 ppm respectively (see Figure 4-7b, c and d). The experimental values in our experiments are $3.8x10^{-3}$, $4.2x10^{-3}$ and $3.4x10^{-3}$ µL.s^{-1} respectively. The theoretical and experimental plots are not overlapped. These discrepancies between the theoretical and experimental values come from the presence of nanoparticles in the system. And it can be observed, that these discrepancies are more significant with the increase of the initial nanoparticle concentration. Although, the reported results are in the same range as the model, in the model the presence of the nanoparticles in the system are not considered. However, since the nanoparticles are not surface active adding this parameter in the model is challenging. Moreover, the errors bars from the experimental results encompass the theoretical values for the Picknett and Bexon model.

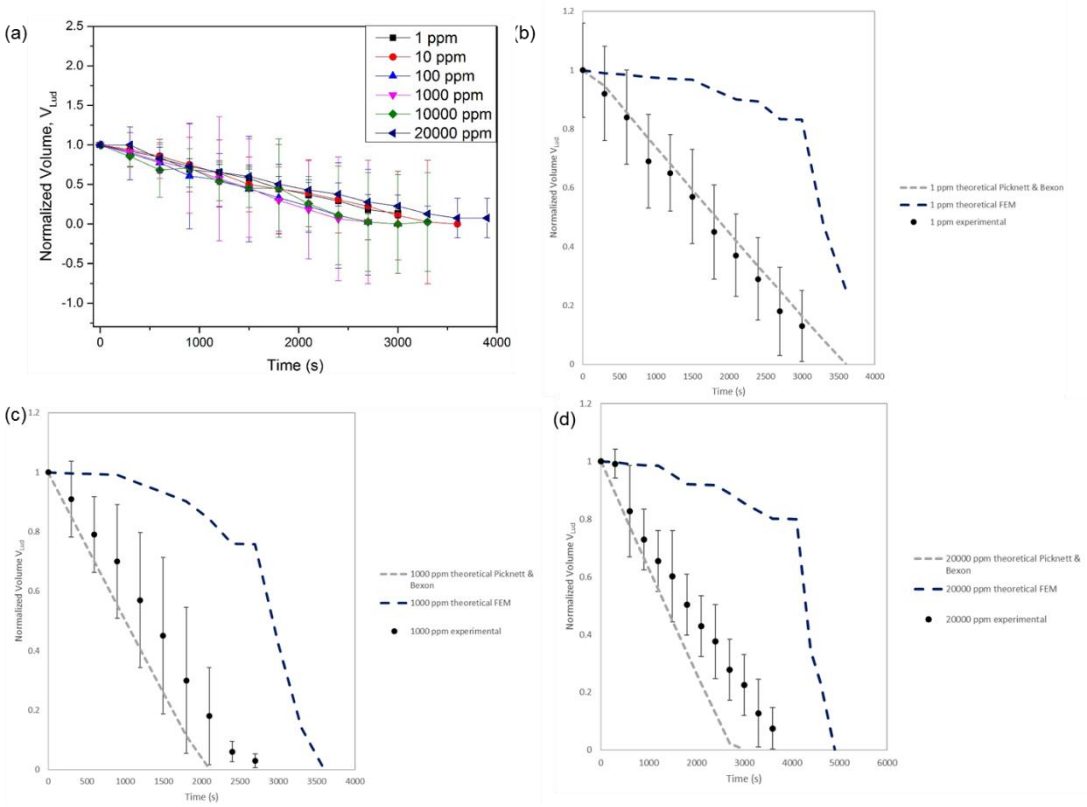

Figure 4-7: (a) Time evolution of sessile droplets normalized volume of Ludox AS-40® silica as a function of nanoparticle concentration on uncoated glass slides. (b), (c) and (d) Comparison between the theoretical and experimental time evolution of sessile droplets volume of Ludox AS-40® silica at three concentrations 1, 1000 and 20000 ppm respectively.

The evaporation rate however is significantly different between the FEM model and the experimental results. This striking difference is due to the droplet initial contact radius. Indeed, this model displays results in good agreements for droplet with an apparent contact angle below 40°. This model is usually used to describe systems with the following characteristics: droplets with an initial contact radius below $r_d \leq 1$ mm and a Bond number, B_o, in the range of 0.03 - 0.04. As seen in Table 4-1, the Bond number calculated for our droplets are 11 times larger than the B_o specified in the model conditions.

The evaporative behaviour of PMMA latex at C_{Lat}= 4000 ppm displays also a similar behaviour which was expected as the “coffee ring effect” is observed

regardless of the particle size (see Appendix A), furthermore, PMMA latex particles are not surface active as well.

4.4.2 Residual dried deposits patterns

- Dried deposit structure analysis

We also aimed to clarify how particles self-assembled upon solvent evaporation and how the initial particle concentration influences the residual deposition patterns.

The optical micrographs of the residual dried deposits formed upon the Milli-Q water evaporation at different initial nanoparticle concentration on uncoated glass slides are shown on Figure 4-8. Although, there is a significant difference between the initial particle concentrations in the aqueous droplets, a ring-like deposit structure was observed upon complete solvent evaporation in every case. For a given initial concentration of nanoparticles, the diameter of the residual deposits is in the same range more precisely from d= 7.0 to 6.4 mm. This characteristic pattern results in the occurrence of the CRE. Indeed, the evaporative behaviour of the droplets reunites the condition leading to a CRE, namely a pinned TPCL and a low initial apparent contact angle as demonstrated previously by other researchers (Deegan et al., 1997; Deegan, 2000). To retain a spherical cap shape and constant droplet diameter as seen experimentally, the volume loss occurs at the droplet periphery by capillary flow. Hence, the particles suspended in the droplet will be carried towards the droplet edge forming the observed ring-like stain. The main difference observed between the different residual deposit patterns is in the edges features. Concretely, the increase of nanoparticle concentration enhances the local particle concentration which promotes the self-pinning effect of the droplet. The pinning enhancement which was previously established, has been experimentally observed as seen in Table 4-2 and in previous work (Deegan, 2000; Weon and Je, 2013; Askounis et al., 2014). Furthermore, as the initial particle concentration is increased the features are emphasized which is characterized by an increase in the edges height and width at low concentration C_{Lud}=1 ppm the edge height is at 434 nm while at 20000 ppm the edge height is at 14 µm. Hodges *et al.* (Hodges et al., 2010) experimentally investigated the relationship between the particle initial concentration and the residual dried deposits ring width and height. In their work at V_{Lud}= 30 µL and with initial concentration of Ludox AS-40® comprised between C_{Lud}= 0.1 to 1000 ppm, a ring-like deposit was observed. They proposed that the particle

self-assembled preferably vertically during the evaporation process, thus leading to a gradual increase of the residual dried deposit height and width with the initial nanoparticle concentrations. Considering their work as well as the current one, it is concluded that the initial particle concentration is the dominant factor that controls the shape and dimensions of the residual dried deposit structures. Consequently, the particle initial concentration and the capillary flow can greatly influence the formation of the dried deposit structure.

The increase in initial particle concentration thus generates a linear enhanced "coffee ring effect", that is confirmed with taller and wider edge rim features.

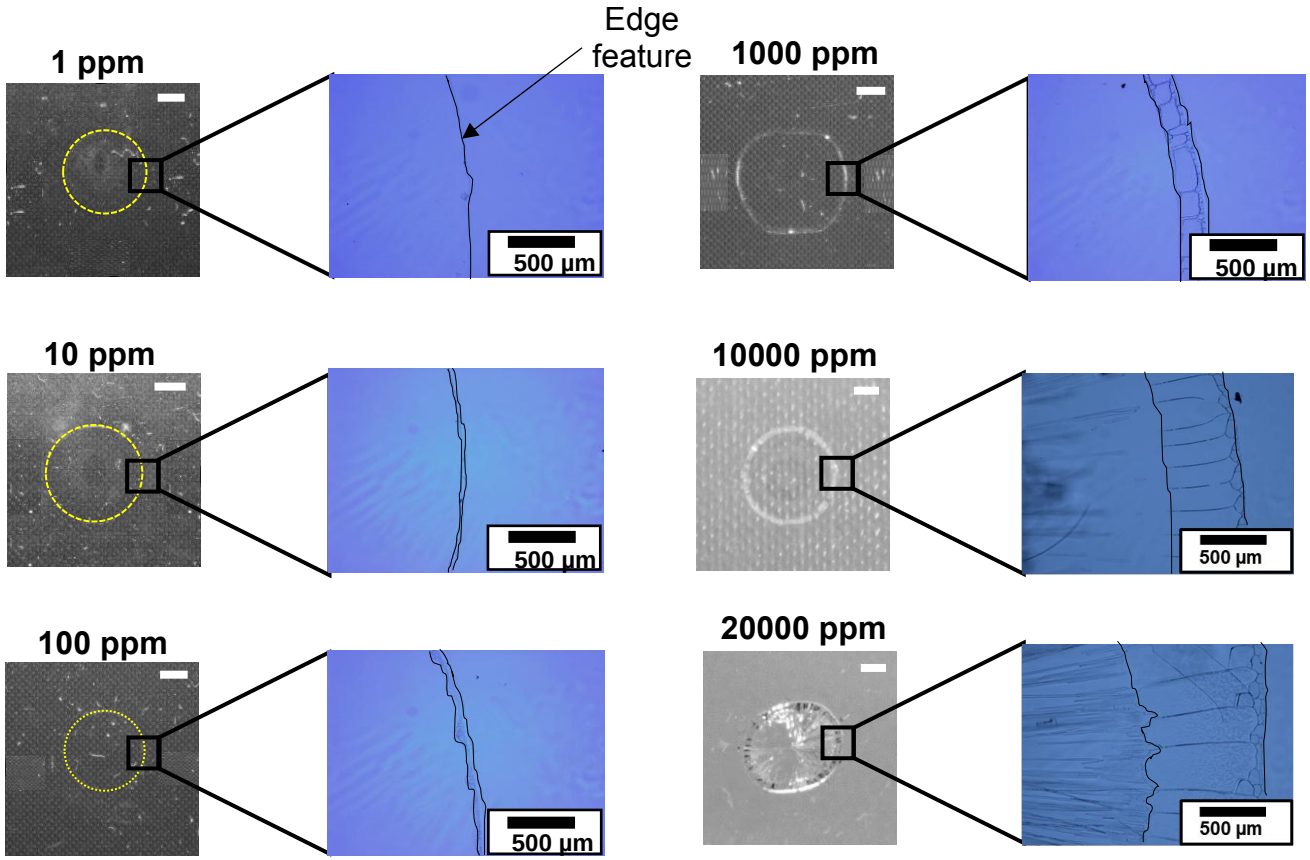

Figure 4-8: Drying patterns photographs of dried sessile micro-droplets of aqueous Ludox AS-40® silica at different concentration (C_{Lud}= 1,10,100,1000,10000 and 20000 ppm) and the optical micrographs corresponding to the magnification of the area inside the black box on uncoated glass slides. The edges features are highlighted by black lines. The white scale bars represent 1 mm on all images.

Table 4-2: Droplet pinning time as a function of Ludox AS-40 (R) nanoparticle concentration.

Ludox AS-40® concentration (ppm)	t_{pinned} (s)
1	1080
10	1511
100	1540
1000	1554
10000	1807
20000	2154

The zoom of the dried deposit edges on Figure 4-8 allows to distinguish cracks in the patterns. It is worth noting from these optical images that the presence of cracks appears on the residual deposit edges for concentration above C_{Lud}= 100 ppm. These cracks are the results of compressive capillary force upon solvent evaporation and are formed to release the stress generated. Concretely, as the solvent evaporates, this creates a local concentration increase and thus the particles self-assemble into a closed packed array. The resistance generated to the deformation, on the film surface due to the pressure differential between the atmospheric pressure and the capillary pressure, leads to the creation of tensile stresses which upon release are characterized with the apparition of cracks in the structure.

It is also observed under the microscope that the edge rim structures are getting wider as the particle concentration increases. In fact, as seen on Figure 4-8, with the self-pinning effect, the droplets edges increase linearly as a function of particle concentration. When the Ludox AS-40® initial concentration is increased, the edge of the rim increases gradually in both height and width which is consistent with previously reported data (Hodges et al., 2010). The Ludox AS-40® deposits are more brittle for concentrations above C_{Lud}= 1000 ppm as evidenced from the sample breaking off.

Subsequently, AFM and White Light Interferometer (WLI) were used to determine the effect of the initial particle concentration on the ring-stain structures. The topographical images of the residual dried deposits from C_{Lud}=1 to 20000 ppm are presented on Figure 4-9. From these results, confirmation of the deposit width increases as a function of Ludox AS-40 ®

concentration is seen. At lower concentration, the dried deposit edge is measured at 434 nm (C_{Lud}= 1 ppm) while at higher concentration it is measured at 3640 nm (C_{Lud}= 3640 nm).

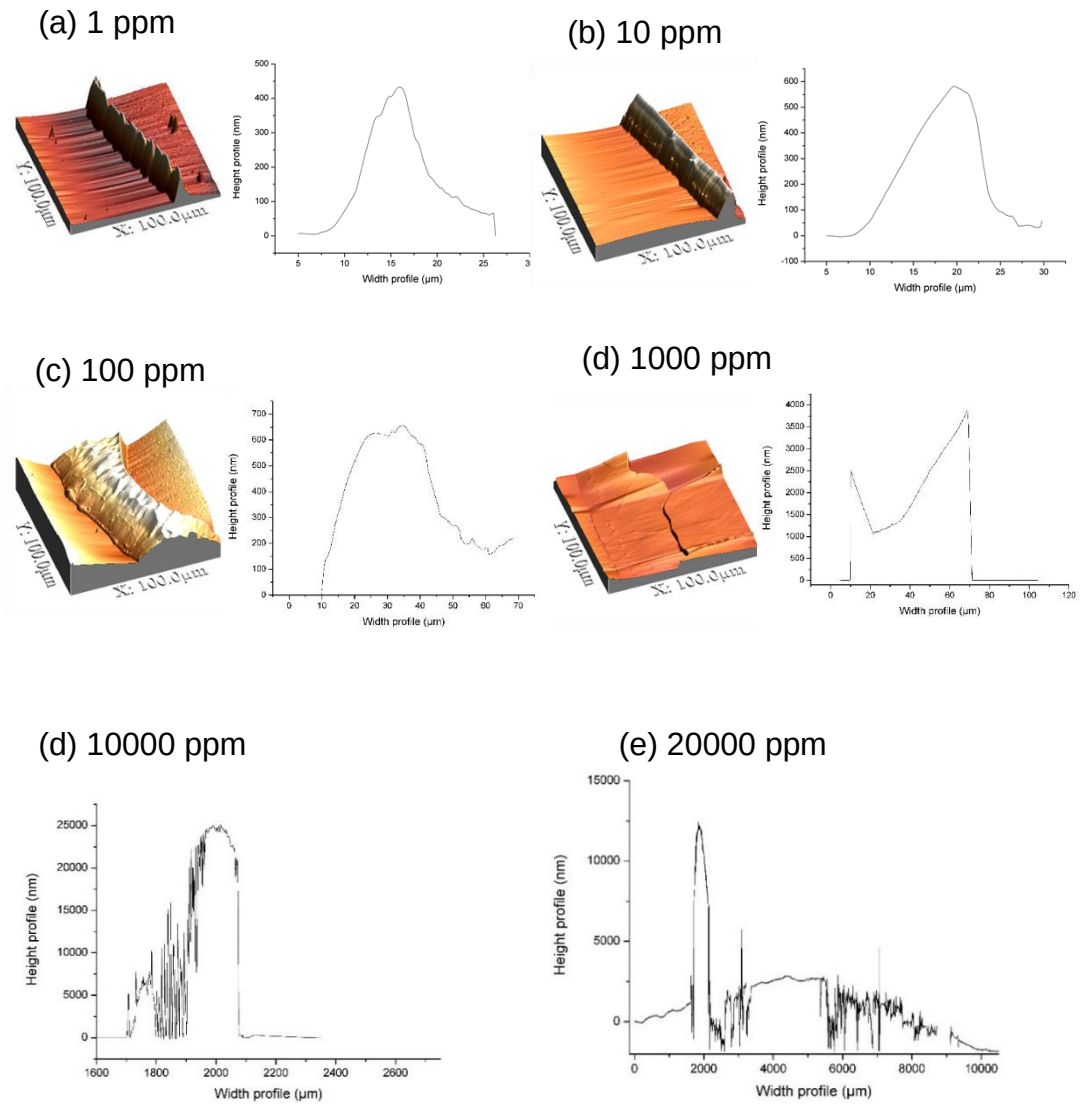

Figure 4-9: Three-dimensional topographical images of the residual dried deposit patterns of Ludox AS-40® on uncoated glass slides (a) to (d) AFM images and corresponding cross-sectional profiles of the left side edge at Ludox particle concentration C_{Lud}= 1,10,100 and 1000 ppm; (d) and (e) WLI images corresponding to cross-sectional profiles of the left side edge at C_{Lud}= 10000 ppm and 20000 ppm respectively.

The difficulty in this experiment arose from the formation of whiskers upon complete solvent evaporation at C_{Lud}=20000 ppm. The presence of whiskers renders the residual deposit to be brittle and challenging to move and analyse. Figure 4-10 presents the dimensionless plot of the measured film thickness,

T_H, and deposit width, W of the residual dried deposit normalised with the initial droplet contact radius r_d against the initial particle concentration. In this study, the film thickness is the apex height of the dried edge deposit features. Due to the brittle character of the sample, at C_{Lud}= 20000 ppm the measured T_H/r_d (T_H/r_d= 4.15x10 $^{-3}$) appears to be lower than C_{Lud}= 10000 ppm (T_H/r_d= 7.28x10^{-3}). However, for the other concentration of Ludox AS-40® C_{Lud}= 1 to 1000 ppm, T_H/r_d increases gradually with the initial particle concentration. This scaling relationship was observed in previous work (Lee and Routh, 2004) and the values were comparable (Hodges *et al*. measured T_H at 3000 nm while in our work T_H was evaluated at 3640 nm at C_{Lud}= 1000 ppm). In previous work, it was established that the width of the ring-shape residual deposit scales with the initial particle concentration following equation (4-10) (Deegan, 2000; Brutin, 2013):

$$\frac{W}{r_d} = A{C_p}^B \quad (4\text{-}10)$$

Where W corresponds to the width of the ring, r_d corresponds to the radius of the ring pattern, C_p corresponds to the initial particle concentration and A (A=1.72 (Deegan, 2000)) and B are constants.

Deegan found that B depended on the polystyrene microparticles size (B=0.78 for 0.1µm particles and 0.86 for 1 µm particles) and observed an ring-shape pattern as well as a complex structure inside the dried residue due to stick-slip motion of the TPCL (Deegan, 2000). Whereas, Brutin determined B=0.346 for his polystyrene nanoparticle system and two sets of dried residual structure emerged at the end of the evaporation process: a ring-shape pattern at lower particles concentration (from C_{PS}= 0.01 to 0.47 vol%) and a flower-shape pattern from C_{PS}=1.15 vol% onwards (Brutin, 2013). Lee *et al.* observed three sets of patterns depending on the initial particle concentrations and substrates: a ring-shape pattern for aluminium oxide nanoparticle below 2 vol% and smaller than 13 nm, a uniform deposit for particles above 3 vol% and larger than 20 nm while titanium dioxide particle displayed a ring-shape pattern regardless of the initial particle concentration (0.01 to 4 vol%) (Lee et al., 2017). In this present work, B=3.4x10^{-3} which is significantly different, however, the configuration of the dried residual deposit patterns of Ludox AS-40® were different from that of the aforementioned work: Brutin studied carboxylate coated polystyrene particles (Brutin, 2013), Deegan worked with micrometer polystyrene particles (Deegan, 2000) and Lee *et al.* worked with more than one substrate (glass, stainless steel and Teflon) (Lee et al., 2017). The droplets analysed in this study are also larger with V_{Lud}= 12.7 µL

compared to droplet initial volume at 0.5, 2.5 and 7 µL for Deegan, Lee and Brutin respectively.

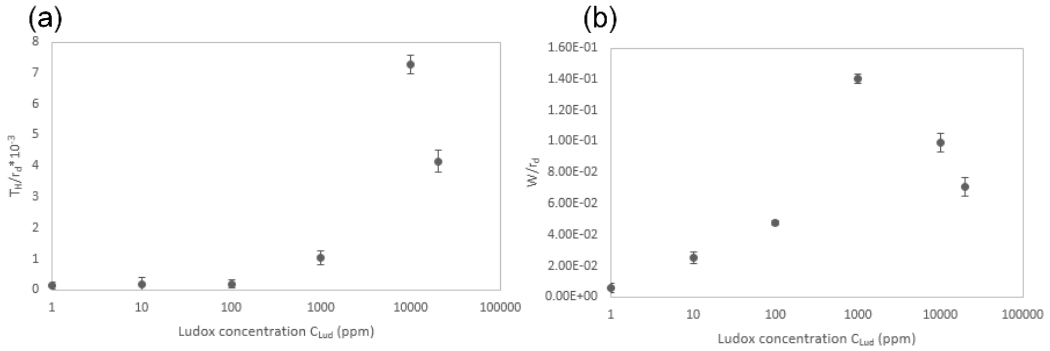

Figure 4-10: (a) Dimensionless analysis of (a) film thickness and (b) width of the residual dried deposit normalised with the initial droplet contact radius against the initial Ludox AS-40® particle concentration extracted from AFM (C_{Lud}=1 to 1000 ppm) and WLI (C_{Lud}=d10000 and 20000 ppm).

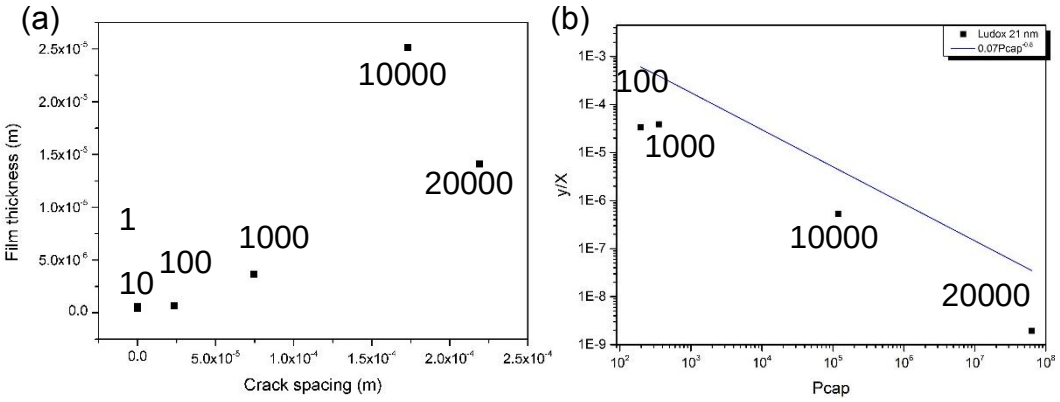

Figure 4-11: (a) Residual dried deposit thickness against cracks spacing for aqueous Ludox AS-40® silica droplets, (C_{Lud}= 1 to 20000 ppm); (b) Collapse of the crack spacing data with the nanoparticle hydrodynamic diameter. The value above the points correspond to the particle concentration in ppm.

- Cracks patterns analysis

During the evaporation process, cracks are originating from the edges and move inward to the centre of the deposit, since the evaporation is faster at the edges. As explained in section 4.3.2, the cracks result from capillary stress. From our experimental work, we have previously observed that the initial particle concentration has an impact on the evaporation rate. Hence, the effect of particle concentration on cracks spacing can be explored.

The graph in Figure 4-11a shows the residual dried deposit thickness against the cracks spacing using logarithmic axes. These data suggests that the cracks spacing seem to scale with the initial particle concentration. Although, this behaviour is not observed at C_{Lud}= 20000 ppm, this difference is due to the brittle characteristic of the sample. It was previously demonstrated that the cracks spacing scales with the film thickness regardless of the particle size and materials (Lee and Routh, 2004). The self-assembly of the particles into a close packed network could explain this scaling behaviour.

Figure 4-11b displays a plot of the crack spacing normalized by the film thickness (T_H) versus P_{cap} for each Ludox initial concentration analysed in this study. Previous work has demonstrated that a flat line should be observed if the critical fracture is independent of the drying conditions ((Lee and Routh, 2004). However, from the results shown in Figure 4-11, it can be concluded that the initial particle concentration has an influence on the crack spacing. The influence of the initial particle concentration could explain the difference of slope (negative slope in our work compared to positive slope in previous work), also in previous work the focus was on various particle size. The collapse of data in Figure 4-11b follows a power law which can be expressed by Equation (4-11)

$$\frac{y}{X} = 3.13 \times 10^{-3} P_{cap}^{-0.8} \quad (4\text{-}11)$$

This suggests that the crack spacing depends on the initial particle concentration scales with the dried droplet residual film thickness. The power of the law is 0.8 which is similar to previous work (Lee and Routh, 2004).

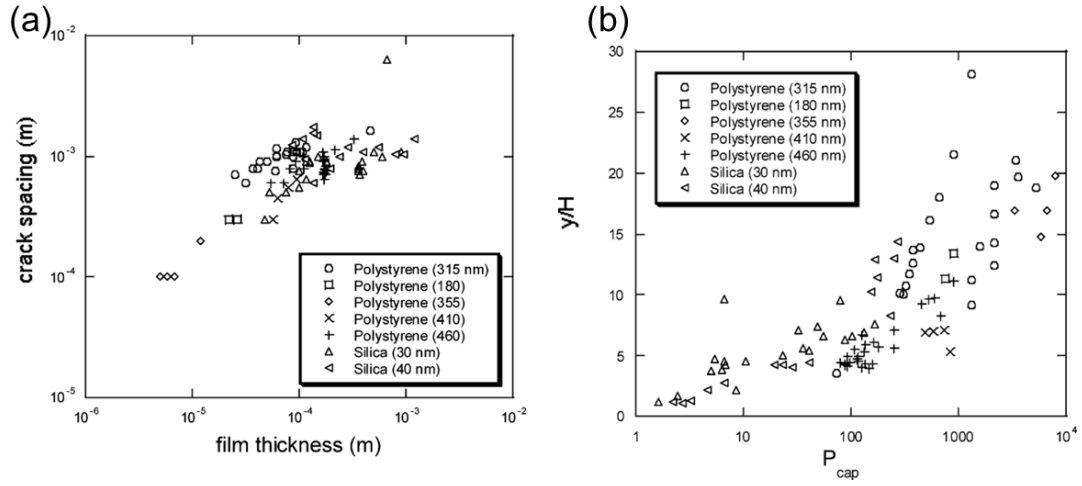

Figure 4-12: (a) Crack spacing as a function of the film thickness (b) Noncollapse of the crack spacing data when scaled with the film thickness. For different dispersions and different particles size (Lee and Routh, 2004)**.**

In their work, the crack spacing *y* normalised with the length scale *X* plotted against the dimensionless value Pcap as seen in Figure 4-12. The data collapses according to this power law (4-12).

$$\frac{y}{X} = 0.07 P_{cap}^{-0.8} \quad (4\text{-}12)$$

As seen, in the appendix, the residual dried deposit pattern of spherical PMMA particles latex give similar features with cracks in the structure and a ring-like stain upon the solvent evaporation (see Appendix A).

4.5 Summary

In this Chapter, the deposition behaviour of aqueous Ludox AS-40® silica nanoparticles with increasing initial particle concentration has been investigated on uncoated glass substrates.

The droplets were pinned indistinguishably of the initial particle concentration with the pinning time increasing with the particle concentration. The drying process followed a classic constant contact radius mode. However, the particle concentration was not enough to retain the pinning of the three-phase contact line throughout the entire evaporation process thus a receding of the contact line was observed as well as a deformation of the droplet shape which lost its spherical cap shape. To further our analysis our experimental evaporation rate results were compared to theoretical evaporation rate values using two models: Picknett and Bexon and Hu and Larson. For the latter model, the evaporation rate expression stems from the analytical solution of their finite element method (FEM) analysis. The comparison between experimental and theoretical evaporation rate of the droplets was determined at the following three initial concentrations: lowest C_{Lud}= 1 ppm, medium C_{Lud}= 1000 ppm and highest C_{Lud}= 20000 ppm. The Picknett and Bexon model predicts more accurately the evaporation rate which we confirmed with the

theoretical evaporation rate included in the experimental evaporation rate error bars results. However, this model diverges with the increase of the initial particle concentration, indeed it does not account for the presence of particles in the system especially if these particles are not surface active. A further model to account for the solute concentration is required to estimate the local solute concentration and discuss if they agree. A significant divergence is observed between the experimental and the theoretical evaporation for the second model at the three different initial particle concentration. This notable discrepancy arises from the size of the initial droplets which display an higher Bond number compared to the Bond number commonly associated for this theoretical model.

The results also show a ring-like stain upon solvent evaporation on uncoated glass slides. These ring-like stains or “coffee ring effect” are enhanced as the initial nanoparticle concentration is increased from C_{Lud}=1 to 20000 ppm due to a pinned three-phase contact line and a capillary flow transporting the particles towards the periphery of the deposit.

Initial particle concentration was also seen to control the thickness in height and width of the residual dried deposit structure. Due to capillary flow, particles are carried towards the three-phase contact line where their self-assembly lead to a gradual increase of the residual dried deposit edge height and width with the initial particle concentration.

Furthermore, during the evaporation process, tensile stresses are generated leading to the formation of cracks. These cracks are observed from $C_{Lud} \geq$ 100 ppm and it seems experimentally that the cracks are enhanced with the initial particle concentration. Initial particle concentration can thus be used to control the residual deposition of particles on a solid substrate.

These observations led us to an experimental investigation to determine the necessary conditions to influence further residual dried deposit patterns. We explore the deposition patterns and evaporation process of spherical Ludox AS-40® at a fixed initial concentration C_{Lud}= 20000 ppm – this concentration was selected to ensure a better visibility of the residual dried deposit patterns- while adding several additives such as: electrolyte (sodium chloride), binary solvent (Milli-Q water and ethanol) and anionic surfactant (sodium dodecyl

sulfate). To gather information for an organic nanoparticle system, we studied spherical PMMA latex at a medium concentration C_{Lat}= 4000 ppm (as it is visible enough to allow appropriate analysis) in similar conditions to inorganic Ludox AS-40® particle in the next chapter.

Chapter 5
Evaporative behaviour and subsequent deposit patterns for spherical silica and PMMA polymeric latex in binary solvent mixtures and with additives (electrolyte and surfactant): analysis of cracks patterns and aggregation of particles

5.1 Introduction

Droplet evaporation is a common and ubiquitous occurrence in many areas as previously discussed in Chapter 2. The drying of a colloidal system is one of the easiest techniques to self-assemble insoluble particulates upon solvent evaporation. This technique is of high interest due to its wide variety of applications and vast arrays of patterns that can be generated. Although, the addition of insoluble soluble solid particles complicates further this apparent system as particles can adsorb at the liquid-vapour interface (Kovalchuk et al., 2014). However, two main drawbacks are seen upon solvent evaporation, the first one is the well-known “coffee ring effect” (Deegan et al., 1997),(Deegan, 2000),(Deegan et al., 2000) and the second is the formation of cracks within the final dried film (Guo and Lewis, 1999), (Ghosh et al., 2015), (Singh and Tirumkudulu, 2007), (Yakhno, 2008).

As thoroughly reviewed in Chapter 2 and observed in Chapter 4, the drying of dispersions of small solid particles typically leaves a ring-shaped stain upon solvent evaporation. Characteristically, most of the solid material is deposited at the periphery of the droplet leading to a non-uniform structure. This non-uniform deposition is observed when the three-phase contact line is pinned and a capillary flow (Deegan et al., 1997),(Deegan, 2000),(Deegan et al., 2000) is generated carrying the suspended solutes from the drop centre towards the edges in order to compensate for the faster solvent evaporation at the edges. This effect is observed regardless of particle size (i.e., from micrometre-sized particles down to macromolecules) (Deegan, 2000),(Sefiane, 2014),(Erbil, 2012), droplet volume or the substrates used (i.e., glass slides, Teflon or silicon wafers) (Dugyala and Basavaraj, 2015),(Sefiane, 2010). Furthermore, this effect is prevalent in most systems. The evaporation of solvent in a drying droplet leads to a film of different homogeneity. Often, in the case of nanoparticle dispersions, the film obtained will present cracks in its structure. The crack patterns are usually the result of the release of tensile stresses created by the deformation of the air-water interface. The cracks patterns have been extensively studied (Guo and Lewis, 1999), (Ghosh et al., 2015), (Singh and Tirumkudulu, 2007), (Yakhno, 2008), however little work has been done to avoid cracks in drying drops (Kim et al., 2015), (Okubo et al., 2009):

Since, the “coffee ring effect” is prevalent in most cases, optimising the composition of the droplets to control the final deposit patterns and thus obtain a uniform film has been done. Usually, to modify the final deposit structure the promotion of a Marangoni flow within the droplet can lead to this desired dried residual deposit (Hu and Larson, 2006). Marangoni flow is generated by thermal surface tension and or solutal surface tension along the liquid-vapour interface. Thermal surface tension can arise from heat transfer from the solid substrate (Hu et al., 2013; Kovalchuk et al., 2014; Zhong and Duan, 2014; Parsa et al., 2015; Zhong and Duan, 2016a). Solutal surface tension arise from a difference in component local concentration (Still et al., 2012; Alexandru Crivoi and Duan, 2013; Parsa et al., 2017). Thus, Marangoni flow can be generated by manipulating the base fluids by adding surfactants or use of a co-solvent such as ethanol/water which is a common occurrence in industrial formulations. Several research groups have focussed their work on unveiling the flow within droplets composed of this binary mixtures at different concentration (Hamamoto et al., 2012), (Christy et al., 2011), (Christy et al., 2010). Further work was also achieved on different substrates such as on gold modified self-assembled monolayers (Cheng et al., 2006), smooth and rough PTFE substrates (Shi et al., 2009), (Sefiane et al., 2003), HDMS silicon (Liu et al., 2008) and silane coated wafers (Fang et al., 2009) albeit of the reliability of the results due to the rough nature of the substrates. However, limited attention have been drawn to the study of drying behaviour of binary or multicomponent-based mixtures and their subsequent final deposits morphologies (Zhong and Duan, 2014), (Kochiya and Ueno, 2009), (Ooi et al., 2016), (Chen et al., 2016), (Yu et al., 2017). The addition of surfactant in the systems has also been proven to be an efficient technique to suppress the “coffee ring effect” (Kajiya, Kobayashi, et al., 2009), (A. Crivoi and Duan, 2013), (Still et al., 2012), (Morales et al., 2013) even if in some cases it can promote the CRE (Alexandru Crivoi and Duan, 2013).

Besides, these two extreme cases: ring-like stain and uniform deposits more complex patterns can be generated especially upon evaporation of biofluids (Gorr et al., 2013), (Dutta Choudhury et al., 2015) . A common method to achieve complex patterns is by electrolyte addition in the system. Several groups have investigated the final deposits of droplets containing electrolyte. From these different studies, many parameters affected by the electrolyte were identified such as: features of the dried film monolayers organisation

(Rödner et al., 2002), the influence of the salt crystallisation process (Shahidzadeh et al., 2015), (Dutta et al., 2013), (Kaya et al., 2010), (Shahidzadeh-Bonn et al., 2008), the effect of the substrate (Takhistov and Chang, 2002), (Choudhury et al., 2013), (Kuncicky and Velev, 2008), how the electrolyte concentration can modified particle shape and thus the final deposit morphology (Sperling et al., 2014). Nonetheless, the effect of electrolyte addition on the wetting behaviour and ensuing deposit patterns a particle-laden system has generated less interest despite the complexity of the end deposit. Furthermore, despite these studies, there is still a lack of knowledge about these types of system and their final dried deposit structure.

The drying of the nanoparticles in aqueous system and their subsequent three-dimensional self-assembly stain as a function of Ludox AS-40® concentration (C_{Lud}= 1 to 20000 ppm) was previously investigated in Chapter 4, while the “coffee ring effect” for PMMA particles at low concentration was also observed (C_{Lat}= 0.4 wt%). In this subsequent chapter, our aim is to shed more light onto the drying behaviour of spherical nanoparticles (Ludox AS-40 ® silica and PMMA latex nanoparticles) in different systems (binary solvent mixtures ethanol/water and with electrolyte and surfactant addition) and the mechanisms leading to the formation of the different final patterns morphologies. We combine the droplets evaporative behaviour and the quantitative image analysis to provide a spanning overview of the key processes leading to the formation of the different final deposit patterns.

5.2 Experimental methods

5.2.1 Materials

The experiments were carried out with two aqueous colloidal suspensions:

- Ludox AS-40® (Sigma-Aldrich, UK) silica particles with diameter ∼21 nm. Amberlite MB-150 resin (MB Biomedicals, UK) was used to purify the Ludox AS-40® by ion exchange to remove residual soluble ions from the commercial sample.
- PMMA polymeric latex particles with a particle diameter of ~ 72.5 nm (see Chapter 4 in the appendix for the synthesis procedure and characterisation of the particles).

5.2.1.1 Binary solvent ethanol/water system

The effect of the ethanol concentration in binary nanofluids was studied for both systems. Its subsequent impact on the dried residual deposit is discussed further.

- Ludox AS ® silica suspensions

The only variable is the ethanol concentration in the binary fluids. More precisely, five different volume fractions of water silica-ethanol mixtures at C_{EtOH}= 50, 60, 70, 80 and 90 vol% were prepared to examine evaporation of V_{Lud}= 8.7±0.4 µL nanofluids droplets deposited on a clean silane coated glass slide surface. The Ludox AS-40® silica nanoparticle was fixed at C_{Lud}=20 000 ppm suspended in Milli-Q water was used as the base fluid. The studied samples were mixed first and sonicated for 5 minutes in each case at room temperature and atmospheric pressure by using an ultrasonic bath before deposition on the substrate. This procedure was followed to ensure the obtention of a well-distributed mixture first before the evaporation process. Evaporation experiments were performed using a Krüss DSA1000 droplet shape analysis contact angle goniometer. The suspensions were used on the day of the preparation.

- PMMA latex suspensions

PMMA polymeric particles were added to different ethanol mixtures more precisely at C_{EtOH}=50, 60, 70, 80 and 90 vol%. Then the evaporative behaviour of droplets of V= 12.1 ± 5.5 µL were examined. These nanofluids droplets were deposited on clean silane coated glass slide surface. The final PMMA latex polymeric particles concentration was fixed at C_{Lat}= 4000 ppm in all the different ethanol mixtures. The PMMA polymeric particles were dispersed for 5 minutes in each case at room temperature and atmospheric pressure by using an ultrasonic bath before deposition on the substrate. The suspensions were used on the day of the preparation and the preparation was made ahead of each deposition. This concentration was selected to determine to provide knowledge for larger particles compare to Ludox AS-40 ® but at medium concentration range.

5.2.1.2 Systems with additives (electrolyte and anionic surfactant)

- Ludox AS ® silica suspensions with added electrolyte

Ludox AS-40® and sodium chloride (NaCl, Sigma Aldrich, UK) were used to prepare Ludox AS-40 ® and varying sodium chloride suspensions. In this

study, the suspensions contained 20 000 ppm Ludox AS-40® with NaCl concentrations ranging from 10 to 300 mM. The subsequent suspensions were used to generate droplets; clean uncoated glass slides were used as evaporating substrates. The droplets volumes were V_{Lud}= 18.8 ± 2.3 µL, leading to deposition coatings with diameters of 6.4 to 7.5 mm. Total evaporation times ranged between 49 and 80 minutes.

- PMMA latex suspensions with added electrolyte

PMMA latex and sodium chloride (NaCl, Sigma Aldrich, UK) were used to prepare PMMA latex and varying sodium chloride suspensions. In this study, the final suspensions contained C_{Lat}= 4000 ppm PMMA latex particles with NaCl concentrations ranging from C_{NaCl}= 0.03 to 1.0 M. The subsequent suspensions were used to generate droplets; clean silane coated glass slides were used as evaporating substrates. The droplets volumes were V_{Lat}=25.2 ± 0.4 µL, leading to deposition coatings with diameters of about 5.0 mm. The droplets total evaporation times was about 6480 seconds.

- System with anionic surfactant addition

Sodium dodecyl sulfate solutions (VWR Prolabo, ≥98%) were added to Ludox-AS® and the suspensions were stirred for 5 minutes before each droplet deposition in an ultrasonic bath. The suspensions prepared correspond to a final SDS concentration from C_{SDS}= 0 to 30 mM and Ludox-AS® at C_{Lud}= 2 wt% by weight. Clean glass slides were used as evaporation substrates following the cleaning method described in Chapter 3. A temperature and relative humidity box was used to avoid air currents. The drop volumes were V_{Lud}= 11.4 ± 2.1 µL, leading to deposition coatings with diameters of $2r_d$= 7.2 to 8.6 mm. Total evaporation times ranged between about 2.5 and 66 minutes.

5.2.2 Characterisation

The evaporation of single sessile droplets was conducted in a chamber and under natural diffusion condition (temperature and humidity were at 24±1°C and 43±3%) for uncoated and silane coated glass slides (Thermo Scientific, hydrophilic) following the method explained in Chapter 3. Each droplet depositions were repeated three times and the variation between measurements was used as the standard deviation.

- Measurement of droplet evaporation using contact angle goniometer

A KSV CAM300 contact angle goniometer was used to study the wetting properties. Sessile droplets were manually generated. The evaporation process was recorded with a high-resolution digital camera at a frequency of 1 frame per second. A droplet profile variation for the different systems: binary solvent, electrolyte and surfactant addition was thus obtained. Ball calibration was conducted before each experiment to minimize experimental errors. Upon complete solvent evaporation, all of the images were post-processed with the associated software as explained in Chapter 3. To ensure the repeatability of our experiments, three tests were conducted for each set of systems.

- Droplet deposit structure imaging

The two-dimensional and three-dimensional topographical characteristics of the dried deposits surfaces were obtained from a White Light Interferometer (WLI, NP FLEX, Bruker, USA). It was used to determine the features of the dried deposit patterns. Additionally, the cracks patterns observed on the dried deposit were studied using an optical microscope, (Olympus, U-MNUA2).

- Investigation of the sedimentation

Turbiscan Lab (Formulaction, Toulouse, France) monitored the sedimentation properties of the PMMA latex particles. A thorough description of a Turbiscan apparatus can be found in Chapter 3 section x. Each dataset was collected for 45 minutes, this timescale was selected because the systems studied evaporates in about 90 minutes, which is half as long as the experiments. Hence, the sedimentation properties can be extrapolated for the entire droplet lifetime. The typical results obtained from a Turbiscan are shown in Appendix B section Y. By use of the Delta Transmission data (Add Fig number) in combination with the Stokes Einstein equation (add cross-reference), it was possible to calculate and determine the particle diameter upon sedimentation.

5.3 Theoretical approach

5.3.1 Description of droplet evaporation

In our experiments, a sessile droplet having the shape of a spherical cap resting on a flat substrate is considered. The droplet shape is limited by the Bond number, $B_0 = \frac{\rho g r_d H}{\gamma_{LV}}$ which as explain in the previous Chapter 2 accounts for the effect of surface tension and gravitational forces on the droplet shape. Here, ρ is the fluid density, g is the acceleration of gravity, r_d is the droplet contact radius, H is the initial height of the droplet at its apex and γ_{LV} is the liquid/air surface tension measured by the pendant drop method. In all the systems, the Bond number is low, $B_0 < 1$, so that the droplet shape can be regarded as a spherical cap (see Table 5-1).

Table 5-1: Bond number and ratio of diffusion time to evaporation time for all systems studied for spherical Ludox and PMMA latex.

System	Bond number, B_0		t_D/t_E	
	Ludox AS-40 ®	PMMA latex	Ludox AS-40 ®	PMMA latex
Co-solvent Water/ethanol	$\sim 5.7\text{x}10^{-1}$	$\sim 6.9\text{x}10^{-1}$	$\sim 9.8\text{x}10^{-10}$	$\sim 1.7\text{x}10^{-9}$
Electrolyte	$\sim 4.5\text{x}10^{-1}$	$\sim 6.4\text{x}10^{-1}$	$\sim 2.2\text{x}10^{-10}$	$\sim 1.5\text{x}10^{-10}$
Surfactant	$\sim 6.5\text{x}10^{-1}$	✓	$\sim 5.6\text{x}10^{-10}$	✓

In Figure 5-1a, a schematic of a spherical cap droplet on a glass slide surface with the interfacial forces balance is presented, under these assumptions, the evaporation process can be described by using three parameters, that of, droplet contact radius r_d, droplet height H and apparent contact angle Θ_{ACA}. Thus, the following relationships are satisfied:

$$\theta_{ACA} = 2\tan^{-1}\left(\frac{H}{r_d}\right) = \cos^{-1}\left(\frac{\gamma_{SV} - \gamma_{SL}}{\gamma_{LV}}\right) \quad (5\text{-}1)$$

$$V = \frac{\pi H(3r_d^2 + H^2)}{6} = \pi {r_d}^3 \frac{\cos\theta^3 - 3\cos\theta + 2}{3\sin {\theta_{ACA}}^3} \quad (5\text{-}2)$$

Where V is the droplet volume, γ_{SV} is the solid/vapour surface tension, γ_{SL} is the solid/liquid surface tension, γ_{LV} liquid/vapour surface tension respectively, and Θ_{ACA} is the equilibrium contact angle of a droplet resting on a surface obtained by the balance of force acting at the three-phase contact line (TPCL) and expressed by the Young-Laplace equation.

The solvents evaporate into the ambient air, with the vapour concentration distributed non-uniformly above the droplet. Thus, at the liquid/vapour interface, the vapour concentration c is assumed to be equal to the saturation value c_s. Far away above the droplet, the vapour concentration approaches the ambient value RHc_s, where RH is the relative humidity of the ambient air. The diffusion time t_D required for the vapour-phase solvent concentration to adjust to modification in the droplet shape is $t_D = r_d^2/D$, where D is the diffusion coefficient of the solvent vapour in air (Haynes, 2017). The ratio of diffusion time to the droplet evaporation is $t_D/t_E = r_d^2/Dt_E \approx c_s(1\text{-}RH)/\rho$, where c_s is the solvent vapour concentration in air. In our experiments, $RH=0.43$,

c_s=1.75x10^{-3} kg/m^3 (Dash and Garimella, 2013), and ρ=997.2988 g/cm^3, so that we obtain $t_D/t_E \ll 1$ (see Table 5-1). Hence, since the solvent vapour concentration adjusts rapidly compared to the time required for the droplet to evaporates, the evaporation process can be considered to be a diffusion controlled quasi-steady state.

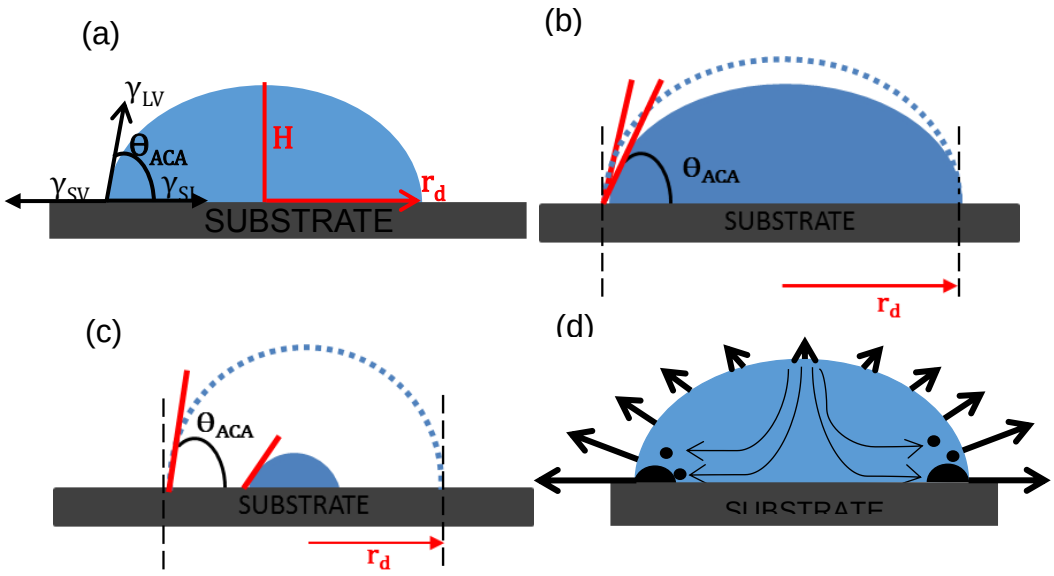

Figure 5-1: Schematics illustration on a solid substrate for (a) droplet parameters: droplet contact radius, r_d, droplet height at its apex, H and apparent contact angle Θ_{ACA} (b) drying mode behaviour for a pinned contact line/ constant contact radius mode (CCRM) and (c) Mixed drying mode (MDM) decreasing contact radius and apparent contact angle. The dashed line represents the initial contact line of the droplet, (d) Schematic illustration of nanoparticle transport during the evaporation process.

The investigation of diffusion-controlled evaporation process has led to the expression of several models. To that effect, Birdi et al. (Birdi et al., 1989), (Birdi and Vu, 1993) expressed the evaporation rate for a water droplet evaporating on a solid surface as:

$$E = -\frac{dV}{dt} = \frac{4\pi r_d}{\rho} D(c_s - c_\infty) f(\theta) \qquad (5\text{-}3)$$

Where, f(Θ) is a function determined by Picknett and Bexon (Picknett and Bexon, 1977), this function enables to account for the effect a solid surface on the vapour field. Through an analogy with an electrostatic problem evaluating the capacitance of a conductor of a spherical cap reminiscent of a sessile droplet, using a polynomial fit f(Θ) was found to be equation (5-4)

and (5-5) depending on the angle values. Since, the boundary conditions are satisfied (the saturated concentration c_s is reached at the droplet surface and the solvent vapour concentration $c_\infty = RHc_s$ far away from the droplet surface), hence equation (5-4) can be rewritten as equation (5-6):

$$f(\theta) = \frac{1}{2} \times (0.6366\theta + 0.09591\theta^2 - 0.06144\theta^3) \quad \text{for} \quad 0 \leq \theta < 10° \tag{5-4}$$

$$\frac{1}{2} \times (0.0008957 + 0.6333\theta + 0.1160\theta^2 - 0.08878\theta^3 + 0.01033\theta^4) \text{ for } 10° \leq \theta \leq 180° \tag{5-5}$$

$$E = \frac{4\pi r_d}{\rho} D c_s (1 - RH) f(\theta) \tag{5-6}$$

5.3.2 Crack patterns

The model used to describe cracking mechanisms can be found in Chapter 4 in the theoretical approach explanation.

In our approach, the dried film thickness corresponds to the apex of the dried residual depositions patterns.

5.4 Results and discussion

5.4.1 Evaporative behaviour and subsequent cracks pattern in ethanol/water binary mixtures

5.4.1.1 Ludox AS-40®: effect of the ethanol concentration in silica nanoparticles laden binary nanofluids droplets

- Stability of suspensions in different ethanol/water mixtures

The relevance of ethanol in laden droplets was examined by varying its concentration within the range from C_{EtOH}= 50 to 90 vol%. The evaporation of drops of C_{Lud}=20 000 ppm Ludox AS-40® silica particles in ethanol/water mixtures (ratios= 50/50, 60/40,70/30,80/20, 90/10 vol%) were carried out. The surface tension of the different mixtures was investigated to have an idea of the effect of the variation of the ethanol content. Figure 5-2: Surface tension measurements of MilliQ-water and Ludox AS-40® silica aqueous

suspensions particle at 20000 ppm in different ethanol/water concentration (C_{EtOH}= 50 to 90 vol%).Figure 5-2 shows the measurements of the surface tension of the pure and particles laden ethanol/water mixtures at the ratio of interest for our study. It is worth noting that despite the increase in EtOH content the measured surface tension does not vary significantly γ_{LV}~ 0.4 mN/m from C_{EtOH}=50 to 80 vol%, while the surface tension drops significantly for the C_{EtOH}=90 vol% to γ_{LV}=23 mN/m which is close to the surface tension of pure EtOH measured at γ_{LV}=22.1 mN/m.

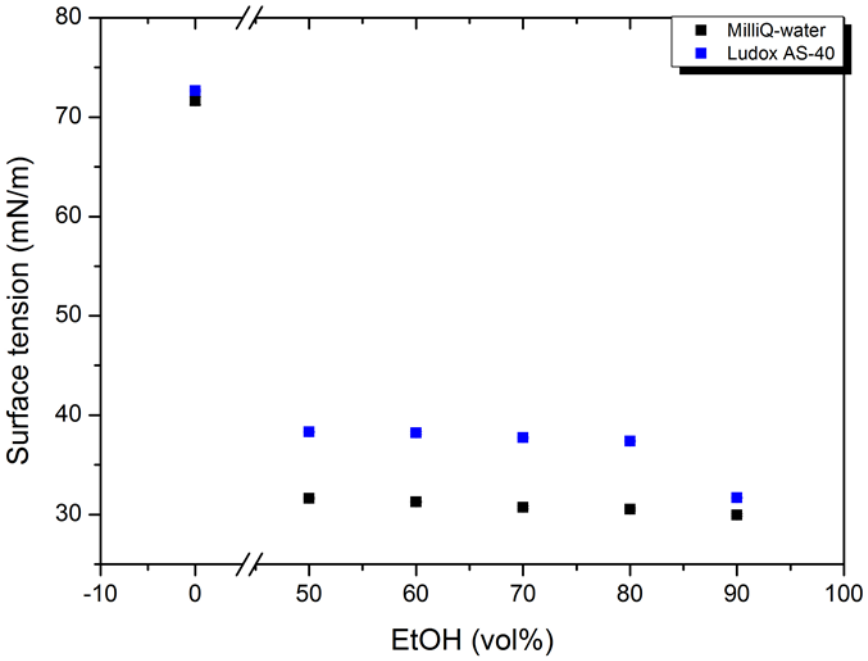

Figure 5-2: Surface tension measurements of MilliQ-water and Ludox AS-40® silica aqueous suspensions particle at 20000 ppm in different ethanol/water concentration (C_{EtOH}= 50 to 90 vol%).

It is observed that the surface tension, γ_{LV} decreases similarly for pure and particle laden system. Hence, particle does not affect the surface tension in ethanol/water system but the C_{EtOH} is the main factor that dictates droplet shape hence its drying dynamics. As lower surface tension will lead to higher wetting surface the droplet depositions were executed on silane coated glass slides substrates.

- Wetting and drying kinetics of silica suspensions in ethanol/water (EtOH/H2O) mixtures

The parameters considered here are droplets volume VLud, contact diameter $2r_d$ and apparent contact angle θ_{ACA}. The drying sequence depicting the visual changes of droplet at the different ethanol concentration from the side

view are presented in Figure 5-3. This drying sequence was used to plot the wetting properties presented in Figure 5-4a, b and c. The experimental data shows that despite the low B_o and initial spherical cap shape of the droplets during the evaporation process the droplet shape was considerably distorted especially near the end of the evaporation.

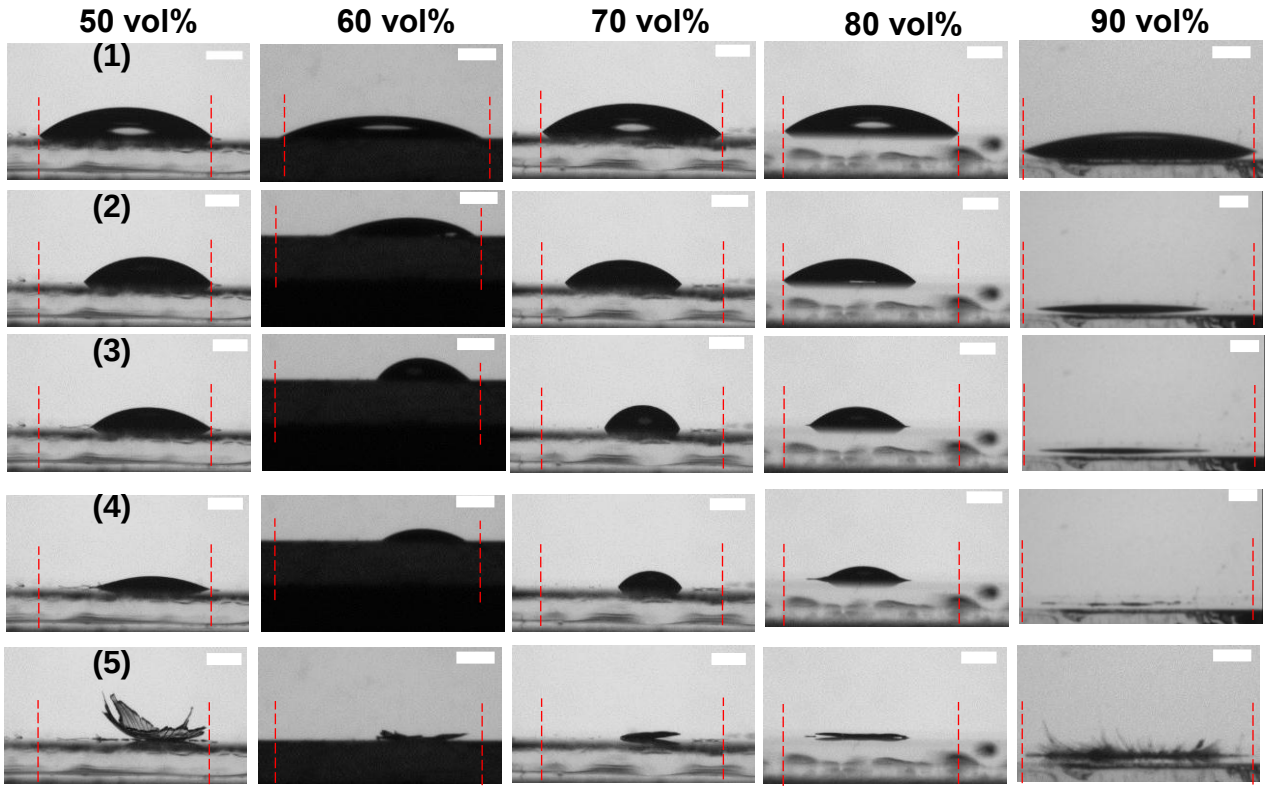

Figure 5-3: Drying sequence of Ludox AS-40® silica droplets (at 20000 ppm) in different water/ethanol mixtures (ethanol concentration, C_{EtOH}= 50 to 90 vol%) at different time of droplet lifetime (1) 0%, (2) 25%, (3) 50%, (4) 75% and (5) 100%. The images are side-view recordings of the deposition using a contact angle goniometer. The scale bars on all images represents 1 mm. The red dotted lines represent the initial droplet contact diameter. Droplets were deposited on silane coated glass slides.

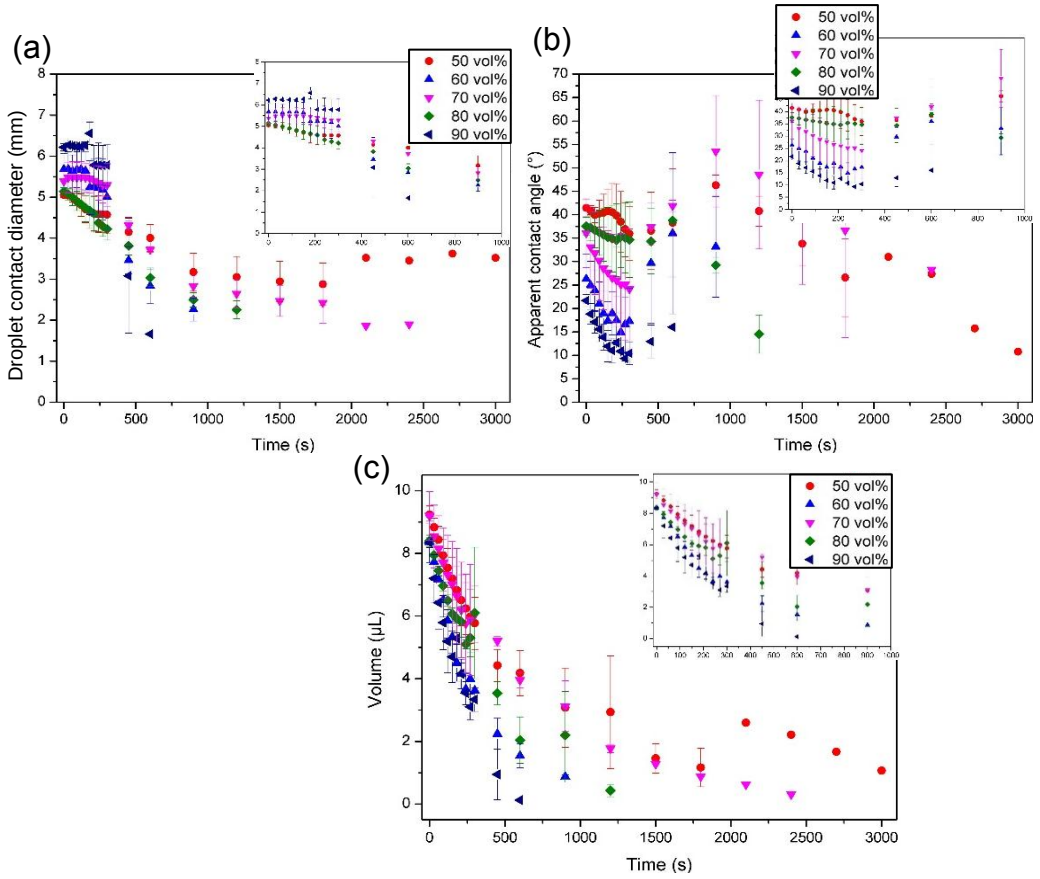

Figure 5-4: Evolution of (a) droplet contact diameter $2r_d$ (b) apparent contact angle θ_{ACA} and (c) volume V of Ludox AS-40® at 2wt% in different water/ethanol mixtures (ethanol concentration, C_{EtOH}= 50 to 90 vol%) with time on the entire droplet lifetime and a zoom in between 0 to 1000 s. The droplets were deposited on silane coated glass slides. The evolution was extracted from contact angle goniometer recordings.

Because of discrepancies for the droplets evaporation lifetimes, we normalized the evaporation with the entire evaporation time for each ethanol conThe droplets with Ludox AS-40® evaporate faster with an increase in the ethanol concentration, this phenomenon can be observed on Figure 5-3 and this is characterized by the decrease of the droplet volume. This has previously been reported for particle free binary droplets with no heating or cooling substrates by Sefiane et al. (Sefiane et al., 2003; Cheng et al., 2006; Liu et al., 2008). It is worth noticing, that it is different from the observation that the addition of nanoparticles in other binary mixtures were seen to promote the pining of the droplet contact line (Zhong and Duan, 2014). However, this is similar to the rapid shrinkage of the TPCL observed during the evaporation of ethanol-water droplets regardless of the substrates (Sefiane et al., 2003). Although in previous work, the evaporation study were

done at lower initial ethanol concentration C_{EtOH}= 0 to 50 vol% (Zhong and Duan, 2014) compare to our study

To obtain qualitative information of the wetting behaviour shown in Figure 5-3, we plotted the variation of the normalized apparent contact angle θ_{ACA}, contact diameter $2r_d$ and V_{Lud} as a function of time. This is discussed further below.

On Figure 5-4a, the droplets diameter variation with time is reported for the different drops mixture. As indicated, the contact diameter is pinned for a short period of time at the beginning of the evaporation process however this behaviour does not show a linear dependence with increasing the ethanol concentration as previously reported (Shi et al., 2009), This discrepancies could be explain by the different system used as in this previous experimental results the EtOH concentrations reported were from 0 to 50 vol% for graphite nanofluids and the depositions were performed on silicon wafer (Zhong and Duan, 2014). It was also found that the wetting behaviour for ethanol/water mixtures have a different behaviour compared to the pure fluids (Sefiane et al., 2003; Liu et al., 2008).

The initial apparent contact angle Θ_{ACA} does not decrease with the ethanol concentration increase as shown in Figure 5-4b. However, in all performed experiments we observed that on our silane-coated glass slides, the Θ_{ACA} follows the same trend. It initially decreases, then increase slightly before decreasing and increasing again. These variations are associated with de-pinning of the droplet TPCL as observed on Figure 5-4b and should be associated with a stick-slip motion of the TPCL (Moffat et al., 2009; Orejon et al., 2011; Anyfantakis and Baigl, 2014). However, the final deposit structure does not display clear concentric rings.

Figure 5-4c shows the variation of the normalized volume over time. This variation which corresponds to the rate of evaporation displays a non-linear decrease in all cases. Because, ethanol is more volatile than deionized water, the droplet containing a higher concentration of ethanol is expected to evaporate faster, which is consistent with the sharper trend of the volume change at a higher ethanol concentration (cf. Figure 5-4). Contrary to what we could expect, a few conclusions are evident from these results: (1) the evaporation rate does not increase as the ethanol concentration increases, which is indicated by a shorter droplet lifetime for the C_{EtOH}= 60 vol% compared to the C_{EtOH}= 80 vol%. Indeed, at C_{EtOH}= 60 vol% EtOH droplets take approximatively 1155 seconds to evaporate, while for 80 vol% EtOH it is about 1362 seconds; (2) for all systems two stages are observed a near

linear volume decrease at the beginning of the evaporation with an apparent switch manifested by a volume increase followed by a volume decrease which could be attributed to a water rich droplet. Which could compare to previous data that showed that at the initial stage of the evaporation process, the droplet interface is rich in EtOH (this could be explain due to a lower boiling point/vapour pressure compare to that of water) dictating the evaporation behaviour followed by a switch in the droplet evaporation behaviour due to a water rich droplet liquid/vapour interface. However, our results are quite different from previously reported data (Sefiane et al., 2003; Cheng et al., 2006; Shi et al., 2009). These discrepancies could be explained by the difference of substrate used. In the previous system, some of the surface were rough (Sefiane et al., 2003; Shi et al., 2009) while others were self-assembled monolayers-modified surfaces (Cheng et al., 2006). Also, in these previous systems, no particles were added to the binary solvent mixtures.

The deviation is more significant with a higher evaporation due to the fact that the initial ethanol evaporation induces a greater change between the initial stage and the late stage of the water dominated evaporation with a lower rate (E= $20.2x10^{-3}$µL/s from 0 to 450 seconds probably ethanol dominated and E= $1.1x10^{-3}$µL/s from 600 seconds probably water-dominated for C_{EtOH}= 60 vol%).

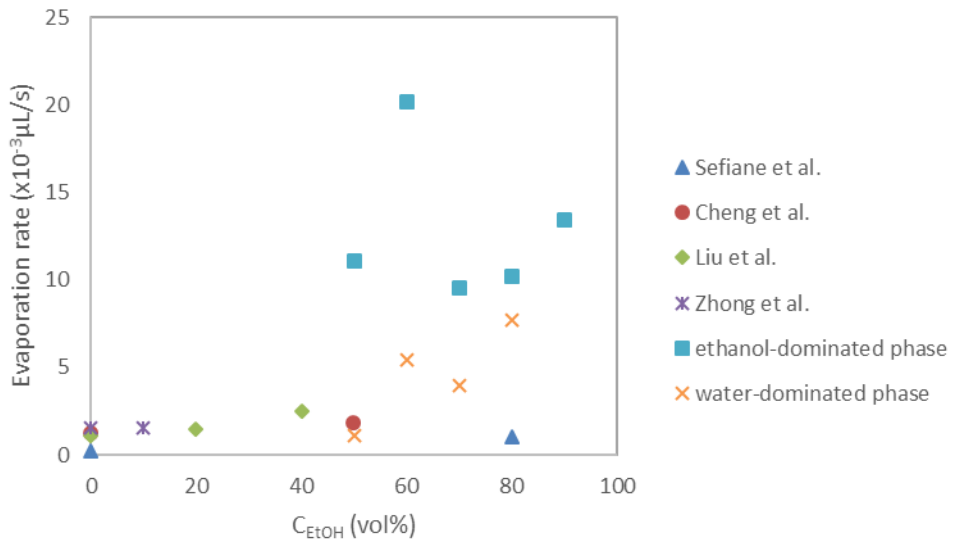

Figure 5-5: The averaged evaporation rate of C_{Lud}= 2 wt% nanofluid droplets as a function of ethanol concentration and the comparison with the literature data where substrates were not heated and cooled (Sefiane et al., 2003; Cheng et al., 2006; Liu et al., 2008; Zhong and Duan, 2014)**.**

The data are summarized and plotted in Figure 5-5 to show the average volume evaporation rates of the Ludox AS-40® ethanol aqueous droplets as a function of ethanol concentration in the binary mixtures. The evaporation rate of the nanofluid droplets increases with the variation of ethanol concentration. At C_{EtOH}= 60 vol%, the evaporation exhibits a significant increase. The evaporation rates are all above those of binary fluids which are particle free. This suggests that the laden particle droplets enhance further the evaporation rate. Although, the initial TPCL is similar for all the C_{EtOH}, the baseline does seem to increase with the highest ethanol concentration. We suggests that this behaviour stem from the difference in vapour pressures between ethanol and water.

- Residual dried deposit patterns for ethanol/water mixtures

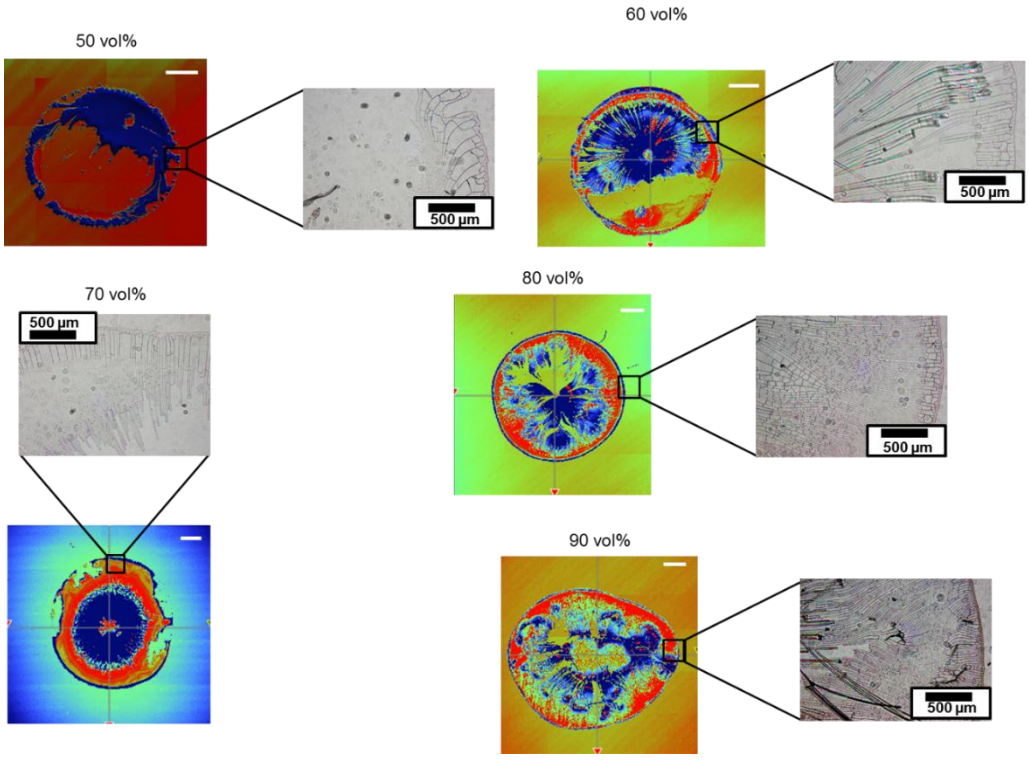

Figure 5-6: Two-dimensional WLI images of dried deposit of Ludox AS-40® silica in different ethanol/water mixtures (C_{EtOH}= 50 to 90 vol%) and optical micrographs corresponding to the magnification of the area inside the black box on uncoated glass slides. The white scale bars represent 1 mm on all images.

On Figure 5-6, the two-dimensional dried residual deposit patterns of Ludox AS-40® silica in the different ethanol/water mixtures are presented. From

these dried deposit structure, it can be seen that the droplets display complex features. It seems that the dried residual patterns depend on the variation of the ethanol concentration. At C_{EtOH}= 50 vol%, the dried residual patterns show a thin outer ring and a relatively uniform particle distribution where a secondary pinning TPCL was observed. As the initial ethanol concentration increase the dried residual deposit is more uniform. Although, we have not measure the flow within in the binary mixture suspensions, we can extrapolate the flow regime from the experimental worked carried out by Christy et al (Christy et al., 2010; Christy et al., 2011; Hamamoto et al., 2012). In their study, it was determined that three regimes occurred during an evaporation process:

-(1) ethanol-dominating stage with chaotic flows and vortices

-(2) intermediate stage with Marangoni flow led by a non-uniform distribution of ethanol at the liquid-vapour interface.

-(3) water-dominating stage characterized by radial flow.

Our observed dried residual patterns could result from these flow regimes. The dried residual deposition patterns are highly influenced by the initial ethanol concentration. This suggests that the ethanol component wields high importance in the three regimes as discussed by Christy et al. (Christy et al., 2011) and as observed by Zhong et al. (Zhong and Duan, 2014) the presence of nanoparticles may influence the flow regimes. We did not investigate the flow regimes inside the droplet. However, previous work from Zhong et al. (Zhong and Duan, 2014) observed strong vortices able to transport the nanoparticles toward the liquid-vapour interface and this nanoparticle accumulation resulted in formation of aggregates. Overtime, these aggregates were seen to be carried toward the droplet centre due to Marangoni flow since the droplet interface is non-uniform and a surface tension gradient along the liquid-vapour interface was generated.

Despite the apparent stick-slip motion of the TPCL during the evaporation process no concentric are observed. Also, the corresponding optical micrographs entails us to see the cracks in the dried deposit structure. The distinction for the dried residual deposition is attributed to the ethanol concentration. One perceptible contrast In these observations is that the nanoparticles did not promote the pinning of the TPCL in comparison to the Ludox AS-40® aqueous droplets has seen in Chapter 4.

Albeit, the underlying mechanism is still unclear at present, there are three possible reasons for the dried residual deposition patterns.

-(1) The non-uniform liquid-vapour interface was modified by both ethanol and Ludox AS-40® aggregates. This generated a surface tension and a subsequent fluid circulation and a more uniform particle distribution.

-(2) Not enough particle accumulated at the droplet TPCL to enhance a pinning effect at the beginning of the evaporation process.

-(3) At about 25% of the droplet lifetime, droplet TPCL is pinned at one side and this pinning effect is less prominent with the increase of the ethanol concentration.

In the subsequent subsection, ethanol/water based nanofluids droplets laden with PMMA nanoparticles is investigated. Similarly, to the Ludox AS-40'® nanofluids system, the effect of ethanol concentration is investigated on the droplets wetting behaviour, aggregation kinetics and the dried residual deposition patterns.

5.4.1.2 PMMA latex in EtOH/H2O binary mixtures

- Wetting and drying kinetics of PMMA latex

The surface tension measurements of PMMA polymeric particles in different ethanol/water mixtures is presented in the appendix (see Figure A-7). The drying sequence which allowed the extraction of the evaporative behaviour data of the droplets can also be find in the appendix (see Figure A-8).

Similarly, to the Ludox AS-40® silica system, the surface tension measured for the PMMA latex particles in the different ethanol concentration C_{EtOH}= 50 to 90 vol% was dictated by the ethanol content (γ_{LV}= 24.5 ± 0.6 mN/m for all systems).

When, the ethanol concentration increases the droplets with PMMA nanoparticle evaporate faster as seen in Table 5-2 and in previous work (Sefiane et al., 2003; Cheng et al., 2006; Liu et al., 2008; Zhong and Duan, 2016b).

Table 5-2: Summary of evaporation rate of ethanol/water droplets laden with PMMA particles at different ethanol/water concentration.

Evaporation rate (10^{-3}µL/s)	Ethanol concentration (vol%)
5.6	50
13.3	60
17	70
21.9	80
30.4	90

To gauge the wetting properties, the droplet contact diameter, volume and apparent contact angle as a function of time are examined further.

On Figure 5-7a, b and c, the evolution of PMMA latex droplets contact diameter $2r_d$, apparent contact angle θ_{ACA} and volume V with time is reported. It can be seen that the TPCL is pinned for most of the droplet lifetime. The decrease towards the end arises due to the droplet losing its spherical cap progressively with the evaporation process. As for the Ludox AS-40® system, the droplet contact diameter on the silane coated glass slides substrates are not affected by the ethanol concentration.

The pinning of the TPCL of the droplet is associated as expected with a decreasing θ_{ACA} (see Figure 5-7b). Also, the θ_{ACA} seems to be depend on the initial ethanol content within the droplet. The increase of θ_{ACA} towards the end of the droplet lifetime to ~ 85° is due to the droplet being mainly water rich and the fact that the droplets were deposited onto silane coated substrates. With time, the evaporating droplets with higher ethanol concentration remains pinned longer compared to C_{EtOH}= 50 vol% where the contact diameter remains pinned for 25% of the droplet lifetime compare to 75% or more for C_{EtOH}= 60 to 90 vol%. This is quite different from previous work (Sefiane et al., 2003; Cheng et al., 2006; Liu et al., 2008; Zhong and Duan, 2016b) where a fast reduction of the droplet contact diameter at the beginning for particle free or for graphite laden binary mixtures were observed. The presence of the particle seems to promote pinning of the droplet contact diameter as well.

The evolution of the volume V (see Figure 5-7c) with time is linear and a break was observed for all systems. We suppose that this break could indicate the switch to an almost pure water droplet system.

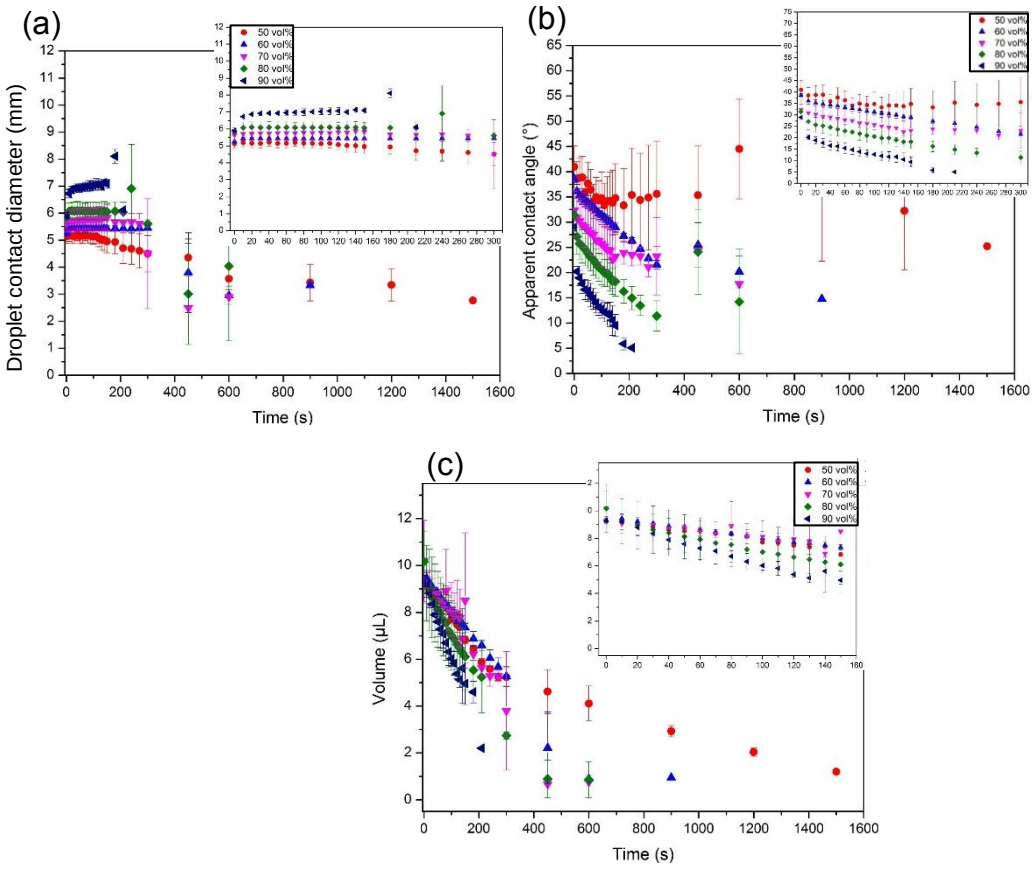

Figure 5-7: Evolution of (a) droplet contact diameter $2r_d$, (b) apparent contact angle θ_{ACA} (c) volume V of PMMA polymeric particles at 0.4 wt% in different ethanol/water mixtures (C_{EtOH}= 50 to 90 vol%) with time on the entire droplet lifetime and a zoom of the evolution between 0 to 300 s is presented. The droplets were deposited on silane coated glass slides. The evolution was extracted from contact angle goniometer recordings.

Two stages seem to be observed. It is more significant for C_{EtOH}=50 vol%.

- Residual dried deposit patterns

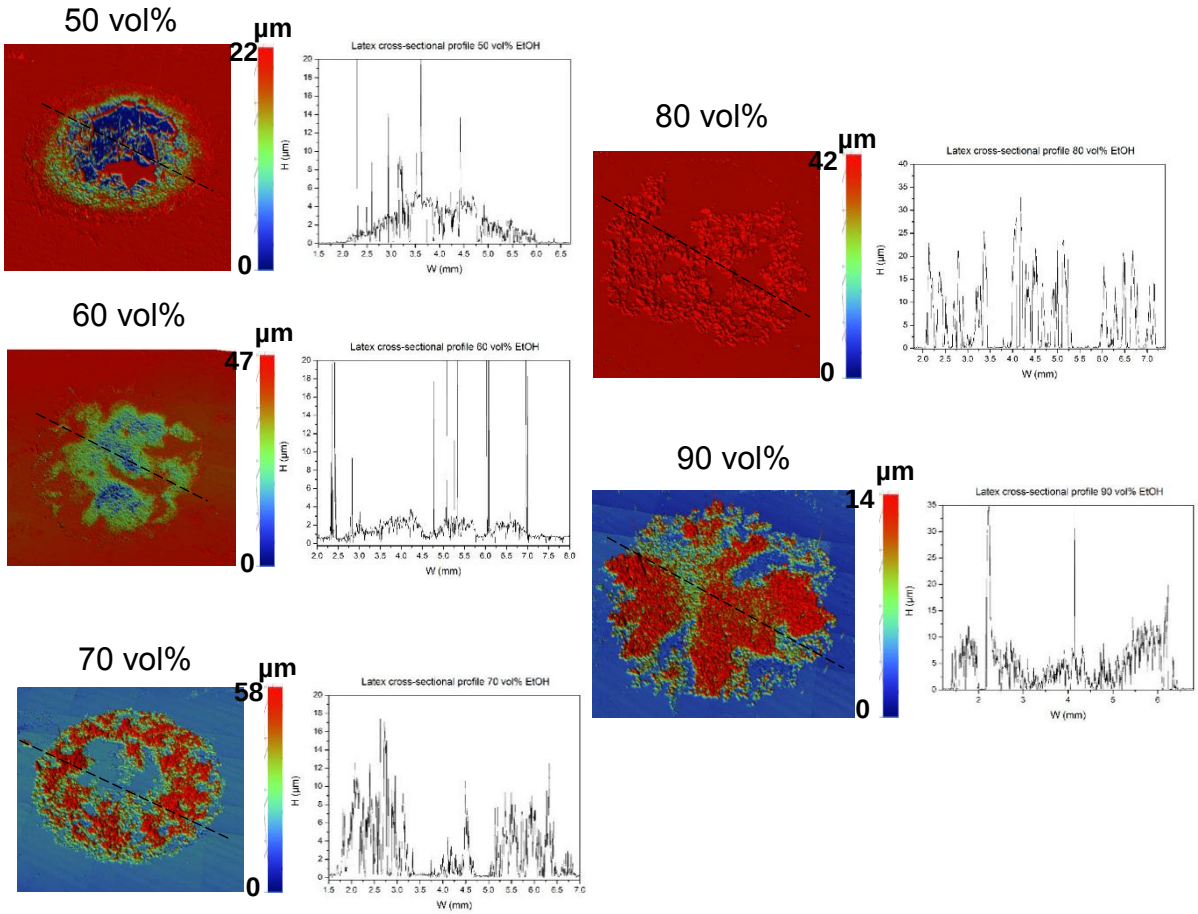

Figure 5-8: Three-dimensional topographical WLI images of PMMA latex dried droplets on silane coated glass slides and corresponding cross-sectional profiles along the black dotted line in different ethanol/water mixtures.

On Figure 5-8, the final dried deposit patterns are presented with their corresponding cross-sectional profiles. The dried residual deposition observed in Figure 5-7 does not seem to be highly dependent on the ethanol concentration. The dried residual patterns are relatively uniform and more so with ethanol concentration increase. From these observed features, despite the droplets following the parameters associated with the “coffee ring effect”, aggregates in the dried deposit were observed in all systems. Previous work has shown that in binary mixtures at C_{EtOH}=90 vol% particle motion are slower (Talbot et al., 2012). At C_{EtOH} above 50 vol%, it was observed that Marangoni glow was not strong enough to completely transport particle toward the droplet centre.

The dried residual deposition patterns result from aggregation of particles and the motions of the aggregates by the droplet internal flows. Indeed, as soon as most of the ethanol evaporates, radial motion carrying particles towards the TPCL will be dominant and this could explain the self-assembly of particles. However, further work could be carried out with even larger size particles has tracer to be able to monitor the nanoparticles motions. It is worth noticing, that ethanol/water mixtures gave relatively uniform deposit regardless of the initial ethanol concentration.

- Particle aggregation process

At the beginning of the experiment, a low amount of light is transmitted through the suspension. However, as more PMMA particles begin to settle/aggregate more light is transmitted through the suspension until a point at which the solution becomes clear and the transmitted light reaches a maximum value 80% for C_{EtOH}=70 vol%.

Indeed, PMMA particles are not stable in this system. In Appendix B, the transmission data are showing that the suspension will aggregate overtime, this is highlighted with the increase in the transmission signal. From these data, it seems that the system which will display the most aggregated particles is at C_{EtOH}= 70 vol%.

From the Stokes sedimentation law, we have determined the diameter of the particles in the different system (we have used the Turbiscan data to determine the settling velocity of the particles in the different ethanol/water mixtures at 26 minutes) and we found that the diameter in all the systems was greater than the particle diameter measured with DLS (see

Chapter 5

Where, η is the solvent viscosity, V_p is the particle settling velocity, $\Delta\rho$ is the density difference between particle and solvent and g is the acceleration of gravity.

Table 5-3).

Stokes sedimentation law (equation 5-9) (Ulmeanu et al., 2009; Sharma et al., 2009):

$$d = \sqrt{\frac{18\eta V_p}{\Delta\rho g}} \qquad (5\text{-}7)$$

Where, η is the solvent viscosity, V_p is the particle settling velocity, $\Delta\rho$ is the density difference between particle and solvent and g is the acceleration of gravity.

Table 5-3: Particle diameter of PMMA particles in the different ethanol/water mixtures with the Stokes sedimentation law and the Turbiscan data.

Concentration in ethanol (vol%)	Particle diameter (µm)
50	10.3
60	34.3
70	131.0
80	110.6
90	106.0

Hence the aggregation of the particles is confirmed. In Milli-Q water, PMMA particles will form “coffee ring effect”; however here we have highlighted that by mixing the particle in different ethanol/water mixtures, this will promote irreversible aggregation of the particle hence the final deposit patterns can be altered. However, the distribution of the particles throughout the surface is not homogeneous.

5.4.2 Evaporative behaviour of Ludox AS-40 ® silica and PMMA latex with added electrolyte

5.4.2.1 Ludox AS-40 ® silica

- Stability of suspensions with added electrolyte

Figure 5-9 shows the effect of monovalent electrolyte NaCl addition to Ludox AS-40 ® silica dispersions (final concentration is at 20000 ppm in different electrolyte concentration). From these data, it can be seen that the addition of NaCl gradually destabilizes the silica suspensions. The critical coagulation concentration (ccc) was found around 220 mM NaCl for our 20 000 ppm suspensions. Therefore, an approximate value of 220 mM NaCl was defined as the ccc. This behaviour is clearly explained by the DLVO theory. Indeed, as thoroughly reviewed in Chapter 2, the electrostatic forces are highly dependent on the amount of electrolyte added to a system. As the electrolyte amount is increased, the ZP decreases while the particle diameter increase due to a thinning of the electrical double layer. Since, the electrical double layer thickness decreases, the repulsive forces are weakened and will no longer overwhelm the attractive Van der Waals forces. The direct consequence of this phenomenon is a destabilisation of the system which is characterised by particles aggregation. From these results, particles aggregation is expected upon solvent evaporation in the deposited droplets. Indeed; as the solvent evaporates from the droplet the local concentration of both the electrolyte and the particles will increase.

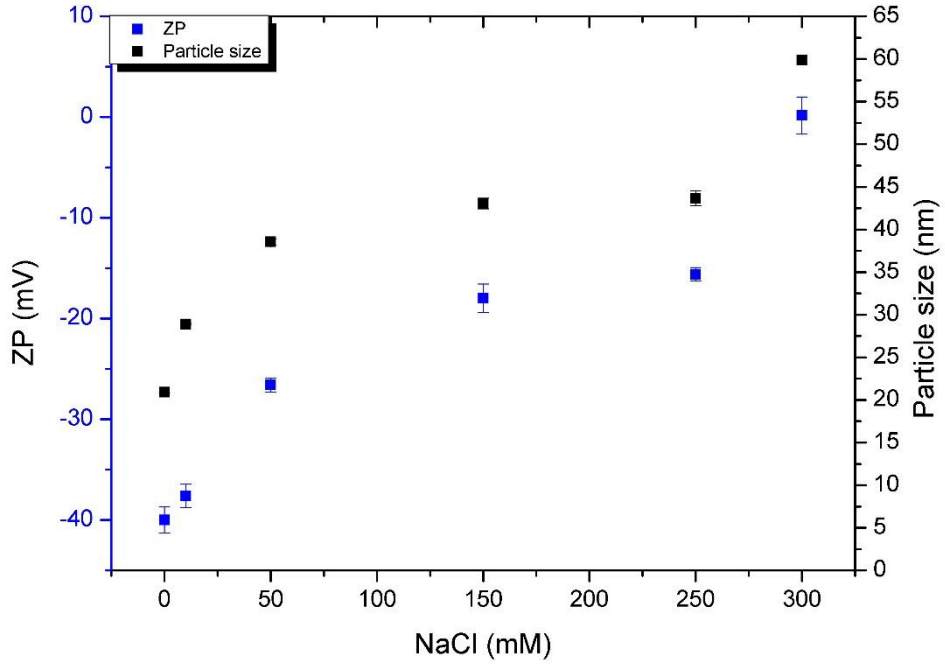

Figure 5-9: Particle size and Zeta-potential (ZP) measurements of Ludox AS-40® at 20 000 ppm as a function of NaCl concentration (C_{NaCl}= 0 to 300 mM).

- Wetting and kinetics study of silica with electrolyte addition droplets

The ensuing droplets are deposited on the uncoated glass slides and the evaporation process was recorded as seen on Figure A-5: Drying sequence of aqueous based Ludox AS-40® droplets on uncoated glass slides as a function of electrolyte concentration (C_{NaCl}= 0 to 300 mM) at different time of droplet lifetime: (1) 0%, (2) 25%, (3) 50%, (4) 75% and (5) 100%. The images were taken from side-view video recordings of the deposition with a contact angle goniometer. The white scale bars represent 1 mm. The red dotted lines represent the initial droplet contact diameter.. From these images, the droplet profile evolution was extracted (see Figure 5-10). It can be seen that the TPCL moves slightly in some cases, more precisely 10 and 250 mM. However, since the variations are weak, the droplets were considered to be pinned throughout the droplet lifetime.

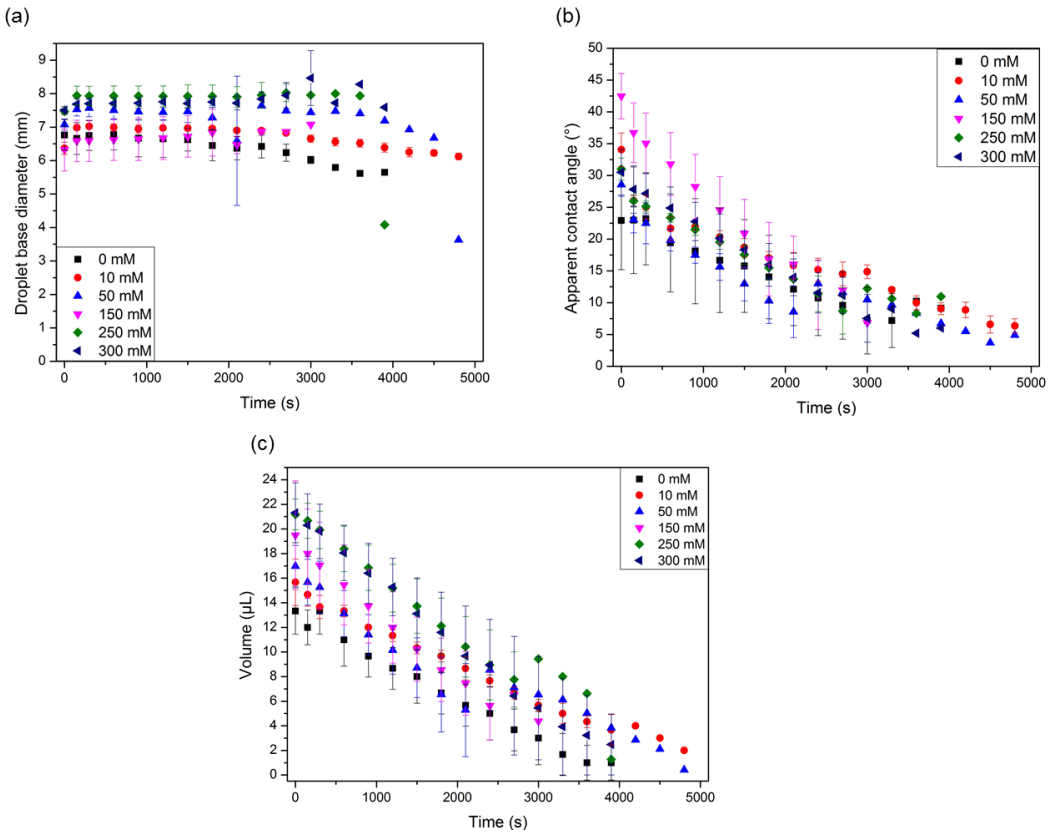

Figure 5-10: Evolution of (a) droplet contact diameter $2r_d$, (b) apparent contact angle θ_{ACA} and (c) droplet volume V with time of Ludox AS-40® (at 20000 ppm) sessile droplets with added electrolyte (C_{NaCl}= 0 to 300 Mm). The droplets were deposited on uncoated glass slides. The evolution was extracted from contact angle goniometer recordings.

From Figure 5-10a, b and c, it can be seen that the increase of electrolyte concentration does not significantly affect the wetting properties of Ludox AS-40® 20000 ppm. For all system, the droplet spreads slightly upon impact which is characterized by a diameter increase. This slight diameter increase is followed by a pinned contact line for all system. The pinned TPCL could be explained by the presence of the nanoparticles and salt. As seen in Chapter 4 and in previous work (Deegan, 2000; Maheshwari et al., 2008; Sangani et al., 2009), the addition of solutes in our case, nanoparticles and salt enhances the pinning effect as such the relative high nanoparticle concentration and the gradual increase of electrolyte concentration will help promote the pinning of the TPCL. The discrepancies towards the end of the drying sequence can be attributed to distortion of the air/water interface and the non-spherical cap shape adopted by the droplets.

As expected by the pinned contact line at all electrolyte concentrations, the apparent contact angle decreases linearly over time (cf. Figure 5-10b). However unlike previously reported data the CCAM is not observed in our system (Soulié et al., 2015).

The pinning of the contact is thus associated with a linear decrease of the volume with time (see Figure 5-10c) as following the Picknett and Bexon expression (see Section 4.3.1). It is worth noting that no trend is observed as a function of nanoparticle concentration. Indeed, on average, the evaporation rate does not seem to be dependent on the electrolyte concentration. This trend is evidence by a longer evaporation rate of Ludox AS-40® 20000 ppm in 50 mM compare to 300 mM.

- Residual dried deposit structure of electrolyte addition system

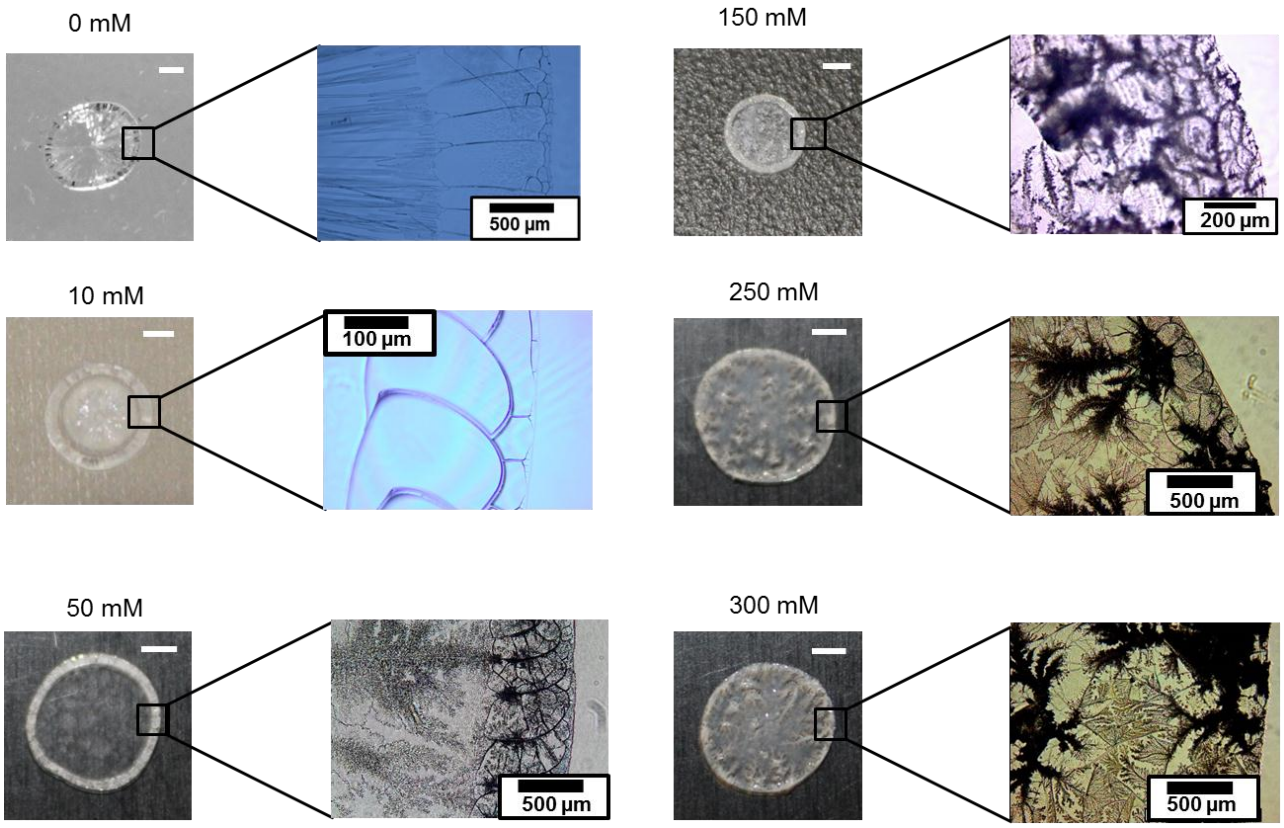

Figure 5-11: Drying patterns photographs of dried micro-droplets of Ludox AS-40® (at 2wt%) and the optical micrographs corresponding to the magnification area inside the black box with different added electrolyte concentration (C_{NaCl}= 0 to 300 mM) on uncoated glass slides. The white scale bars represent 1 mm on all images.

On Figure 5-11, the final deposits and a zoom in of the dried deposit edge are shown. From these experimental observations it can be seen that the electrolyte concentration seems to influence and affect the final deposit patterns. Indeed, from 0 to 150 mM a clear CRE is observed whereas at 250 mM and 300 mM it seems that the deposit is a bit more uniform with salt crystals scattered within the deposit structure. It is worth noticing that the dried deposits structure difference is clearly seen for a salt concentration above the ccc. Contrary to previous data, a dendritic pattern was observed for concentration above C_{NaCl}= 50 mM (previous study used, a different monovalent salt KCl (Okubo et al., 2009)). It is also worth noticing that despite the electrolyte concentration being above the ccc and the expected aggregates are not clearly seen in the structure. From the dark structures present in the deposit and most notable from 150 mM, we can suppose that larger aggregates are formed. In this experiment, aggregates are formed as the solvent evaporates. Some aggregates are then transported towards the droplet periphery by capillary flow (Gorr et al., 2013). However, when the initial concentration of NaCl is increased, the aggregates and salt crystals will form earlier during the drying process. Hence, the formation of regular patterns could occur. This phenomenon should be characterised by a decrease of the deposit edge width as seen previously however in our experiments the edge width does not vary significantly with the electrolyte concentration. Indeed, the edge width is the same at 10,50 and 300 mM (0.5 mm) and the edge width was found at 0.6 mm at 150 mM and 0.9 mm at 250 mM.

The electrolyte addition in the suspensions favours the self-assembly of the nanoparticles. Indeed, due to the electrolyte addition as seen on Figure 5-15 according to the DLVO theory the electrical double layer will decrease, thus despite the same charge of the particles, the aggregation will be possible.

However, unlike previously reported results no stick-slip motion of the TPCL was observed hence several concentric rings were not observed in the final deposit pattern (Chen and Mohamed, 2010).

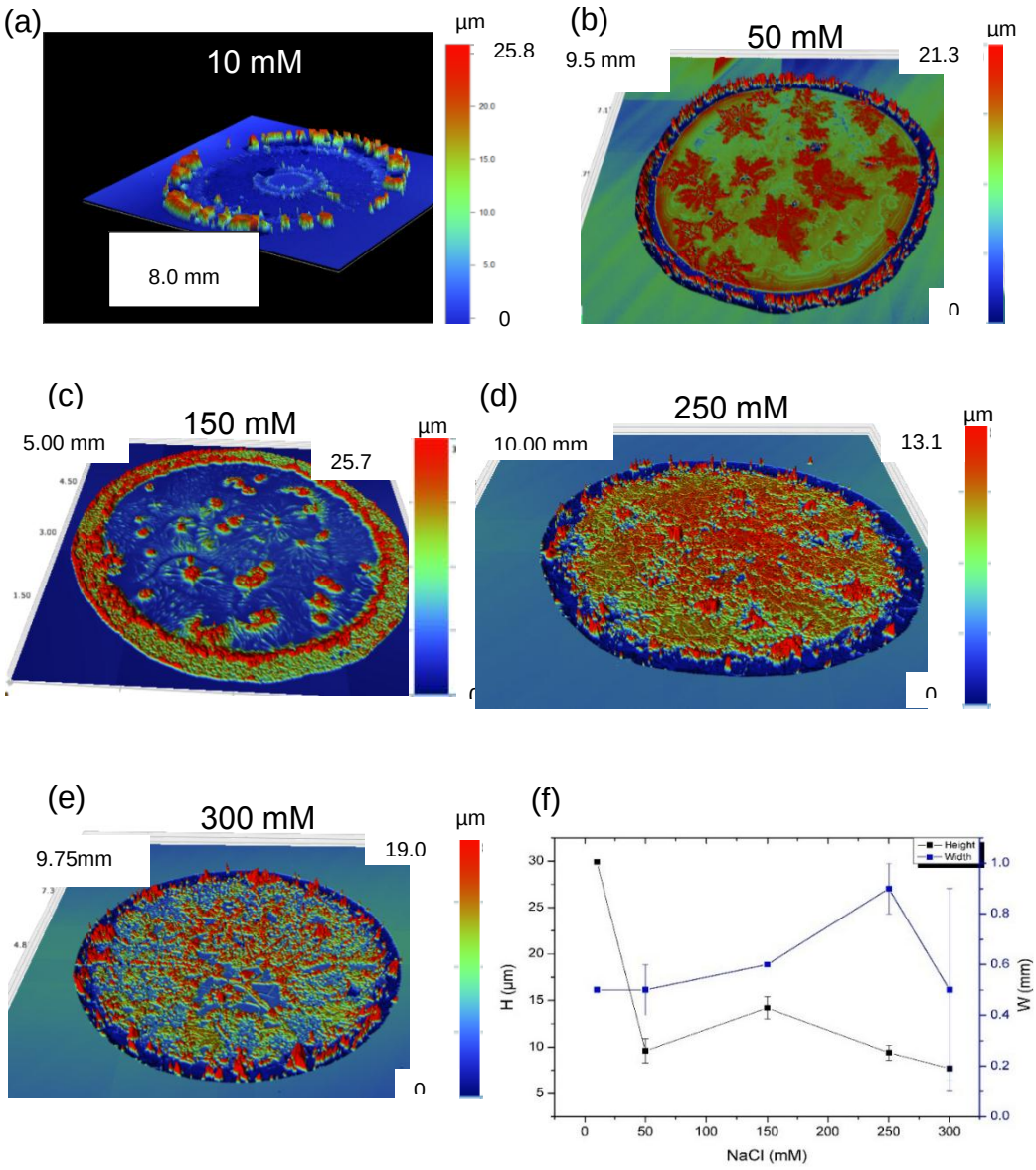

Figure 5-12:Three-dimensional topographical WLI images of Ludox AS-40® dried droplets on uncoated glass slides at 20 000 ppm as a function of NaCl concentration: (a) 10 mM, (b) 50 mM, (c) 150 mM (d) 250 mM, (e) 300 mM and (d) chart represents the influence of NaCl concentration on the dried deposits edges features (height and width).

5.4.2.2 PMMA latex with added electrolyte

- Wetting properties

A pinned TPCL is observed throughout the drying process for all system (see Figure 5-13a) however the final deposit patterns observed was not a ring-like deposit. As expected with a pinned TPCL, the θ_{ACA} observed a linear decrease with time. As the deposition were done on silane coated glass slides the initial θ_{ACA} remains similar for all the system (θ_{ACA} = 89 ± 2.9 °) The

volume variation was also seen to decrease linearly with time in all cases (see Figure 5-13c).

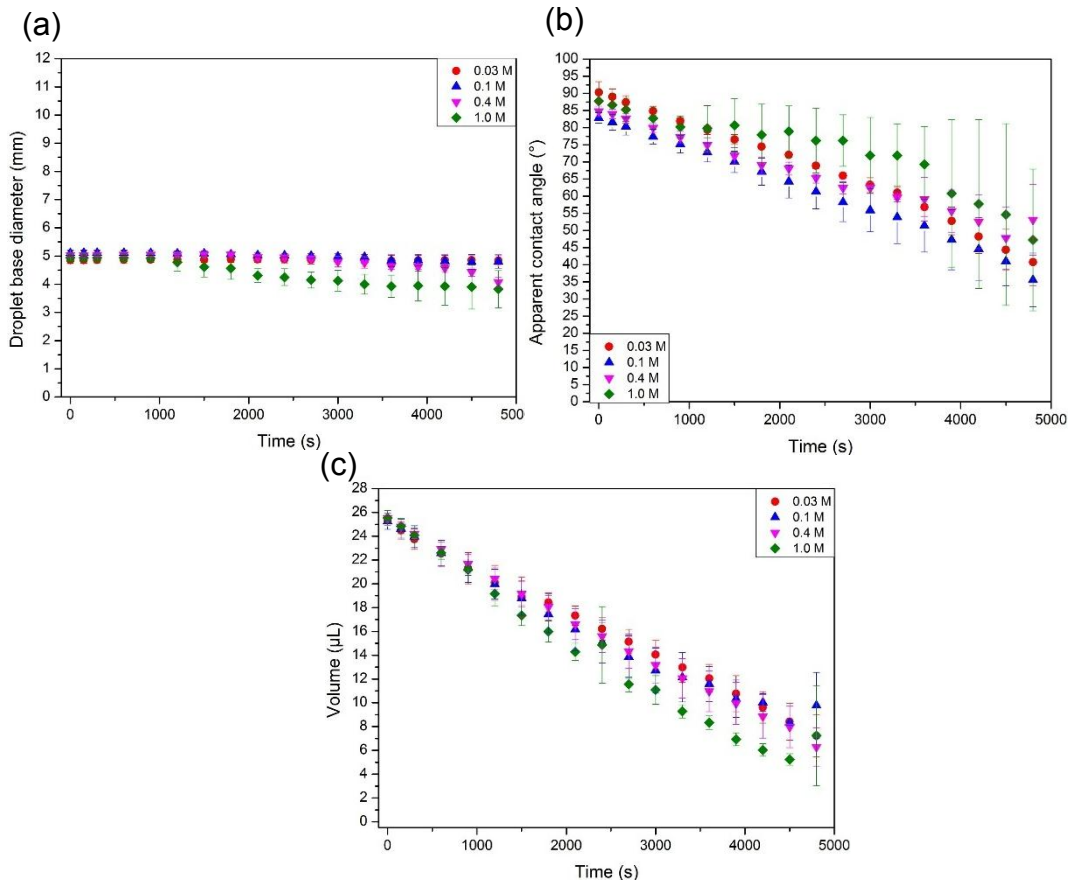

Figure 5-13: Evolution of (a) droplet contact diameter $2r_d$, (b) apparent contact angle θ_{ACA} and (c) volume V with time of PMMA latex at 0.4 wt% sessile droplets with added electrolyte (C_{NaCl}= 0.03 to 1.0 M). the droplets were deposited on silane coated glass slides. The different evolutions were extracted from contact angle goniometer recordings.

- Sedimentation characteristics

In Figure A-13, the backscattered profiles of the PMMA latex with added electrolyte (C_{NaCl}= 0.03 to 1.0 M) is presented. It can be seen, that the backscattered values increase along with time in all the added electrolyte concentration. From the Stokes sedimentation law (see equation 5-9) we have determined the particle diameter and it is much higher than the measured PMMA particles which is consistent with an aggregation within the system (see Table 5-4).

Table 5-4: Particle diameter of PMMA particles with electrolyte addition using the Stokes sedimentation law and the Turbiscan data.

Electrolyte concentration (M)	Calculated particle diameter (mm)
0.03	1.1 ± 0.7
0.1	2.7 ± 0.1
0.4	2.5 ± 0.1
1.0	2.7 ± 0.1

From the calculation of the particle diameter, it can be seen that sedimentation will occur within the droplet during the evaporation. Hence, the addition of electrolyte to the suspension lead to aggregation of the particles in the droplet.

- Residual dried deposit patterns

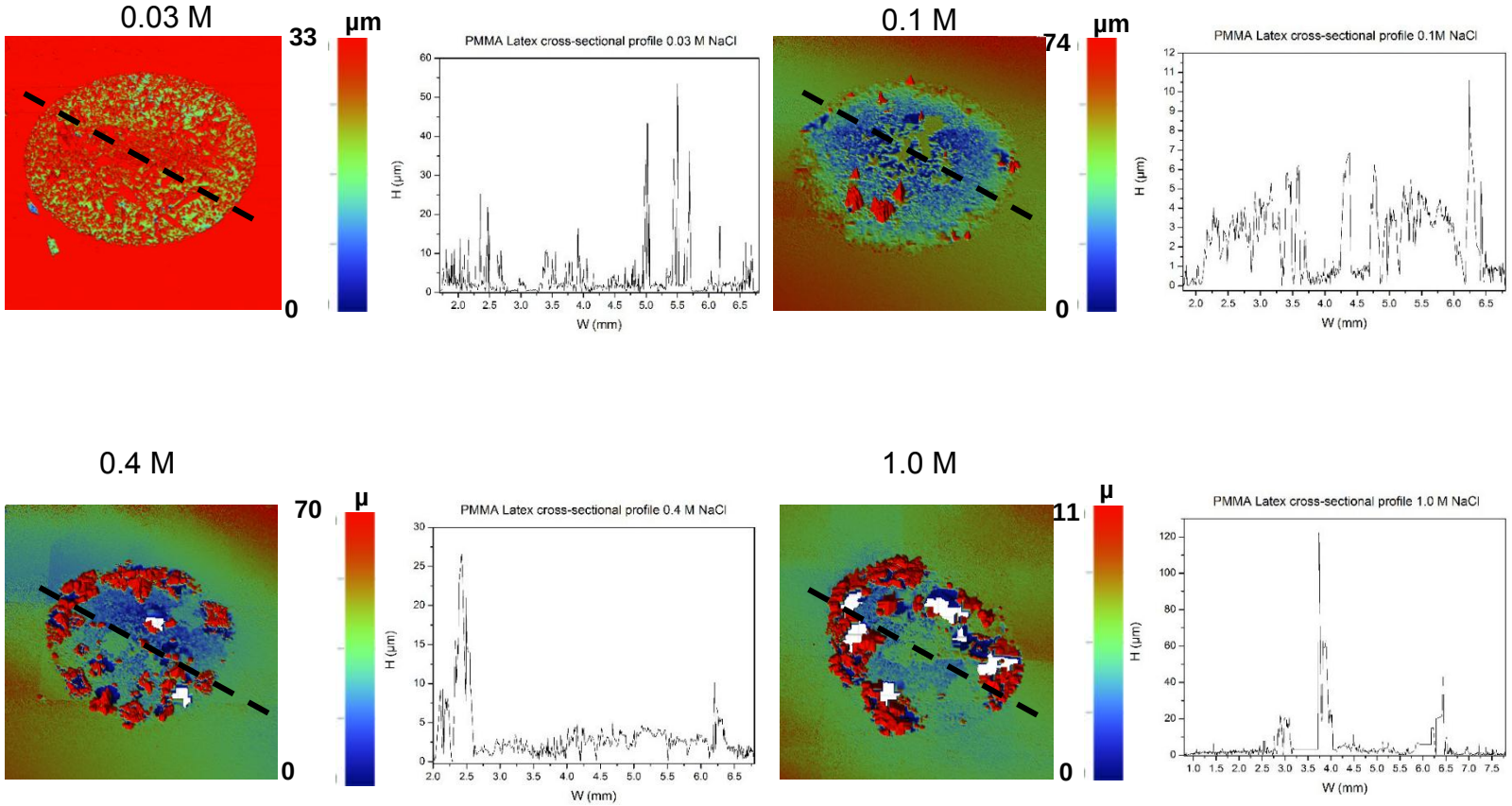

Figure 5-14: Three-dimensional topographical WLI images of dried droplets of PMMA latex (at 0.4 wt%) on silane coated glass slides and corresponding cross-sectional profiles along the black dotted line with added electrolyte (C_{NaCl}= 0.03 to 1.0 M).

On Figure 5-14, the three-dimensional topographical images of the dried PMMA latex droplets are reported along with their associated cross-sectional profiles. It can be seen that the particles are aggregated in the final structure as expected from our sedimentation predictions. Also, the final deposit is not homogeneous throughout the surface, hence we hypothesized that due to the aggregation of the particles it is harder for the aggregated to be carried towards the TPCL.

In summary, from a seemingly similar evaporative behaviour (pinned TPCL, decreasing θ_{ACA} and decreasing volume V) very different final deposit patterns can be observed and generated. However, the two sets of particles system were deposited on uncoated and coated substrates.

In the next subsection, Ludox AS-40® with added anionic surfactant has been investigated. Indeed; the addition of surfactant in droplets has shown great promises in hindering the “coffee ring effect” (Still et al., 2012; Sempels et al., 2013).

5.4.3 Evaporative behaviour of Ludox AS-40 ® silica with added anionic surfactant

- Stability and adsorption of surfactant

We investigated the effects of surfactants in Ludox AS-40® nanofluids by varying its concentration below and above it cmc from C_{SDS}=4 to 30 mM.

In order to identify the surfactant/particle interaction, we measured the zeta-potential ζ of their mixtures (Figure 5-15). The surfactant concentration was selected at below and above the cmc. Hence, the contribution to zeta-potential above the cmc can come from both particles and surfactant whereas below cmc we can consider that the main contribution arises from the particle. For surfactant free system, we measured ζ= -37.6 ± 1.3 mV (Figure 5-15), which indicate a stabilized suspension due to negative charge at the particle surface. The zeta-potential did not significantly varied with addition of SDS, this suggest that the adsorption is negligible. This was an expected behaviour since SDS and Ludox AS-40® are both negatively charged, thus electrostatic repulsion are at play between particle and SDS polar head.

The size switches from d_{Lud}~ 21 nm in pure MilliQ-water to 36 nm between C_{SDS}= 7.5 and 15 mM to 47 nm at 30 mM, this size increase could be explained by the adsorption of SDS onto the Ludox-AS® as previously observed (Li and Ishiguro, 2016).

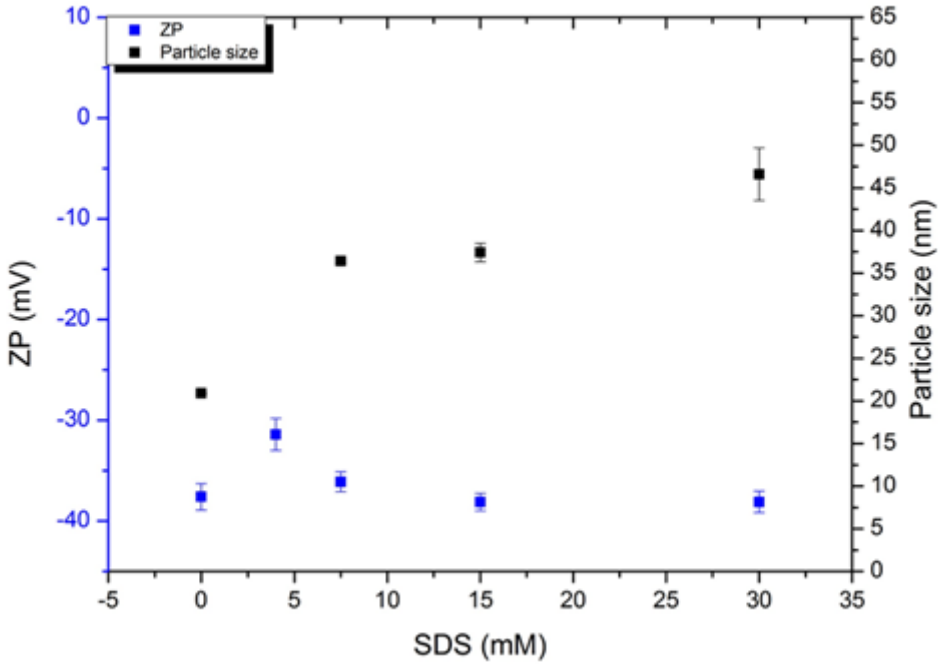

Figure 5-15: Particle size and zeta-potential (ZP) of aqueous based Ludox AS-40® suspensions with different added SDS concentration (C_{SDS}= 0 to 30 mM).

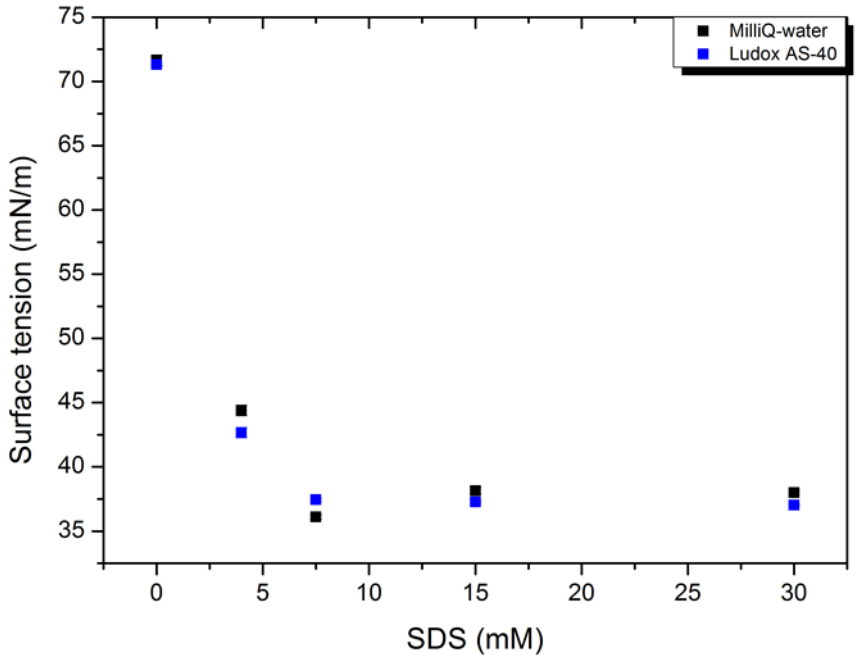

Figure 5-16: Surface tensions measurements of aqueous based Ludox-AS® suspensions (C_{Lud}= 2 wt% in final suspensions) with and without addition of SDS (C_{SDS}= 0 to 30 mM).

The pure Ludox-AS® in aqueous suspension is not surface active, the initial surface tension is at 71.1 mN/m which is close to the experimental surface tension of pure MilliQ-water at 70.9 mN/m at 25°C. When SDS is added to the system the surface tension decreases dramatically to reach ~ 37.3 mN/m as seen in Figure 5-16. However, close and above the cmc the surface tension variation is negligible. Hence, the surface tension is nearly constant and consistent with a pure system of SDS considering that the critical micelle concentration for SDS is at 8.3 mM. This behaviour can be explained by saturation of the liquid-vapour interface of the droplet especially when concentration of SDS is above cmc.

- Wetting and kinetics study of Ludox AS-40 ® silica with surfactant addition

In order to examine the influence of surfactant concentration, the wetting property of a drop containing Ludox-AS® at C_{Lud}= 2 wt% while varying SDS concentration was investigated.

On the drying droplet sequence it can be seen that the droplet was pinned without any surfactant addition. The droplet contact diameter was seen to increase with the presence of SDS at 7.5 mM, at 15 mM little variation of the TPCL is seen which can be associated with a pinned TPCL. Finally, at 30 mM the droplet contact variation is similar to a stick-slip motion of the TPCL (see Figure 5-17 and Figure A-6). It is our understanding, that the droplets contact diameter increased due to the negative charge of both the SDS and the glass slide substrate, this same charge causes the contact radius not to be pinned (Anyfantakis et al., 2015). However, the discrepancies could arise from the complete spreading of the droplet over the substrate.

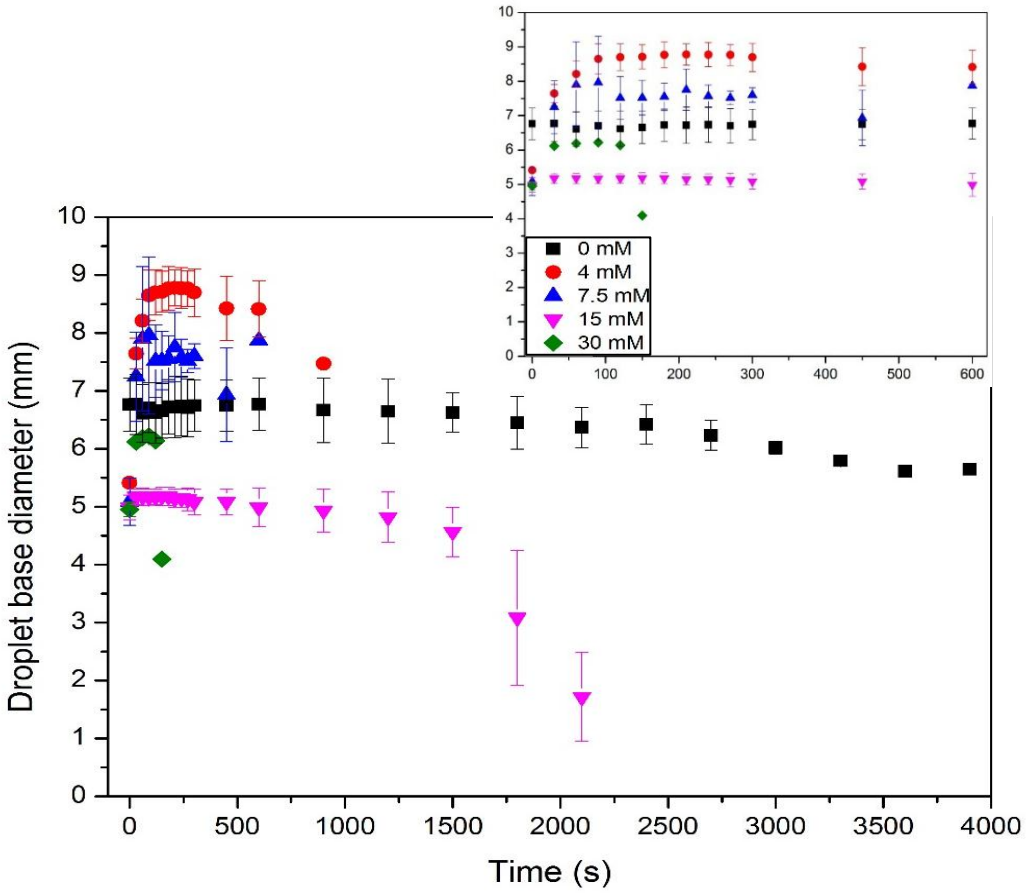

Figure 5-17: Evolution of droplet contact diameter $2r_d$ of Ludox AS-40® at 2 wt% droplets with different added SDS concentration (C_{SDS}= 0 to 30 mM) with time on the entire droplet lifetime and a zoom in between 0 to 600 s. The droplets were deposited on uncoated glass slides. The evolution was extracted from contact angle goniometer recordings.

During, drying process, solvent evaporates hence local concentration of both surfactant and nanoparticles increase.

On Figure 5-18 the evolution of the θ_{ACA} with time can be seen. From this experimental data it is seen that θ_{ACA} variation is not linear nor a function of the surfactant addition. Indeed, the initial θ_{ACA} of Ludox AS-40® with 15 mM is higher compared to the other SDS added concentration while 30 mM has the lowest initial θ_{ACA}. The θ_{ACA} is also seen to decrease gradually and faster at 15 and 30 mM compared to 4 mM. The evaporation rate difference is singular for 15 and 30 mM SDS as both are above the SDS cmc (cmc= 8.3 mM (Still et al., 2012), therefore the droplet surface should be saturated by the surfactant hence the evaporative behaviour should be the constant; however this is not our observation compare to previous work (Still et al., 2012).These discrepancies could be explained by the adsorption of the surfactant at the particle interface. Yet, even with this phenomenon, the different behaviour for the two concentrations above the cmc is unexpected. Previous study, suggested the saturation of the air/water interface by the surfactant and the local surfactant concentration difference within the droplet will lead to a surface tension gradient thus creating a Marangoni flow (Still et al., 2012). In fact, the presence of SDS at the liquid-vapour interface generate a strong However, the presence of a Marangoni flow within our system is unsure.

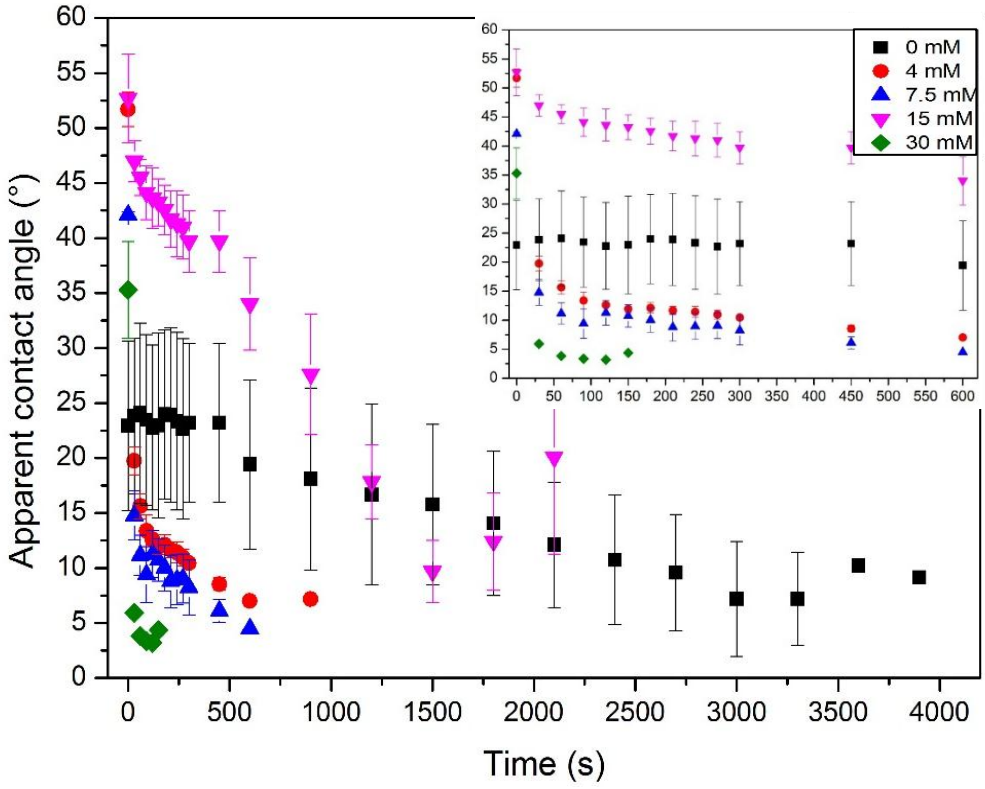

Figure 5-18: Evolution of apparent contact angle θ_{ACA} of Ludox AS-40® at 2wt% as with different added SDS concentration (C_{SDS}= 0 to 30 mM) with time on the entire droplet lifetime and a zoom in between 0 to 600 s. The droplets were deposited on uncoated glass slides. The evolution was extracted from contact angle goniometer recordings.

On Figure 5-19a, the evolution of the volume V is characterised. It can be seen, that the volume does not fluctuates with the surfactant addition. Indeed, the evaporation rate is smaller for the SDS concentration above the cmc (see Table 5-5). The evaporation rate was extracted from the Figure 5-19.

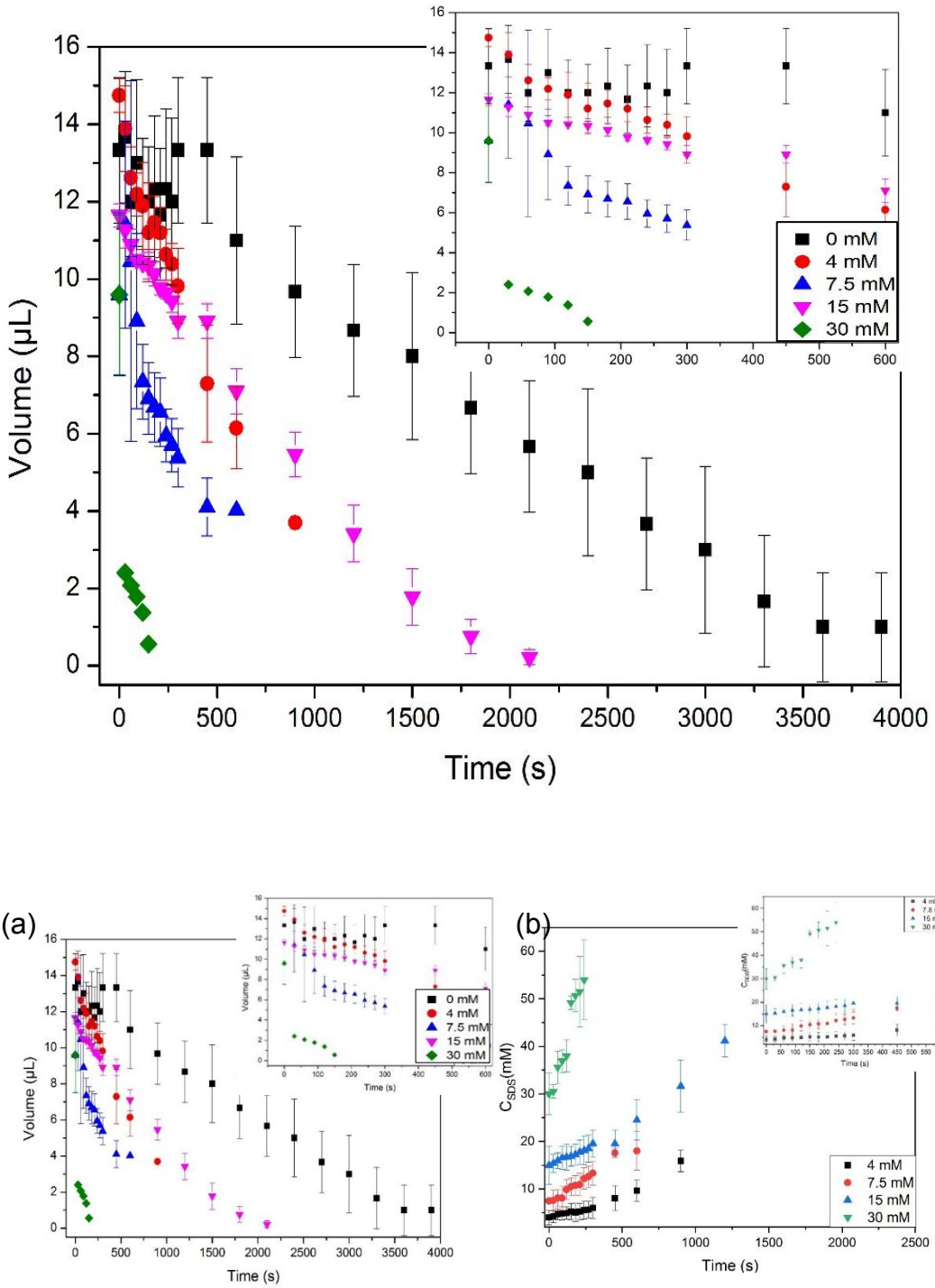

Figure 5-19: (a) Evolution of volume V of Ludox AS-40® at 2wt% with different added SDS concentration (C_{SDS}= 0 to 30 mM) with time on the entire droplet lifetime and a zoom in between 0 to 600 s. The droplets were deposited on uncoated glass slides. The evolution was extracted from contact angle goniometer recordings.(b) Evolution of SDS local concentration in the micro-droplets with time in the different initial concentration C_{SDS}= 4 to 30 mM.

Table 5-5: Evaporation rate of Ludox AS-40® at 2 wt% with different added SDS concentration CSDS= 4 to 30 mM.

SDS concentration (mM)	Evaporation rate (10^{-3}µL/s)
4	12.2
7.5	12.2
15	6.5
30	4.6

However, the Ludox AS-40® sessile droplets with added surfactant spread highly on the glass substrates, hence the droplet is not assuming a spherical cap shape, thus the determination of the droplet contact diameter, apparent contact angle and volume are more challenging.

- Residual dried deposit strucutres

The interferometer allows us to explore the topographical features of the whole dried deposit in the different system. On Figure 5-20, the two-dimensional topographical image and the corresponding optical micrographs zoom in can be seen. The final deposit patterns are complex and several concentric rings are observed at 7.5 and 15 mM while a de-pinning of the TPCL was not observed during the analysis of the droplet evaporative behaviour. From, the optical micrographs, it can be seen that the addition of SDS seems to alter the final deposit patterns and the presence of the cracks within the dried deposit structure.

The addition of SDS to the system decrease the cracks spacing cf. Figure 5-21b. The addition of SDS seems to affect the stress formation during the drying process hence the final dried deposit structure. The study of the wetting properties was not sufficient to corroborate the dried deposit structure. Especially at 7.5 and 15 mM, a de-pinning effect is not observed which could explain the formation of several concentric rings in the dried deposit structure. When the droplet is pinned unless the system is surfactant free, a coffee ring stain is not observed upon solvent evaporation. The difference in the dried deposit structure could be explain with the generation of a depletion flocculation in the system at concentration above the cmc. The attenuation of cracks patterns could be explained by a faster drying of the

suspensions which could prevent the formation of tensile stress toward the end of the evaporation. Thus, the observation of cracks patterns at the edges at 30 mM and the absence of cracks in the centre of the drop compare to radial cracks towards the centre at the other concentration (7.5 and 15 mM).

Previous work, has been done to explain the cracks presence in dried deposit (Lee and Routh, 2004) and the theoretical assumption can be seen in 5.3.2. In order, to evaluate the effect of the SDS on the cracks patterns, the cracks spacing have been determined from the optical micrographs pictures and the collapse of the crack spacing versus the hydrodynamic scaling has been done. In our case, the film thickness has been determined as the apex height in the edge of the dried deposit patterns in the different added SDS concentration as shown on Figure 5-21a. The cracks spacing appeared to be dependent on the SDS concentration see Figure 5-21b.

Similarly, to previous work, the scaling of the crack spacing with the film thickness was evaluated (Lee and Routh, 2004). A partial scaling is obtained, the dependence on the SDS concentration close and above the cmc is possible.

The collapse of data from Figure 5-21 is according to the following power law:

$$\frac{y}{X} = 3.10^{-4} P_{cap}^{-1.6} \qquad (5\text{-}8)$$

On Figure 5-19b, the evolution of the local SDS concentration is plotted. This plot allows us to determine how long after the start of the drying process the cmc is matched for the lower concentration. The cmc is matched after 450 seconds for C_{SDS} =4 mM and after 120 seconds for C_{SDS}= 7.5 mM. At the cmc, the SDS is saturating the micro-droplets air/water interface. Since, the droplet composition is similar once the cmc is matched in all droplet, further investigation need to be undertaken to help better understand the significant different residual dried deposit structures.

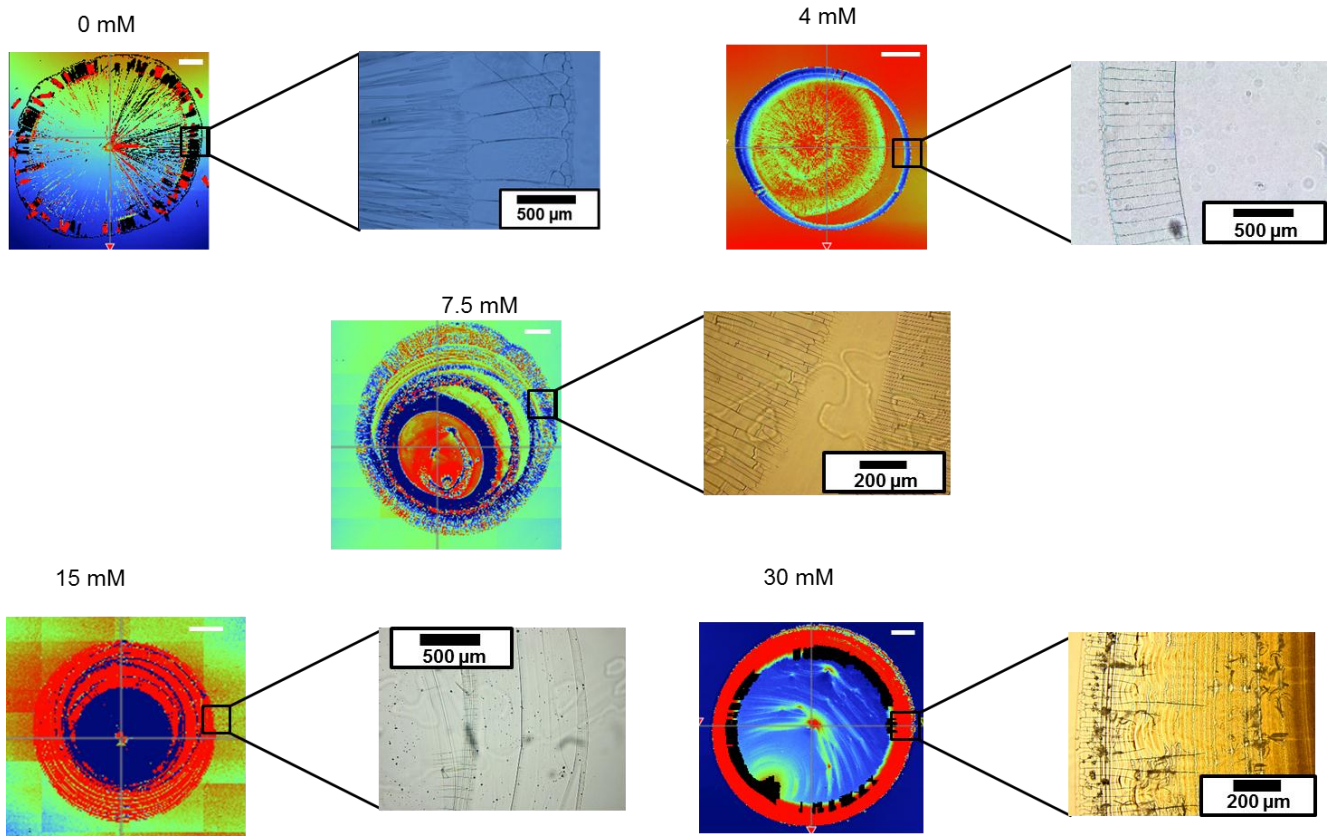

Figure 5-20: Two-dimensional WLI images of dried deposit of Ludox AS-40® silica with different added SDS concentration (C_{SDS}= 0 to 30 mM) and optical micrographs corresponding to the magnification of the area inside the black box on uncoated glass slides. The white scale bars represent 1 mm on all images.

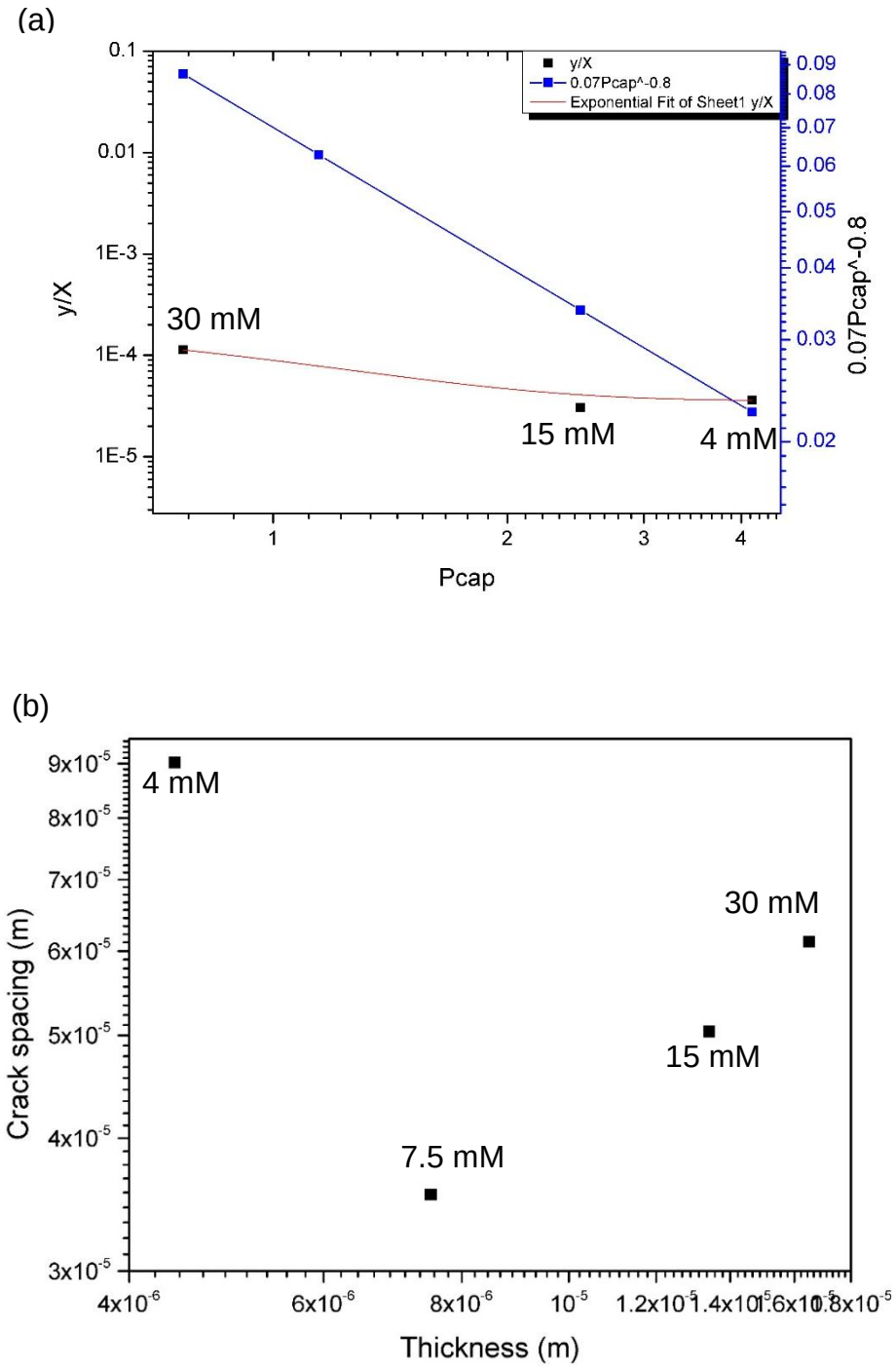

Figure 5-21: Data for aqueous based Ludox AS-40® suspensions with different added SDS concentration (C_{SDS}= 0 to 30 mM) (a) collapse of crack spacing data with hydrodynamic scaling and (b) cracks spacing as a function of film thickness.

This give that the crack spacing scales with the dried film thickness to the power of 1.6, the evaporation to the power of 0.8, and the particle size to the power of 0.6.

5.5 Summary

In this Chapter, the evaporative behaviour and subsequent dried deposit structure of spherical Ludox AS-40® and PMMA polymeric nanoparticles were investigated on silane coated and uncoated glass slides.

For the first system, aqueous Ludox AS-40® silica (C_{Lud}= 2 wt%) in binary solvent mixtures (C_{EtOH}= 50 to 90 vol%) deposited on silane coated glass slides, the evaporative behaviour was influenced by the ethanol content. However, the dried deposit patterns were found to be irregular in appearance and the cracks patterns seemed to increase with the increase of the ethanol content. Also, with this system the final deposit is rather complex, and the evaporative behaviour does not allow us to confirm and infirm clearly the particle motion within the droplet. Further work could thus be explored to investigate the importance of ethanol concentration for particle laden droplet. To this effect, a new experimental method comprised of a top view camera could be used to monitor the evaporation process. This new camera should have to be assembled with an infrared set up, which would allow us to also map the thermal variation of the droplet surface.

The second system consists of PMMA polymeric particles at a lower initial concentration compared to the Ludox AS-40® (C_{Lat}= 4000 ppm). The evaporation and wetting properties of ethanol/water binary of PMMA nanoparticles sessile droplets deposited on silane coated substrates were investigated. In this system, the particles aggregate within the droplet. It is our understanding, that due to the size of the aggregate, the aggregates are not transported towards the TPCL by capillary flow. Hence, forming the “coffee ring effect” is prevented, despite the pinned TPCL and evaporating solvent. The variations in apparent contact angle, droplet contact diameter and volumes could be divided in three stages. In the initial stage, the evaporation rate and wetting behaviours are ethanol-dominated, this is more pronounced at higher C_{EtOH}. Whereas, at the later stage of the evaporation

process when most of ethanol has evaporated, it is water-dominated with particles carried by outward flow. Although, PMMA nanoparticles aggregated rapidly as seen by Stokes-Einstein equation. The most significant difference between other binary mixtures solvent stem from the two stages observed. Droplet contact diameter remains pinned roughly for the entire evaporation process when the initial ethanol concentration increase. This is more pronounced when the mixture is above C_{EtOH}=50 vol%. The variations characteristics are dictated by the droplet volume as well as the depinning of the droplet contact diameter. The fact that particle aggregates rapidly, it is assumed that particles deviate from the internal flow and are not transported throughout the droplet periphery. Although, to clarify the mechanism a new set up and tracer particles should be used such as larger PMMA nanoparticles.

Such patterns, a more uniform nanoparticles distribution have not been previously observed at these ethanol concentrations. It implies that the addition of ethanol to the base fluid does not seem to alter greatly the distribution of PMMA nanoparticles from C_{EtOH}=50 vol%

When, electrolyte (C_{NaCl}= 0 to 300 mM) were added in the system, for Ludox AS-40® silica, dendritic structure was observed within the dried deposit patterns. The amount of salt in the system influenced greatly the final deposit patterns.

For the PMMA polymeric particles, the final deposit patterns observed was similar to the one observed in the binary solvent mixtures. Indeed, an irreversible aggregation occurred during the evaporation process. Similarly, it is thought that due to the size of the aggregates, the aggregate can deviate from the stream within the droplet hence avoid the formation of the “coffee ring effect” upon total solvent evaporation.

Finally, when surfactant was added to the Ludox AS-40® system above and below the surfactant cmc various patterns arose. No pinning of the TPCL was observed unlike in previous work. A fast-complete wetting of substrate was

monitored and it seem to become faster with the increase of SDS concentration. Although, several concentric rings were observed in the final dried deposit, the evaporative behaviour did not display any clear “stick-slip” motion behaviour. Also, the presence of surfactant seems to affect the cracks observed in the final dried deposit pattern. From our experimental observation, it seems that the gradual increase of surfactant concentration leads to less pronounce cracks patterns. This is a novel explanation for the observed decrease of cracks spacing and the scaling collapses experimental data for silica particles with added anionic surfactant. Further work could be conducted to understand the internal flow in the drop and the formation of several concentric rings, particularly as the droplet evaporates the local concentration will be above the cmc regardless of the initial surfactant concentration.

Chapter 6
Study of disk-like clay Laponite sessile droplets on solid surfaces: formation of film deposit by sol-gel transition and complex structure with electrolyte addition

6.1 Introduction

In the previous chapters, we have investigated the drying behaviour and ensuing final microstructures patterns of spherical nanoparticles suspensions (Ludox AS-40® silica nanoparticles and PMMA latex nanoparticles). From these investigations, it was observed that the change of the suspensions characteristics can lead to the formation of different patterns ranging from ring-like stains (due to the “coffee ring effect” to several circular rings (due to stick-slip motion of the three phase contact line and dendritic structure due to the presence of electrolyte). This paramount knowledge gain could be used to tailor suspensions composition in order to obtain specific particles distribution upon solvent evaporation for different industrial applications.

To further our knowledge, a new particle system was investigated a synthetic disk-like clay Laponite nanoparticles (these particles previously introduced in Chapter 3 are characterized with a thickness of about 1 nm and a diameter of 25-30 nm (Li et al., 2009)). Laponite nanoparticles were selected as it has a wide range of interesting properties and can be used to manufacture electrically conductive, transparent, antistatic and barrier coatings, (Holley et al., 1995; Majumdar et al., 1999; Dundigalla et al., 2005) or as an extra coating layer to enhance image durability and quality for inkjet printing processes (Rao et al., 2005), (Majumdar et al., 2003).

Also, Laponite nanoparticles when dispersed in water exhibit heterogeneous charge. Indeed, the particles edges are positively charged hence making it pH-dependent while their faces are negatively charge (Thompson and Butterworth, 1992), (Jatav and Joshi, 2014). The electrostatic interaction between Laponite particles lead to a complex ageing dynamics along with several non-ergodic arrested states (Kegel and Lekkerkerker, 2011), (Ruzicka and Zaccarelli, 2011). This singular phase diagrams (Mourchid et al., 1995; Mourchid et al., 1998; Bonn et al., 1999; Levitz et al., 2000; Ruzicka et al., 2004; Mongondry et al., 2005; Ruzicka et al., 2006; Cummins, 2007; Jabbari-Farouji, Mizuno, et al., 2008; Jabbari-Farouji, Tanaka, et al., 2008; Ruzicka et al., 2011; Ruzicka and Zaccarelli, 2011; Kegel and Lekkerkerker, 2011) have been thoroughly studied recently along with the complex ageing dynamics (Mourchid and Levitz, 1998; Saunders et al., 1999; Knaebel et al., 2000; Ruzicka et al., 2007; Joshi et al., 2008; Shahin and Joshi, 2012; Zulian et al., 2014; Angelini et al., 2014; Pek-Ing and Yee-Kwong, 2015). From these successive works, the following main states have been identified in clear dependence with the initial Laponite concentration in weight

(C_{Lap}) (Kegel and Lekkerkerker, 2011; Ruzicka and Zaccarelli, 2011; Ruzicka et al., 2011):

- Mixed state of separated sol and gel phases C_{Lap}<1 wt%
- Stable gel, equilibrium gel 1 wt% < C_{Lap} < 2wt%
- Repulsive glass or Wigner glass 2wt% <C_{Lap} < 3wt%
- Nematic gel C_{Lap}>3 wt%

Thus, the initial amount of Laponite concentration C_{Lap} can affect several parameters such as viscosity (Shahin and Joshi, 2012), apparent surface tension (Chen et al., 2011) and effective diffusion coefficient (Petit et al., 2009). Furthermore, the ageing kinetics of Laponite based nanofluids are also dependent on the initial concentration of Laponite (Ruzicka et al., 2010; Ruzicka et al., 2011; Kegel and Lekkerkerker, 2011). During the ageing of aqueous based Laponite nanofluids due to its heterogeneous a “house of cards” structure is expected. This structure is held together by the edge-to-face bonds (commonly referred to as T-bonds) and the particles platelets are paired in parallel and partially overlapping (usually known as PPO) configurations. The T-bonds are resulting from the interactions of the negatively charged face with the positively charged edges respectively, and this association lead the platelets to assemble into T-bonded networks and aggregates. The ageing of these aqueous nanofluids is also paired up with the evolution overtime of the viscosity, elastic modulus, electrical conductivity and effective diffusion coefficient among several characteristics of aqueous based Laponite suspensions (Rich et al., 2011; Shahin and Joshi, 2012).

Due to its properties, during drying of sessile droplets of aqueous based Laponite, the gelling phenomena could play a paramount role, reflecting the concentration changes overtime of Laponite, its ageing behaviour and its drying-incited gelling. However, despite these interesting characteristics, to the best of our knowledge little to no work has investigated the drying behaviour of sessile droplets of Laponite based nanofluids in different systems and their following complex final deposit patterns upon complete solvent evaporation (Lebovka et al., 2014), (Talbot et al., 2015), (Hodges et al., 2010). In these previous studies, the final dried deposit structure was explained by the collapse of the Laponite particle network at the edge of the deposit (Hodges et al., 2010). Other structure were explained by a sol-gel transition occurring while increasing the Laponite particles concentration or its local particles concentration increase which are believed to suppress radial flow and hence promote formation of a uniform deposit (Lebovka et al., 2014; Talbot et al., 2015).

In this present chapter, a systematic analysis of the evaporative behaviour of disk-like Laponite based nanofluids in different composition was carried out. During the

evaporation of these sessile droplets, the probability of gelling within the droplet is considered. To begin with, similarly to previous studies an initial investigation of the complex patterns formation of Laponite as a function of concentration was done (Hodges et al., 2010; Lebovka et al., 2014). From the knowledge obtained during this initial comparative study, we further our enquiries by fixing the initial aqueous based Laponite nanofluids concentration (at low initial concentration C_{Lap}=0.1 wt%) and modifying the composition of the aqueous phase in order to observe the effect on the final dried deposits patterns. As the sol-gel transition has been previously efficient in suppressing radial flow and promoting the formation of a uniform deposit (Lebovka et al., 2014). A comparison is drawn between the different systems to identify the more effective one able to suppress ring-like stains.

6.2 Materials and experimental methods

6.2.1 Suspensions preparation and characterization

The experiments investigated aqueous suspensions of colloidal Laponite RD (Rockwood Additives, UK) a synthesized clay powder found to be a disk-like nanoparticles, negatively charged on the face surfaces and positively charge on the edges (Jatav and Joshi, 2014). These particles are commonly found to have a thickness about 1 nm and a diameter between 25-30 nm (Li et al., 2009). Its synthetic chemical composition is 59.5 wt% Si_2O, 27.5 wt% MgO, 2.8 wt% Li_2O and 0.7% Na_2O and it density is found at 2.53 $g.cm^{-3}$ (Hodges et al., 2010),(Labanda and Llorens, 2004). All suspensions freshly prepared were used within 24 hours following their preparation.

- Aqueous suspensions

An initial stock suspension of Laponite was prepared by adding the appropriate amount of Laponite in Milli-Q water in order to give a final particle concentration of 2.5 wt% which is equivalent to 25 000 ppm in weight without any purification nor pH adjustments. The suspension was left to stir for 4 hours to assure an appropriate dissolution of Laponite and to obtain an optically final transparent suspension. Subsequent dilution of the stock sample was then undertaken with Milli-Q water to generates the desired concentrations studied between C_{Lap} = 1 to 20 000 ppm. All suspensions freshly prepared were used on the same day.

- Electrolyte addition suspensions

Sodium chloride solutions (NaCl, Sigma Aldrich, UK) were added to aqueous suspensions containing Laponite. The final concentration of Laponite was fixed at C_{Lap} = 0.1 wt% while the concentration of NaCl ranged between C_{NaCl} = 1 to 10 mM. Each suspension was sonicated for 5 minutes in an ultrasonic water-bath to ensure the homogeneity of the suspensions. All suspensions were freshly prepared and droplet were deposited on the same day.

- Binary solvent ethanol/water mixture suspensions

Several volume fractions of water clay-ethanol mixtures were prepared. The examined proportions of ethanol in water span from C_{EtOH} = 50 to 90 vol%. The already suspended Laponite nanoparticles were added to the right

amount of ethanol to obtain the different desired suspensions. Each suspension was sonicated for 5 minutes by using an ultrasonic water-bath upon droplet depositions. The final concentration of Laponite in the different mixture was fixed at C_{Lap} = 0.1 wt%. The final suspensions were freshly prepared and droplet depositions were carried out on the same day.

- Anionic surfactant addition suspensions

Sodium dodecyl sulfate solutions (SDS, VWR Prolabo, ≥98%) at different initial concentrations were added to Laponite clay suspensions. The obtained suspensions were thoroughly stirred for 5 minutes to ensure the formation of homogeneous suspensions. The final SDS concentrations range from C_{SDS} = 0 to 30 mM while the final concentration of Laponite was fixed at C_{Lap} = 0.1 wt%. The suspensions were deposited on the day of preparation.

6.2.2 Drying process monitoring

The evaporation of single sessile droplets was conducted in an atmospheric chamber and under natural diffusion condition on uncoated and silane coated glass slides (Thermo scientific, UK) following the cleaning procedures explicated in previous Chapter 3, Section 3.4.1. A Krüss contact angle goniometer was used to record the wetting properties of the aqueous Laponite based suspensions. While a KSV CAM200 contact angle goniometer was used to record the side-view of the deposit sessile droplets over time until complete solvent evaporation for the binary solvent mixtures and suspensions with additives (surfactant and electrolyte) system. Each drying deposition was repeated three times and the inherent variation between measurements was used as standard deviation. The measurements were collected at environmental temperature and humidity at 24±1°C and 43±3%.

6.2.3 Deposition morphology measurements and characterization

An optical microscope was used to analyse the dried deposit structure of the droplet. An interferometer (Bruker, NPFlex, USA) was used to determine the two-dimensional and three-dimensional topographical structure of the dried deposit structure. The cross-sectional profiles of each dried deposit obtain upon complete solvent evaporation were extracted from the collected dataset.

6.2.4 Theoretical model

6.2.4.1 Main assumptions

The evaporation process is assumed to be a quasi-steady state (indeed the ratio of the diffusion time to the evaporation time t_E is shown below in Table 6-1) and that the droplets retain a spherical cap shape during the evaporation, as seen in Table 6-1, the Bond number, Bo is low for microliter droplets. The deposit substrates are assumed to be smooth and chemically homogeneous.

Table 6-1: Measurements of Bond number for aqueous based Laponite, in binary mixtures and with additives (surfactant and electrolyte)

System	Bond number, B_o	t_D/t_E
Aqueous	$\sim 4.0 \times 10^{-1}$	$\sim 4.6 \times 10^{-10}$
Binary	$\sim 3.0 \times 10^{-1}$	$\sim 9.3 \times 10^{-10}$
Surfactant	$\sim 3.5 \times 10^{-1}$	$\sim 4.1 \times 10^{-10}$
Electrolyte	$\sim 3.5 \times 10^{-1}$	$\sim 2.3 \times 10^{-10}$

Under these boundaries conditions, the gravitational forces can be neglected and thus the different droplets wetting characteristics can be determined. The sessile droplet resting on a solid substrate, thus retain a spherical shape. As the droplet is spherical, the volume, V is determined from equation (6-1) while the droplet θ_{ACA} is determined from equation (6-2).

$$V = \frac{\pi H(3r_d^2 + H^2)}{6} = \pi r_d^3 \frac{\cos\theta_{ACA}^3 - 3\cos\theta_{ACA} + 2}{3\sin\theta_{ACA}^3} \qquad \textbf{(6-1)}$$

$$\theta_{ACA} = 2\tan^{-1}\frac{H}{r_d} \qquad \textbf{(6-2)}$$

6.2.4.2 Sol-gel transition

During the evaporation process of a sessile droplet laden with a nanofluids, two phenomena can occur. For the first case, the interaction between particles

will occurs due to mechanical impacts. Due to these impacts, a porous medium will be generated which suppress bulk flow while an enhanced evaporation at the surface will be observed due to drainage (Bhardwaj et al., 2009). In the second case, strong bonds between particles can be generated, this is the case of aqueous based Laponite nanofluids due to its heterogeneous charge (Thompson and Butterworth, 1992), (Jatav and Joshi, 2014) and its phase diagram (Kegel and Lekkerkerker, 2011), (Ruzicka and Zaccarelli, 2011).

Previously it has been demonstrated that during an evaporation process different mode happened, however in the case of aqueous based Laponite nanofluids, the main assumption is that the gelation time (t_G) is much larger than the evaporation time (t_E). In this case, the gelled phase will be located at the TPCL (this is due to a faster evaporation process at the droplet edge since the droplet is the thinnest at this location (Deegan et al., 1997)) and the central area of the droplet will be in a liquid phase (Lebovka et al., 2014). Since the gelation starts at the TPCL, the gelation will propagate inwardly.

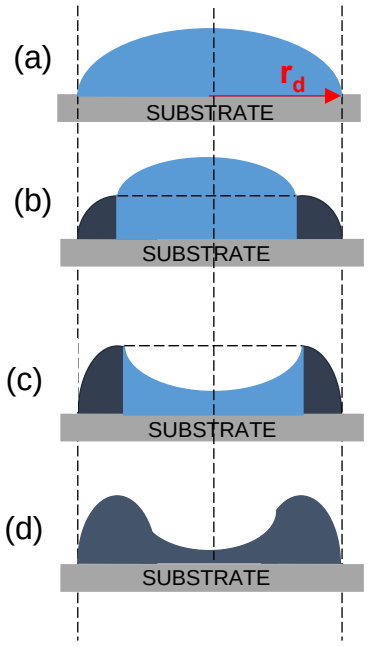

Figure 6-1: Side-view evolution profile of an evaporation-driven sol-gel Laponite sessile droplet of contact radius r_d. The light blue represents the sol part while the dark blue represents the gel part of the deposit.

When gelation occurs within a droplet during an evaporation process, several stages will be observed (Jung et al., 2009):

- At the beginning of the evaporation process, the droplet is only in a liquid phase (Figure 6-1a). The suspended particles will be carried towards the TPCL until the suspended particles reach a critical value of the volume fraction. The particle-riche area is narrower compared to the central region of the droplet where the volume fraction is nearly constant along its radius (Yu. Yu. Tarasevich and Pravoslavnova, 2007; Yu.Yu. Tarasevich and Pravoslavnova, 2007; Tarasevich et al., 2010).
- In-between of the evaporation process, two phases will be observed (Figure 6-1b, c). The gel phase is located at the droplet TPCL and moves towards the droplet centre.
- Last stage of the evaporation process (Figure 6-1d).

6.3 Results and discussion

6.3.1 Drying of sessile droplet of Laponite-base aqueous suspensions and deposit patterns

- Surface activity of Laponite nanoparticles

First, the surface activity of Laponite RD was determined as a function of nanoparticle concentration. The surface tension measured for Laponite-based suspensions is in the same range as the surface tension of pure Milli-Q water at low particle concentration ($C_{Lap} \leq 2$wt%, $\gamma_{LV} \approx 71.6$-72.8 mN/m).

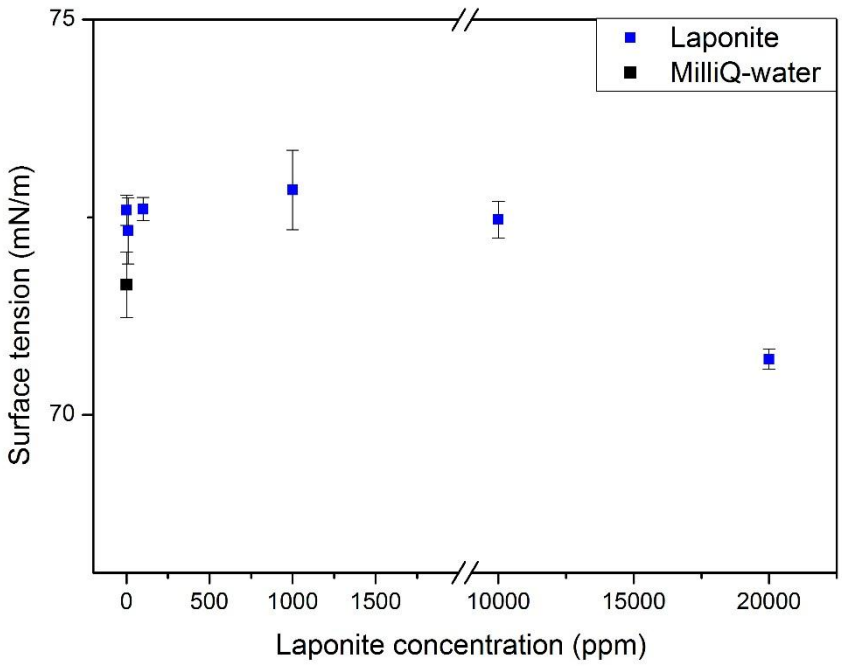

Figure 6-2: Surface tension measurements of MilliQ-water and aqueous based Laponite suspensions as a function of Laponite concentration (C_{Lap}= 1 to 20000 ppm).

However, as the nanoparticle concentration is increase a drop in the surface tension is observed as previously reported for similar concentration of Laponite aqueous based suspensions (Chen et al., 2011) see Figure 6-2.

- Wetting properties of Laponite aqueous base suspensions as a function of Laponite concentration

The experiments have shown that the total evaporation time was comprised between t_E=1560 to 3937 s. This time was seen to increase with the increase of Laponite concentration unlike previous reported data (Lebovka et al., 2014). In this previously reported data the droplet was monitored overtime with a weighing balance to assess the drying time whereas in our results the evaporation time was determined as the time at which the droplets apparent contact angle reached zero see Figure 6-3. However, towards the end of the droplets lifetime, it is difficult to determine the droplet contact diameter accurately hence this could explain the discrepancies observed for the different Laponite concentrations.

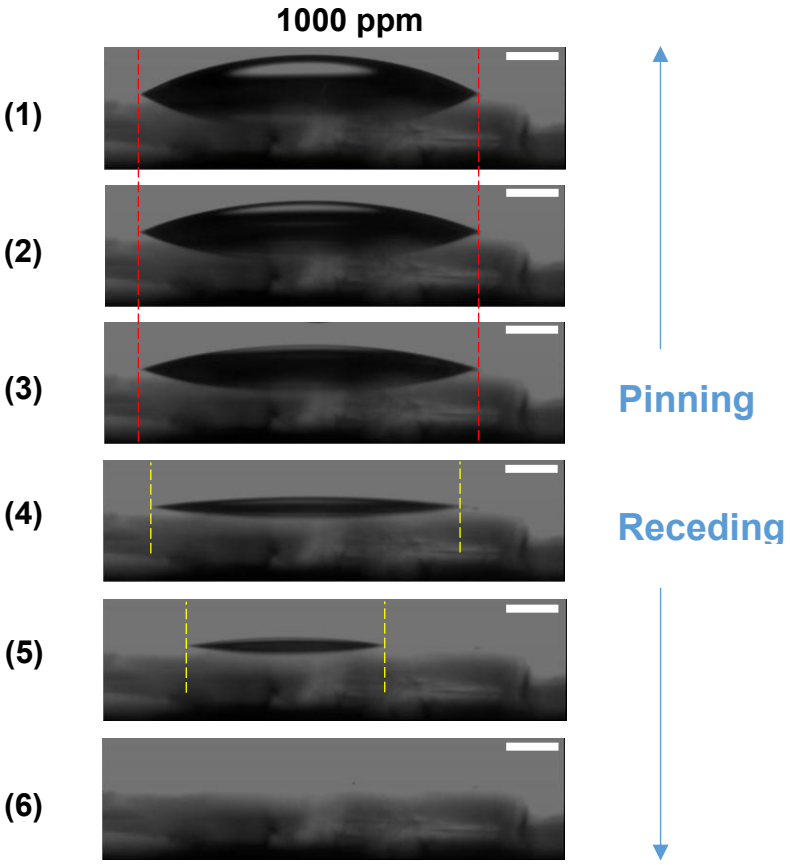

Figure 6-3: Drying sequence of Laponite sessile droplets (at C_{Lap}= 1000 ppm) at different time of droplet lifetime (1) 0%, (2) 12.5%, (3) 25%, (4) 50% and (5) 75% and (6) 100%. The images are side-view recordings of the deposition using a contact angle goniometer. The scale bars on all images represents 1 mm. The red dotted lines represent the initial droplet contact diameter while the yellow dotted lines represent the receding of the droplet contact diameter. Droplets were deposited on uncoated glass slides

The wetting properties of the Laponite droplets were determined from the droplet profile evolution of the sessile droplets (see Figure 6-3, Figure A-16). As explained in the section 6.2.4, the droplet shape has a spherical cap shape thus the volume and apparent contact angle can be extracted from the known droplet height and contact radius over time.

Figure 6-4a displays the evolution of droplet contact diameter over time. It was experimentally observed that the contact angle remained pinned when the Laponite concentration was C_{Lap}≤ 1 wt% and above (C_{Lap}=2 wt%) a slight contact diameter increased was observed. After this pinning period, a

receding of the contact line was observed. This receding was manifested by a linear decrease of the contact diameter for Laponite concentration (0.0001 to 2 wt%). From this pinning period, a “coffee ring effect” can be expected for C_{Lap}≤1 wt%.

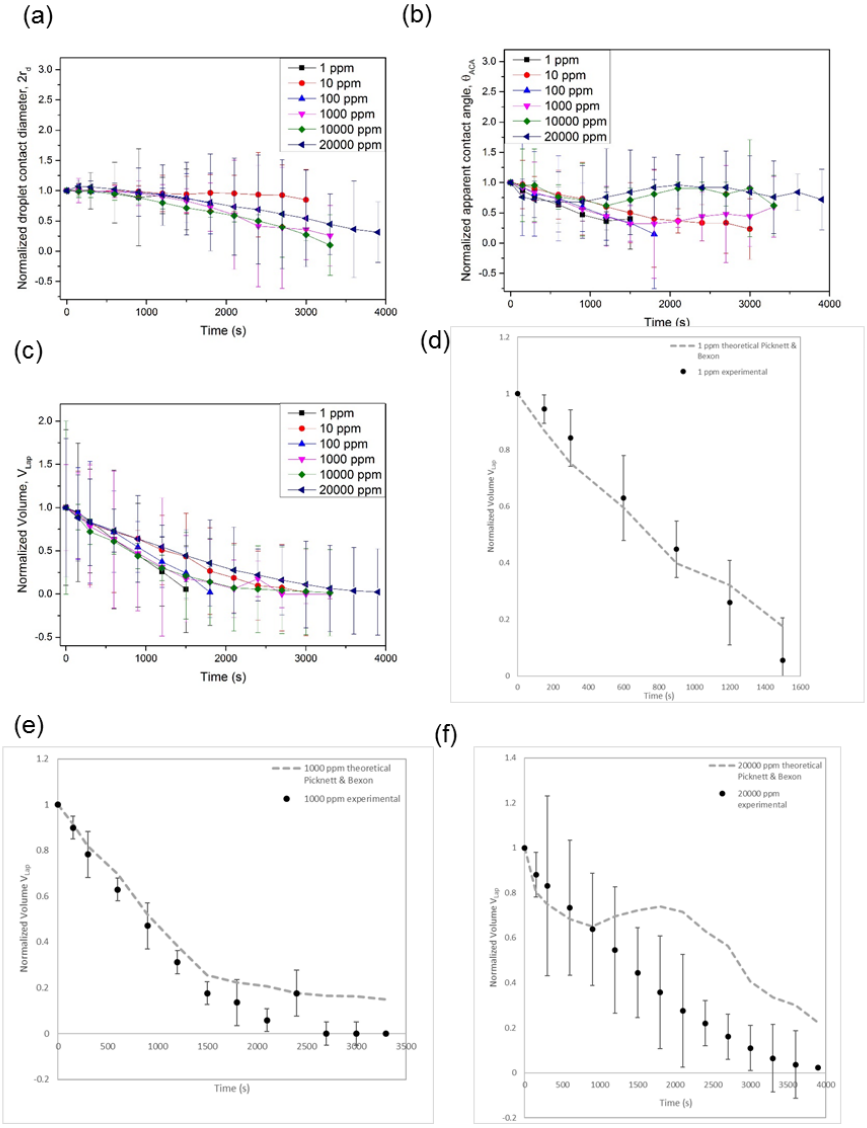

Figure 6-4: Evolution of normalized (a) droplet contact diameter $2r_d$ (b) apparent contact angle θ_{ACA} and (c) volume V of aqueous based Laponite suspensions at different concentration C_{Lap}=1 to 20000 ppm with time on the entire droplet lifetime. The droplets were deposited on uncoated glass slides. The evolution was extracted from contact angle goniometer recordings.(d), (e) and (f) comparison between the theoretical and experimental time evolution of sessile droplets volume of Laponite at three concentrations 1, 1000 and 20000 ppm.

On the Figure 6-4b, the apparent diameter increase of the droplet contact diameter can be attributed to the snapshot resolution and the difficulty to measure appropriately the diameter. Furthermore, towards the end of the droplet lifetime the droplet shape was highly deformed by the gravity hence the spherical cap shape approximation is less accurate.

On Figure 6-4c, the apparent contact angle variation of aqueous Laponite sessile droplets is presented. It was observed that as expected with a pinned contact line, the apparent contact angle decrease over time in the early stage of the droplets lifetime regardless of the initial Laponite concentration. Also, at all Laponite concentrations an increase of the apparent contact angle was observed in the later stage of the droplets lifetime. This droplets profile evolution has previously been reported (Lebovka et al., 2014). The increase of the apparent contact angle could also be attributed to the jump of the droplet contact diameter due to a receding of the contact line.

The experimental and theoretical evaporation rate were determined and compared on Figure 6-4d, e and f. For the theoretical evaporation rate, the Picknett and Bexon model was used. The initial nanoparticle concentration evaluated were at lowest (C_{Lap}= 1 ppm), medium (C_{Lap}= 1000 ppm) and highest (C_{Lap}= 20000 ppm). used. The evaporation was determined from the experimental Θ_{ACA} variation with time. The theoretical values for aqueous Laponite suspension are: $0.5x10^{-3}$, $0.3x10^{-3}$ and $0.1x10^{-3}$µL.s^{-1} for C_{Lap}= 1, 1000 and 20000 ppm respectively. The experimental values in our experiments are $8.1x10^{-3}$, $9.3x10^{-3}$ and $7.6x10^{-3}$µL/s^{-1}. The Picknett and Bexon model give a good estimation at low and medium concentration. However, for C_{Lap}= 1000 ppm, the errors bars from the experimental results do not encompass the theoretical towards the end of the droplet drying lifetime and a divergence is observed. Whereas, for the highest concentration CLap= 20000 ppm, a significant divergence is observed early in the droplet drying lifetime. It is also worth noticing that despite being in the same order, the theoretical evaporation rate is lower than the experimental evaporation rate.

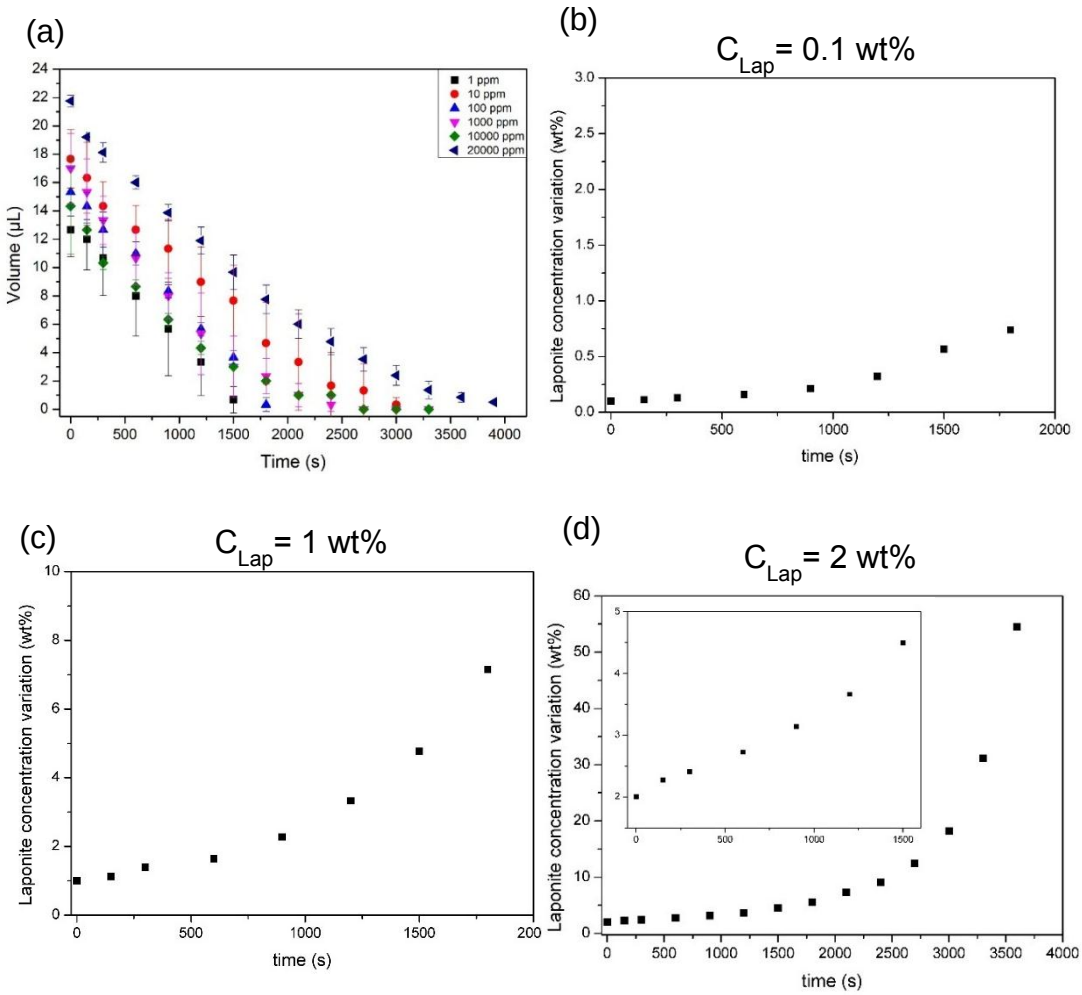

Figure 6-5: (a) Evolution of volume V of aqueous based Laponite droplets at different Laponite concentration (C_{Lap}=1 to 20000 ppm) with time on the entire droplet lifetime. Evolution of local Laponite concentration of aqueous based Laponite droplets at (b) 1000 ppm, (c) 10000 ppm and (d) 20000 ppm. The droplets were deposited on uncoated glass slides. The evolution was extracted from contact angle goniometer recordings.

Figure 6-5a exhibits the evolution of volume, V with time of the Laponite sessile droplets as a function of the initial Laponite concentration. The local concentration increase within the droplet at low and higher Laponite concentration was also determined (see Figure 6-5b, c and d). From this evolution it can be noticed that for C_{Lap}= 1 wt%, the gelation concentration which is at $C_{Lap, gel}$= 3 wt% in our laboratory will be reached at around ~1200 s, while it will be reached at ~745 s for C_{Lap}= 2 wt%.

The evaporation rate variation was similar for the different Laponite concentration see Table 6-2. However, a higher evaporation rate was observed for the initial Laponite concentration C_{Lap} = 0.0001 and 0.01 wt%. These discrepancies could be explained by the experimental procedure. The evaporation rate reported in Table 6-2 corresponds to the slope extracted from the variation of Laponite volume over time plotted on Figure 6-5.

Table 6-2: Summary of different evaporation rate of aqueous based Laponite droplets as a function of initial Laponite concentration (C_{Lap}= 0.0001 to 2 wt%)

Concentration (wt%)	Evaporation rate (10^{-3} µL/s)
0.0001	8.1
0.001	6.5
0.01	7.9
0.1	9.3
1	7.5
2	7.6

Figure 6-6 and Figure 6-7 shows the final patterns obtained upon complete solvent evaporation at different initial concentrations for the aqueous based Laponite sessile droplets. Their corresponding cross-sectional profiles were also extracted and plotted. Despite the de-pinning of the droplet contact diameter, the final patterns display the characteristic ring-like patterns which are usually associated with the “coffee ring effect” (Deegan et al., 1997; Deegan, 2000; Deegan et al., 2000). This coffee ring effect was obvious at rather low Laponite concentration C_{Lap}≤ 0.1 wt%. A uniform deposit is observed at higher concentration as seen on Figure 6-7 and confirmed with the dried deposit profiles extracted and seen on Figure 6-6. It was previously reported and confirmed that the “coffee ring effect” would be observed for Laponite at concentration below 1wt% while a uniform film would be seen at

higher concentration due to the sol-gel transition in the droplet (Lebovka et al., 2014).

- Dried deposit patterns analysis

The corresponding dried deposit profiles can be seen on Figure 6-6 and Figure 6-7. From there it was confirmed that the dried deposits were ring-like deposit (C_{Lap}≤ 1 wt%) while a film was obtained at higher Laponite concentrations (CLap≥1 wt%). The ring-like deposit structure was observed at lower Laponite concentrations however this structure is usually associated with a pinned contact line. So, our hypothesis to explain these structures at lower Laponite concentration was that at the beginning of the drying of the droplets while the contact line is pinned the capillary flow transport the majority of the particles towards the contact line forming the coffee stain and later on the drying as the majority of the particles were transported little to no particles are remaining in the aqueous explaining the few particles in the centre of the deposit. For the higher Laponite concentration droplets the sol-gel transition must occurs. Indeed, on the drying sequence of Laponite at 0.1 wt% for example the pinning of the contact line was observed for 25% of the evaporation time. Also, in our laboratory the gelation concentration of Laponite suspensions was obtained at $C_{Lap,\ gel}$= 3 wt%.

This is confirmed by the local Laponite concentration increase seen on Figure 6-5b, c and d and could explain the different final patterns for Laponite droplets at 1 and 2 wt%.

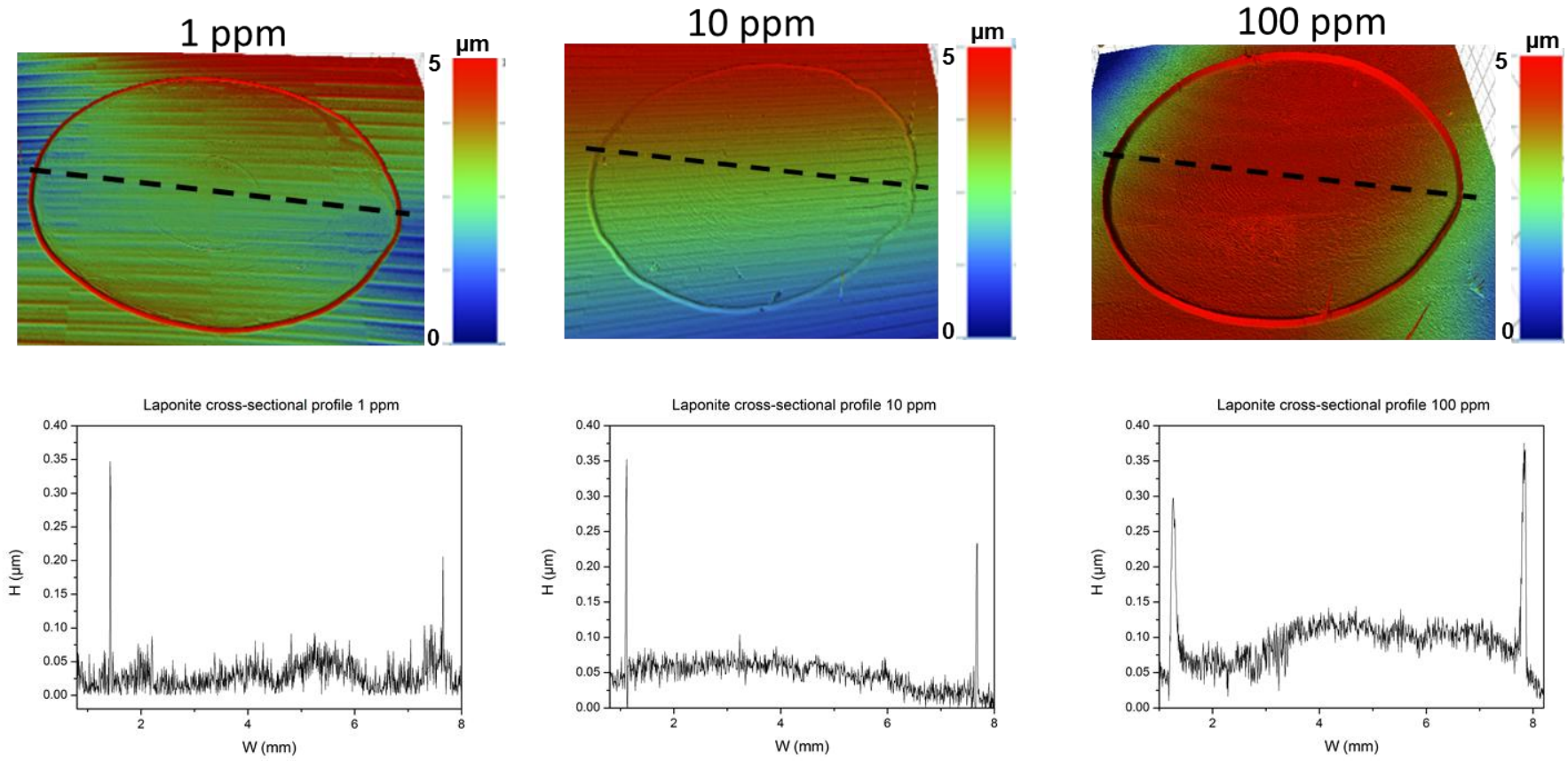

Figure 6-6: Three-dimensional topographical WLI images of dried droplets of aqueous based Laponite (at C_{Lap}=1,10 and 100 ppm) on uncoated glass slides and corresponding cross-sectional profiles along the black dotted line.

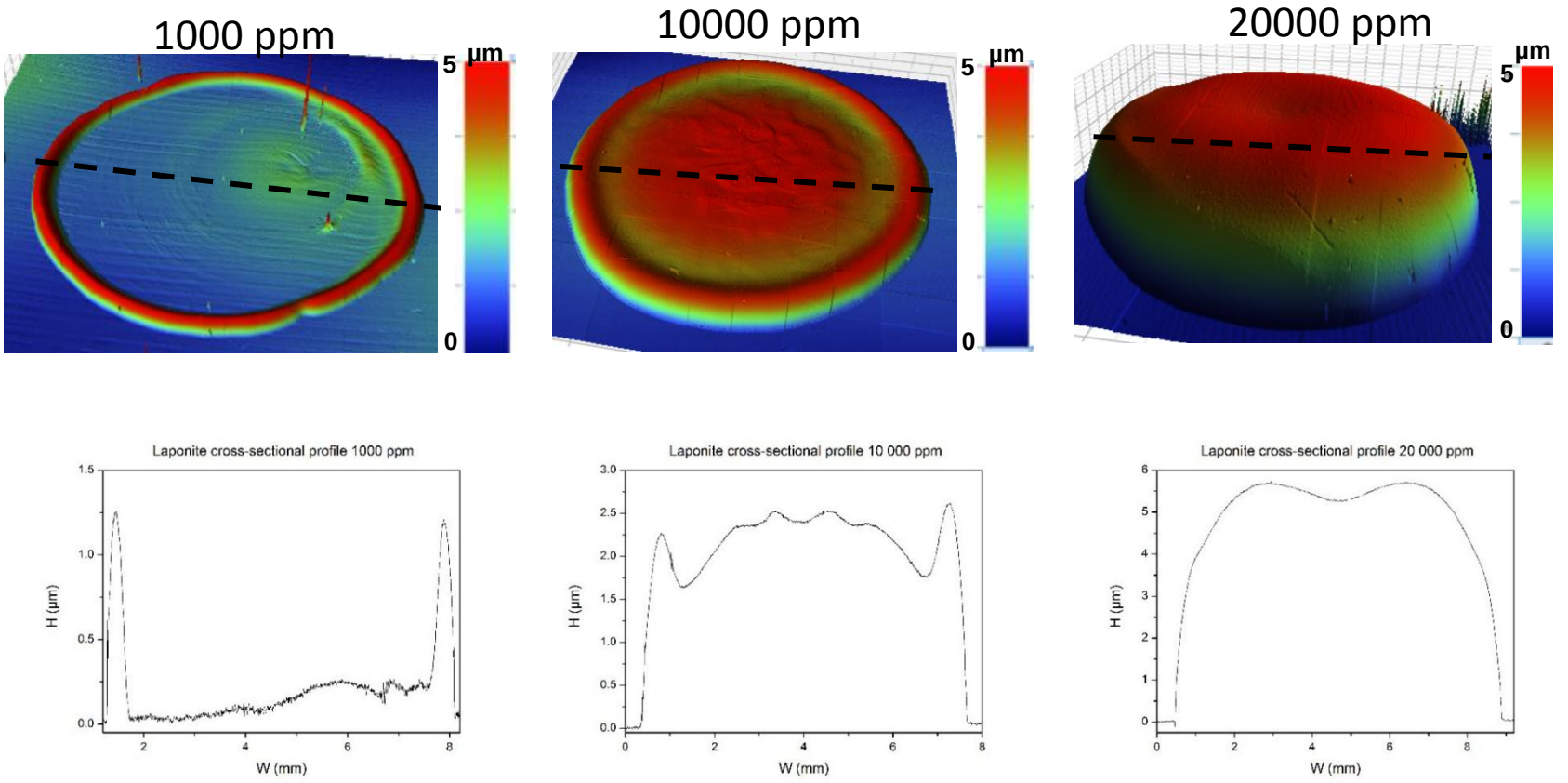

Figure 6-7: Three-dimensional topographical WLI images of dried droplets of aqueous based Laponite (at C_{Lap}=1000 to 20000 ppm) on uncoated glass slides and corresponding cross-sectional profiles along the black dotted line.

Figure 6-8 presents the overall variation in width and height of the aqueous based Laponite as a function of concentration. A clear trend was observed. The dried deposit height was seen to increase gradually with the Laponite concentration increase. Contrary to previously reported, the increase in Laponite concentration does not results in the collapse of the dried deposit structure (Hodges et al., 2010).

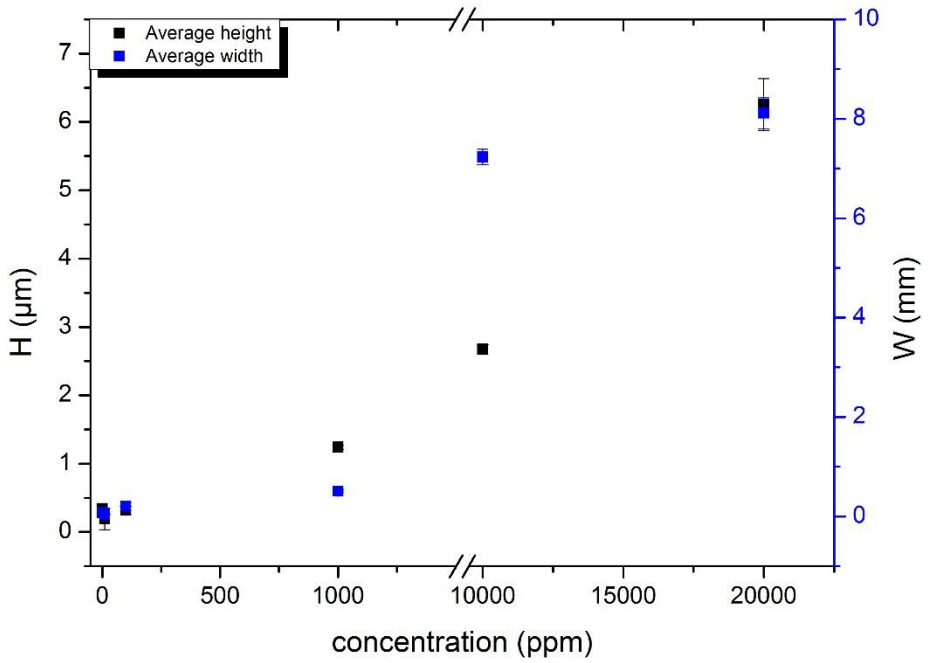

Figure 6-8: Influence of Laponite concentration (C_{Lap}= 1 to 20000 ppm) on the droplet dried deposits features (height and width).

From these experimental results and previously reported data, further drying of sessile Laponite droplets were investigated. The hypothesis that we tried to demonstrate was that at low Laponite concentration 0.1 wt% a sol-gel transition could be obtained. The main hypothesis was that the presence of additives in the system and the presence of another solvent were mandatory to reach these results.

In the following sections, the experimental results with additives (surfactant and electrolyte) and in binary mixtures and their subsequent dried deposit structure are presented as well as interpretation to explain the dried deposit structures patterns.

6.3.2 Drying of sessile droplets of Laponite-base effect of co-solvent addition

The drying behaviour of Laponite droplets at a fixed nanoparticles concentration of 0.1wt% in different vol% of ethanol mixtures were studied. The content of ethanol was increased gradually from C_{EtOH}= 50 to 90 vol% and the subsequent effect of this variation was monitored. This gradual increase in ethanol concentration does not change fundamentally the surface tension of the droplets (see Figure A-14).

- Wetting properties

The evolution of the Laponite sessile droplets diameter was measured and is presented on Figure 6-9. It was found that on the silane-coated glass slides the evaporation process can be divided into four main stages. During the first stage (I) which corresponds to the early phase of evaporation, the drop contact diameter remains pinned regardless of the initial ethanol content. However, when the ethanol content was increased this first stage seems to be dependent on the initial ethanol concentration. In the second stage (II), the drop diameter decreases linearly before reaching the third phase (III) which is a second pinning period. The third stage is thought to be depend on the EtOH content and appears to be longer as the EtOH content is decrease. Finally, a fourth stage (IV) was observed during which the droplet contact diameter decrease linear again. This decrease is more evidently observed a lower concentration of EtOH. These different stages could be linked to the direct EtOH content, in the first stage the EtOH is reaching the air-liquid interface and dictates the drying behaviour of the droplets. Indeed, previous work has already evidence such “stick-slip” behaviour of the TPCL (Moffat et al., 2009). In the second stage, the water dominates the evaporation droplet behaviour (Cheng et al., 2006). For “stick-slip” motion, part of the evaporation process takes place in the CCRM with a pinned contact line, followed by a receding contact line and in some cases not always the apparent contact angle will be constant. However, this is not the CCAM behaviour observed in our experimental case. These differences could be explained by the fastest evaporation of the TPCL and the sol-gel transition due to the local increase of Laponite concentration within the droplet.

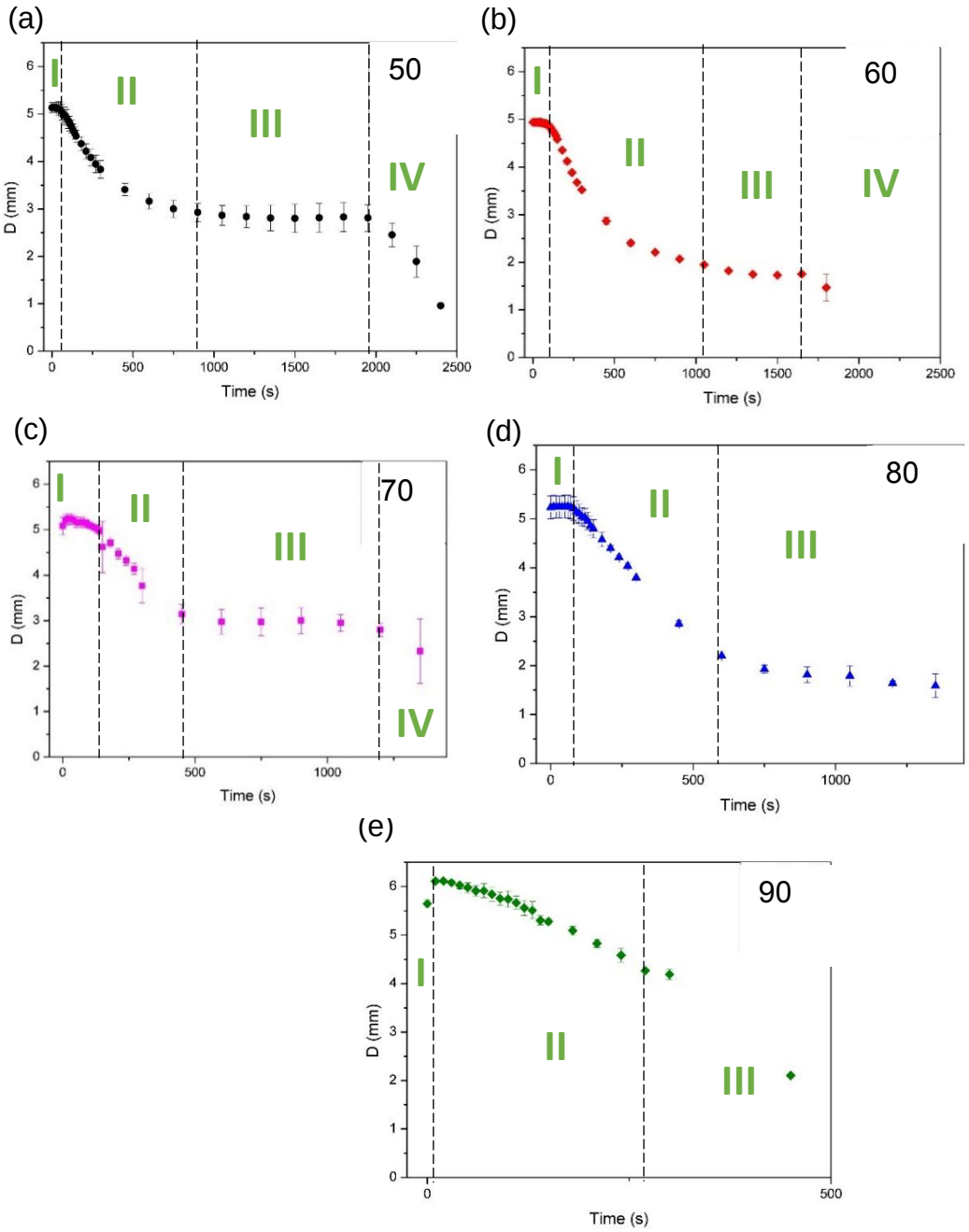

Figure 6-9: Evolution of contact diameter $2r_d$ with time of aqueous based Laponite (C_{Lap}= 0.1 wt%) micro-droplets in different ethanol/water mixtures on silane-coated substrates (a) 50 vol%, (b) 60 vol%, (c) 70 vol%, (d) 80 vol%, (e) 90 vol%. The different evolutions were extracted from contact angle goniometer recordings

As shown on Figure 6-10, due to the silane-coating of the glass slides the influence of the ethanol concentration on the initial apparent contact angle cannot be clearly identified unlike previously reported work (Sefiane et al.,

2003; Liu et al., 2008). Indeed, for all the ethanol concentration the initial apparent contact angle is found at 39 ± 5°. Due to this silane-coating, the hydroxyl group of the glass slides are replaced by hydrophobic groups (-CH_3 terminated) hence the wetting is not favoured. Also, as the surface is hydrophobic the variation of ethanol concentration will not change the initial apparent contact angle. Moreover, at room temperature, the ethanol vapour pressure (~7.0 kPa) is higher than that of water (~2.8 kPa) (Liu et al., 2008), as such, the droplet surface and surrounding vapour will be enrich with ethanol molecules rather than water molecules. Thus, as the ethanol concentration is increased in the different suspensions, it is our understanding that the majority of ethanol will rich the air-liquid interface and will significantly dictate the surface tension.

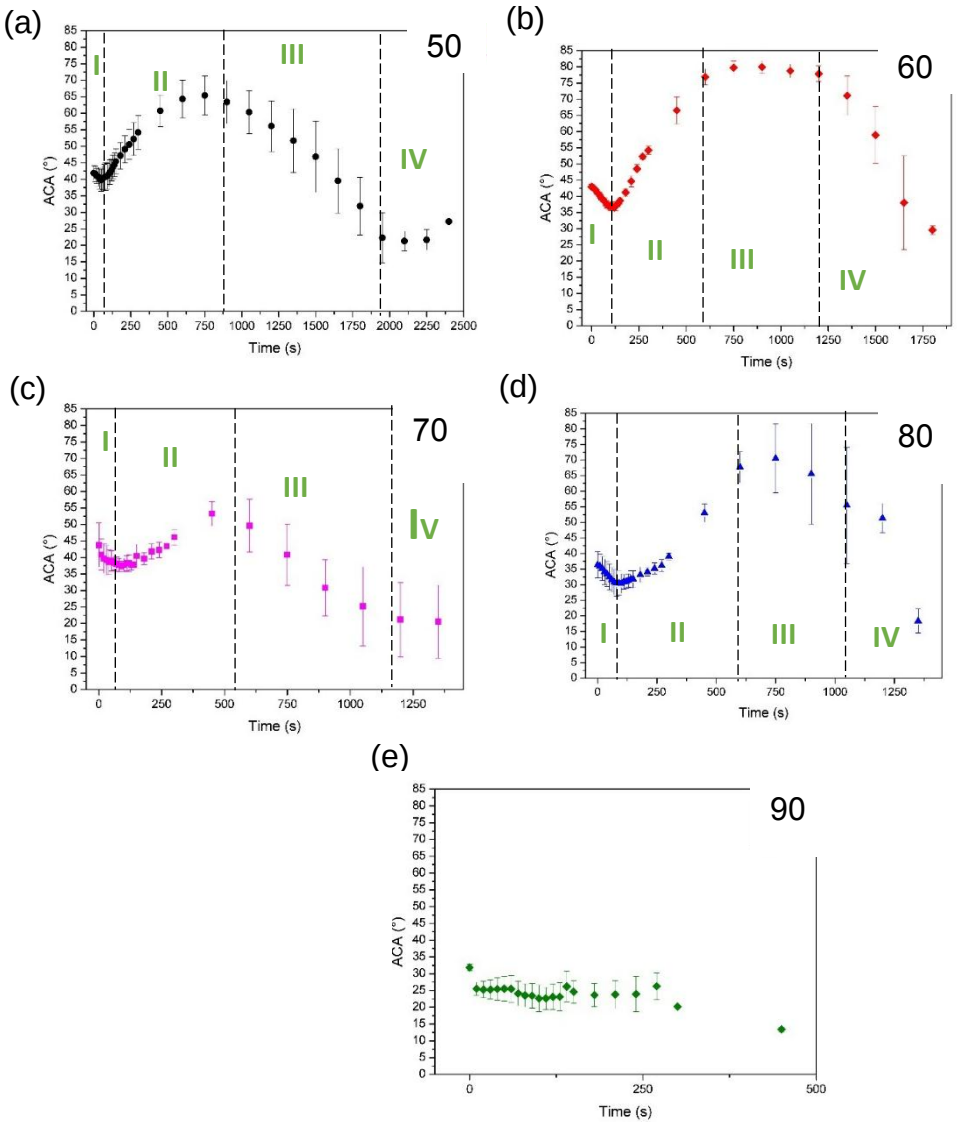

Figure 6-10: Evolution of apparent contact angle θ_{ACA} with time of aqueous based Laponite at C_{Lap}= 0.1 wt% sessile droplets in different ethanol/water mixtures (a) 50 vol%, (b) 60 vol%, (c) 70 vol%, (d) 80 vol% and (e) 90 vol%. The droplets were deposited on silane coated glass slides. The different evolutions were extracted from contact angle goniometer recordings.

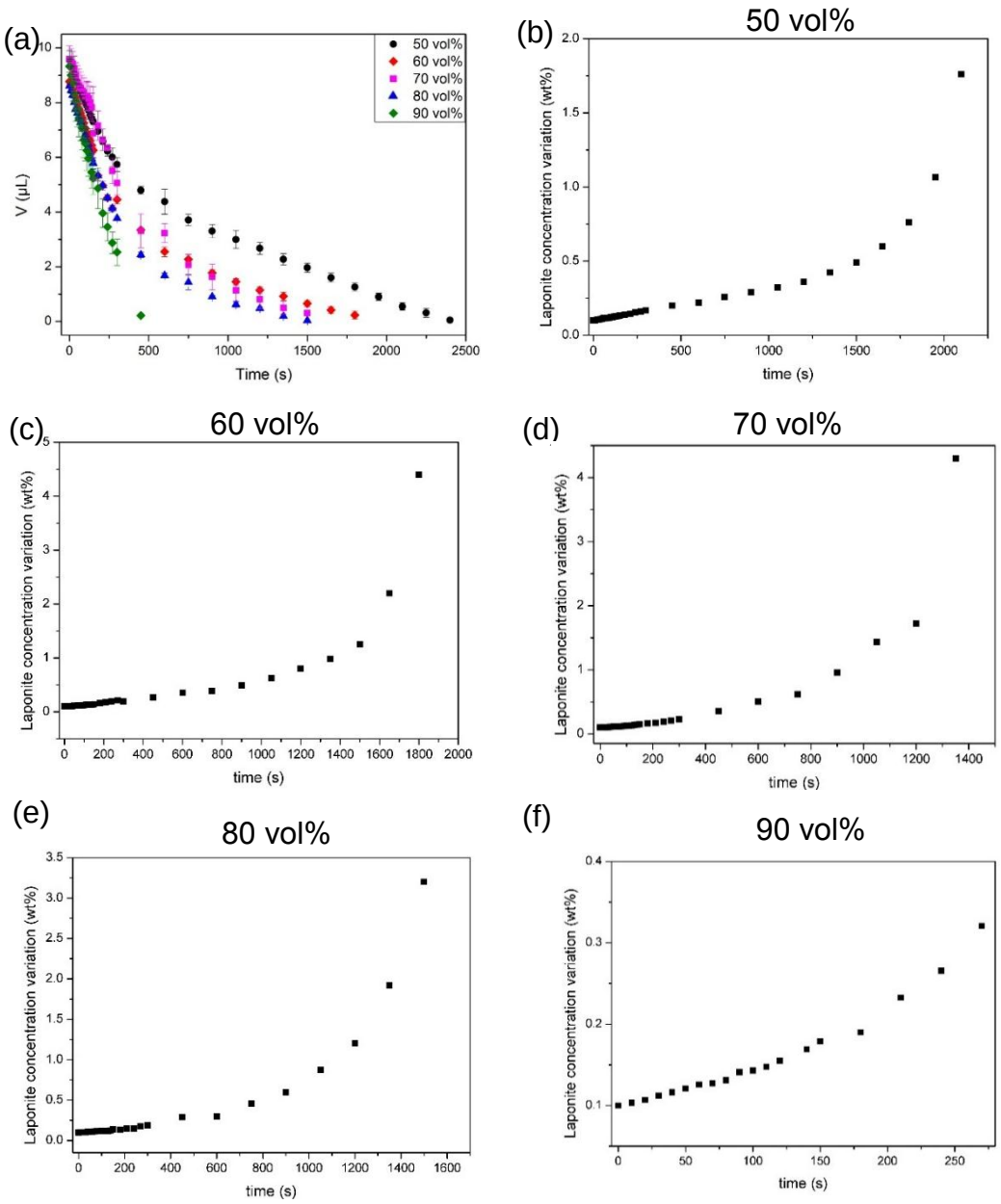

Figure 6-11: (a) Evolution of volume V with time of aqueous based Laponite at C_{Lap}= 0.1 wt% **sessile droplets in different ethanol/water mixtures (C_{EtOH}= 50 to 90 vol%). Evolution of Laponite local concentration in the micro-droplets with time in the different ethanol/water mixtures at (b) 50 vol%, (c) 60 vol%, (d) 70 vol%, (e) 80 vol% and (f) 90 vol%. The droplets were deposited on silane coated glass slides. The different evolutions were extracted from contact angle goniometer recordings.**

The droplet volume V evolution with time was plotted for all the five different EtOH concentrations (Figure 6-11). The local concentration of Laponite within the droplet was also seen to increase with the ethanol concentration between C_{EtOH}= 50 to 80 vol%. A non-linear decrease over time was observed for all cases. As the variation of droplet volume corresponds directly to the rate of evaporation, a few conclusions can be drawn out from these data:

- The rate of evaporation increases with the ethanol concentration, this behaviour is evidenced by the different droplets lifetimes. Indeed, a 50 vol% EtOH micro-droplets takes about 2456 seconds to dry whereas for a 90 vol% EtOH micro-droplets it is only about 530 seconds
- The evaporation rate was similar for all cases near the end indeed the slope towards the end of the evaporation was found at 2.0×10^{-3} µL/s in all cases. This suggests that the composition of the droplets towards the end is the same and more precisely only one component is present in the final stage of the evaporation process.

As it has been previously demonstrated, in the later stage of the evaporation process, only one solvent remains in the droplet in other word water (Cheng et al., 2006; Shi et al., 2009; Christy et al., 2010; Hamamoto et al., 2012). This behaviour is confirmed as in the later stage of the evaporation process, the apparent contact angle increases dramatically up to ~85° for 50 vol% which is close to the apparent contact angle of a pure droplet of Milli-Q water (see Chapter 3).

Also, in previous chapters, it was demonstrated that the evaporation process for pure droplets was a quasi-steady-state. Despite the variation of evaporation rate, previous work on evaporation of ethanol-water mixtures has proven that a quasi-steady-state was also at play in multicomponent droplets. The explanation comes from the fact that in the early stage of the evaporation process the fast evaporation of the more volatile component Is ongoing. From this behaviour, we can assume as previous work demonstrated that the

temperature of the droplet surface temperature will decrease due to an evaporative cooling (Hopkins et al., 2006), (Hopkins and Reid, 2006).

- Final deposit patterns upon total solvent evaporation

The final patterns of Laponite micro-droplets in ethanol-water mixtures arising upon total solvent evaporation are presented on Figure 6-12. We can observe that the initial ethanol concentration directly influences the final deposit patterns. Indeed, from 50 to 80 vol% included the dried deposit display a ring-like deposit. However, this ring-like deposit does not consist of a nanoparticle free centre, indeed the centre of the deposit as an average height of ~1.5 µm (for $C_{EtOH} \leq$ 80 vol%). The three-dimensional deposit of 70 vol% EtOH appears to be a complete uniform film however the cross-sectional profile reveals a ring-like with a thick centre deposit similarly to the other concentrations.

The only singular pattern observed was when the ethanol concentration reached C_{EtOH}= 90 vol%. At this concentration, the final pattern was ring-like however, a high depletion is observed between the centre of the deposit and the edges of the deposit.

These differences in final deposit patterns could be explained by the variation of surface tension due to change in ethanol concentration. This variation could modify the internal flows and hence the nanoparticles transport inside the droplets. Also, as evidenced by the evolution of the local concentration increase of Laponite, the gelation concentration of Laponite $C_{Lap,\ gel}$= 3 wt% is reached for all the different ethanol concentration C_{EtOH}= 50 to 80 vol% but C_{EtOH}= 90 vol%.

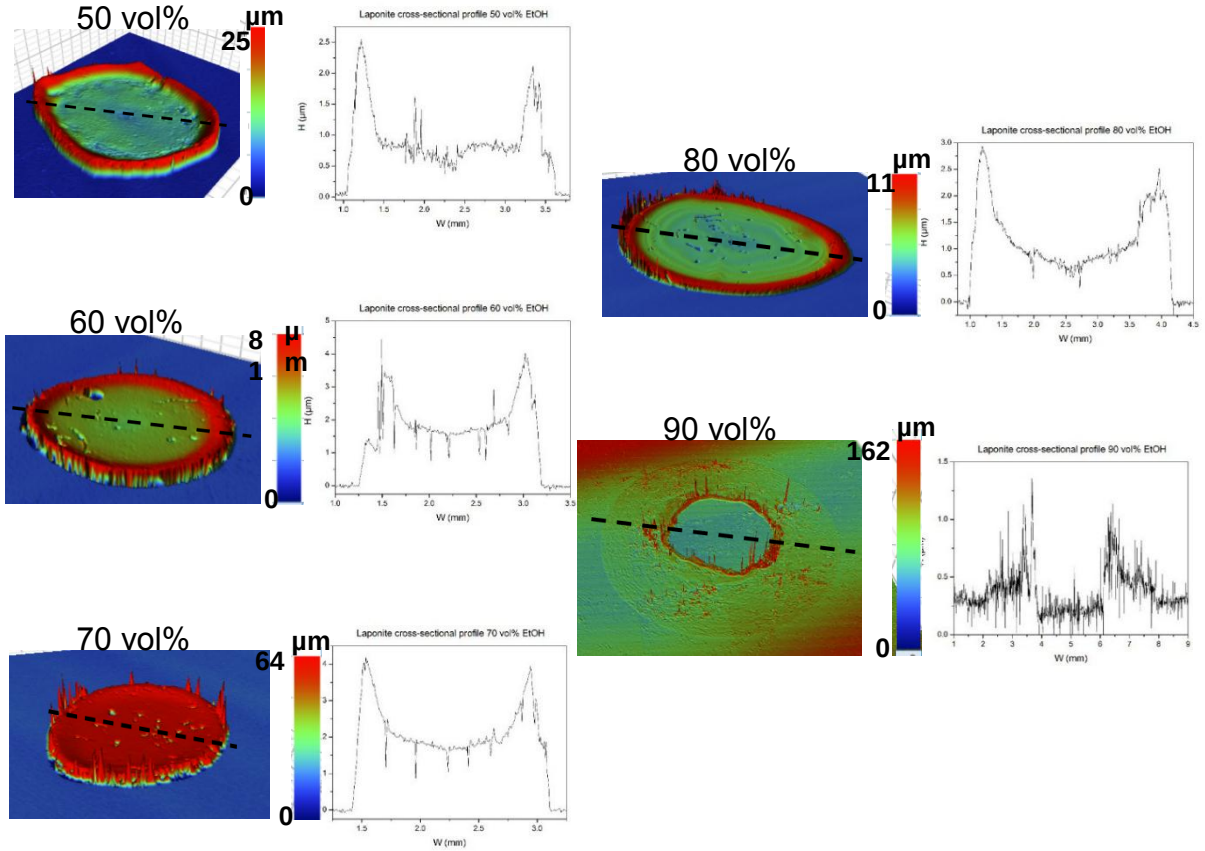

Figure 6-12: Three-dimensional topographical WLI images of aqueous based Laponite at C_{Lap}= 0.1wt% dried droplets on silane coated glass slides in different ethanol/water mixtures (C_{EtOH}=50 to 90 vol%) and the corresponding cross-sectional profiles along the black dotted lines.

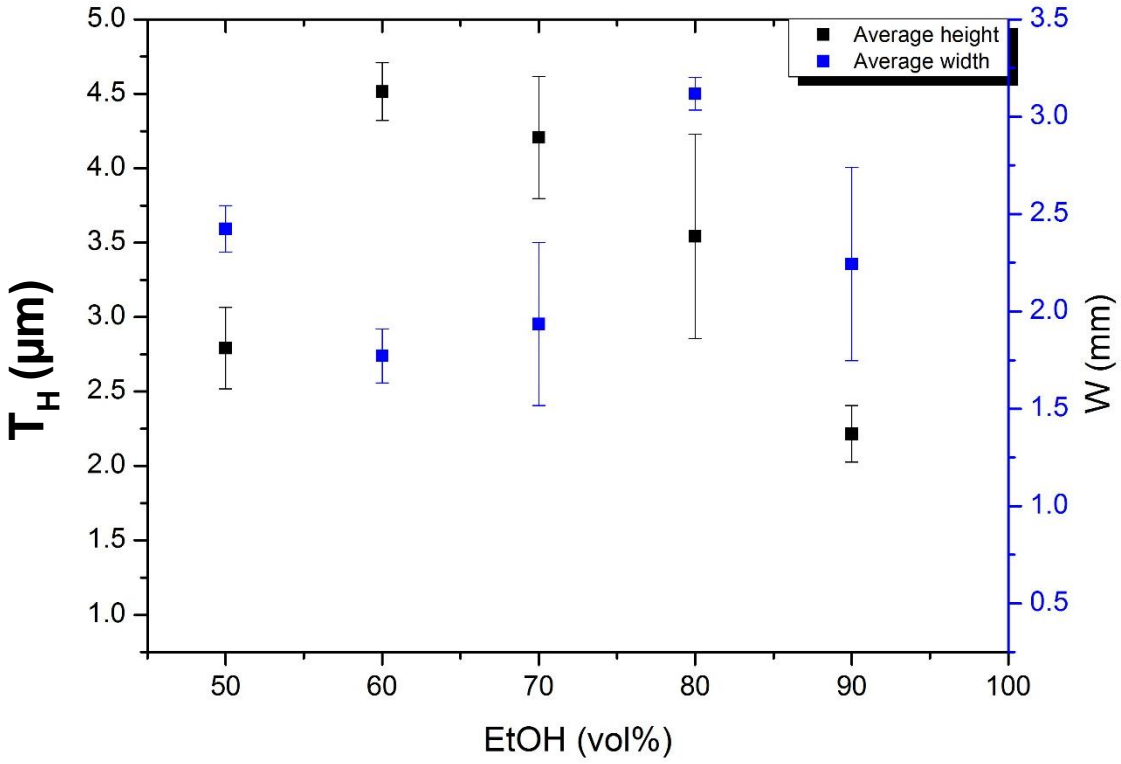

Figure 6-13: Evolution of dried deposit features (width W and height T_H) of aqueous based Laponite droplets C_{Lap}= 0.1wt% in different ethanol/water mixtures (C_{EtOH}=50 to 90 vol%). The droplets were deposited on silane coated glass slides.

The influence of ethanol concentration on the height and width of the final deposit patterns can be seen on Figure 6-13.

The thickness plotted on this figure represents the highest height of the final dried deposit. From these data it can be concluded that:

- The concentration of ethanol influences the final deposit patterns and the highest thickness are seen for 60 and 70 vol%. (T_H= 4.5 ± 0.2 µm for C_{EtOH}= 60 vol% and T_H= 4.2 ±0.4 µm for C_{EtOH}= 70 vol%)
- The deposit width was determined as the overall length of the deposit. As the final length is close to the initial length, its variation was not significant for the different deposits.

6.3.3 Effect of surfactant addition at low Laponite particles concentration

The evaporative behaviour of aqueous based Laponite droplets with added surfactant were explored in the following subsection.

Indeed, previous work demonstrated that by surfactant addition a Marangoni flow could be generated inside a droplet and thus control the final deposit patterns (Still et al., 2012; Sempels et al., 2013).

As such, we have investigated this phenomenon with a disk-like particle system. Our main interest was to study Laponite concentration at low concentration (C_{Lap}= 0.1 wt%) and observe whether the sol gel transition was still the driving force leading to a more uniform deposit for the final patterns (Still et al., 2012).

- Wetting behaviour of aqueous based Laponite sessile droplets with surfactant addition

The wetting behaviour of Laponite C_{Lap}= 0.1 wt% with anionic surfactant addition are presented on Figure 6-14a, b and c.

On Figure 6-14a, the droplet diameter variation is reported. From the experimental results, we can see that the addition of surfactant increases the wetting properties of the suspensions. Indeed, the droplet diameter decreases considerably with the addition of surfactant, this behaviour was expected as the addition of surfactant decreases significantly the droplet surface tension as seen on Figure A-15. However, when the cmc of the surfactant is reached, the surface tension will not decrease anymore as the surface will be saturated by the SDS surfactant.

It can be seen that the higher the surfactant concentration, the faster the droplet contact diameter increases.

Figure 6-14a shows the variation in base diameter with time for pure Laponite 0.1 wt% and Laponite 0.1 wt% with different added concentration of SDS.

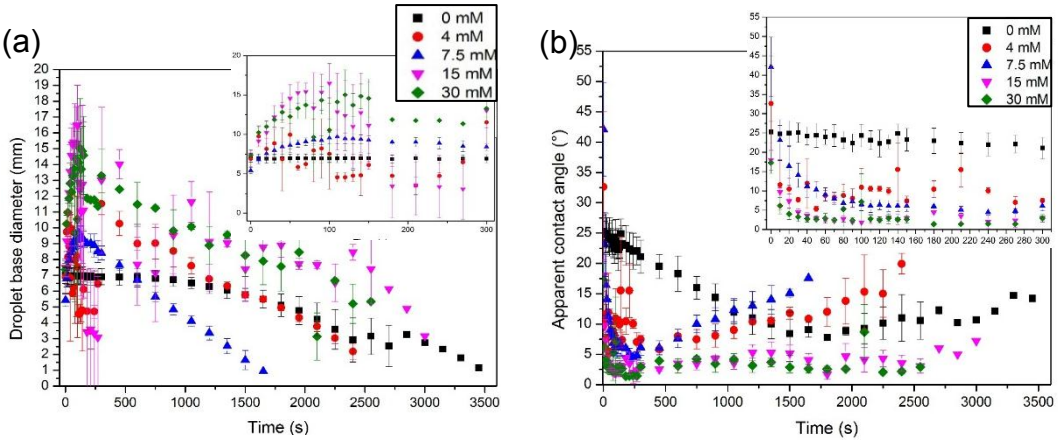

Figure 6-14: Evolution of (a) droplet contact diameter $2r_d$ and (b) apparent contact angle θ_{ACA} with time of aqueous based Laponite at C_{Lap}=1000 ppm droplets with different added surfactant concentration (C_{SDS}= 0 to 30 mM) over the entire droplets lifetime and a zoom in between 0 to 300s. The droplets were deposited on uncoated glass slides. The evolution was extracted from contact angle goniometer recordings.

The variation in apparent contact angle, θ_{ACA} with time can be seen on Figure 6-14b. It can be seen that the θ_{ACA} variation seems to be dependent on the concentration of SDS. It appears that the θ_{ACA} decreases inversely with the concentration of SDS.

The evolution of volume, V with time is reported on Figure 6-15a while the local concentration increase of Laponite with time are reported on Figure 6-15b, c and d. It seems that the evaporation rate depends on the concentration of SDS, it has previously been demonstrated (Doganci et al., 2011; Still et al., 2012; Doganci and Erbil, 2013; Doganci et al., 2014).

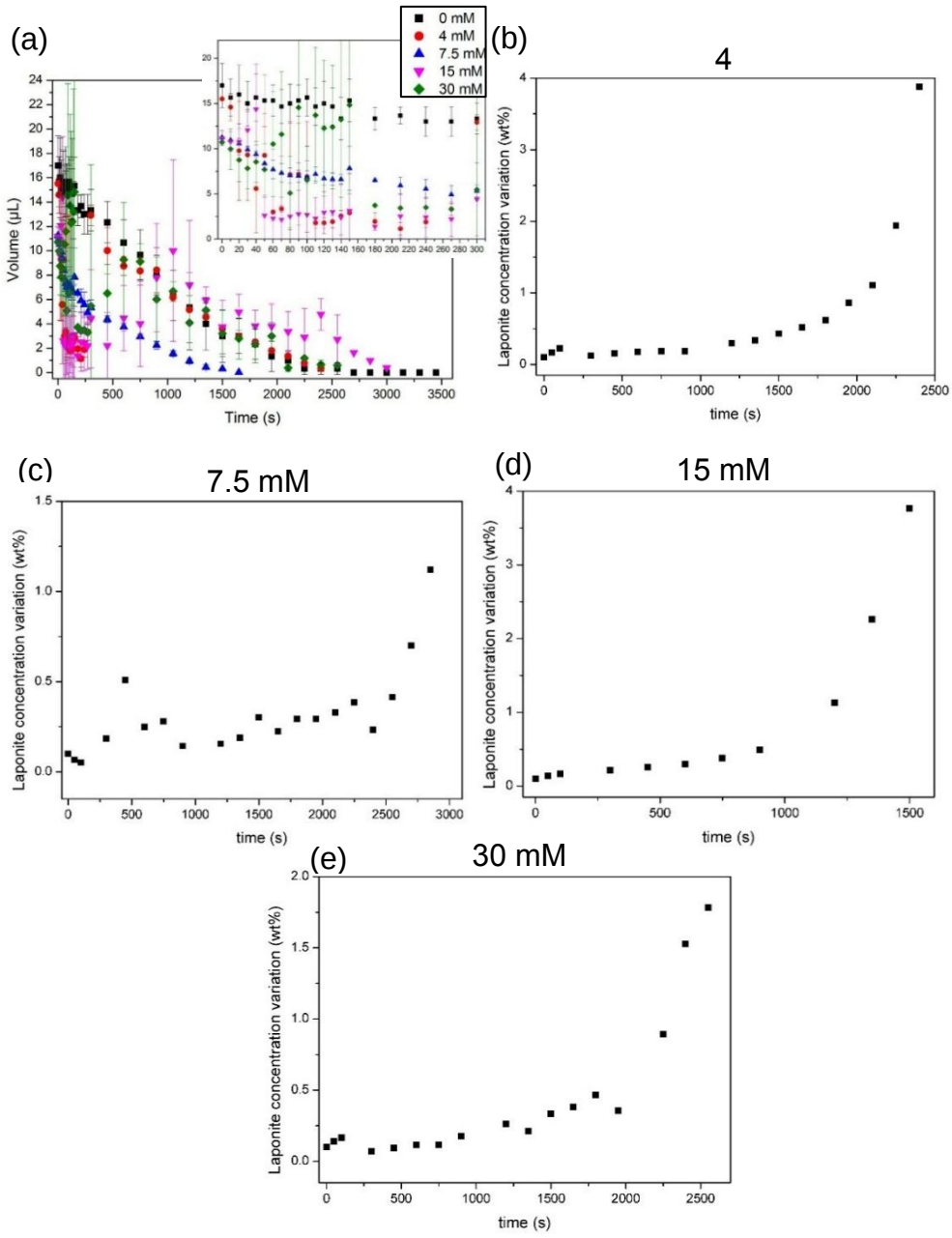

Figure 6-15: (a) Evolution of volume V with time of aqueous based Laponite at C_{Lap}=0.1 wt% sessile droplets with different added surfactant concentration (C_{SDS}= 0 to 30 mM). Evolution of local concentration in aqueous based Laponite sessile droplets with different added surfactant concentration b) 4 mM (c) 7.5 mM (d) 15 mM and (e) 30 mM. The droplets were deposited on uncoated glass slides. The different evolutions were extracted from contact angle goniometer recordings.

- Final deposit patterns analysis

Upon complete solvent evaporation, several pattern were obtained (see Figure 6-16). Below the surfactant cmc a ring-like stain was obtained while for

concentration above the cmc a mountain-like dried deposit structure was observed. Below, the cmc (C_{SDS}= 4 mM) the variation of concentration of SDS is not significant enough to induce a surface tension gradient along the air/water interface hence generating a Marangoni flow. Thus, the particles within the droplet can be transported towards the TPCL. Also, at C_{SDS}= 4 mM the gelation concentration of Laponite is not reached $C_{Lap,\ gel}$= 3 wt% with time Whereas, at concentration C_{SDS}≥ 7.5 mM we can assume that the cmc will be reached early on during the evaporation process. Moreover, above this concentration, the surface will be saturated with surface which could explain the similar dried deposit patterns from 7.5 to 30 mM.

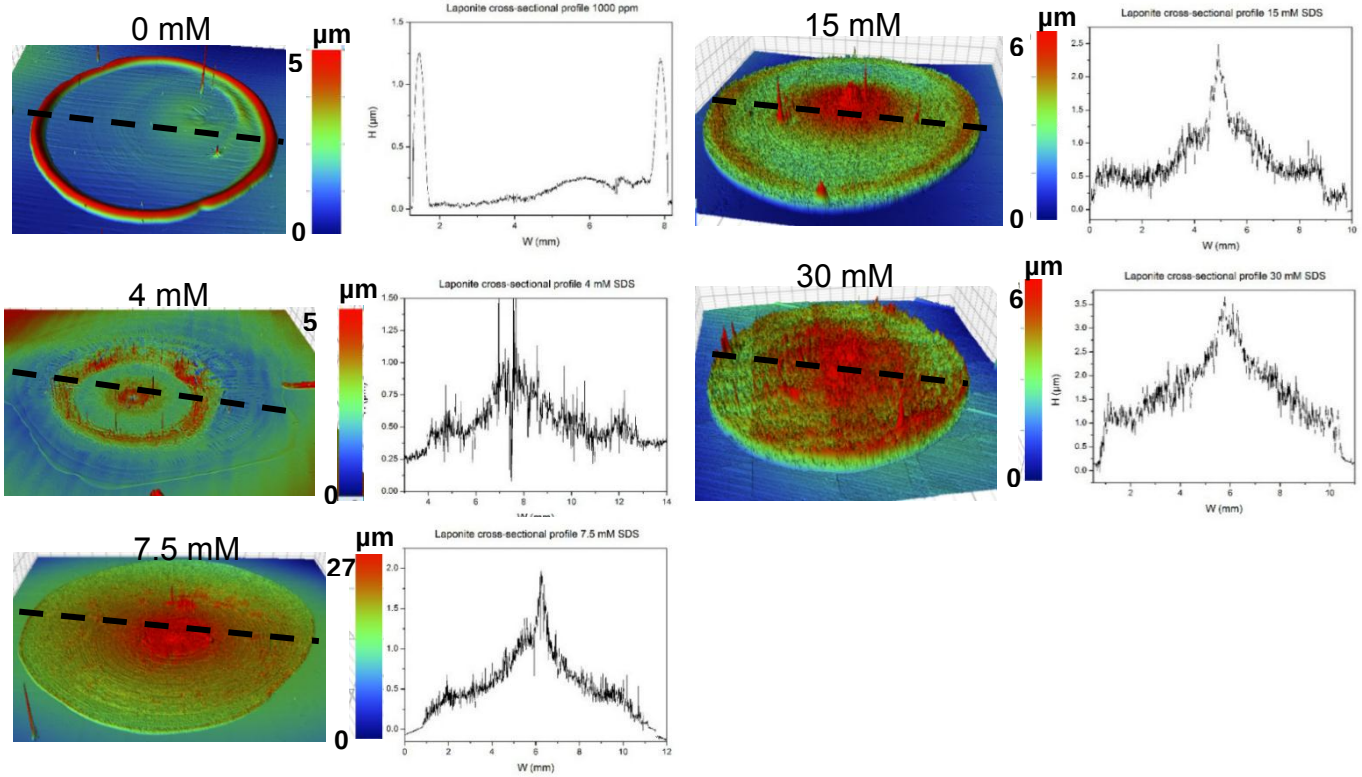

Figure 6-16: Three-dimensional topographical WLI images of aqueous based Laponite (at C_{Lap}= 0.1 wt%) dried deposits on uncoated glass slides with different added surfactant concentration (C_{SDS}= 0 to 30 mM) and their corresponding cross-sectional profiles along the black dotted line.

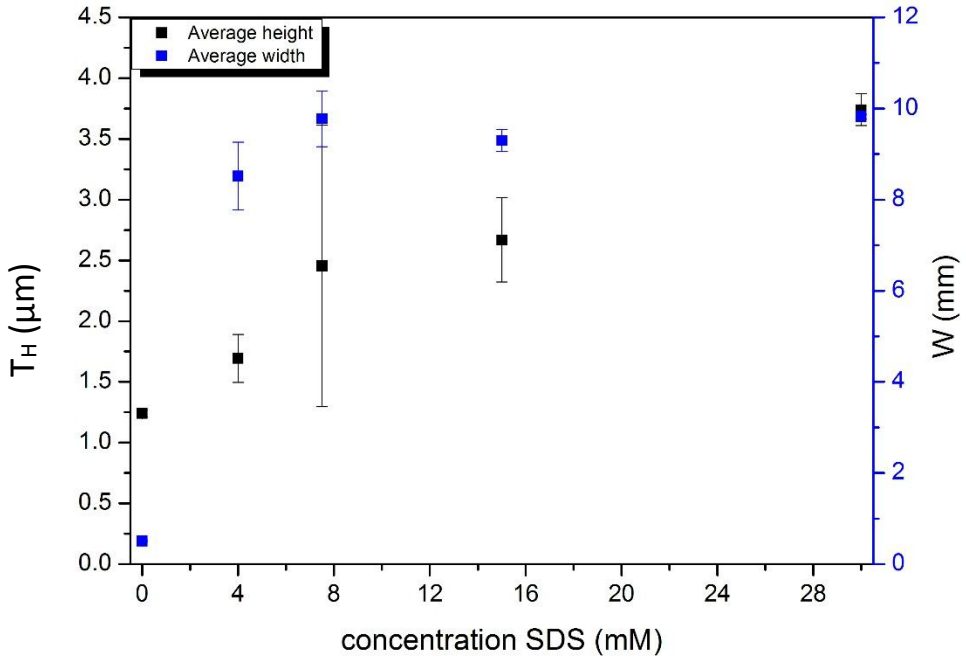

Figure 6-17: Features (height, T_H and width W) evolution of dried deposits of aqueous based Laponite sessile droplets at C_{Lap}= 0.1 wt% with different added surfactant concentration (C_{SDS}= 0 to 30 mM).

The influence of SDS concentration on the height and width of the final deposit patterns can be seen on Figure 6-17.

The thickness plotted on this figure represents the highest height of the final dried deposit. From these data it can be concluded that:

- The concentration of SDS does not influence significantly the final deposit patterns when the cmc is reached whether it is reached during the solvent evaporation process or when the final SDS within the suspension was already above the cmc.

The deposit width was determined as the overall length of the deposit and similarly the variation was not significant for the different deposits.

6.3.4 Formation of complex dried deposit patterns

In this subsection, the influence of salt addition on the deposit patterns of Laponite sessile droplets has been explored.

In fact, previous work studied the phase diagram of Laponite at different range of both Laponite and salt concentration (Levitz et al., 2000; Li et al., 2005; Huang and Berg, 2006). Furthermore, it has already been established and explained previously that as Laponite ages the properties of the suspensions are modified and different phases can be highlighted (Mourchid and Levitz, 1998; Saunders et al., 1999; Knaebel et al., 2000; Ruzicka et al., 2007; Joshi et al., 2008; Shahin and Joshi, 2012; Zulian et al., 2014; Angelini et al., 2014; Pek-Ing and Yee-Kwong, 2015).

Considering all of these previous factors, we focused our investigation on fixed Laponite particles concentration in weight at C_{Lap}= 0.1 wt% while varying the salt concentration C_{NaCl}= 1-10 mM (this corresponds to the final concentration in the different aqueous based suspensions).

- Wetting properties and drying kinetics

On Figure 6-18a, the evolution of Laponite sessile droplets contact diameter is presented. The inset on the plot represents a zoom of the diameter variation from 0 to 300 seconds. From these experimental results, it can be observed that the contact diameter variation follows two mains stage. The first stage during which, the contact diameter is initially pinned regardless of the addition of salt in the suspensions. It is worth noting that this phenomenon was expected as the electrolyte is not surface active. And a second phase where the droplet contact diameter decreases overtime. This two main stages are consistent with an initial pinning effect characterised by a ring-like stain as seen on Figure 6-20 and the second stage which sees the contact diameter decrease can be explained by a receding of the contact line. Indeed, the initial Laponite concentration is low C_{Lap} = 0.1 wt% and the added electrolyte concentration is also low as such it cannot promote the pinning of the contact line throughout the entire drying process (Deegan, 2000; Maheshwari et al., 2008; Sangani et al., 2009; Weon and Je, 2013). Also, a slight increase in droplet contact diameter is observed towards the end of the droplet lifetime, this increase is due to a difficulty in clearly assessing the spherical shape of the droplet deposit hence in the calculation.

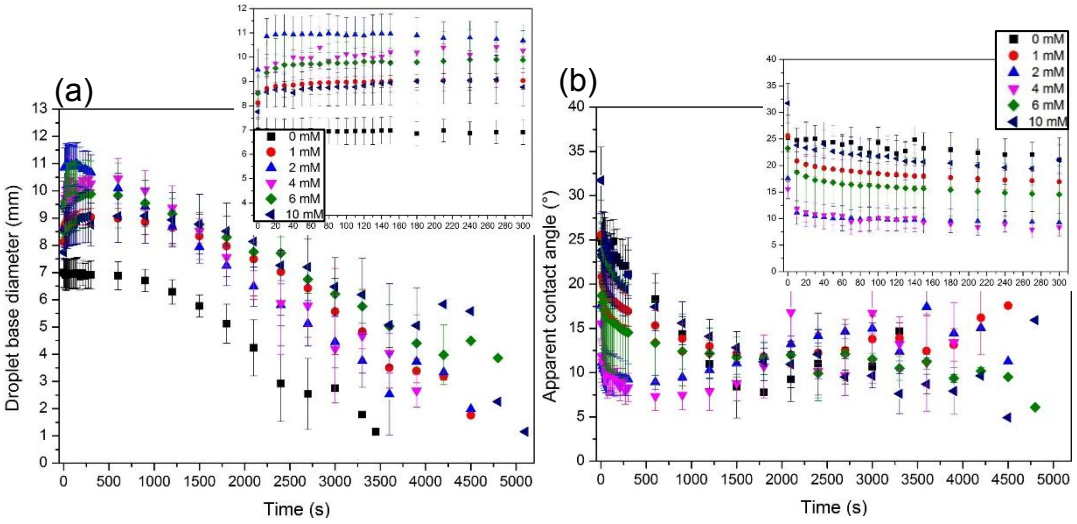

Figure 6-18: Evolution of (a) droplet contact diameter $2r_d$ and (b) apparent contact angle θ_{ACA} of Laponite at C_{Lap}=0.1wt% with different added electrolyte concentrations (C_{NaCl}= 1 to 10 mM) with time on the entire droplet lifetime and a zoom in between 0 to 300 s. The droplets were deposited on uncoated glass slides. The evolution was extracted from contact angle goniometer recordings.

From the droplet contact diameter and height, the apparent contact angle, θ_{ACA} can be extracted. As such, Figure 6-18b presents the variation as a function time of the angle formed by the sessile droplet and the solid substrate. In order, to determinate this angle, it is assumed a continuous equilibrium state of the droplet and that the solid surface is smooth. Experimentally, as expected the apparent contact angle is seen to decrease gradually overtime. This behaviour is expected especially since it was previously seen that the contact diameter of the droplets was pinned. However, towards the end of the drying the erratic trend of the apparent contact angle could be explain as seen due to the lack of clarity on the image and the gradual loss of the spherical shape of the droplet.

From the droplet contact diameter, the variation of volume over time can also be extracted. On Figure 6-19, the plot of the volume variation is thus displayed. From this results it can be concluded that the addition of electrolyte to the system does not influence the evaporation rate in any way. Indeed, the evaporation rate which corresponds to the slope of the volume variation is similar in all cases from the no salt addition to the 10 mM (cf. Table 6-3).

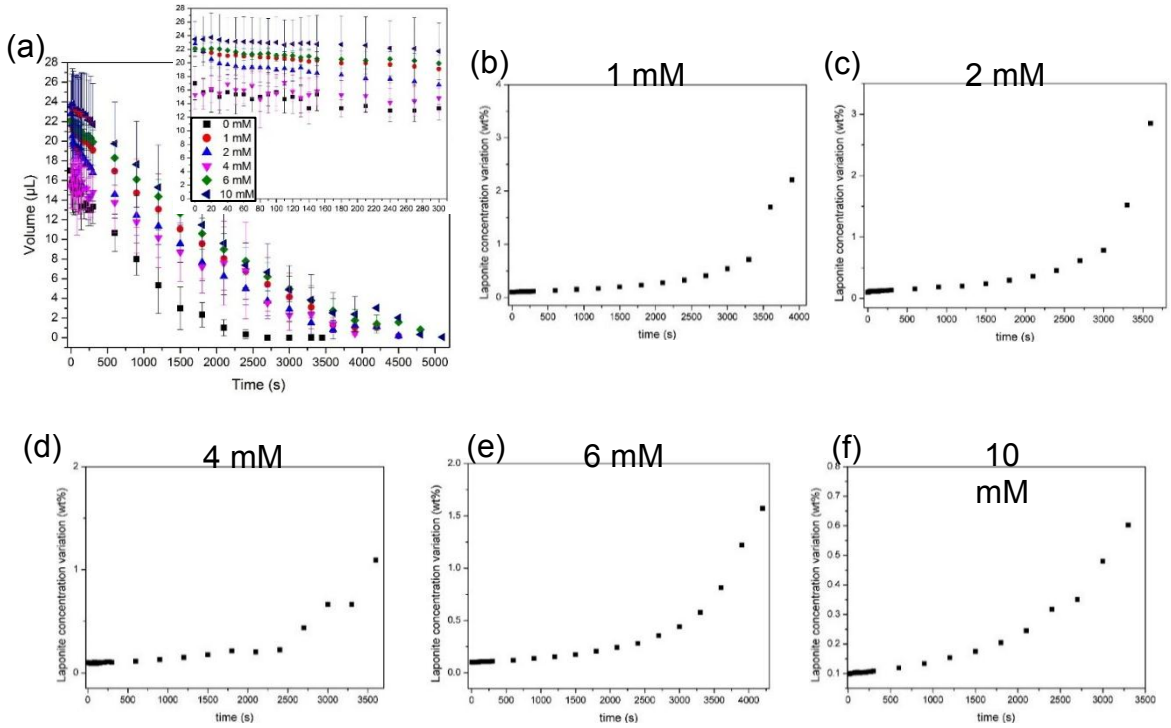

Figure 6-19: (a) Evolution of volume V with time of aqueous based Laponite at C_{Lap}=0.1 wt% sessile droplets with different added electrolyte concentration (C_{NaCl}= 1 to 10 mM). Evolution of local concentration in aqueous based Laponite sessile droplets with different added electrolyte concentration b) 1 mM (c) 2 mM (d) 4 mM (e) 6 mM and (e) 30 mM. The droplets were deposited on uncoated glass slides. The different evolutions were extracted from contact angle goniometer recordings.

Table 6-3: Summary of the different evaporation rate of Laponite sessile droplets with and without added electrolyte (C_{NaCl}= 0 to 10 mM).

C_{NaCl} (mM)	Evaporation rate (10^{-3}µL/s)
0	5.8
1	5.3
2	5.0
4	4.2
6	5.0
10	5.2

- Final deposit patterns analysis

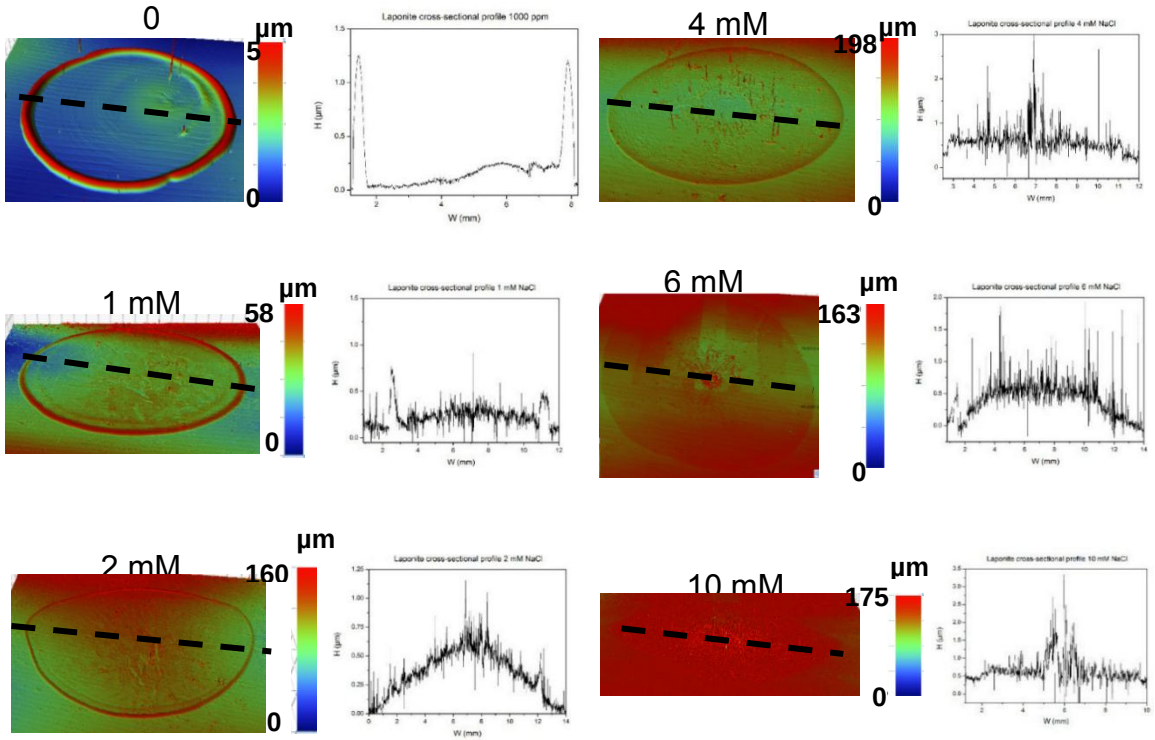

Figure 6-20: Three-dimensional topographical WLI images of dried deposits of Laponite at C_{Lap}= 1000 ppm with different added electrolyte concentration (C_{NaCl}= 1 to 10 mM) and their corresponding cross-sectional profiles along the black dotted lines. The droplets were deposited on uncoated glass slides.

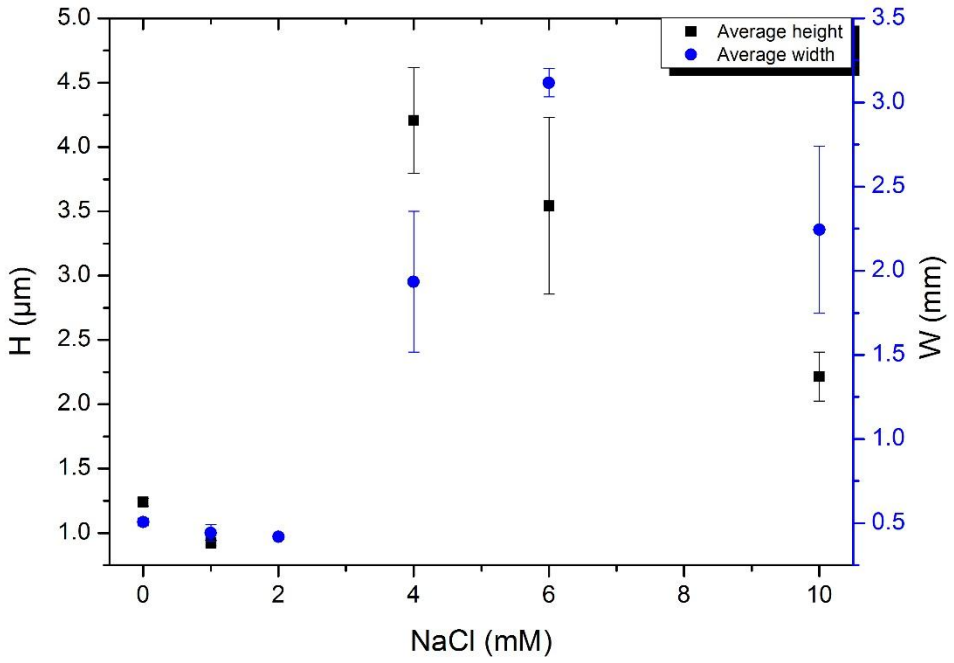

Figure 6-21: Features variation of dried deposit (height, T_H and width W) of aqueous based Laponite droplets at C_{Lap}= 0.1wt% with different added electrolyte concentration (CNaCl= 1 to 10 mM).

Figure 6-21 displays the influence of electrolyte concentration for Laponite 0.1wt% droplets on the final deposit patterns. From these results no clear trends can be drawn out. Indeed, the features of the dried deposit patterns are not clearly dependent on the electrolyte concentration. Rather, the behaviour seems to be similar at very electrolyte concentration ($0 \leq C_{NaCl} \leq 2$ mM) with width and height in the same range. Whereas, the edge features seems to increase dramatically at C_{NaCl}= 4 mM before starting to decrease again from C_{NaCl}= 6 mM.

6.4 Summary

The control of the final deposit during a printing process is a complex and challenging phenomenon. Several parameters can be tailored in order to obtained a specific morphology of the final deposit. This chapter has focused on the variation of Laponite sessile droplets characteristics and how it could influence the formation of various complex patterns.

In first instance, the evaporation process of Laponite as a function of Laponite concentration was investigated. From this investigation, it was confirmed that due to the inherent property of Laponite with its different ergodic state, a sol-gel transition lead to a film deposit as a final deposit patterns at high concentration ($C_{Lap} \geq$ 1wt%). At low Laponite concentration C_{Lap} <1wt% the classic “coffee ring effect” was observed as the final deposit pattern. Also, it was confirmed that the dried deposit structure (deposit height and width) was dependent on the initial Laponite concentration. Last but not least a scaling relation was also identified: the final droplet deposit height and width were seen to increase with the initial Laponite concentration increase.

Further evaporative study in binary solvent mixtures (ethanol/water mixtures) were also reviewed. While working at a fixed initial Laponite concentration (C_{Lap} = 0.1wt%) and increasing the concentration of ethanol in the systems (C_{EtOH} = 50-90 vol%), two main patterns were observed. For an initial concentration of ethanol of 50 vol%<C_{EtOH} < 80 vol% a film deposit was generated whereas a ring-like stain at C_{EtOH} = 90 vol% was generated. It was our understanding that an evaporation-driven sol-gel transition occurred. Hence, it was believed that the convective flow toward the three-phase contact line (which lead to the formation of a ring-like deposit) was altered for the ethanol concentration $C_{EtOH} \leq$ 80 vol%. However, at a concentration of ethanol of C_{EtOH} = 90 vol%, it was believed that too much radial flow was generated hence a ring-like stain was produced.

The analysis of the drying of sessile droplets of Laponite based nanofluids with added surfactant (SDS) (above and below the cmc with C_{SDS} =4-30 mM) were also carried out. For all the selected surfactant concentration a film was observed upon complete solvent evaporation. A similar evaporation-driven sol-gel transition was suggested to explain this final deposit patterns.

However, from our study it was also demonstrated that the addition of a new component to the formulation could have singular effect. Indeed, we stumbled upon complex patterns with added electrolyte in our system. It was not believed that an evaporation-driven sol-gel transition occurred for this electrolyte concentration range (C_{NaCl} = 1-10 mM).

Chapter 7
Conclusions and Future work

Throughout this thesis several aspects of droplet evaporation and their subsequent dried residual patterns have been investigated. To this end, the study on the mechanisms at work during wetting and evaporation of nanoparticle laden fluids has been carried out. Generation of droplets and wetting behaviour studies have been carried out systematically in different systems and with different type of particles to explore further the particle-particle, particle-solid, particle-liquid and liquid-solid interactions in nanofluids droplets at a variety of scales namely from macro- to nanoscale. These systems were studied in controlling conditions thanks to the use of a temperature and relative humidity ceramic chamber. The ceramic chamber was fitted to a droplet deposition stage to reveal the evaporation mechanisms and particle self-assembly upon complete solvent evaporation. Using wetting parameters such as droplet apparent contact angle, droplet contact diameter, droplet volume, evaporation rate, droplet thickness and sedimentation kinetics have been extracted from the results to aid explanation of the different drying behaviours observed. Two novels scaling laws to examine the cracks patterns as a function of particle concentration and surfactant concentration have been determined and validated. Both scaling laws are based on Alex Routh work. Alex Routh law is a model which depicts the scaling between cracks in drying colloidal dispersions. The main achievements observed during this experimental work, which goals was to increase knowledge on the complex phenomena behind drying droplets on solid surfaces are summarised in the following section.

7.1 Key findings

7.1.1 Enhancing the “Coffee Ring Effect” for spherical particles,

The direct influence of the initial nanoparticle concentration on their self-assembly upon solvent evaporation was further studied. The cracks patterns observed at higher nanoparticles were investigated further. Interestingly, the addition of electrolyte, or use of binary solvent mixtures were found to generate various deposits patterns. Disordered ring-like stains alongside attenuation of cracks patterns were observed. Moreover, a power law relationship between the surfactant concentration and the dried deposit edges

features (thickness and width) were observed for the nanofluids droplets with added electrolyte and in binary mixtures. Also, the aggregation of PMMA polymeric particles lead to unexpected patterns. Despite, similar characteristics (spherical particles and negatively charged), the aggregation kinetics and the probable density difference could explain the aggregated final deposit patterns.

7.1.2 Attenuation of crack patterns with anionic surfactant addition and formation of complex patterns

In this section, the influence of an anionic surfactant concentration on the dried residual deposit was examined in the case of Ludox AS-40® nanoparticles. While considering the wetting behaviour no clear stick-slip motion was observed however several concentric rings were observed in the final deposition patterns. A singular finding is that above the cmc, when the droplet surface will be saturated with the surfactant two different dried residual patterns were generated. A scaling law of the cracking pattern and the initial surfactant concentration was established and validated. An attenuation of the crack patterns was also observed, however more work need to be done to uncover the reason behind this behaviour.

In ethanol/water mixtures, the wetting behaviour is singular, and the dried residual pattern is quite interesting. A tracking of the particles using either bigger particles or a new set-up could aid our understanding for the overall dried deposit patterns observed.

When sedimentation occur within the droplet laden with PMMA latex nanoparticles, no coffee ring effect was observed in either ethanol/water mixtures and with electrolyte addition. It is proposed that these dried residual deposits are analysed further, especially the influence of the evaporation rate.

7.1.3 Suppression of “Coffee Ring Effect” by sol-gel transition with disk-like particles

Upon establishing the production of various ring-like patterns for ring-like spherical nanoparticles, we then examined another shape: disk-like clay Laponite nanoparticles. To summarize, aqueous based suspensions were studied with and without additives (electrolyte and surfactant) and in binary mixtures (ethanol/water mixtures at different ratios). We found that a film

deposit was observed while increasing nanoparticles concentration. This film is due to the sol-gel transition and it is usually observed. A particularly interesting observation is that at an initial concentration well below the sol-gel transition with some additives the formation of a uniform film was possible upon total solvent evaporation.

7.2 Future work

Despite, our thorough investigation of the evaporative behaviour and structuring of spherical and disk-like nanoparticles several questions remain elusive. Thus in this section, some future research ideas are presented.

For example, the influence of nanoparticles concentration on the final deposit patterns while modifying the substrate characteristics (honeycomb, cellulose, living cells or hydrophobic substrates) should be investigated. This could help to propose a universal mechanism for the particle self-assembly.

The study of spherical Ludox AS-40® silica and PMMA polymeric particles in binary EtOH/H2O mixtures and with electrolyte addition was rather inconclusive. Therefore, more spherical silica and PMMA polymeric particles concentration and size should be investigated in order to fully understand the effect of the particles on the resulting patterns. As the addition of SDS proved to attenuated the cracks features and hence the particle self-organisation, various concentration of these silica particles as well as more complex systems such as EtOH/SDS/H_2O should be examined. This study could potentially lead to further crack patterns attenuation and more uniform dried deposit.

Furthermore, the evaporative behaviour of disk-like clay Laponite nanoparticles at lower concentration the generation of the occurrence of sol-gel transition should be further investigated. The rheology change and the corresponding states of the Laponite should be determined to improve the phase diagram in EtOH/H2O mixtures and SDS. This information could potentially lead to more uniform films deposits.

7.3 Limitations of this work

At this stage, it is essential to recognize some limitations pertaining to this work. One limitation that stands out is the lack of information regarding the droplet mass variations to improve the evaporation rate monitoring. A data logger could be used to monitor the droplet weight evolution, which could help a better identification of the different evaporation rate. Another limitation is the lack of knowledge in regard to the roughness of the silane coated glass substrates to further understand the influence of the substrate on the wetting properties. Finally, the droplet deposition only gives a side view which does not allow to see flow within the drop to better explain the dried residual deposition patterns. These limitations are mainly linked to the current experimental set up and thus could be resolved by implementing a new apparatus including: a microbalance to the system, a top view camera coupled with an infrared system. If more time was available, the experiment should be carried out on a wider variety of substrates, should involve mixtures of spherical and disk-like particles, should determine Marangoni numbers throughout the evaporation process to check to effect of Marangoni flow.

7.4 Concluding statement

This thesis has highlighted several important original contributions to the field of microliter droplets evaporation and the control of their subsequent dried residual deposit have been made. For spherical particles, two novels scaling law have been provided which validate the dependence of crack patterns with the initial particle concentration and the concentration of additive such as anionic surfactant. In the case of disk-like particles, it has been developed and validated that for an initial low particle concentration (C_{Lap}= 1000 ppm) in some systems, more precisely ethanol/water mixtures and with anionic surfactant a film was formed as the dried residual deposit.

References

Abramchuk, S.S., Khokhlov, A.R., Iwataki, T., Oana, H. and Yoshikawa, K. 2001. Direct observation of DNA molecules in a convection flow of a drying droplet. *Europhysics Letters*. **55**(2), pp.294–300.

Alam, P., Toivakka, M., Backfolk, K. and Sirviö, P. 2007. Impact spreading and absorption of Newtonian droplets on topographically irregular porous materials. *Chemical Engineering Science*. **62**(12), pp.3142–3158.

Allain, C. and Limat, L. 1995. Regular patterns of cracks formed by directional drying of a colloidal suspension. *Physical Review Letters*. **74**(15), pp.2981–2985.

Angelini, R., Zaccarelli, E., de Melo Marques, F.A., Sztucki, M., Fluerasu, A., Ruocco, G. and Ruzicka, B. 2014. Glass-glass transition during aging of a colloidal clay. *Nature communications*. **5**, p.4049.

Anyfantakis, M. and Baigl, D. 2014. Dynamic photocontrol of the coffee-ring effect with optically tunable particle stickiness. *Angewandte Chemie - International Edition*. **53**(51), pp.14077–14081.

Anyfantakis, M., Geng, Z., Morel, M., Rudiuk, S. and Baigl, D. 2015. Modulation of the coffee-ring effect in particle/surfactant mixtures: the importance of particle–interface interactions. *Langmuir*. **31**(14), pp.4113–4120.

Arayanarakool, R., Shui, L., van den Berg, A. and Eijkel, J.C.T. 2011. A new method of UV-patternable hydrophobization of micro- and nanofluidic networks. *Lab Chip*. **11**(24), pp.4260–4266.

Askounis, A., Sefiane, K., Koutsos, V. and Shanahan, M.E.R. 2014. Effect of particle geometry on triple line motion of nano-fluid drops and deposit nano-structuring. *Advances in Colloid and Interface Science*. **222**(Reinhard Miller), pp.44–57.

Attension Theta 2015. *Theory Note 2 Static and dynamic surface tension and their measurement techniques*.

Baretta, M.A., Enriquez, A.L., Cartagena, J. and Garcia, J.A. 2006. System and method for optically tracking objects using a spectral fingerprint of fluorescent compounds. , pp.1–8.

Bartell, F.E. and Shepard, J.W. 1953. Surface roughness as related to hysteresis of contact angles. I. The system paraffin-water-air. *The Journal of Physical Chemistry*. **57**(2), pp.211–215.

Bermel, A.D. and Bugner, D.E. 1999. Particle size effects in pigmented ink jet inks. *Journal of Imaging Science and Technology*. **43**(4), pp.320–324.

Bhardwaj, R., Fang, X. and Attinger, D. 2009. Pattern formation during the evaporation of a colloidal nanoliter drop: a numerical and experimental study. *New Journal of Physics*. **11**(July), p.075020.

Bhardwaj, R., Fang, X., Somasundaran, P. and Attinger, D. 2010. Self-assembly of colloidal particles from evaporating droplets: role of DLVO

interactions and proposition of a phase diagram. *Langmuir*. **26**(11), pp.7833–42.

Bi, W., Wu, X. and Yeow, E.K.L. 2012. Unconventional multiple ring structure formation from evaporation-induced self-assembly of polymers. *Langmuir*. **28**(30), pp.11056–11063.

Bigioni, T.P., Lin, X.-M., Nguyen, T.T., Corwin, E.I., Witten, T.A. and Jaeger, H.M. 2006. Kinetically driven self assembly of highly ordered nanoparticle monolayers. *Nature Materials*. **5**(4), pp.265–270.

Birdi, K.S. and Vu, D.T. 1993. Wettability and the evaporation rates of fluids from solid surfaces. *Journal of Adhesion Science and Technology*. **7**(6), pp.485–493.

Birdi, K.S., Vu, D.T. and Winter, A. 1989. A study of the evaporation rates of small water drops placed on a solid surface. *The Journal of Physical Chemistry*. **93**(9), pp.3702–3703.

Biswas, S., Gawande, S., Bromberg, V. and Sun, Y. 2010. Effects of Particle Size and Substrate Surface Properties on Deposition Dynamics of Inkjet-Printed Colloidal Drops for Printable Photovoltaics Fabrication. *Journal of Solar Energy Engineering*. **132**(2), p.021010.

Boland, T., Xu, T., Damon, B. and Cui, X. 2006. Application of inkjet printing to tissue engineering. *Biotechnology journal*. **1**(9), pp.910–7.

Bonn, D., Kellay, H., Tanaka, H., Wegdam, G. and Meunier, J. 1999. Laponite: what is the difference between a gel and a glass? *Langmuir*. **15**(22), pp.7534–7536.

Breinlinger, T. and Kraft, T. 2014. A simple method for simulating the coffee stain effect. *Powder Technology*. **256**(April), pp.279–284.

Brunet, P. 2012. Particle deposition after droplet evaporation on ultra-hydrophobic micro-textured surfaces. *Soft Matter*. **8**(44), pp.11294–11301.

Brutin, D. 2013. Influence of relative humidity and nano-particle concentration on pattern formation and evaporation rate of pinned drying drops of nanofluids. *Colloids and Surfaces A: Physicochemical and Engineering Aspects*. **429**, pp.112–120.

Brutin, D., Sobac, B., Loquet, B. and Sampol, J. 2011. Pattern formation in drying drops of blood. *Journal of Fluid Mechanics*. **667**, pp.85–95.

Butt, H.-J., Cappella, B. and Kappl, M. 2005. Force measurements with the atomic force microscope: Technique, interpretation and applications. *Surface Science Reports*. **59**(1–6), pp.1–152.

Caddock, B.D. and Hull, D. 2002. Influence of humidity on the cracking patterns formed during the drying of sol-gel drops. *Journal of Materials Science*. **37**(4), pp.825–834.

Carle, F. and David, B. 2015. Chapter 9: Convection *In*: *Droplet Wetting and Evaporation From Pure to Complex Fluids*. Elsevier Inc., pp.115–128.

Carrier, O. and Bonn, D. 2015. Chapter 2: Contact angles and the surface

free energy of solids *In*: *Droplet Wetting and Evaporation From Pure to Complex Fluids*., pp.15–23.

Cassie, A.B.D. and Baxter, S. 1944. Wettability of porous surfaces. *Transactions of the Faraday Society*. **40**(5), pp.546–551.

Cecere, A., Buffone, C. and Savino, R. 2014. Self-induced Marangoni flow in evaporating alcoholic solutions. *International Journal of Heat and Mass Transfer*. **78**, pp.852–859.

Chau, T.T., Bruckard, W.J., Koh, P.T.L. and Nguyen, A. V. 2009. A review of factors that affect contact angle and implications for flotation practice. *Advances in Colloid and Interface Science*. **150**(2), pp.106–15.

Chen, G. and Mohamed, G.J. 2010. Complex protein patterns formation via salt-induced self-assembly and droplet evaporation. *European Physical Journal E*. **33**(1), pp.19–26.

Chen, L. and Evans, J.R.G. 2010. Drying of colloidal droplets on superhydrophobic surfaces. *Journal of Colloid And Interface Science*. **351**(1), pp.283–287.

Chen, L. and Evans, J.R.G.J. 2009. Arched structures created by colloidal droplets as they dry. *Langmuir*. **25**(19), pp.11299–301.

Chen, P., Toubal, M., Carlier, J., Harmand, S., Nongaillard, B. and Bigerelle, M. 2016. Evaporation of binary sessile drops: Infrared and acoustic methods to track alcohol concentration at the interface and on the surface. *Langmuir*. **32**(38), pp.9836–9845.

Chen, R.-H., Phuoc, T.X. and Martello, D. 2011. Surface tension of evaporating nanofluid droplets. *International Journal of Heat and Mass Transfer*. **54**(11–12), pp.2459–2466.

Cheng, A.K.H., Soolaman, D.M. and Yu, H.-Z. 2006. Evaporation of microdroplets of ethanol-water mixtures on gold surfaces modified with self-assembled monolayers. *The Journal of Physical Chemistry B*. **110**(23), pp.11267–11271.

Chhasatia, V.H., Joshi, A.S. and Sun, Y. 2010. Effect of relative humidity on contact angle and particle deposition morphology of an evaporating colloidal drop. *Applied Physics Letters*. **97**, p.231909.

Chon, C.H., Paik, S., Tipton, J.B. and Kihm, K.D. 2007. Effect of Nanoparticle Sizes and Number Densities on the Evaporation and Dryout Characteristics for Strongly Pinned Nanofluid Droplets. *Langmuir*. **23**(6), pp.2953–2960.

Choudhury, M.D., Dutta, T. and Tarafdar, S. 2013. Pattern formation in droplets of starch gels containing NaCl dried on different surfaces. *Colloids and Surfaces A: Physicochemical and Engineering Aspects*. **432**, pp.110–118.

Christy, J.R.E., Hamamoto, Y. and Sefiane, K. 2011. Flow transition within an evaporating binary mixture sessile drop. *Physical Review Letters*. **106**(20), p.205701.

Christy, J.R.E., Sefiane, K. and Munro, E. 2010. A study of the velocity field

during evaporation of sessile water and water/ethanol drops. *Journal of Bionic Engineering*. **7**(4), pp.321–328.

Cosgrove, T. 2005. *Colloid Science: Principles, methods and applications*. Wiley.

Crivoi, A. and Duan, F. 2013. Amplifying and attenuating the coffee-ring effect in drying sessile nanofluid droplets. *Physical Review E*. **87**(4), p.042303.

Crivoi, A. and Duan, F. 2013. Effect of surfactant on the drying patterns of graphite nanofluid droplets. *The Journal of Physical Chemistry B*. **117**(19), pp.5932–5938.

Crivoi, A. and Duan, F. 2014. Three-dimensional Monte Carlo model of the coffee-ring effect in evaporating colloidal droplets. *Scientific reports*. **4**, p.4310.

Cui, L., Zhang, J., Zhang, X., Huang, L., Wang, Z., Li, Y., Goa, H., Zhu, S., Wang, T. and Yang, B. 2012. Suppression of the Coffee Ring Effect by Hydrosoluble Polymer Additives. *Applied Materials & Interfaces*. **4**(5), pp.2775–2780.

Cummins, H.Z. 2007. Liquid, glass, gel: the phases of colloidal Laponite. *Journal of Non-Crystalline Solids*. **353**(41), pp.3891–3905.

Dash, S. and Garimella, S. V. 2013. Droplet evaporation dynamics on a superhydrophobic surface with negligible hysteresis. *Langmuir*. **29**(34), pp.10785–10795.

Deegan, R. 2000. Pattern formation in drying drops. *Physical Review E*. **61**(1), pp.475–485.

Deegan, R., Bakajin, O. and Dupont, T. 1997. Capillary flow as the cause of ring stains from dried liquid drops. *Nature*. **389**(6653), pp.827–829.

Deegan, R.D., Bakajin, O., Dupont, T.F., Huber, G., Nagel, S.R. and Witten, T.A. 2000. Contact line deposits in an evaporating drop. *Physical Review E*. **62**(1 Part B), pp.756–765.

Derby, B. 2010. Inkjet printing of functional and structural materials: Fluid property requirements, feature stability, and resolution. *Annual Review of Materials Research*. **40**(1), pp.395–414.

Doganci, M.D., Cavusoglu, S., Oksuz, M. and Erbil, H.Y. 2014. Effect of surface free energy to control the deposit morphology during evaporation of graphite/SDS dispersion drops. *Colloids and Surfaces A: Physicochemical and Engineering Aspects*. **461**, pp.310–322.

Doganci, M.D. and Erbil, H.Y. 2013. Shape and diameter control of C60 fullerene micro-stains by evaporation of aqueous SDS–fullerene dispersion drops. *Colloids and Surfaces A: Physicochemical and Engineering Aspects*. **432**, pp.104–109.

Doganci, M.D., Sesli, B.U. and Erbil, H.Y. 2011. Diffusion-controlled evaporation of sodium dodecyl sulfate solution drops placed on a hydrophobic substrate. *Journal of colloid and interface science*. **362**(2), pp.524–31.

Dugyala, V.R. and Basavaraj, M.G. 2014. Control over coffee-ring formation in evaporating liquid drops containing ellipsoids. *Langmuir*. **30**(29), pp.8680–8686.

Dugyala, V.R. and Basavaraj, M.G. 2015. Evaporation of sessile drops containing colloidal rods: coffee-ring and order-disorder transition. *The journal of physical chemistry. B*. **119**(9), pp.3860–7.

Dundigalla, A., Lin-Gibson, S., Ferreiro, V., Malwitz, M.M. and Schmidt, G. 2005. Unusual multilayered structures in poly(ethylene oxide)/laponite nanocomposite films. *Macromolecular Rapid Communications*. **26**(3), pp.143–149.

Dutta Choudhury, M., Dutta, T. and Tarafdar, S. 2015. Growth kinetics of NaCl crystals in a drying drop of gelatin: transition from faceted to dendritic growth. *Soft Matter*. **11**(35), pp.6938–6947.

Dutta, T., Giri, A., Choudhury, M.D. and Tarafdar, S. 2013. Experiment and simulation of multifractal growth of crystalline NaCl aggregates in aqueous gelatin medium. *Colloids and Surfaces A: Physicochemical and Engineering Aspects*. **432**, pp.127–131.

Eral, H.B., Augustine, D.M., Duits, M.H.G. and Mugele, F. 2011. Suppressing the coffee stain effect: how to control colloidal self-assembly in evaporating drops using electrowetting. *Soft Matter*. **7**(10), p.4954.

Erbil, H.Y. 2012. Evaporation of pure liquid sessile and spherical suspended drops: a review. *Advances in colloid and interface science*. **170**(1), pp.67–86.

Everett, D.H. 1988. Chapter 1: What are colloids? *In*: *Basic principles of colloid science*. The Royal Society of Chemistry, pp.1–15.

Fabien, G., Antoni, M. and Sefiane, K. 2011. Use of IR thermography to investigate heated droplet evaporation and contact line dynamics. *Langmuir*. **27**(11), pp.6744–6752.

Faers, M.A. and Pontzen, R. 2008. Factors influencing the association between active ingredient and adjuvant in the leaf deposit of adjuvant-containing suspoemulsion formulations. *Pest Management Science*. **64**(8), pp.820–833.

Fang, X., Li, B., Wu, J., Maldarelli, C., Sokolov, J.C., Rafailovich, M.H. and Somasundaran, P. 2009. Imaging and estimating the surface heterogeneity on a droplet containing cosolvents. *The journal of physical chemistry. B*. **113**(29), pp.9636–9.

Fuller, S. 2002. Ink-jet printed nanoparticle microelectromechanical systems. *Journal of Microelectromechanical Systems*. **11**(1), pp.54–60.

Gate, B. 2014. Rainy summer day raindrops on window glass. Available from: http://revelwallpapers.net/w/f3i25WAEoJ9Vjfxd7rGrqH/rainy-summer-day-raindrops-on-window-glass-wallpapers.html.

Ghosh, U.U., Chakraborty, M., Bhandari, A.B., Chakraborty, S. and DasGupta, S. 2015. Effect of Surface Wettability on Crack Dynamics and Morphology of Colloidal Films. *Langmuir*. **31**(22), pp.6001–6010.

Girard, F., Antoni, M. and Sefiane, K. 2008. On the effect of Marangoni flow on evaporation rates of heated water drops. *Langmuir*. **24**(17), pp.9207–9210.

Good, R.J. 1952. A thermodynamic derivation of Wenzel's modification of Young's equation for contact angles; together with a therory of hysteresis. *Journal of American Chemical Society*. **74**(20), pp.5041–5042.

Gorr, H.M., Zueger, J.M., McAdams, D.R. and Barnard, J. a 2013. Salt-induced pattern formation in evaporating droplets of lysozyme solutions. *Colloids and surfaces. B, Biointerfaces*. **103**, pp.59–66.

Guerrero-Martínez, A., Pérez-Juste, J., Carbó-Argibay, E., Tardajos, G. and Liz-Marzán, L.M. 2009. Gemini-surfactant-directed self-assembly of monodisperse gold nanorods into standing superlattices. *Angewandte Chemie - International Edition*. **48**, pp.9484–9488.

Guo, J.J. and Lewis, J.A. 1999. Aggregation Effects on the Compressive Flow Properties and Drying Behavior of Colloidal Silica Suspensions. . **58**.

Hamamoto, Y., Christy, J.R.E. and Sefiane, K. 2012. The flow characteristics of an evaporating ethanol water mixture droplet on a glass substrate. *Journal of Thermal Science and Technology*. **7**(3), pp.425–436.

Hamon, C., Novikov, S., Scarabelli, L., Basabe-desmonts, L., Liz-marzán, L.M. and Liz-marzán, L.M. 2014. Hierarchical self-assembly of gold nanoparticles into patterned plasmonic nanostructures. *ACS Nano*. **8**(10), pp.10694–10703.

Harris, D.J., Hu, H., Conrad, J.C. and Lewis, J.A. 2007. Patterning colloidal films via evaporative lithography. *Physical Review Letters*. **98**(14), p.148301.

Haynes, W.M. 2017. Chapter 6: Diffusion coefficients in liquids at infinite dilution *In*: C. Press, ed. *CRC Handbook of chemistry and physics*. Boca Raton, Florida: Taylor & Francis, pp.250–251.

Haynes, W.M. 2015. Vapor Pressure and Other Saturation Properties of Water *In*: *CRC Handbook of Chemistry and Physics, 96th Edition*. Boca Raton, Florida, pp.6–5.

Hoath, S.D. 2016. *Fundamentals of Inkjet Printing*. Wiley-VCH.

Hodges, C.S., Ding, Y. and Biggs, S. 2010. The influence of nanoparticle shape on the drying of colloidal suspensions. *Journal of colloid and interface science*. **352**(1), pp.99–106.

Holley, L., Lovelace, J.D. and Williams, G.D. 1995. Electrostatic dissipating cover tape. (US 5447784 A).

Hopkins, R.J., Howle, C.R. and Reid, J.P. 2006. Measuring temperature gradients in evaporating multicomponent alcohol/water droplets. *Physical chemistry chemical physics : PCCP*. **8**(24), pp.2879–88.

Hopkins, R.J. and Reid, J.P. 2006. A Comparative Study of the Mass and Heat Transfer Dynamics of Evaporating Ethanol/Water,

Methanol/Water, and 1-Propanol/Water Aerosol Droplets. *The Journal of Physical Chemistry B*. **110**(7), pp.3239–3249.

Hu, H. and Larson, R.G. 2005. Analysis of the effects of Marangoni stresses on the microflow in an evaporating sessile droplet. *Langmuir*. **21**(19), pp.3972–3980.

Hu, H. and Larson, R.G. 2002. Evaporation of a sessile droplet on a substrate. *The Journal of Physical Chemistry B*. **106**(6), pp.1334–1344.

Hu, H. and Larson, R.G. 2006. Marangoni effect reverses coffee ring depositions. *The Journal of Physical Chemistry B*. **110**(14), pp.7090–4.

Hu, Y.-C., Zhou, Q., Ye, H.-M., Wang, Y.-F. and Cui, L.-S. 2013. Peculiar surface profile of poly(ethylene oxide) film with ring-like nucleation distribution induced by Marangoni flow effect. *Colloids and Surfaces A: Physicochemical and Engineering Aspects*. **428**, pp.39–46.

Huang, A.Y. and Berg, J.C. 2006. High-salt stabilization of Laponite clay particles. *Journal of colloid and interface science*. **296**(1), pp.159–64.

Jabbari-Farouji, S., Mizuno, D., Derks, D., Wegdam, G.H., MacKintosh, F.C., Schmidt, C.F. and Bonn, D. 2008. Effective temperatures from the fluctuation-dissipation measurements in soft glassy materials. *Europhysics Letters (EPL)*. **84**(2), p.6.

Jabbari-Farouji, S., Tanaka, H., Wegdam, G.H. and Bonn, D. 2008. Multiple nonergodic disordered states in Laponite suspensions: a phase diagram. *Physical Review E*. **78**(6), p.061405.

Jatav, S. and Joshi, Y.M. 2014. Chemical stability of Laponite in aqueous media. *Applied Clay Science*. **97–98**, pp.72–77.

Jeong, J.-A., Lee, J., Kim, H., Kim, H.-K. and Na, S.-I. 2010. Ink-jet printed transparent electrode using nano-size indium tin oxide particles for organic photovoltaics. *Solar Energy Materials and Solar Cells*. **94**(10), pp.1840–1844.

Jokinen, V., Sainiemi, L. and Franssila, S. 2011. Controlled lateral spreading and pinning of oil droplets based on topography and chemical patterning. *Langmuir : the ACS journal of surfaces and colloids*. **27**(11), pp.7314–20.

Joshi, Y.M., Reddy, G.R.K., Kulkarni, A.L., Kumar, N. and Chhabra, R.P. 2008. Rheological behaviour of aqueous suspensions of Laponite: new insights into the ageing phenomena. *Proceedings of the Royal Society A: Mathematical, Physical and Engineering Sciences*. **464**, pp.469–489.

Jung, J., Kim, Y., Yoo, J., Koo, J. and Kang, Y. 2010. Forces acting on a single particle in an evaporating sessile droplet on a hydrophilic surface. *Analytical chemistry*. **82**(3), pp.784–788.

Jung, Y., Kajiya, T., Yamaue, T. and Doi, M. 2009. Film formation kinetics in the drying process of polymer solution enclosed by bank. *Japanese Journal of Applied Physics*. **48**(3), p.031502.

Kajiya, T., Kobayashi, W., Okuzono, T. and Doi, M. 2009. Controlling the drying and film formation processes of polymer solution droplets with

addition of small amount of surfactants. *The Journal of Physical Chemistry B*. **113**(47), pp.15460–6.

Kajiya, T., Monteux, C., Narita, T., Lequeux, F. and Doi, M. 2009. Contact-line recession leaving a macroscopic polymer film in the drying droplets of water-poly(N, N-dimethylacrylamide) (PDMA) solution. *Langmuir*. **25**(12), pp.6934–6939.

Kaya, D., Belyi, V.A. and Muthukumar, M. 2010. Pattern formation in drying droplets of polyelectrolyte and salt. *The Journal of chemical physics*. **133**(11), p.114905.

Kegel, W.K. and Lekkerkerker, H.N.W. 2011. Colloidal gels: Clay goes patchy. *Nature materials*. **10**(1), pp.5–6.

Kim, D., Jeong, S., Park, B. and Moon, J. 2006. Direct writing of silver conductive patterns: Improvement of film morphology and conductance by controlling solvent compositions. *Applied physics letters*. **89**(26), p.264101.

Kim, H.-S., Park, S.S. and Hagelberg, F. 2010. Computational approach to drying a nanoparticle-suspended liquid droplet. *Journal of Nanoparticle Research*. **13**(1), pp.59–68.

Kim, J.H., Park, S.B., Kim, J.H. and Zin, W.C. 2011. Polymer transports inside evaporating water droplets at various substrate temperatures. *Journal of Physical Chemistry C*. **115**(31), pp.15375–15383.

Kim, J.Y., Cho, K., Ryu, S., Kim, S.Y. and Weon, B.M. 2015. Crack formation and prevention in colloidal drops. *Scientific Reports*. **5**, p.13166.

Knaebel, A., Bellour, M., Munch, J.-P., Viasnoff, V., Lequeux, F. and Harden, J.L. 2000. Aging behavior of Laponite clay particle suspensions. *Europhysics Letters (EPL)*. **52**(1), p.73.

Kochiya, K. and Ueno, I. 2009. Effect of suspended particles on the drying process of a carrier-fluid droplet sitting on a solid surface. *Annals of the New York Academy of Sciences*. **1161**, pp.234–9.

Kovalchuk, N.M., Trybala, A. and Starov, V.M. 2014. Evaporation of sessile droplets. *Current Applied Physics*. **19**, pp.336–342.

Kuncicky, D.M. and Velev, O.D. 2008. Surface-guided templating of particle assemblies inside drying sessile droplets. *Langmuir*. **24**(4), pp.1371–1380.

Labanda, J. and Llorens, J. 2004. Rheology of Laponite colloidal dispersions modified by sodium polyacrylates. *Colloids and Surfaces A: Physicochemical and Engineering Aspects*. **249**(1–3), pp.127–129.

Larsen, S.T. and Taboryski, R. 2009. A Cassie-like law using triple phase boundary line fractions for faceted droplets on chemically heterogeneous surfaces. *Langmuir*. **25**(3), pp.1282–1284.

Lazarus, V. and Pauchard, L. 2011. From craquelures to spiral crack patterns: influence of layer thickness on the crack patterns induced by desiccation. *Soft Matter*. **7**, pp.2552–2559.

Lebovka, N.I., Gigiberiya, V. a., Lytvyn, O.S., Tarasevich, Y.Y., Vodolazskaya, I.V. and Bondarenko, O.P. 2014. Drying of sessile droplets of laponite-based aqueous nanofluids. *Colloids and Surfaces A: Physicochemical and Engineering Aspects*. **462**, pp.52–63.

Lee, D.J. and Oh, J.H. 2010. Shapes and morphologies of inkjet-printed nanosilver dots on glass substrates. *Surface and Interface Analysis*. **42**(6–7), pp.1261–1265.

Lee, H.H., Fu, S.C., Tso, C.Y. and Chao, C.Y.H. 2017. Study of residue patterns of aqueous nanofluid droplets with different particle sizes and concentrations on different substrates. *International Journal of Heat and Mass Transfer*. **105**, pp.230–236.

Lee, W.P. and Routh, A.F. 2004. Why do drying films crack? *Langmuir*. **20**(23), pp.9885–8.

Léopoldès, J., Dupuis, A., Bucknall, D.G. and Yeomans, J.M. 2003. Jetting micron-scale droplets onto chemically heterogeneous surfaces. *Langmuir*. **19**(23), pp.9818–9822.

Levitz, P., Lecolier, E., Mourchid, A., Delville, A. and Lyonnard, S. 2000. Liquid-solid transition of Laponite suspensions at very low ionic strength : long-range electrostatic stabilisation of anisotropic colloids. *Europhysics Letters (EPL)*. **49**(5), pp.672–677.

Li, C., Liu, Q., Mei, Z., Wang, J., Xu, J. and Sun, D. 2009. Pickering emulsions stabilized by paraffin wax and Laponite clay particles. *Journal of Colloid and Interface Science*. **336**(1), pp.314–321.

Li, L., Harnau, L., Rosenfeldt, S. and Ballauff, M. 2005. Effective interaction of charged platelets in aqueous solution: investigations of colloid laponite suspensions by static light scattering and small-angle x-ray scattering. *Phys Rev E Stat Nonlin Soft Matter Phys*. **72**(5 Pt 1), p.51504.

Li, P. and Ishiguro, M. 2016. Adsorption of anionic surfactant (sodium dodecyl sulfate) on silica. *Soil Science and Plant Nutrition*. **62**(3), pp.223–229.

Lim, J.A., Lee, W.H., Lee, H.S., Lee, J.H., Park, Y.D. and Cho, K. 2008. Self-organization of ink-jet-printed triisopropylsilylethynyl pentacene via evaporation-induced flows in a drying droplet. *Advanced Functional Materials*. **18**(2), pp.229–234.

Lim, J.H., Ko, Y.H., Leem, J.W. and Yu, J.S. 2015. Improvement in light harvesting of dye-sensitized solar cells with antireflective and hydrophobic textile PDMS coating by facile soft imprint lithography. *Optics express*. **23**(3), pp.A169-79.

Liu, C., Bonaccurso, E. and Butt, H.-J. 2008. Evaporation of sessile water/ethanol drops in a controlled environment. *Physical chemistry chemical physics : PCCP*. **10**(47), pp.7150–7.

Lobb, D. 2016. Raindrops on leaves. Available from: http://www.dvps.org.au/?q=node/151.

Lyklema, J. 2005. *Fundamentals of interface and colloids science, Volume*

IV: Particulate colloids. Elsevier Ltd.

Magdassi, S. 2010. The Chemistry of Inkjet Inks *In*: S. Magdassi, ed. *The Chemistry of inkjet inks*. Singapore: World Scientific Publishing Co. Pte. Ltd.

Maheshwari, S., Zhang, L., Zhu, Y. and Chang, H.C. 2008. Coupling between precipitation and contact-line dynamics: Multiring stains and stick-slip motion. *Physical Review Letters*. **100**(4), pp.1–4.

Majumdar, D., Blanton, T.N. and Schwark, D.W. 2003. Clay–polymer nanocomposite coatings for imaging application. *Applied Clay Science*. **23**(5–6), pp.265–273.

Majumdar, D., Melpolder, S.M., Anderson, C.C., Christian, P.A. and Blanton, T.N. 1999. Clay containing electrically-conductive layer for imaging elements.

Majumder, M., Rendall, C.S., Eukel, J.A., Wang, J.Y.L., Behabtu, N., Pint, C.L., Liu, T., Orbaek, A.W., Mirri, F., Nam, J., Barron, A.R., Hauge, R.H., Schmidt, H.K. and Pasquali, M. 2012. Overcoming the “Coffee-Stain” Effect by Compositional Marangoni- Flow Assisted Drop-Drying. *Journal of Physical Chemistry B*. **116**(22), pp.6536–6542.

Mampallil, D. 2014. Some physics inside drying droplets. *Resonance*. **19**(2), pp.123–134.

Mampallil, D., Eral, H.B., van den Ende, D. and Mugele, F. 2012. Control of evaporating complex fluids through electrowetting. *Soft Matter*. [Online]. **8**(41), p.10614.

Marín, Á.G., Gelderblom, H., Lohse, D. and Snoeijer, J.H. 2011a. Order-to-disorder transition in ring-shaped colloidal stains. *Physical review letters*. **107**(8), p.085502.

Marín, Á.G., Gelderblom, H., Lohse, D. and Snoeijer, J.H. 2011b. Rush-hour in evaporating coffee drops. *Physics of Fluids*. **23**(9), pp.091111-1.

Martín, A., Schopf, C., Pescaglini, A., Wang, J.J. and Iacopino, D. 2014. Facile formation of ordered vertical arrays by droplet evaporation of au nanorod organic solutions. *Langmuir*. **30**(34), pp.10206–10212.

Matter, S., Chhasatia, V.H. and Sun, Y. 2011. Interaction of bi-dispersed particles with contact line in an evaporating colloidal drop. *Soft Matter*. **7**(21), p.10135.

Ming, T., Kou, X., Chen, H., Wang, T., Tam, H.-L., Cheah, K., Chen, J.-Y. and Wang, J. 2008. Ordered Gold Nanostructure Assemblies Formed By Droplet Evaporation. *Angewandte Chemie*. **120**(50), pp.9831–9836.

Moffat, J.R., Sefiane, K. and Shanahan, M.E.R. 2009. Effect of TiO2 nanoparticles on contact line stick-slip behavior of volatile drops. *The Journal of Physical Chemistry B*. **113**(26), pp.8860–6.

Molesa, S., Redinger, D.R., Huang, D.C. and Subramanian, V. 2003. High-quality inkjet-printed multilevel interconnects and inductive components on plastic for ultra-low-cost RFID applications *In*: *Mat. Res. Soc. Symp. Proc.* , pp.253–258.

Mongondry, P., Tassin, J.F. and Nicolai, T. 2005. Revised state diagram of Laponite dispersions. *Journal of Colloid and Interface Science*. **283**(2), pp.397–405.

Monteux, C. and Lequeux, F. 2011. Packing and sorting colloids at the contact line of a drying drop. *Langmuir : the ACS journal of surfaces and colloids*. **27**(6), pp.2917–22.

Morales, V.L., Parlange, J., Wu, M., Peez-Reche, F.J., Zhang, W., Sang, W. and Steenhuis, T.S. 2013. Surfactant-mediated control of colloid pattern assembly and attachment strength in evaporating droplets. *Langmuir*. **29**, pp.1831–1840.

Mott, M., Song, J. and Evans, J. 2004. Microengineering of Ceramics by Direct Ink-Jet Printing. *Journal of the American Ceramic Society*. **82**(7), pp.1653–1658.

Mourchid, A., Delville, A., Lambard, J., Lécolier, E. and Levitz, P. 1995. Phase diagram of colloidal dispersions of anisotropic charged particles: equilibrium properties, structure, and rheology of Laponite suspensions. *Langmuir*. **11**(6), pp.1942–1950.

Mourchid, A., Lécolier, E., Van Damme, H. and Levitz, P. 1998. On viscoelastic, birefringent, and swelling properties of Laponite clay suspensions: revisited phase diagram. *Langmuir*. **14**(17), pp.4718–4723.

Mourchid, A. and Levitz, P. 1998. Long-term gelation of laponite aqueous dispersions. *Physical Review E*. **57**(5), pp.R4887–R4890.

Nakamura, M., Kobayashi, A., Takagi, F., Watanabe, A., Hiruma, Y., Ohuchi, K., Iwasaki, Y., Horie, M., Morita, I. and Takatani, S. 2005. Biocompatible inkjet printing technique for designed seeding of individual living cells. *Tissue engineering*. **11**(11–12), pp.1658–1666.

Nguyen, V. and Stebe, K. 2002. Patterning of Small Particles by a Surfactant-Enhanced Marangoni-Bénard Instability. *Physical Review Letters*. [Online]. **88**(16), p.164501.

Nishiyama, Y., Henmi, C., Iwanaga, S., Nakagawa, H., Yamaguchi, K., Akita, K., Mochizuki, S. and Takiura, K. 2008. Ink jet three-dimensional digital fabrication for biological tissue manufacturing: Analysis of Alginate microgel beads produced by ink jet droplets for three dimensional tissue fabrication. *Journal of Imaging Science and Technology*. [Online]. **52**(6), pp.060201-060201-6.

Noguera, R., Lejeune, M. and Chartier, T. 2005. 3D fine scale ceramic components formed by ink-jet prototyping process. *Journal of the European Ceramic Society*. **25**(12 SPEC. ISS.), pp.2055–2059.

Okubo, T., Tsuchida, A. and Togawa, H. 2009. Drying dissipative patterns of aqueous solutions of simple electrolytes and their binary mixtures on a cover glass. *Colloid and Polymer Science*. **287**(4), pp.443–454.

Ooi, C.H., Bormashenko, E., Nguyen, A. V., Evans, G.M., Dao, D. V. and Nguyen, N.-T. 2016. Evaporation of Ethanol–Water Binary Mixture Sessile Liquid Marbles. *Langmuir*. **32**(24), pp.6097–6104.

Orejon, D., Sefiane, K. and Shanahan, M.E.R. 2011. Stick-slip of evaporating droplets: Substrate hydrophobicity and nanoparticle concentration. *Langmuir*. **27**(21), pp.12834–12843.

Parada, A. 2011. Dew drops on a cobweb on a cool morning in theprovince of Zamora, Spain. Available from: http://albertoparada.electrofolio.com/en/c11/Cobweb.

Park, J. and Moon, J. 2006. Control of colloidal particle deposit patterns within picoliter droplets ejected by ink-jet printing. *Langmuir*. **22**(8), pp.3506–3513.

Parsa, M., Boubaker, R., Harmand, S., Sefiane, K., Bigerelle, M. and Deltombe, R. 2017. Patterns from dried water-butanol binary-based nanofluid drops. *Journal of Nanoparticle Research*. **19**(8).

Parsa, M., Harmand, S., Sefiane, K., Bigerelle, M. and Deltombe, R. 2015. Effect of substrate temperature on pattern formation of nanoparticles from volatile drops. *Langmuir*. **31**(11), pp.3354–3367.

Pauliac-Vaujour, E., Stannard, A., Martin, C.P., Blunt, M.O., Notingher, I., Moriarty, P.J., Vancea, I. and Thiele, U. 2008. Fingering instabilities in dewetting nanofluids. *Physical Review Letters*. **100**(17), p.176102.

Pek-Ing, A. and Yee-Kwong, L. 2015. Surface chemistry and rheology of Laponite dispersions — Zeta potential, yield stress, ageing, fractal dimension and pyrophosphate. *Applied Clay Science*. **107**, pp.36–45.

Petit, L., Barentin, C., Colombani, J., Ybert, C. and Bocquet, L. 2009. Size dependence of tracer diffusion in a Laponite colloidal gel. *Langmuir*. **25**(20), pp.12048–12055.

Picknett, R.G. and Bexon, R. 1977. The evaporation of sessile or pendant drops in still air. *Journal of Colloid and Interface Science*. **61**(2), pp.336–350.

Polte, J. 2015. Fundamental Growth Principles of Colloidal Metal Nanoparticles - a new Perspective. *CrystEngComm*. **17**(5), pp.6809–6830.

Popov, Y. 2005. Evaporative deposition patterns: Spatial dimensions of the deposit. *Physical Review E*. **71**(3), p.036313.

Poulard, C. and Damman, P. 2007. Control of spreading and drying of a polymer solution from Marangoni flows. *Europhysics Letters (EPL)*. [Online]. **80**(6), p.64001.

Rao, Y., Kress, R.J., Demejo, L.P. and Nesbitt, S.D. 2005. Ink jet printing process.

Rich, J.P., McKinley, G.H. and Doyle, P.S. 2011. Size dependence of microprobe dynamics during gelation of a discotic colloidal clay. *Journal of Rheology*. **55**(2), p.273.

Ristenpart, W., Kim, P., Domingues, C., Wan, J. and Stone, H. 2007. Influence of substrate conductivity on circulation reversal in evaporating drops. *Physical Review Letters*. [Online]. **99**(23), pp.1–4.

Rödner, S.C., Wedin, P. and Bergström, L. 2002. Effect of electrolyte and

evaporation rate on the structural features of dried silica monolayer films. *Langmuir*. **18**(24), pp.9327–9333.

Ruzicka, B. and Zaccarelli, E. 2011. A fresh look at the Laponite phase diagram. *Soft Matter*. **7**(4), p.1268.

Ruzicka, B., Zaccarelli, E., Zulian, L., Angelini, R., Sztucki, M., Moussaïd, A., Narayanan, T. and Sciortino, F. 2011. Observation of empty liquids and equilibrium gels in a colloidal clay. *Nature materials*. [Online]. **10**(1), pp.56–60.

Ruzicka, B., Zulian, L. and Ruocco, G. 2007. Ageing dynamics in Laponite dispersions at various salt concentrations. *Philosophical Magazine*. **87**(3–5), pp.449–458.

Ruzicka, B., Zulian, L. and Ruocco, G. 2004. Ergodic to non-ergodic transition in low concentration Laponite. *Journal of Physics: Condensed Matter*. **16**(42), pp.S4993–S5002.

Ruzicka, B., Zulian, L. and Ruocco, G. 2006. More on the phase diagram of Laponite. *Langmuir : the ACS journal of surfaces and colloids*. **22**(3), pp.1106–11.

Ruzicka, B., Zulian, L., Zaccarelli, E., Angelini, R., Sztucki, M., Moussaïd, A. and Ruocco, G. 2010. Competing interactions in arrested states of colloidal clays. *Physical Review Letters*. **104**(8), pp.1–4.

Sangani, A.S., Lu, C., Su, K. and Schwarz, J.A. 2009. Capillary force on particles near a drop edge resting on a substrate and a criterion for contact line pinning. *Physical Review E - Statistical, Nonlinear, and Soft Matter Physics*. **80**(1), pp.1–15.

Sanyal, A., Basu, S. and Chaudhuri, S. 2015. Agglomeration front dynamics: Drying in sessile nano-particle laden droplets. *Chemical Engineering Science*. **123**, pp.164–169.

Saunders, J.M., Goodwin, J.W., Richardson, R.M. and Vincent, B. 1999. A Small-Angle X-ray Scattering study of the structure of aqueous Laponite dispersions. *Journal of Physical Chemistry B*. **103**(43), pp.9211–9218.

Sefiane, K. 2010. On the formation of regular patterns from drying droplets and their potential use for bio-medical applications. *Journal of Bionic Engineering*. **7**(SUPPL.), pp.S82–S93.

Sefiane, K. 2014. Patterns from drying drops. *Advances in colloid and interface science*. **206**, pp.372–81.

Sefiane, K., Fukatani, Y., Takata, Y. and Kim, J. 2013. Thermal patterns and hydrothermal waves (HTWs) in volatile drops. *Langmuir*. **29**(31), pp.9750–9760.

Sefiane, K., Tadrist, L. and Douglas, M. 2003. Experimental study of evaporating water–ethanol mixture sessile drop: influence of concentration. *International Journal of Heat and Mass Transfer*. **46**(23), pp.4527–4534.

Sempels, W., De Dier, R., Mizuno, H., Hofkens, J. and Vermant, J. 2013. Auto-production of biosurfactants reverses the coffee ring effect in a

bacterial system. *Nature communications*. **4**, p.1757.

Shahidzadeh-Bonn, N., Rafai, S., Bonn, D. and Wegdam, G. 2008. Salt crystallization during evaporation: Impact of interfacial properties. *Langmuir*. **24**(16), pp.8599–8605.

Shahidzadeh, N., Schut, M.F.L., Desarnaud, J., Prat, M. and Bonn, D. 2015. Salt stains from evaporating droplets. *Scientific reports*. **5**, p.10335.

Shahin, A. and Joshi, Y.M. 2012. Physicochemical effects in aging aqueous laponite suspensions. *Langmuir*. **28**(44), pp.15674–15686.

Shanahan, M.E.R. and Sefiane, K. 2009. Kinetics of triple line motion during evaporation. *6th International Symposium on Contact Angle, Wettability and Adhesion*. **6**, pp.19–31.

Sharma, V., Park, K. and Srinivasarao, M. 2009. Colloidal dispersion of gold nanorods: Historical background, optical properties, seed-mediated synthesis, shape separation and self-assembly. *Materials Science and Engineering: R: Reports*. **65**(1–3), pp.1–38.

Shen, X., Ho, C. and Wong, T. 2010. Minimal size of coffee ring structure. *The Journal of Physical Chemistry B*. **114**, pp.5269–5274.

Shi, L., Shen, P., Zhang, D., Lin, Q. and Jiang, Q. 2009. Wetting and evaporation behaviors of water-ethanol sessile drops on PTFE surfaces. *Surface and Interface Analysis*. **41**(12–13), pp.951–955.

Shuttleworth, R. and Bailey, G.L.J. 1948. The spreading of a liquid over a rough solid. *Discussions of the Faraday Society*. **3**, pp.16–22.

Singh, K.B. and Tirumkudulu, M.S. 2007. Cracking in drying colloidal films. *Physical Review Letters*. **98**(21), p.218302.

Smalyukh, I.I., Zribi, O. V., Butler, J.C., Lavrentovich, O.D. and Wong, G.C.L. 2006. Structure and Dynamics of Liquid Crystalline Pattern Formation in Drying Droplets of DNA. *Physical Review Letters*. **96**(17), p.177801.

Sobac, B. and Brutin, D. 2015. Chapter 8: Pure diffusion *In*: *Droplet Wetting and Evaporation From Pure to Complex Fluids*., pp.102–114.

Sobac, B. and Brutin, D. 2011. Triple-line behavior and wettability controlled by nanocoated substrates: Influence on sessile drop evaporation. *Langmuir*. **27**(24), pp.14999–15007.

Soltman, D. and Subramanian, V. 2008. Inkjet-printed line morphologies and temperature control of the coffee ring effect. *Langmuir*. **24**(5), pp.2224–31.

Soulié, V., Karpitschka, S., Lequien, F., Prené, P., Zemb, T., Moehwald, H. and Riegler, H. 2015. The evaporation behavior of sessile droplets from aqueous saline solutions. *Phys. Chem. Chem. Phys.* **17**(34), pp.22296–22303.

Sperling, M., Velev, O.D. and Gradzielski, M. 2014. Controlling the shape of evaporating droplets by ionic strength: formation of highly anisometric silica supraparticles. *Angewandte Chemie International Edition*. **53**(2),

pp.586–90.

Still, T., Yunker, P.J. and Yodh, A.G. 2012. Surfactant-induced Marangoni eddies alter the coffee-rings of evaporating colloidal drops. *Langmuir*. **28**(11), pp.4984–4988.

Sumner, A.L., Menke, E.J., Dubowski, Y., Newberg, J.T., Penner, R.M., Hemminger, J.C., Wingen, L.M. and Finlayson-pitts, B.J. 2004. The nature of water on surfaces of laboratory systems and implications for heterogeneous chemistry in the troposphere. *Phys. Chem. Chem. Phys.* **6**(2), pp.604–6013.

Sun, Y., Bromberg, V., Gawande, S., Biswas, S. and Singler, T. 2009. Transport processes associated with inkjet printing of colloidal drops for printable electronics fabrication. *Proceedings - Electronic Components and Technology Conference*., pp.1349–1355.

Takhistov, P. and Chang, H. 2002. Complex Stain Morphologies. *Ind. Eng. Chem. Res.* [Online]. **41**(25), pp.6256–6269. Available from: http://pubs.acs.org/doi/abs/10.1021/ie010788+.

Talbot, E., Berson, A., Brown, P.S. and Bain, C. 2012. Drying and Deposition of Picolitre Droplets of Colloidal Suspensions in Binary Solvent Mixtures. *NIP28: 28th International conference on digital printing technologies/ Digital fabrication 2012*. (JUNE), pp.420–423.

Talbot, E.L., Berson, A., Yang, L. and Bain, C.D. 2013. Internal Flows and Particle Transport Inside Picoliter Droplets of Binary Solvent Mixtures. *29th International Conference on Digital Printing Technologies, and Digital Fabricaion 2013*. **44**(Septembre/Octobre), pp.307–312.

Talbot, E.L., Yow, H.N., Yang, L., Berson, A., Biggs, S.R. and Bain, C.D. 2015. Printing small dots from large drops. *ACS applied materials & interfaces*. **7**(6), pp.3782–90.

Tang, Y., He, W., Wang, S., Tao, Z. and Cheng, L. 2014. The superiority of silver nanoellipsoids synthesized via a new approach in suppressing the coffee-ring effect during drying and film formation processes. *Nanotechnology*. **25**(12), p.125602.

Tarasevich, Y.Y., Isakova, O.P., Kondukhov, V. V. and Savitskaya, A. V. 2010. Effect of evaporation conditions on the spatial redistribution of components in an evaporating liquid drop on a horizontal solid substrate. *Technical Physics*. **55**(5), pp.636–644.

Tarasevich, Y.Y. and Pravoslavnova, D.M. 2007. Drying of a multicomponent solution drop on a solid substrate : qualitative analysis. *Technical Physics*. **52**(2), pp.159–163.

Tarasevich, Y.Y. and Pravoslavnova, D.M. 2007. Segregation in desiccated sessile drops of biological fluids. *European Physical Journal E*. **22**(4), pp.311–314.

Thompson, D.W. and Butterworth, J.T. 1992. The nature of Laponite and its aqueous dispersions. *Journal of Colloid and Interface Science*. **151**(1), pp.236–243.

Thomson, J. 1855. On certain curious motions observable at the surfaces

of wine and other alcoholic liquors. *The London, Edinburgh and Dublin Philosophical Magazine and Journal of Science*. **10**(July), p.330.

Truskett, V.N. and Stebe, K.J. 2003. Influence of surfactants on an evaporating drop: Fluorescence images and particle deposition patterns. *Langmuir*. **19**(20), pp.8271–8279.

Ulmeanu, M., Zamfirescu, M. and Medianu, R. 2009. Self-assembly of colloidal particles on different surfaces. *Colloids and Surfaces A: Physicochemical and Engineering Aspects*. **338**(1–3), pp.87–92.

Vicente, C.M.S., André, P.S. and Ferreira, R.A.S. 2012. Simple measurement of surface free energy using a web cam. *Revista Brasileira de Ensino de Física*. **34**(3), p.3312.

Vrancken, R.J., Blow, M.L., Kusumaatmaja, H., Hermans, K., Prenen, A.M., Bastiaansen, C.W.M., Broer, D.J. and Yeomans, J.M. 2013. Anisotropic wetting and de-wetting of drops on substrates patterned with polygonal posts. *Soft Matter*., pp.674–683.

Walker, D.A., Browne, K.P., Kowalczyk, B. and Grzybowski, B.A. 2010. Self-assembly of nanotriangle superlattices facilitated by repulsive electrostatic interactions. *Angewandte Chemie International Edition*. **49**(38), pp.6760–6763.

Wang, W., Yin, Y., Tan, Z. and Liu, J. 2014. Coffee-ring effect-based simultaneous SERS substrate fabrication and analyte enrichment for trace analysis. *Nanoscale*. **6**(16), p.9588.

Wenzel, R.N. 1936. Resistance of solid surfaces to wetting by water. *Journal of Industrial and Engineering Chemistry (Washington, D. C.)*. **28**(8), pp.988–994.

Weon, B. and Je, J. 2010. Capillary force repels coffee-ring effect. *Physical Review E*. **82**(1), pp.1–4.

Weon, B.M. and Je, J.H. 2013. Self-pinning by colloids confined at a contact line. *Physical Review Letters*. **110**(2), p.028303.

Wong, T.S., Chen, T.H., Shen, X. and Ho, C.M. 2011. Nanochromatography driven by the coffee ring effect. *Analytical Chemistry*. **83**(6), pp.1871–1873.

Xie, Y., Guo, S., Ji, Y., Guo, C., Liu, X., Chen, Z., Wu, X. and Liu, Q. 2011. Self-assembly of gold nanorods into symmetric superlattices directed by OH-terminated hexa(ethylene glycol) alkanethiol. *Langmuir*. **27**(18), pp.11394–11400.

Xu, L., Fan, H., Yang, C. and Huang, W.M. 2008. Contact line mobility in liquid droplet spreading on rough surface. *Journal of Colloid and Interface Science*. **323**(1), pp.126–132.

Xu, X., Luo, J. and Guo, D. 2012. Radial-velocity profile along the surface of evaporating liquid droplets. *Soft Matter*. **8**(21), pp.5797–5803.

Yakhno, T. 2008. Salt-induced protein phase transitions in drying drops. *Journal of colloid and interface science*. **318**(2), pp.225–30.

Yan, Q., Gao, L., Sharma, V., Chiang, Y.M. and Wong, C.C. 2008. Particle

and substrate charge effects on colloidal self-assembly in a sessile drop. *Langmuir*. **24**(20), pp.11518–11522.

Yang, X., Li, C.Y. and Sun, Y. 2014. From multi-ring to spider web and radial spoke: competition between the receding contact line and particle deposition in a drying colloidal drop. *Soft matter*. **10**(25), pp.4458–63.

Yarin, A.L. 2006. Drop impact dynamics: Splashing, spreading, receding, bouncing…. *Annual Review of Fluid Mechanics*. **38**(1), pp.159–192.

Young, T. 1805. An essay on the cohesion of fluids. *Philosophical Transactions of the Royal Society of London*. **95**, pp.65–87.

Yu, Y.S., Wang, M.C. and Huang, X. 2017. Evaporative deposition of polystyrene microparticles on PDMS surface. *Scientific Reports*. **7**(1), pp.1–9.

Yunker, P., Lohr, M., Still, T., Borodin, A., Durian, D. and Yodh, A. 2013. Effects of particle shape on growth dynamics at edges of evaporating drops of colloidal suspensions. *Physical Review Letters*. **110**(3), pp.035501-5.

Yunker, P.J., Still, T., Lohr, M.A. and Yodh, A.G. 2011. Suppression of the coffee-ring effect by shape-dependent capillary interactions. *Nature*. **476**(7360), pp.308–311.

Zavelani-Rossi, M., Krahne, R., Della Valle, G., Longhi, S., Franchini, I.R., Girardo, S., Scotognella, F., Pisignano, D., Manna, L., Lanzani, G. and Tassone, F. 2012. Self-assembled CdSe/CdS nanorod micro-lasers fabricated from solution by capillary jet deposition. *Laser and Photonics Reviews*. **6**(5), pp.678–683.

Zhong, X. and Duan, F. 2016a. Dewetting transition induced by surfactants in sessile droplets at the early evaporation stage. *Soft Matter*. **12**(2), pp.508–513.

Zhong, X. and Duan, F. 2014. Evaporation of sessile droplets affected by graphite nanoparticles and binary base fluids. *The Journal of Physical Chemistry B*. **118**(47), pp.13636–13645.

Zhong, X. and Duan, F. 2016b. Flow regime and deposition pattern of evaporating binary mixture droplet suspended with particles. *European Physical Journal E*. **39**(18).

Zulian, L., Augusto de Melo Marques, F., Emilitri, E., Ruocco, G. and Ruzicka, B. 2014. Dual aging behaviour in a clay-polymer dispersion. *Soft matter*. **10**(25), pp.4513–21.

Nomenclature

Latin letters

Acceleration due to gravity	g
Area of thickness	dh
Asymmetry factor	g_a
Backscattered light flux	BS
Boltzmann constant	k_B
Bond number	B_0
Cantilever deflection	x
Capillary length	L_C
Centre to centre between two particles	d_p
Concentration of ethanol	C_{EtOH}
Concentration of Laponite	C_{Lap}
Concentration of Ludox AS-40®	C_{Lud}
Concentration of PMMA latex	C_{Lat}
Concentration of sodium chloride	C_{NaCl}
Concentration of sodium dodecyl sulfate	C_{SDS}
Diffusion coefficient	D
Diffusion time	t_D
Droplet contact radius	r_d
Droplet height	H
Droplet mass	M
Electrophoretic mobility	U_E
Electrostatic repulsive interaction	W_R

Enthalpy of vaporisation	$\Delta_{vap}H$
Evaporation time	t_E
Evaporative flux	J
Force	F
Fundamental charge	e
Hamaker constant	A_H
Henry's function	$f(Ka)$
Hydrodynamic diameter	r_H
Ion valence	z
Length separating two approaching particles	h
Net force	W_T
Particle diffusion rate	D_p
Particle mean diameter	d
Particle radius	R
Particle settling velocity	Vp
Photon mean free path of light	l
Photon transport mean free path	l^*
Radial distance to the centre	r
Radius of a sphere reshaping spherical cap of the droplet	R_S
Roughness factor	r_w
Saturated concentration	c_S
Scattering efficiency factor	Q_s
Spring constant	k
Surface area	S
Temperature	T

Transmission	T_r
Van der Waals attractive force	W_{VdW}
Vapour phase concentration far away	c_∞
Volume	V

Greek letters

Advancing contact angle	θ_A
Apparent contact angle	θ_{ACA}
Cassie-Baxter contact angle	θ_{CB}
Debye screening length	κ^{-1}
Density difference	Δ_ρ
Dielectric constant	ε
Dielectric constant of solution	ε_r
Fluid density	ρ_f
Liquid/solid interfacial tension	γ_{LS}
Liquid/vapour interfacial tension	γ_{LV}
Mobility of the particles	μ
Number density of ions	ρ_{Ni}
Particle density	ρ_p
Particle volume fraction	φ
Particle volume fraction	Φ
Permittivity of vacuum	ε_0
Proportion of solid and air surface in contact with liquid	Φ_S

Real contact angle	θ_{RE}
Receding contact angle	θ_R
Reduced surface potential	γ_0
Shape factor	β
Solid/vapour interfacial tension	γ_{SV}
Surface potential	Ψ
Surface tension	γ
Viscosity of the liquid	η
Wenzel contact angle	θ_W
Young-Laplace/Equilibrium contact angle	θ
Zeta potential	ζ

Abbreviations

Critical coagulation concentration	ccc
Critical micelle concentration	cmc
Chlorotrimethylsilane	TMSCL
Dynamic Light Scattering	DLS
Ethanol	EtOH
Hydrochloric acid	HCl
Methanol	MeOH
Polymethylmethacrylate	PMMA
Relative humidity of ambient air	RH
Sodium dodecyl benzene sulfonate	SDBS
Potassium chloride	KCl
Sodium chloride	NaCl
Sodium dodecyl sulfate	SDS

Appendix A

A.1 Matlab codes

A.1.1 Evaporation rate calculation

The theoretical value of the evolution of the volume with was calculate using this following code. Below is an example for a Ludox AS-40® droplet at 1 ppm.

```
% Calculating the evolution of volume as a function of time

theta = 0:0.0872665:0.523599;

theta = fliplr(theta);

R = 3.2e-3;

D = 24.2e-6;

Cs = 1.75e-3;

RH = 0.4;

rho = 997.2988;

for i = 1:length((theta))

f_theta(i) = 0.5*(0.00008957+ (0.6333*theta(i)) + (0.116*theta(i)^2) - (0.08878*theta(i)^3) + (0.01033*theta(i)^4)); %This is for f(theta)

beta_theta(i) = (2- (3*cos(theta(i))) + cos(theta(i))^3 )/ (sin(theta(i)^3));

dV(i) = (4*pi()/rho) * D*R*Cs*(1-RH)*f_theta(i);

end
```

A.1.2 P_{cap} calculation

The data of gamma (surface tension), E (evaporation rate) and T_H (thickness of dried deposits features) for each Ludox AS-40 ® concentrations were entered and P_{cap} was calculated. Below example for Ludox 100 ppm.

```
gamma=72.6e-3;

nu=1.00e-3;

E=4.20e-9;

R=0.5*21e-9;

phi=0.64;

mu=9.61e-4;

TH =6.79e-7;

Pcap=(20/75)*(((3*gamma*nu)/E)^0.5)*((R*(1-
phi)^2)/(mu*phi^2*TH ));
```

A.2 PMMA polymeric particles in aqueous suspensions

A.2.1 Synthesis of PMMA polymeric particles and purification process

- Synthesis

The PMMA polymeric particles were synthesized by Atom Transfer Radical Polymerization (ATRP) by Mr Mohmed Mulla.

To achieve this polymerization, the following synthesis protocol was performed:

A stock solution was prepared by adding 0.003 g of 4-cyano-4-[(dodecylsulfanylthiocarbonyl)sulfanyl]pentoic acid (Cyacid) to 51 mL of MMA (Methyl MethAcrylate), then the solution was degassed by N_2 for 1 hour under magnetic stirring at 400 rpm.

The next step was the dissolution of 1.65 g of SDS and $NaHCO_3$ in 29 mL of Milli-Q water. Then 19 g of MMA was added to the mixture drop-wise at 0.2 g/min under magnetic stirring while the reaction media was deoxygenated for

1 hour. Then 12.5 mL of the original stock solution prepared was added drop-wise at 0.4 g/min to the previous mixture. The temperature of the reaction was increased to 70 °C during the stock solution addition. When the solution temperature reached 70 °C, 0.02 g of 2,2'-Azobis(2-methylpropionamide) dihydrochloride (AIBA) was dissolved in 10 mL of Milli-Q water, then this mixture was added slowly to the reaction media at a rate of 1.5 g/min. The polymerization was then allowed to process for 2 hours to reach its completion.

The resulting particle dispersion was filtrated through glass wool before collection and storage in a freezer at <10 °C.

- Purification

The dialysis was the process used to purify the synthesized PMMA latex particles, by removing the excess of SDS surfactant and any other salt or small impurities from the synthesis. A dialysis tubing cellulose membrane from Fischer (Cellulose 8000 MWCO) was used in this process. The dialysis bag was washed thoroughly with MilliQ-water.

The bag was then pressed to remove the excess water as much as possible. Then one end of the bag was folded and clipped using a blue peg. A funnel was used to pour the synthesized particles suspension, before proceeding further the bag was tested for any leakage. Once all the liquid was transferred, the other end of the tubing was folded and clipped. The dialysis bag was then place in a larger beaker filled with MilliQ-water –used as the external water phase- and containing a magnetic stirrer. It was left to stirred for 3 weeks, and the water was changed daily. The surface tension of the MilliQ-water was regularly checked until it reached 70.8 mN/m which is close to the surface tension of particle-free Milli-Q water measured at 72.8 mN/m. The system was then assumed to be surfactant free. The final size of the synthesized particles was then checked using Dynamic Light Scattering and Scanning Electron Microscopy (cf Figure A-1).

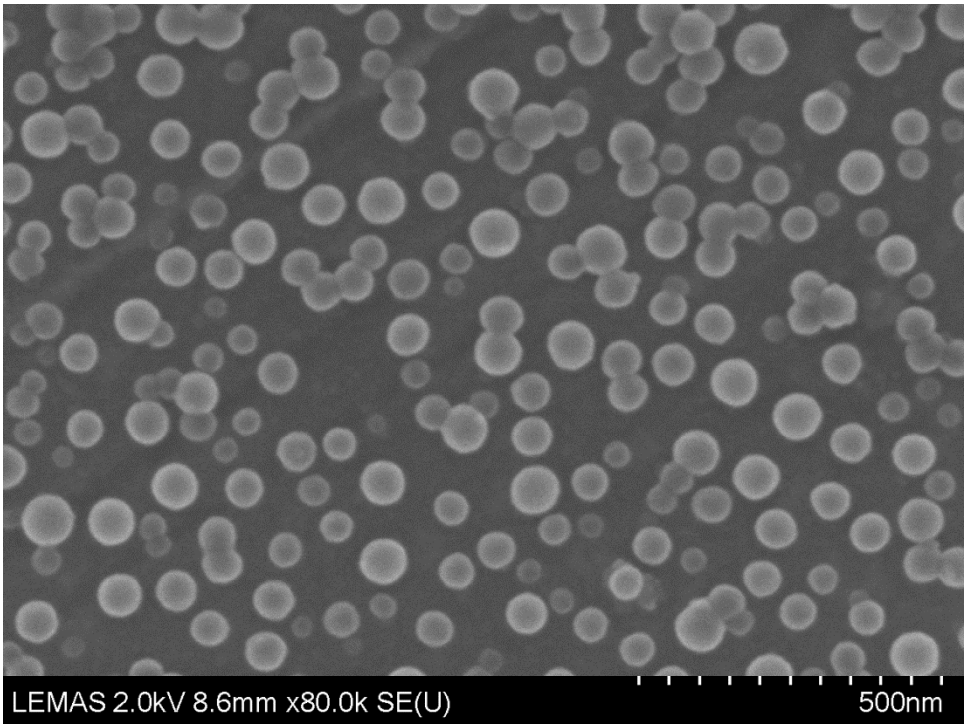

Figure A-1: FE-SEM micrograph of PMMA latex particles at 0.03 wt% after purification with average diameter Dp= 32 ± 9 nm.

- Particle characterization

The hydrodynamic diameter was determined using a DLS (Malvern). The morphology and the size of the nanoparticles were also analysed using a SEM. The obtained nanoparticle diameter was at 72.5±0.5 nm for DLS and 63.0 ±8.7 nm with SEM. 126 particles were used in the SEM image to determine the particle size distribution with ImageJ software. The electrostatic properties of this system was also determined using the Zeta Sizer Nano and the surface charge of the nanoparticle was found to be at -40.1 ±2.1 mV

A.2.2 Drying sequence and dried deposit pattern

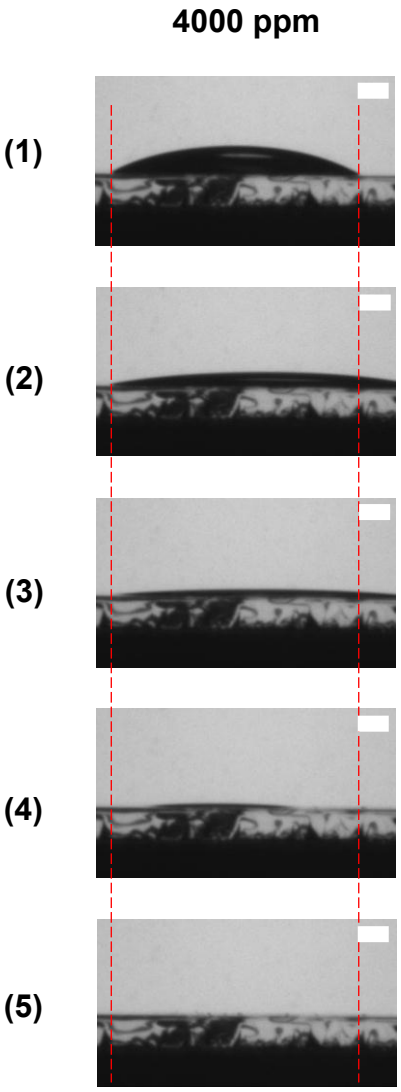

Figure A-2: Drying sequence of aqueous based PMMA latex particles droplets on uncoated glass slides at C_{Lat}= 4000 ppm at different time of droplet lifetime: (1) 0%, (2) 25%, (3) 50%, (4) 75% and (5) 100%. The images were taken from side-view video recordings of the deposition with a contact angle goniometer. The white scale bars represent 1 mm. The red dotted lines represent the initial droplet contact diameter.

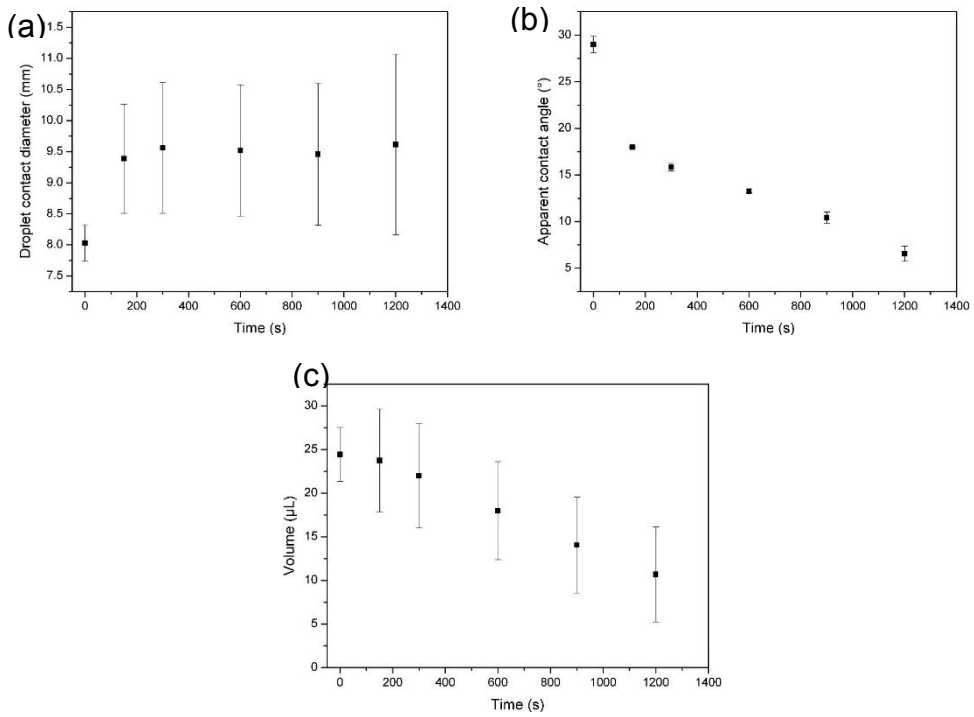

Figure A-3: Evolution of (a) droplet contact diameter $2r_d$ (b) apparent contact angle θ_{ACA} and (c) volume V_{Lat} of PMMA latex at C_{Lat}= 0.4 wt% with time on the entire droplet lifetime. The droplets were deposited on uncoated glass slides. The evolution was extracted from contact angle goniometer recordings.

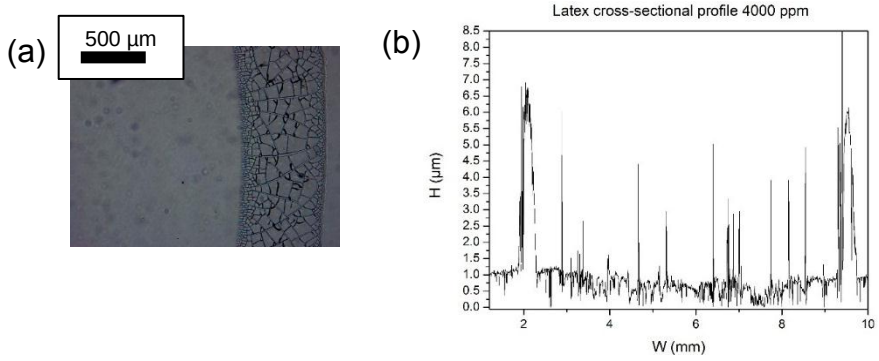

Figure A-4: Dried deposit of PMMA latex droplets (C_{Lat}= 4000 ppm) (a) optical micrograph of right side of the deposit, (b) three-dimensional topographical cross-sectional profile WLI image of dried deposit.

A.3 Spherical Ludox AS-40 ®

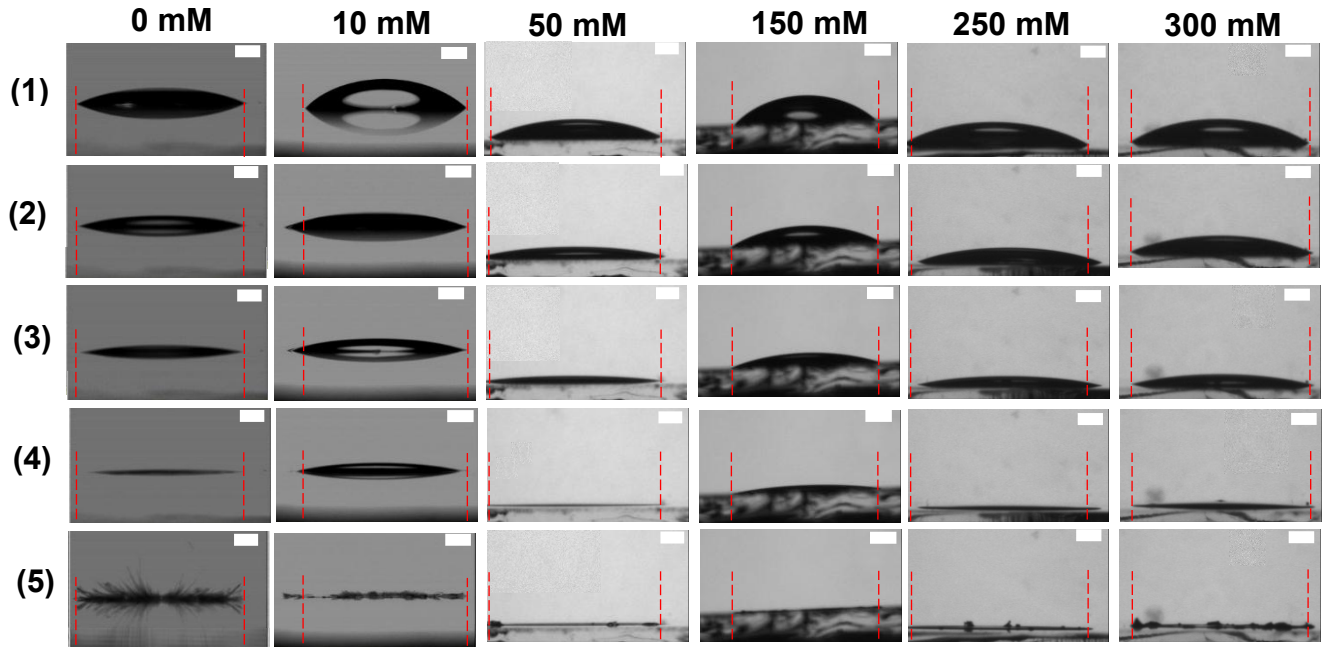

Figure A-5: Drying sequence of aqueous based Ludox AS-40® droplets on uncoated glass slides as a function of electrolyte concentration (C_{NaCl}= 0 to 300 mM) at different time of droplet lifetime: (1) 0%, (2) 25%, (3) 50%, (4) 75% and (5) 100%. The images were taken from side-view video recordings of the deposition with a contact angle goniometer. The white scale bars represent 1 mm. The red dotted lines represent the initial droplet contact diameter.

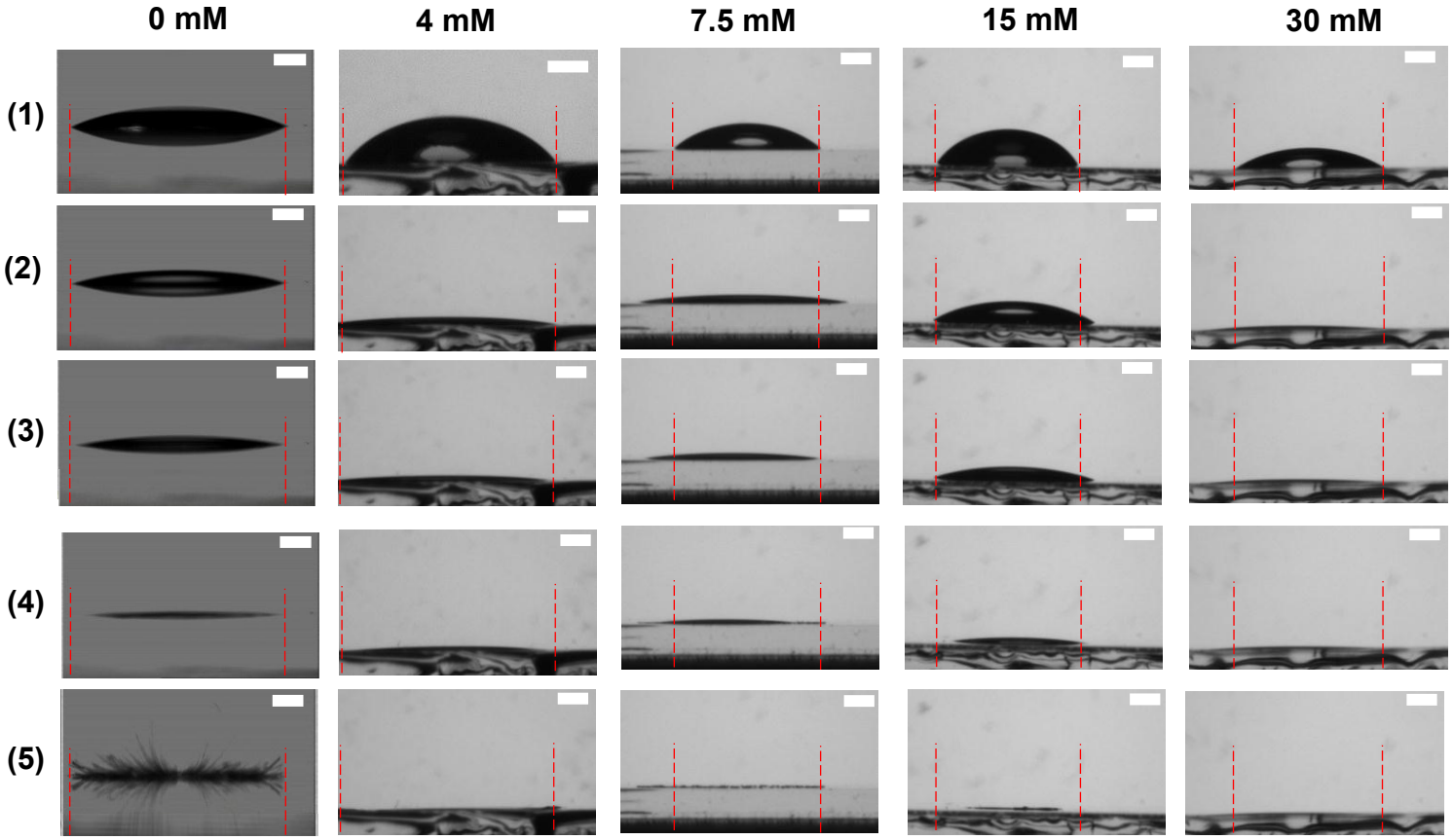

Figure A-6: Drying sequence of aqueous based Ludox AS-40® droplets on uncoated glass slides as a function of surfactant concentration (C_{SDS}= 0 to 30 mM) at different time of droplet lifetime: (1) 0%, (2) 25%, (3) 50%, (4) 75% and (5) 100%. The images were taken from side-view video recordings of the deposition with a contact angle goniometer. The white scale bars represent 1 mm. The red dotted lines represent the initial droplet contact diameter.

A.4 Spherical PMMA latex

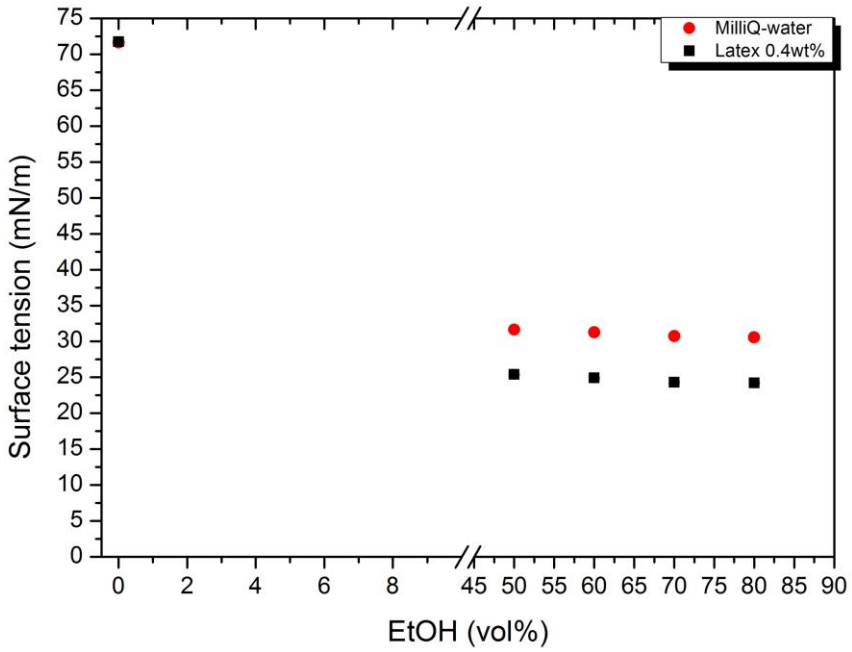

Figure A-7: Surface tension of PMMA latex at C_{Lat}= 4000 ppm in different ethanol concentration C_{EtOH}= 50 to 90 vol%.

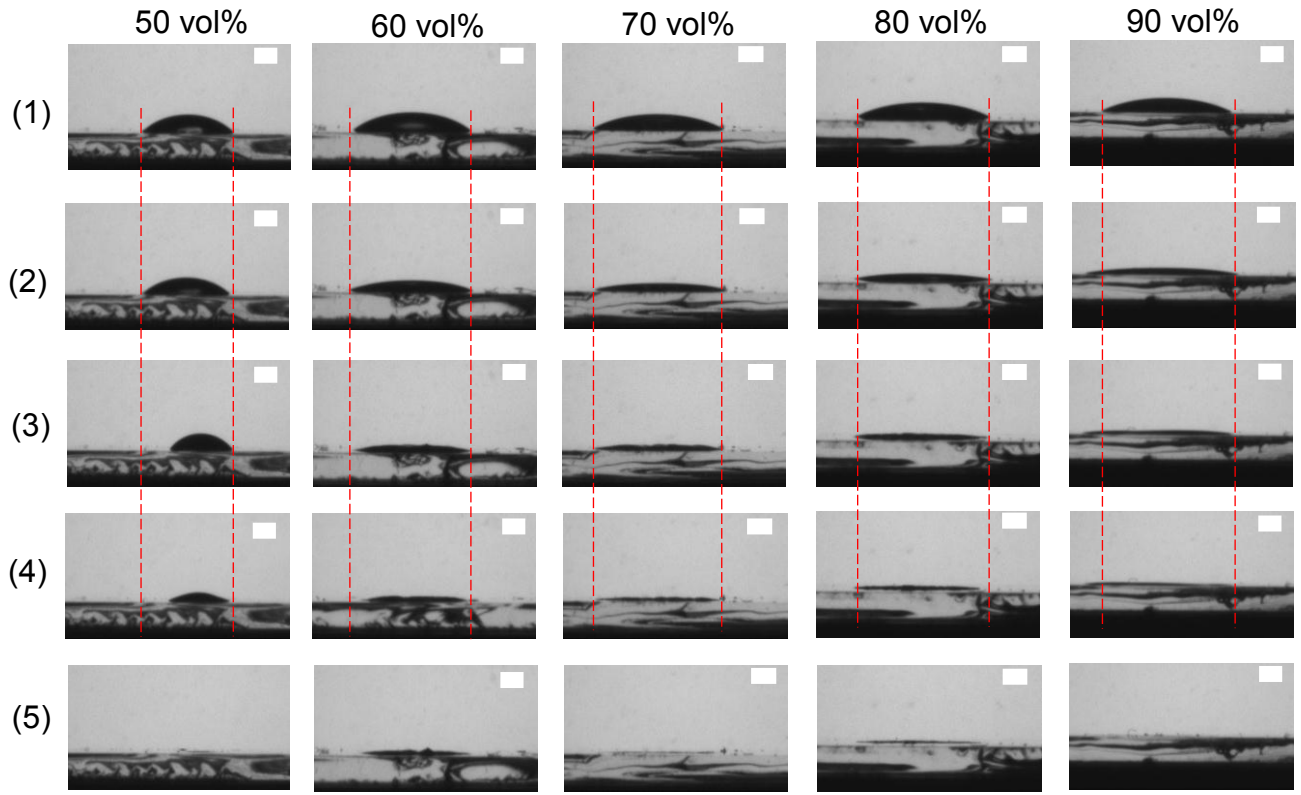

Figure A-8: Drying sequence of aqueous based PMMA latex particles droplets on silane coated glass slides as a function of ethanol/water concentration (C_{EtOH}= 50 to 90 vol%) at different time of droplet lifetime: (1) 0%, (2) 25%, (3) 50%, (4) 75% and (5) 100%. The images were taken from side-view video recordings of the deposition with a contact angle goniometer. The white scale bars represent 1 mm. The red dotted lines represent the initial droplet contact diameter.

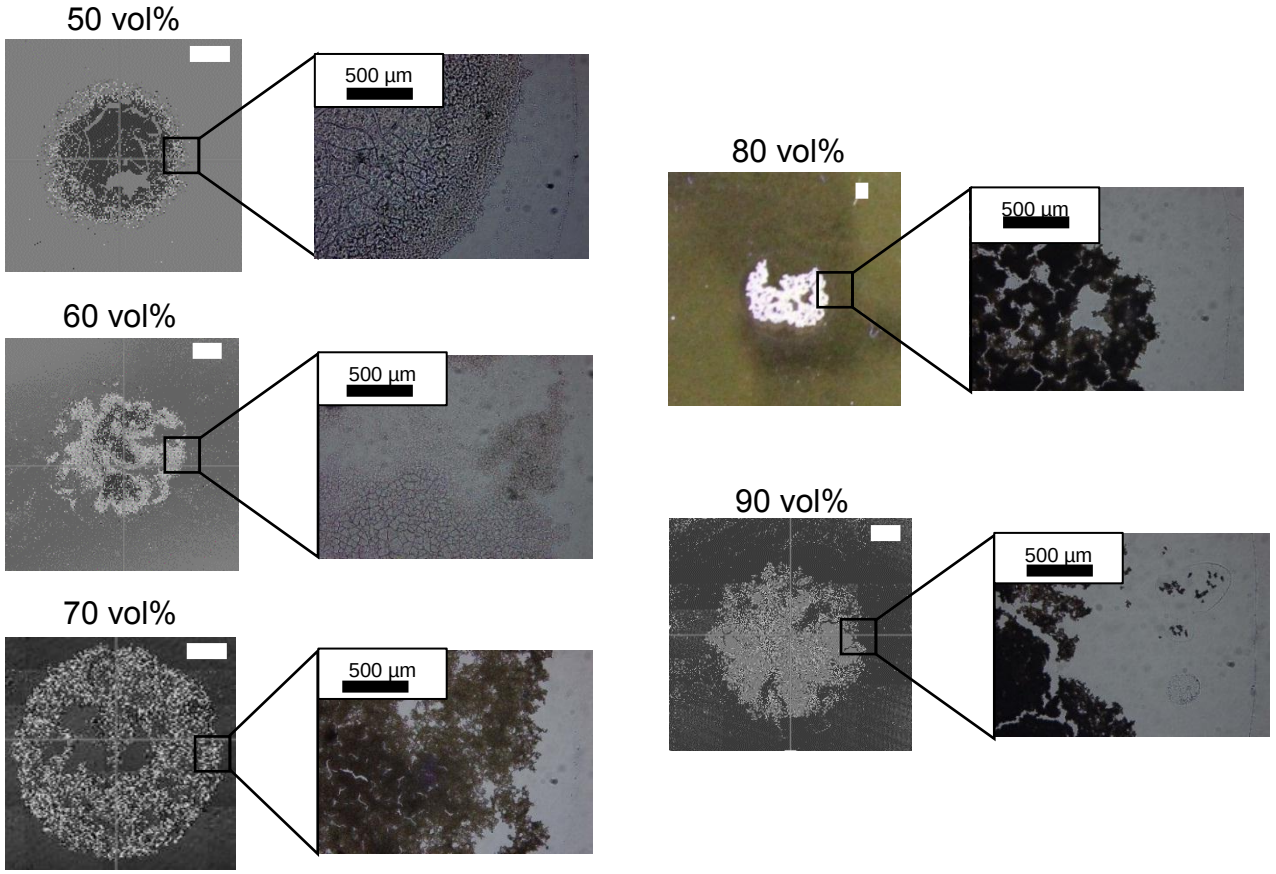

Figure A-9: Two-dimensional topographical WLI images of dried deposit of PMMA latex particles droplets in different ethanol/water mixtures (C_{EtOH}= 50 to 90 vol%) and optical micrographs corresponding to the magnification of the area inside the black box on silane coated glass slides. The white scale bars represent 1 mm on all images.

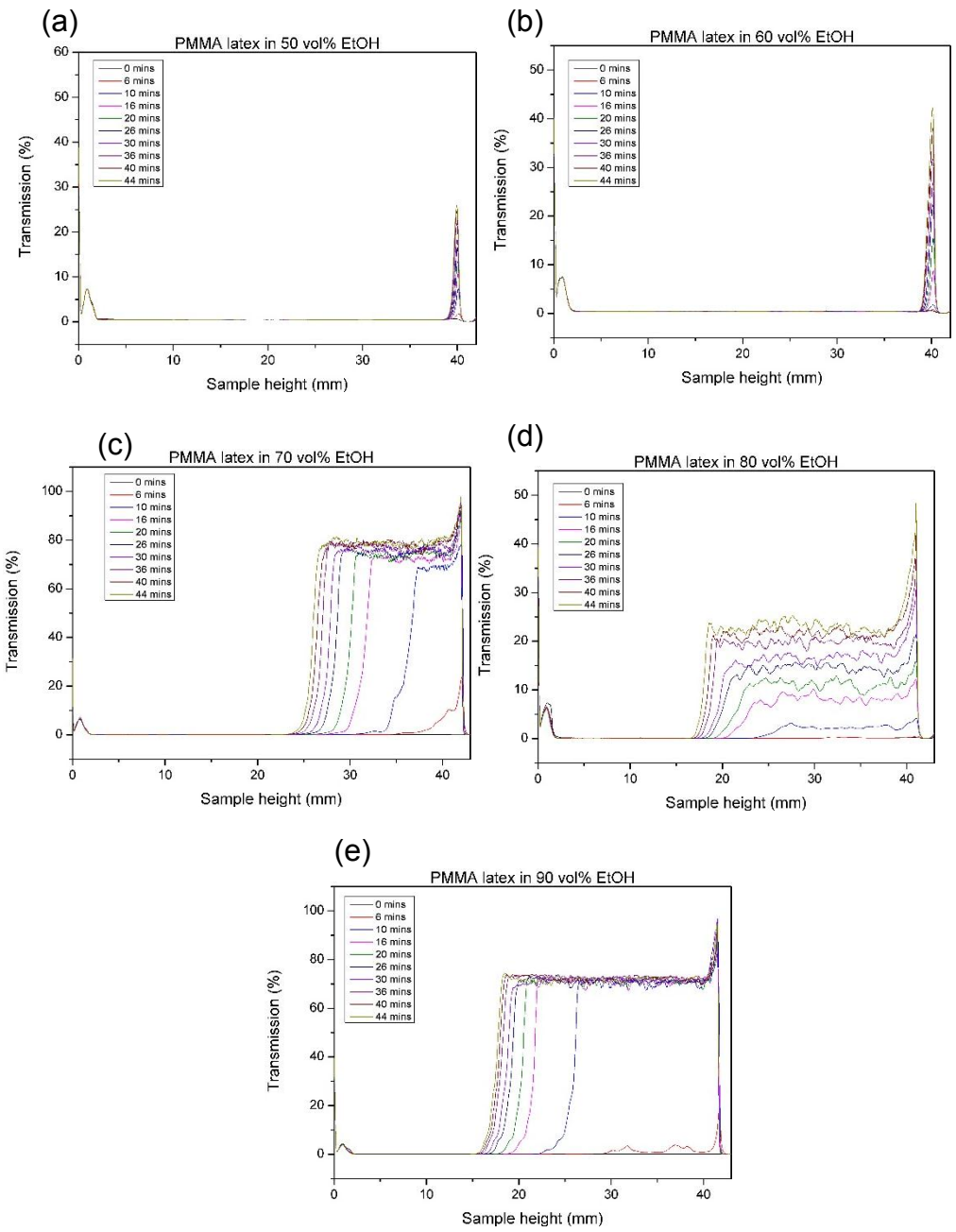

Figure A-10:Transmitted intensity profiles given by Turbiscan as a function of the height of the sample and versus time for the PMMA latex in different EtOH/H2O mixtures (a) 50 vol%, (b) 60 vol%, (c) 70 vol%, (d) 80 vol% and (e) 90 vol%.

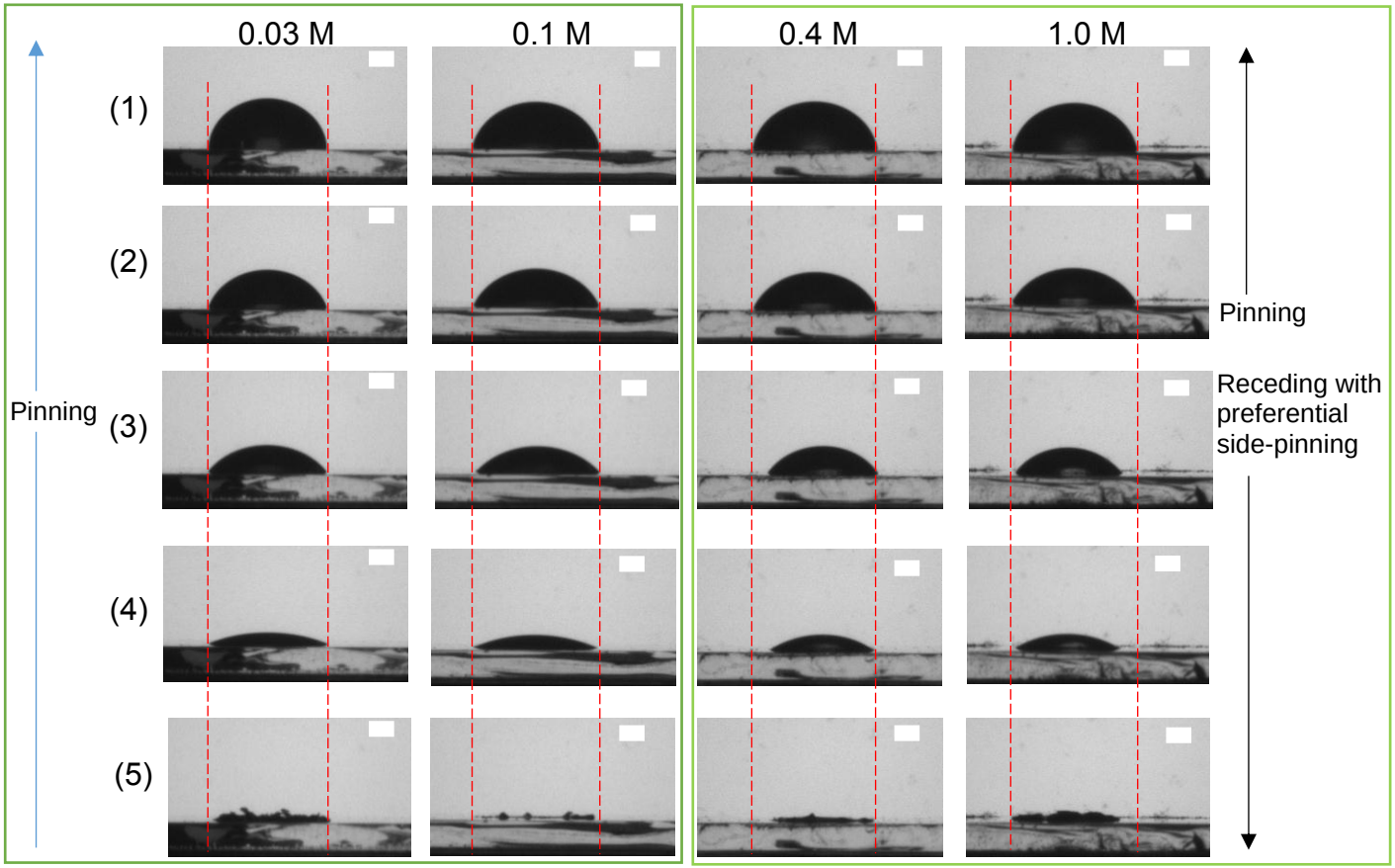

Figure A-11: Drying sequence of aqueous based PMMA latex particles droplets on silane coated glass slides as a function of electrolyte concentration (C_{NaCl}= 0.03 to 1.0 M) at different time of droplet lifetime: (1) 0%, (2) 25%, (3) 50%, (4) 75% and (5) 100%. The images were taken from side-view video recordings of the deposition with a contact angle goniometer. The white scale bars represent 1 mm. The red dotted lines represent the initial droplet contact diameter.

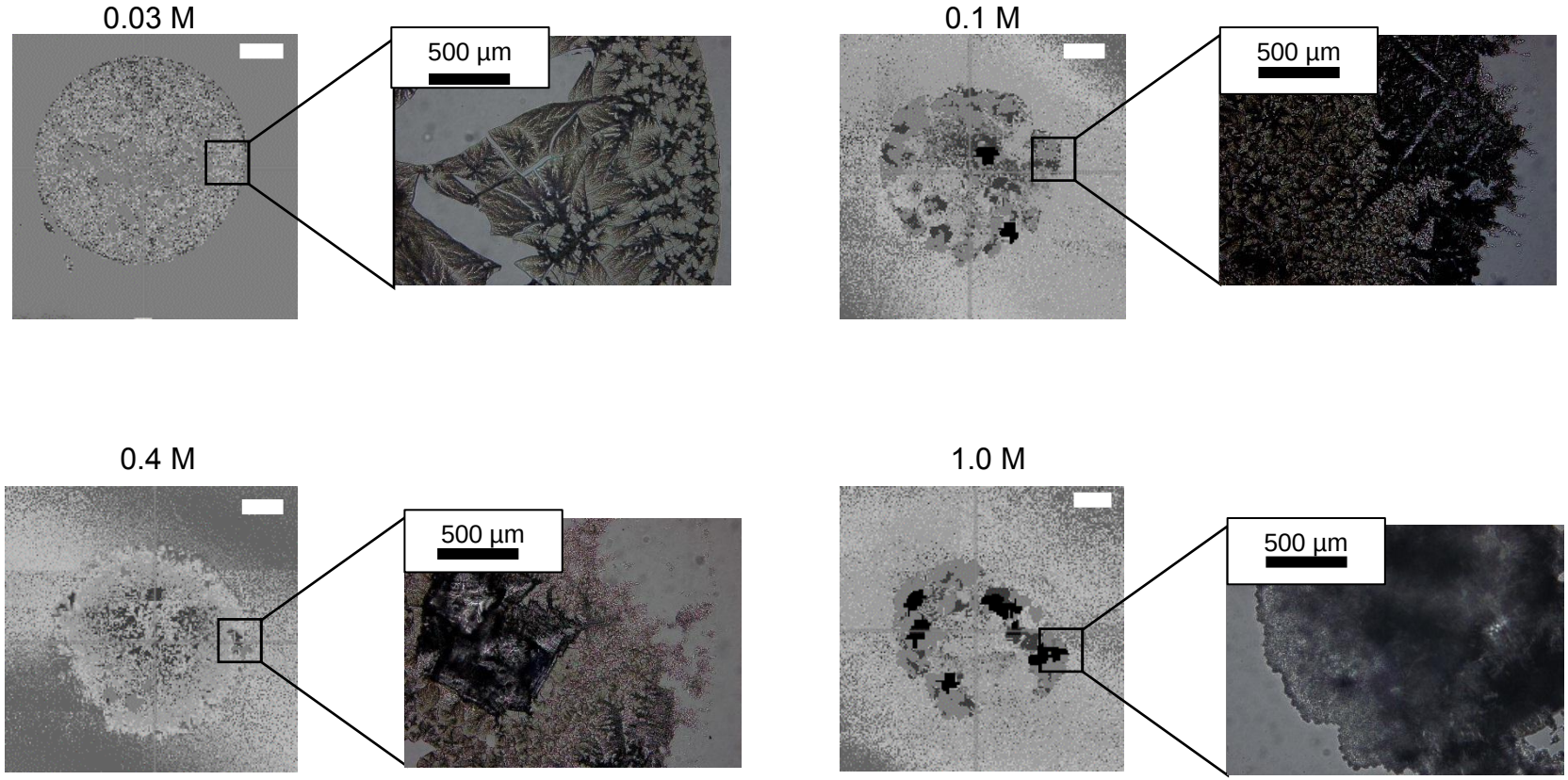

Figure A-12: Two-dimensional topographical WLI images of dried deposit of PMMA latex particles with different added electrolyte concentration (C_{NaCl}= 0.03 to 1.0 M) and optical micrographs corresponding to the magnification of the area inside the black box on uncoated glass slides. The white scale bars represent 1 mm on all images.

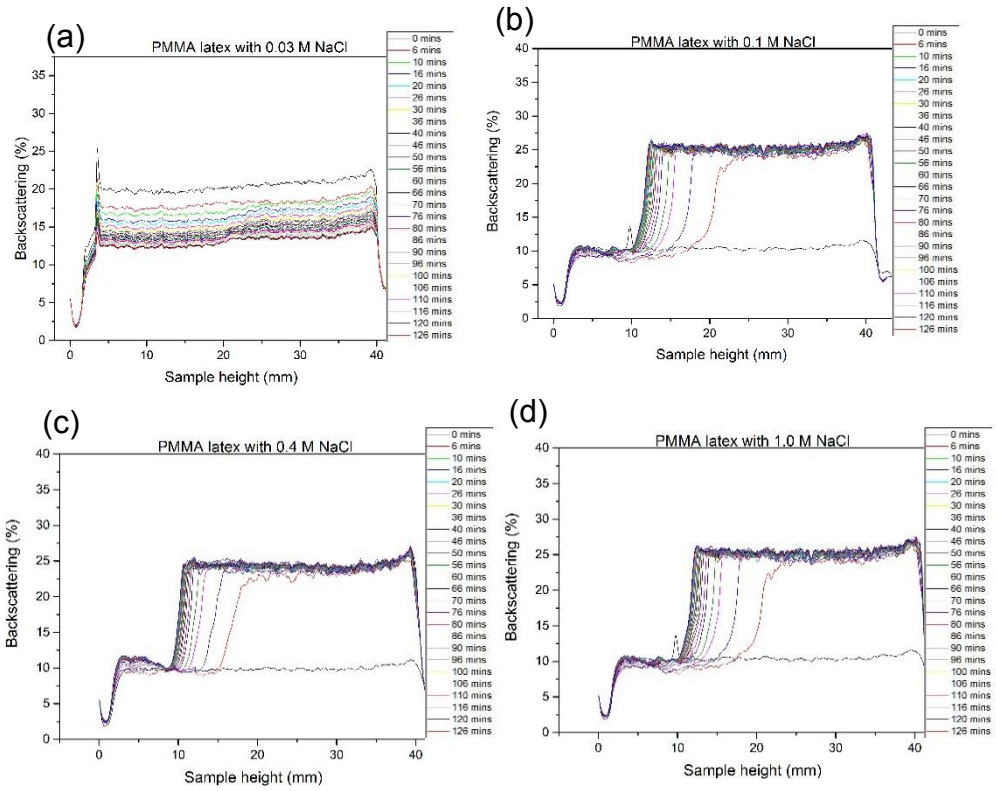

Figure A-13:Backscattered intensity profiles given by Turbiscan as a function of the sample height and versus time for the PMMA latex with different added NaCl concentration (a) 0.03 M, (b) 0.1 M, (c) 0.4 M and (d) 1.0 M.

A.5 Matlab codes

The following codes where used to determine the local Laponite concentration increase in the droplets over time from the different formulations suspensions studied. V and C represents the different initials Laponite volume and concentrations in the different formulations.

A.5.1 Aqueous system

```
clear all
data=importdata('Donnees_Lapwater.txt');
time=data.data(:,1);
C1=0.1;
C2=1;
C3=2;
V01=data.data(:,3);
V1=data.data(:,4);
V2=data.data(:,5);
time


for i=1:14
    if (V01(i)>0 || V1(i)>0|| V2 (i)>0 )
Ct(1,i)=(C1*17.0)/V01(i);
Ct(2,i)=(C2*14.3)/V1(i);
Ct(3,i)=(C3*21.8)/V2(i);
    else
        Ct(1,i)=0;
        Ct(2,i)=0;
        Ct(3,i)=0;
             end
end

Ct'
```

A.5.2 System in binary solvent mixtures

```
clear all
data=importdata('Donnees_Mahoulo.txt');
time=data.data(:,1);
C=0.1;
V50=data.data(:,3);
V60=data.data(:,4);
V70=data.data(:,5);
V80=data.data(:,6);
V90=data.data(:,7);
time


for i=1:35
    if (V50(i)>0 || V60(i)>0|| V70 (i)>0 || V80(i)>0|| V90 (i)>0)
Ct(1,i)=(C*9.6)/V50(i);
Ct(2,i)=(C*8.8)/V60(i);
Ct(3,i)=(C*8.6)/V70(i);
Ct(4,i)=(C*9.6)/V80(i);
Ct(5,i)=(C*9.3)/V90(i);
    else
        Ct(1,i)=0;
        Ct(2,i)=0;
        Ct(3,i)=0;
        Ct(4,i)=0;
        Ct(5,i)=0;
     end
end

Ct'
```

A.5.3 System with added electrolyte

```
clear all
data=importdata('Donnees_Lapsalt.txt');
time=data.data(:,1);
C=0.1;
V1=data.data(:,3);
V2=data.data(:,4);
V4=data.data(:,5);
V6=data.data(:,6);
V10=data.data(:,7);
time



for i=1:35
    if (V1(i)>0 || V2(i)>0|| V4 (i)>0 || V6(i)>0|| V10 (i)>0)
Ct(1,i)=(C*22.1)/V1(i);
Ct(2,i)=(C*22.8)/V2(i);
Ct(3,i)=(C*15.3)/V4(i);
Ct(4,i)=(C*22.0)/V6(i);
Ct(5,i)=(C*23.5)/V10(i);
    else
        Ct(1,i)=0;
        Ct(2,i)=0;
        Ct(3,i)=0;
        Ct(4,i)=0;
        Ct(5,i)=0;
     end
end

Ct'
```

A.5.4 System with surfactant addition

```
clear all
data=importdata('Donnees_Lapsurfactant.txt');
time=data.data(:,1);
C=0.1;
V4=data.data(:,3);
```

```
V7=data.data(:,4);
V15=data.data(:,5);
V30=data.data(:,6);
time


for i=1:42
    if (V4(i)>0 || V7(i)>0|| V15 (i)>0 || V30(i)>0)
Ct(1,i)=(C*15.5)/V4(i);
Ct(2,i)=(C*11.3)/V7(i);
Ct(3,i)=(C*11.2)/V15(i);
Ct(4,i)=(C*10.7)/V30(i);
    else
        Ct(1,i)=0;
        Ct(2,i)=0;
        Ct(3,i)=0;
        Ct(4,i)=0;
             end
end

Ct'
```

A.6 Surface tension and drying sequences

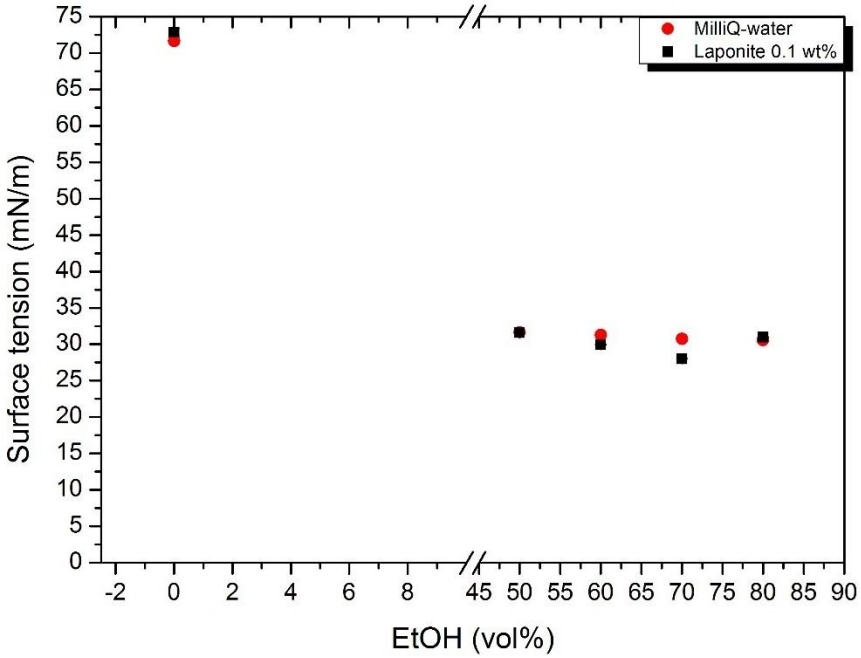

Figure A-14: Surface tension measurements of MilliQ-water and aqueous based Laponite suspensions (at C_{Lap}= 0.1 wt%) as a function of ethanol concentration (C_{EtOH}= 50 to 90 vol%).

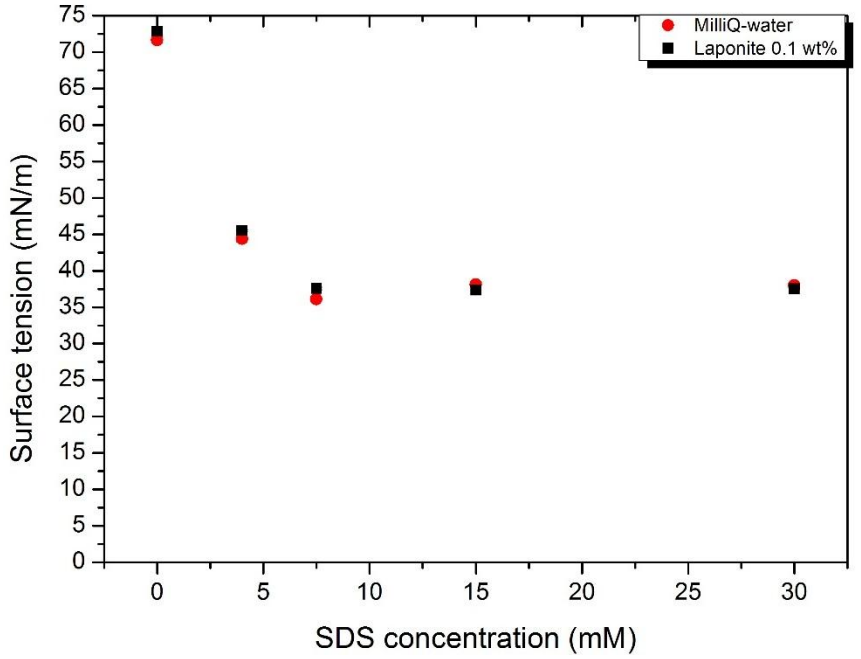

Figure A-15: Surface tension measurements of MilliQ-water and aqueous based Laponite suspensions (at C_{Lap}= 0.1 wt%) as a function of SDS concentration (C_{SDS}= 4 to 30 mM).

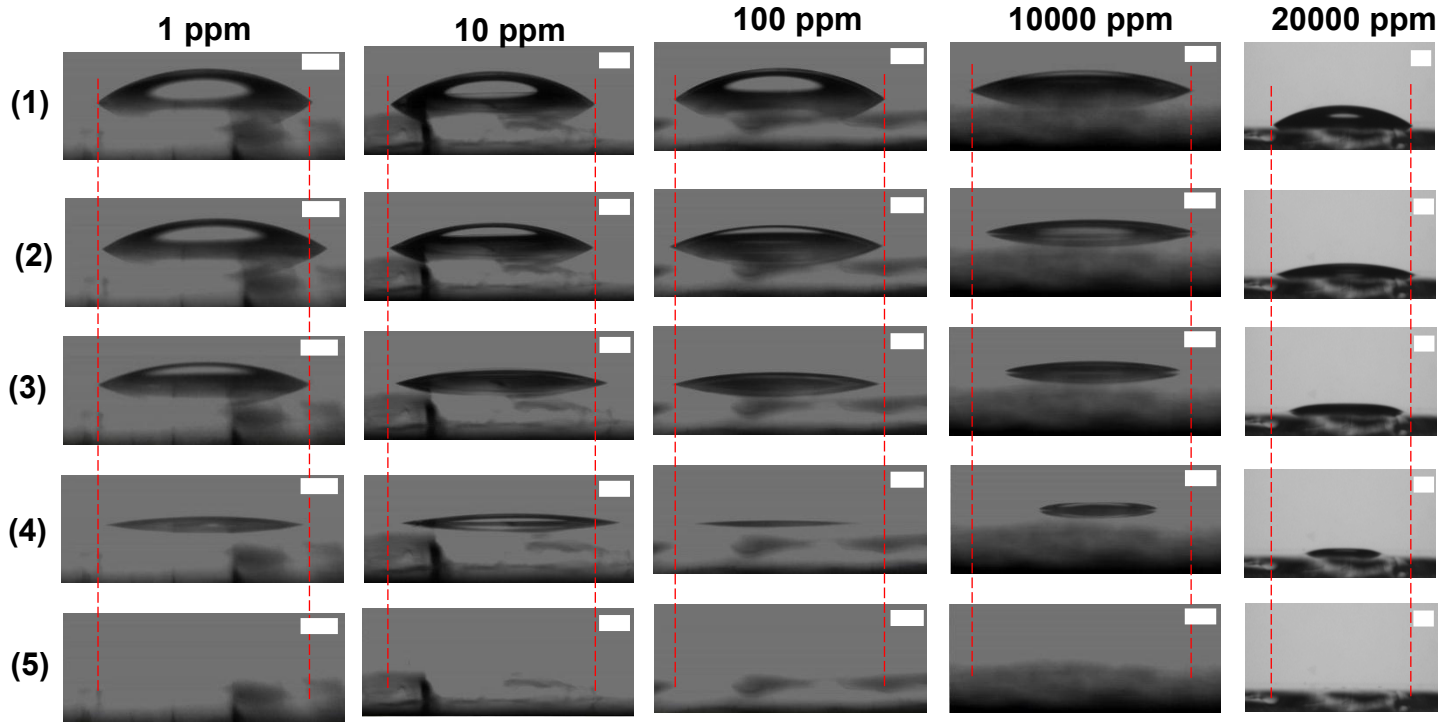

Figure A-16: Drying sequence of aqueous based Laponite droplets on uncoated glass slides as a function of Laponite concentration (C_{Lap}= 0 to 20000 ppm) at different time of droplet lifetime: (1) 0%, (2) 25%, (3) 50%, (4) 75% and (5) 100%. The images were taken from side-view video recordings of the deposition with a contact angle goniometer. The white scale bars represent 1 mm. The red dotted lines represent the initial droplet contact diameter.

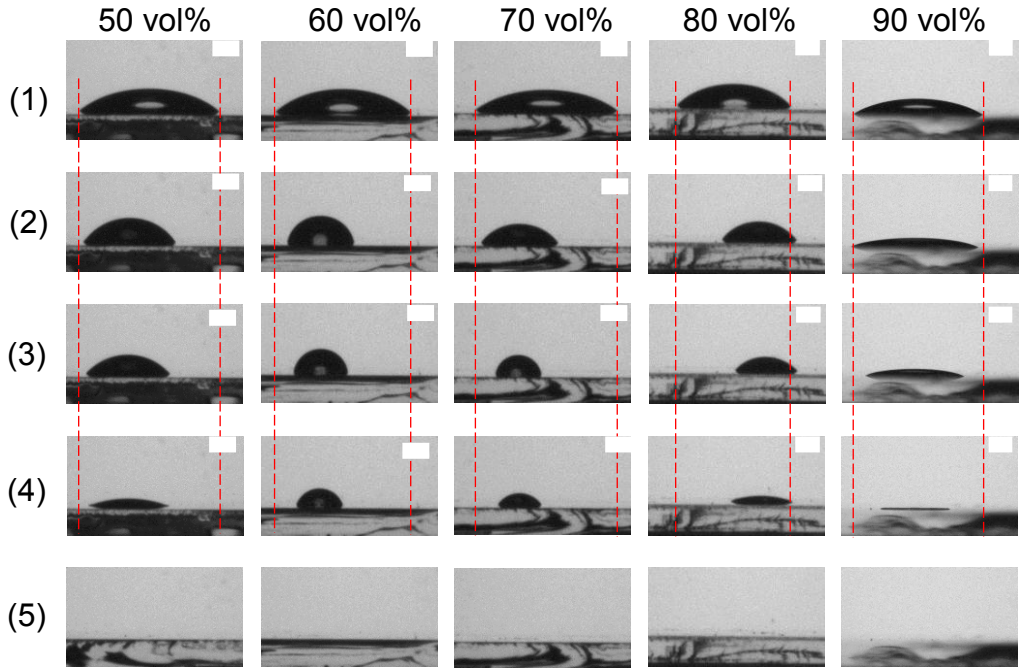

Figure A-17: Drying sequence of aqueous based Laponite droplets on silane coated glass slides as a function of ethanol concentration (C_{EtOH}= 50 to 90 vol%) at different time of droplet lifetime: (1) 0%, (2) 25%, (3) 50%, (4) 75% and (5) 100%. The images were taken from side-view video recordings of the deposition with a contact angle goniometer. The white scale bars represent 1 mm. The red dotted lines represent the initial droplet contact diameter.

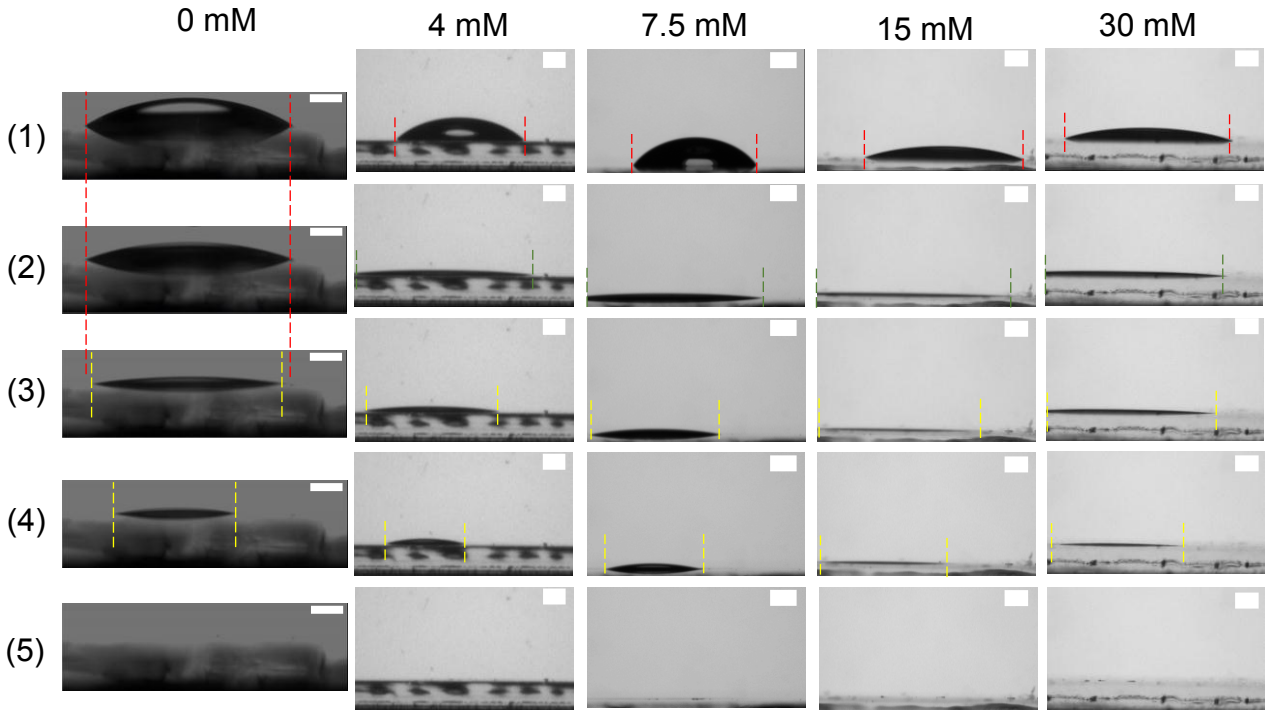

Figure A-18: Drying sequence of aqueous based Laponite droplets on uncoated glass slides with different added surfactant concentration (C_{SDS}= 0 to 30 mM) at different time of droplet lifetime: (1) 0%, (2) 25%, (3) 50%, (4) 75% and (5) 100%. The images were taken from side-view video recordings of the deposition with a contact angle goniometer. The white scale bars represent 1 mm. The red, green and yellow dotted lines represent the initial, advancing and receding droplet contact diameter respectively.

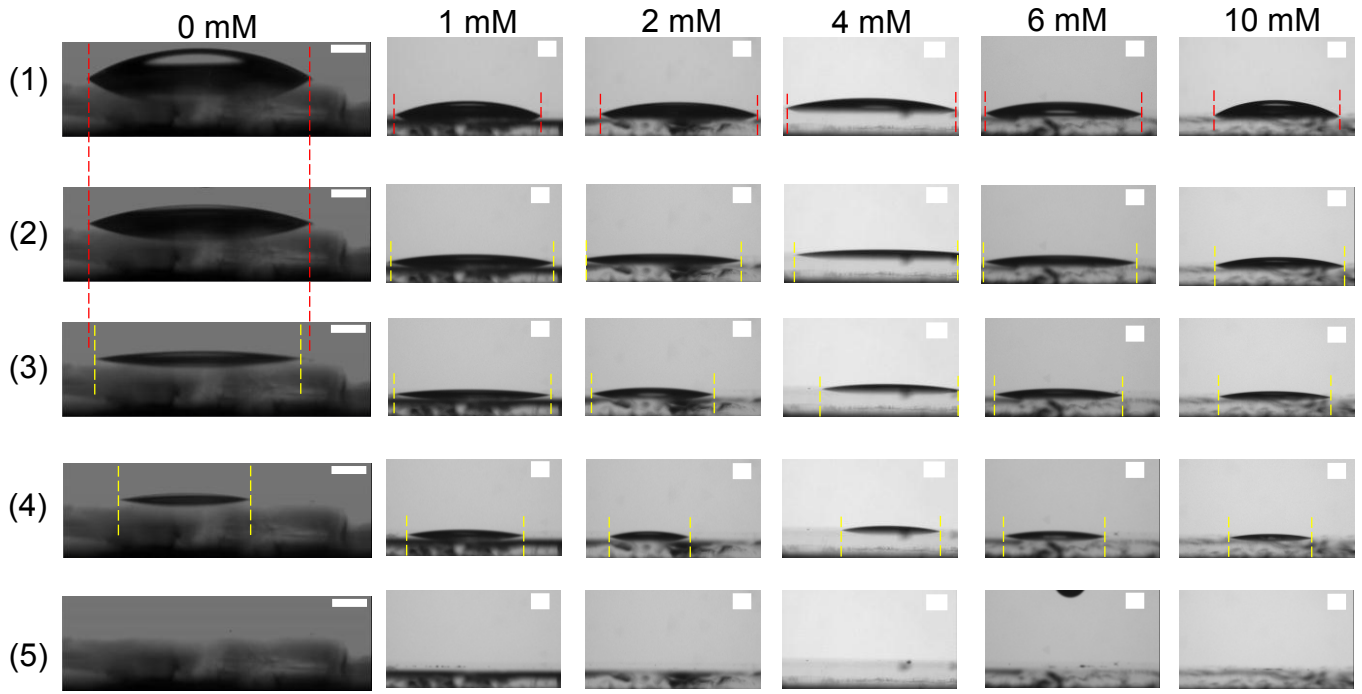

Figure A-19: Drying sequence of aqueous based Laponite droplets on uncoated glass slides with different added electrolyte concentration (C_{NaCl}= 0 to 10 mM) at different time of droplet lifetime: (1) 0%, (2) 25%, (3) 50%, (4) 75% and (5) 100%. The images were taken from side-view video recordings of the deposition with a contact angle goniometer. The white scale bars represent 1 mm. The red and yellow dotted lines represent the initial and receding droplet contact diameter respectivel